RAPID MATERIAL INTERROGATION USING X RAYS FROM A DENSE PLASMA FOCUS

by

MOHAMED ISMAIL ABDELAZIZ MOHAMED ISMAIL

M.Sc. Zagazig University, Egypt, 2007

AN ABSTRACT OF A DISSERTATION

submitted in partial fulfillment of the requirements for the degree

DOCTOR OF PHILOSOPHY

Department of Mechanical and Nuclear Engineering
College of Engineering

KANSAS STATE UNIVERSITY
Manhattan, Kansas

2015

Abstract

Dense Plasma Focus (DPF) devices are multi-radiation sources of X rays, neutrons (when working with deuterium), ions, and electrons in pulses typically of a few tens of nanoseconds. The Kansas State University device (KSU-DPF) was commissioned to be used as a radiation source with the Mechanical and Nuclear Engineering Department. The device is operated by a 12.5 μF capacitor which can be charged up to 40 kV storing an energy of 10 kJ. The static inductance and resistance of the device L_0 and r_0 were measured to be 91±2 nH and 13±3 mΩ.

Experiments have shown that the KSU-DPF device produces 2.45 MeV neutrons with a neutron yield of $\sim 2 \times 10^7$ and 1.05×10^7 n/shots in both axial and radial directions. Ions up to 130 keV were measured using a Faraday Cup. The measured hard X-ray spectrum shows an X-ray emission in the range from 20 to 120 keV with a peak at 50 keV while the average effective energy was estimated, using a step filter method, to be 59 ± 3 keV.

The KSU-DPF device was used as a pulsed hard X-ray source for material interrogation studies using the signature-based radiation-scanning (SBRS) technique. The SBRS technique uses template matching to differentiate targets that contain certain types of materials, such as chemical explosives or drugs, from those that do not. Experiments were performed with different materials in cans of three sizes. Nitrogen-rich fertilizers and ammonium nitrate were used as explosive surrogates. Experiments showed 100% sensitivity for all sizes of used samples while 50% specificity for 5 and 1- gallon and 28.57% for quart samples.

Simulations using MCNP-5 gave results in good agreement with the experimental results. In the simulations, a larger number of materials, including real explosives were tested. To ensure the feasibility of using the DPF devices for this purpose a second device was simulated and the results were encouraging.

Experimental and simulation results indicate that use of DPF devices with simple, room-temperature detectors may provide a way to perform rapid screening for threat materials, especially for places where large number of packages need to be investigated.

RAPID MATERIAL INTERROGATION USING X RAYS FROM A DENSE PLASMA FOCUS

by

MOHAMED ISMAIL ABDELAZIZ MOHAMED ISMAIL

M.Sc., Zagazig University, Egypt, 2007

A DISSERTATION

submitted in partial fulfillment of the requirements for the degree

DOCTOR OF PHILOSOPHY

Department of Mechanical and Nuclear Engineering
College of Engineering

KANSAS STATE UNIVERSITY
Manhattan, Kansas

2015

Approved by:
Major Professor
Dr. William L. Dunn

Copyright

Abstract

Dense Plasma Focus (DPF) devices are multi-radiation sources of X rays, neutrons (when working with deuterium), ions, and electrons in pulses typically of a few tens of nanoseconds. The Kansas State University device (KSU-DPF) was commissioned to be used as a radiation source with the Mechanical and Nuclear Engineering Department. The device is operated by a 12.5 μF capacitor which can be charged up to 40 kV storing an energy of 10 kJ. The static inductance and resistance of the device L_0 and r_0 were measured to be 91±2 nH and 13±3 mΩ.

Experiments have shown that the KSU-DPF device produces 2.45 MeV neutrons with a neutron yield of $\sim 2 \times 10^7$ and 1.05×10^7 n/shots in both axial and radial directions. Ions up to 130 keV were measured using a Faraday Cup. The measured hard X-ray spectrum shows an X-ray emission in the range from 20 to 120 keV with a peak at 50 keV while the average effective energy was estimated, using a step filter method, to be 59 ± 3 keV.

The KSU-DPF device was used as a pulsed hard X-ray source for material interrogation studies using the signature-based radiation-scanning (SBRS) technique. The SBRS technique uses template matching to differentiate targets that contain certain types of materials, such as chemical explosives or drugs, from those that do not. Experiments were performed with different materials in cans of three sizes. Nitrogen-rich fertilizers and ammonium nitrate were used as explosive surrogates. Experiments showed 100% sensitivity for all sizes of used samples while 50% specificity for 5 and 1- gallon and 28.57% for quart samples.

Simulations using MCNP-5 gave results in good agreement with the experimental results. In the simulations, a larger number of materials, including real explosives were tested. To ensure the feasibility of using the DPF devices for this purpose a second device was simulated and the results were encouraging.

Experimental and simulation results indicate that use of DPF devices with simple, room-temperature detectors may provide a way to perform rapid screening for threat materials, especially for places where large number of packages need to be investigated.

Table of Contents

List of Figures

List of Tables

Acknowledgements

I would like to acknowledge the following persons. Without their efforts and support, this work will not be completed. To them I owe my deepest gratitude.

- **Dr. William L. Dunn** (my current advisor) for his guidance and great support since he became my advisor despite his many other academic and professional commitments. His wisdom, knowledge and commitments motivated me to finish this work.
- **Dr. Ali E. Abdou** (my former advisor) who gave me the opportunity to be here at K-State. I really appreciate his support from the beginning teaching me what is the dense plasma focus and fusion. I appreciate his continues encouraging, motivating and advices.
- **Amgad Mohamed** (my friend and colleague) who worked with me in the experimental work hands by hand through my 5 years at K-State. He shared with me all moments of hardship and ease and he was the best supporter. I also acknowledge his contribution in the MATLAB programming.

Dedication

To my wife Reham and my children, Saifelden, Eyad and Salma, thank you so much for you loving, caring and endless dedication.

Chapter 1- Introduction

1.1 Overview

Advances in transportation and communication have changed the world into a more accessible place. It is now very easy to transfer goods between countries and between different locations within a country. Millions of packages are shipped daily all over the world, and it is important, for homeland security purposes, to check packages for threat materials that might cause problems or even disasters. Threat materials include chemical explosives, special nuclear material, biological agents, and narcotics. In recent decades terrorist attacks using hidden explosives have become all too common. An example of this is the bombing that happened at the Boston Marathon in April 2013. Many researchers have been trying to find ways to rapidly detect threat materials, especially explosives, to avoid damage to victims and property. Various techniques have been introduced that depend on different characteristics of explosive materials, including chemical composition, geometry, smell and density. In this work we investigate a rapid way to detect explosives at stand-off using X rays emitted from a dense plasma focus (DPF) device.

1.2 Dense plasma focus

The DPF device is a coaxial plasma accelerator that generates, accelerates and pinches a plasma by self-generated electromagnetic forces. The rapidly formed plasma pinch is hot and dense enough to produce fusion reactions when the working gas is deuterium or a mixture of deuterium and tritium. DPF devices produce different types of radiations, such as neutrons, hard and soft X rays, high energy ions and electrons, over short times, typically tens of nanoseconds. The Kansas State University DPF (KSU-DPF) device was commissioned in 2010 in the Mechanical and Nuclear Engineering department to be used as a radiation source for a variety of applications. The KSU-DPF stores energy up to 10 kJ in a 12.5 μF capacitor and has a total inductance of 91 ± 2 nH and a resistance of 13 ± 3 mΩ. The device produces a hard X-ray emission in pulses of ~200 ns each. The emission spectrum ranges from 20 to 120 keV with a most probable value of 50 keV and an average effective energy of 59 ± 3 keV.

1.3 Signature-based radiation scanning method

The method used in this work is called signature-based radiation scanning (SBRS). SBRS is an active interrogation method developed by Dunn et al. at Kansas State University. Photons,

neutrons or both can be used as interrogating radiation in this technique. This method is not limited to explosive detection but also can be used to detect drugs, nuclear materials, and so forth. However, this work focuses on detecting only nitrogen-rich explosive materials. The main idea of SBRS is to compare the scattered or generated radiation responses (signatures) from an unknown sample with the signatures of one or more templates. A template is a set of signatures from a target known to contain a material of interest. By doing this template matching, the user obtains an indication of whether a sample under investigation is an explosive, an inert or a suspect. The decision here is made automatically, which means it doesn't rely on operator opinion or experience. This fact gives this method an advantage over other methods that depend on the ability of a human operator to remain focused. Another important advantage of SBRS is that it is capable of working at standoff. This means that the operator is not in direct contact with the sample under investigation, which lowers the risks to humans.

Experimental and simulation work are described in this dissertation. Experiments have been performed with different samples in different sizes by using a nitrogen-rich fertilizer to construct a template. On the other hand, simulations using the MCNP-5 code allows us to study more samples, including real explosives. The X-ray spectrum from the KSU-DPF was used as the source in the simulations. Results were compared to results using the spectrum from another DPF device called GN1 to see if the results were strongly spectrum dependent.

1.4 Dissertation outline

Chapter 2 presents some theory and history about dense plasma focus devices. In addition, general information about their construction, theory of operation and emission types is given there. In Chapter 3 the KSU-DPF will be introduced in detail. The device hardware will be explained in addition to all electrical and radiation diagnostic tools involved in this work. The radiation emission from the device will be characterized in Chapter 4 through different experiments that have been performed with some emphasis on the hard X-ray production that will be used in the explosive detection process. Chapter 5 will present a background describing different explosive detection techniques. At the end of the chapter the SBRS technique and its theory will be explained in detail. The experimental work, including procedures and devices in addition to the experimental results will be presented in Chapters 6 and 7. Finally, the simulations will be discussed in Chapter

8, which begins with a brief description of the MCNP-5 code used in the simulation and then discusses the problem simulated and the results obtained.

Chapter 2- Dense Plasma Focus Devices

2.1 Introduction and brief history

Plasma accelerators have been studied from the beginning of research on controlled fusion. In the United States, John Marshal [1] studied coaxial gun systems and, guided by John E. Osher [2], explored the fast coaxial gun mode, which led to the high pressure mode operation. Dense plasma focus (DPF) devices were developed in the early 1960s independently by J. W. Mather [3] in the United States of America and N. V. Filippov [4] in the former Soviet Union. In these devices, a plasma sheath is accelerated and then magnetically compressed to a short-lived (50-200 ns) and dense plasma pinch ($\sim 10^{19}$ cm^{-3}).

2.2 Device configuration

The main difference between Mather and Filippov types is in geometry as shown in Figure 2-1. They have different inner electrode aspect ratios. The aspect ratio is the ratio of axial to transverse dimensions, $A = \frac{Z_0}{2a}$, of the inner electrode. For Mather type [3], $A > 1$ (5-10) while in Filippov type, $A<1$ ($\sim$0.2). Although Mather and Filippov have different configurations, both consist of two coaxial electrodes, an anode and a cathode, separated by an insulator. In addition, both devices are subject to current sheath dynamics, a neutron emission scaling law, and characteristic emission of ions and electrons. Mather type is simpler in design and has an easy access to various diagnostic tools. The Kansas State University dense plasma focus (KSU-DPF) device is a Mather type. As a result, the following discussion will be limited to this type only.

In general, any DPF device is composed of three principal parts: electrical parts which initiate and drive the plasma discharge, mechanical and vacuum hardware, and finally the diagnostic system. A brief description for each part will be given in following sections.

2.2.1 *Electrical circuit*

The electrical circuit of the DPF is composed of a power supply that delivers energy at high voltage to a capacitor/capacitor bank. The capacitor energy is then discharged between the

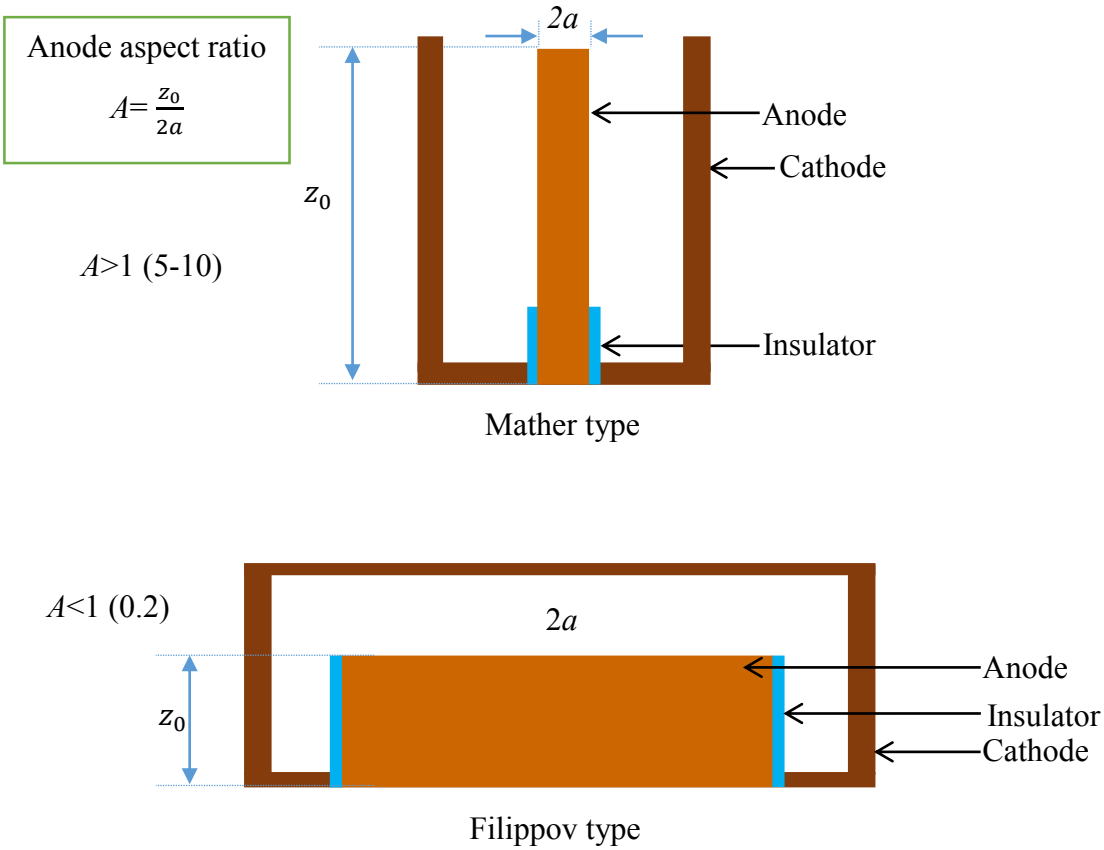

Figure 2-1. Mather and Filippov configurations.

two electrodes by means of an electrical fast switch that is triggered by a separate circuit. The connecting wires and switches have a resistance and an inductance of r_0 and L_0, respectively. The plasma is represented also by a variable resistance and inductance r_p *and* L_p. The wiring diagram of the DPF and its equivalent electrical circuit at the time of discharge is shown in Figure 2-2.

The dense plasma focus is a rich source of multiple energetic radiations such as:

- Fast electrons (0.01-1 MeV).
- Fast ions (0.01-100 MeV).
- Soft (0.1-10 keV) and hard (10-1000 keV) X rays.
- Fusion neutrons, which can be monoenergetic (2.45 and 14.1 for D-D and D-T reactions, respectively) or over a broad range (2 - 11.3 MeV).

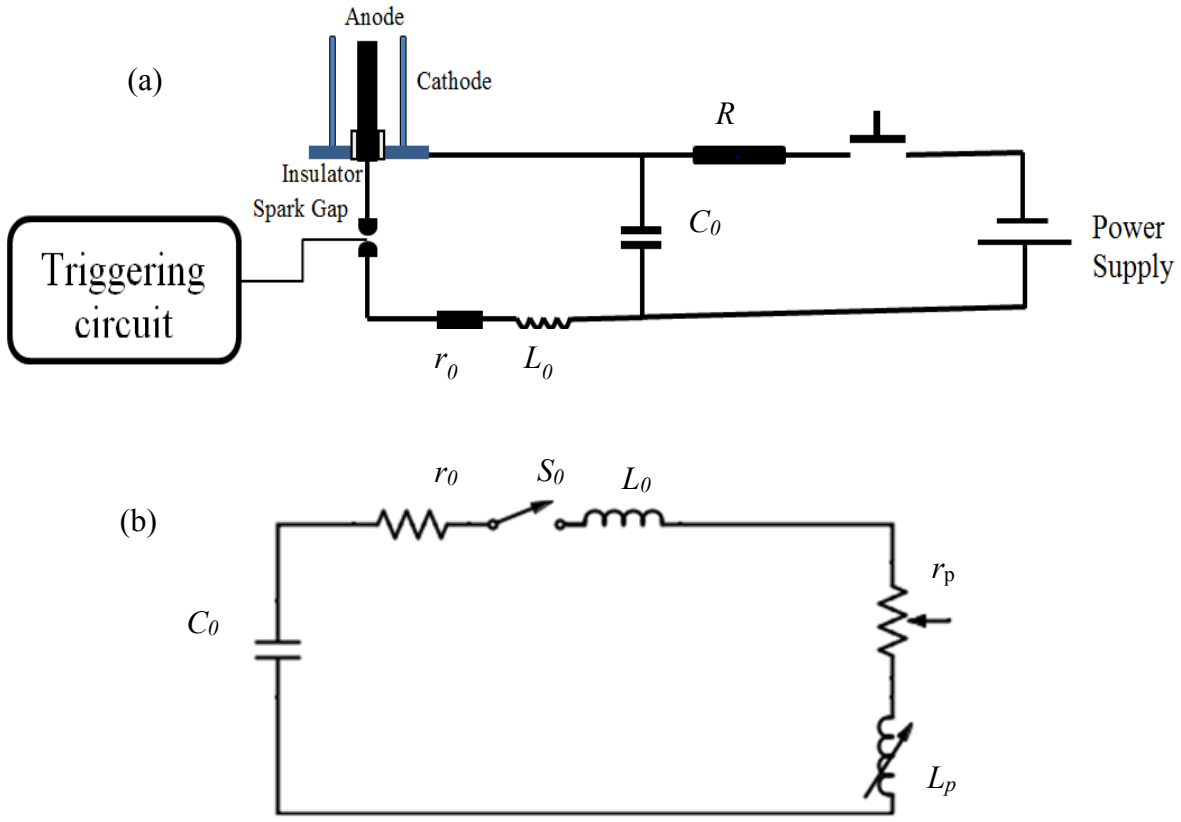

Figure 2-2. Wiring diagram of the DPF device (a) and its equivalent electrical circuit at the time of discharge (b).

Since 1960, much research has been conducted to understand the physics of DPF devices over a wide range of stored energy, from a few hundred Joules, like the FMPF-1 device [5], up to mega joules, like the PF1000 [6].

2.2.2 *Mechanical and vacuum hardware*

The device coaxial electrodes are enclosed inside a vacuum chamber, which is connected to the pumping station to evacuate the chamber a pressure in the range of 10^{-5} mbar before feeding gas. The pumping station is composed of one or more vacuum pumps to evacuate the chamber to the desired pressure in addition to some vacuum valves to control the evacuating process. The pressure inside is monitored by a pressure gauge.

2.2.3 *Diagnostic system*

Diagnostic tools in the dense plasma focus field can be divided into two main categories. The first category is used to measure electrical parameters such as current and voltage, which are

very important to monitor the device operation, while the second category is used to measure the emitted radiations from the device. The basic diagnostics should be measuring the current flowing at the plasma and the voltage drop at the discharging moment. The most commonly used tool for measuring discharge current is a Rogowski coil to measure the total current and a magnetic probe to measure the localized current distribution. Voltage probes are used to measure the transient voltage during the plasma discharge. In the second category, Faraday cups are often used for ion measurements in addition to X-ray and neutron detectors. Signals are typically collected and registered using an oscilloscope and then processed and saved.

2.3 Operation and device dynamics

Running a DPF device is started by charging the capacitor (C_0) using a high voltage power supply through a charging resistor (R), as shown in Figure 2-2 (a). Once the capacitor is charged, it is rapidly discharged by triggering the switch, which directly applies the capacitor high voltage between the two electrodes. The application of that high voltage starts the plasma production as is explained in more detail in the next section. At the time of discharge, the device can be modeled as a simple RLC circuit, shown in Figure 2-2(b). Any DPF operation can be divided into three distinct phases: the breakdown phase, the axial acceleration (axial rundown) phase, and the radial phase. Figure 2-3 (a) shows the three phases while Figure 2-3(b) shows typical corresponding signals for current, voltage, and the time derivative of the current.

2.3.1 *Breakdown phase*

Once the high voltage pulse is applied between the two electrodes, an azimuthally symmetric electrical discharge starts in the working gas under a suitable pressure. According to Paschen's law [7], for deuterium as a working gas in the range from 1 to 10 mbar, the breakdown voltage is less than 1 kV. This value is about an order of magnitude less than the voltage used in most DPF devices, from 10 to 60 kV. Therefore, the breakdown phase in a DPF is always an overvoltage phenomenon. The production of a high current discharge in a DPF device depends on many factors including initial gas condition [8, 9], electrodes, insulator parameters [10, 11] and polarity [12].

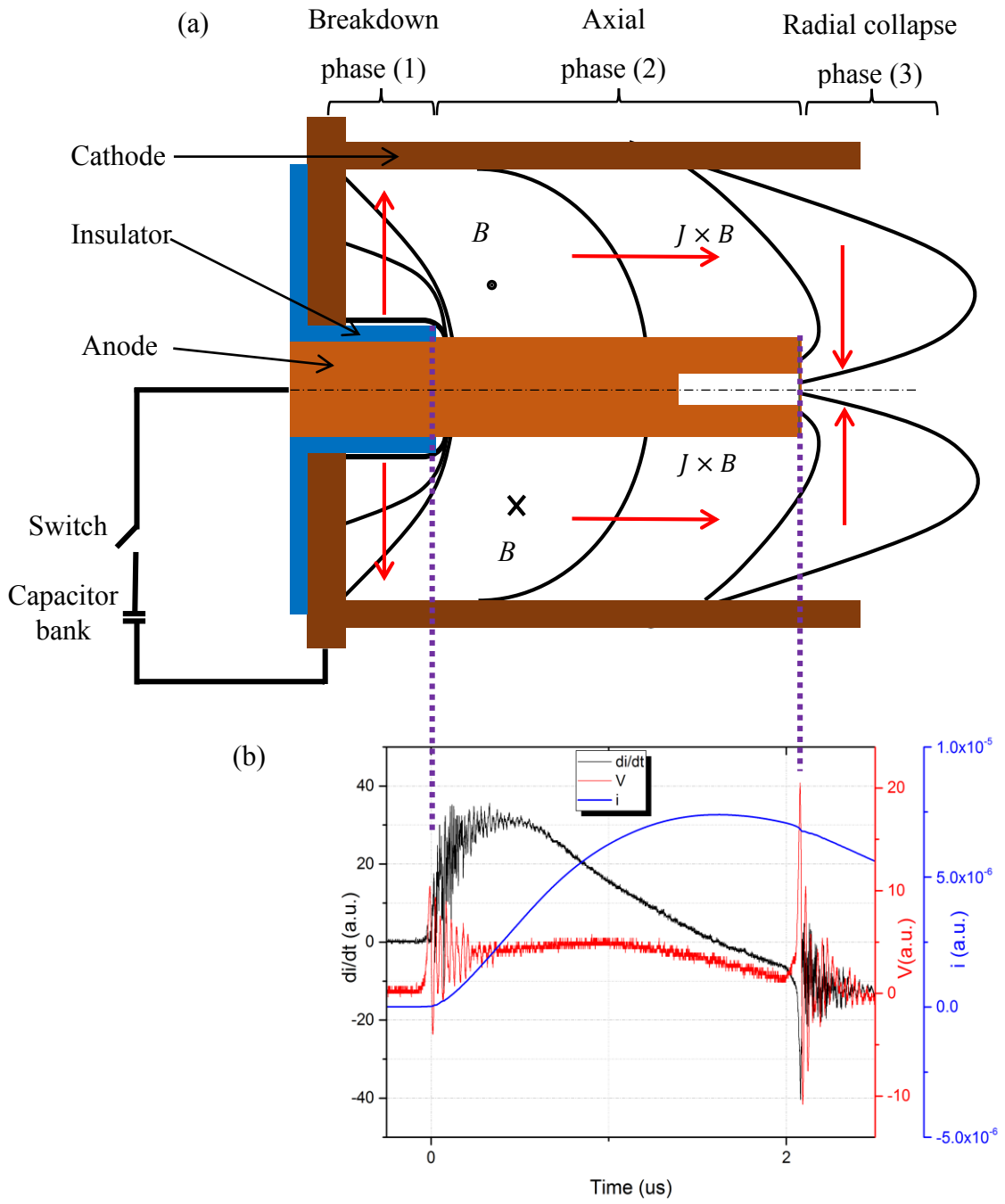

Figure 2-3. Current sheath dynamics in DPF (a) and the corresponding current and voltage signals (b).

Many experimental observations were performed to investigate the breakdown phase using different diagnostics such as an image converter camera, magnetic probes, and a Rogowski coil. Sliding discharge can be developed at the insulator surface at the optimum gas pressure. In the case of a pressure lower or greater than the optimum, either the discharge can be developed in the entire volume or accompanied by filamentary discharge between the two electrodes [10]. The initial discharge starts at the outer electrode edge where the highest electric field exists. Depending on the gas and surface conditions, the ionization propagates to the end of the insulator surface. Once the discharge reaches the insulator end it connects the two electrodes together. The full breakdown happens when the sliding discharge conductance becomes high enough to convert the discharge into a plasma sheath.

Discharging time is independent, within certain limits, of the applied voltage but mainly depends on the gas pressure [13]. The operational pressure range is that range at which initial sliding discharge can be developed properly. Other parameters that affect the discharge developments are insulator material and dimensions [13]. Once the current sheath is formed, current flows symmetrically from the anode to the cathode through the insulator surface. The sheath will be then lifted off outward from the insulator surface by the effect of the Lorentz force, $\vec{J} \times \vec{B}$, in an inverse pinch manner to reach the inner surface of the outer electrode in a process that takes from 50 to 500 ns [14] which prepares for the next stage as shown in Figure 2-3(a). Many investigations have been conducted to simulate the ignition/breakdown phase using one or two dimensional models [15-18].

2.3.2 *Axial acceleration phase*

When the plasma sheath reaches the inner surface of the outer electrode, it starts to accelerate axially to the open end of the coaxial electrodes by the effect of a Lorenz force, $\vec{J} \times \vec{B}$. The radial component of this force pushes the sheath to the outer electrode while the axial component drives it to the coaxial electrode open end. Due to the $1/r$ dependency of the current density J_r and magnetic field B_θ, the Lorenz force value will be higher near the inner electrode, which leads to higher velocity for the sheath around it than anywhere else. Therefore, while it is moving, the sheath will form a parabolic shape while maintaining its axial symmetric character [19], as shown in Figure 2-3(a). K. H. Kwek, T. Y. Tou and S. Lee [20] described the current sheath in the axial

phase as a strong shock wave, driven by a magnetic piston, which ionizes the swept up gas while moving. Between the shock wave and magnetic piston a finite volume of plasma is compressed.

Dense plasma focus devices are designed such that the current sheath reaches the coaxial electrodes open end at a moment close to the first maximum of the charging current, preferably immediately after this moment. This condition is common for all pinch devices and represents the optimization of the energy transfer from the capacitor bank to the plasma pinch. The difference between the current maximum and the end of the axial phase was provided by optimization studies for an optimum energy transfer under given conditions for each device. During the axial acceleration phase the plasma temperatures range from 30 to 60 eV.

Many diagnostic tools have been used to investigate the axial accelerating phase. These tools include magnetic probes [21] and optical detection systems that use Schlieren imaging [20], shadowgraphy, interferometry or image converting cameras. For a wide range of dense plasma focus devices, the measured axial speed ranges from 1.5 to 15 $\mathrm{cm}/\mu\mathrm{s}$ and the sheath thickness ranges from 1 to 4 cm [22]. Experimental observations showed that only 60 to 70% of the total discharge current contributes in the final focus phase [19, 23, 24].

Axial acceleration phase dynamics has been modeled by the snowplow model [25], which estimated reasonably both the current sheath velocity and the phase duration [26, 27] in addition to the 2D sheath profile [28]. Two loss factors were taken into account while fitting the experimental data to the computational model. The first one is the current shedding loss or leakage (f_c), which occurred because of the slow moving diffuse current layer behind the main current sheath or the current retained at the insulator surface. The second factor is the mass loss (f_m) which occurs because of the pressure gradient in the slanted current sheath [20, 29].

2.3.3 *Radial phase*

After arriving at the inner electrode (usually anode) end, the current sheath sweeps around this end and finally collapses under the effect of the radially inward force $\vec{J} \times \vec{B}$. For medium to high energy DPF devices and depending on the device characteristics, this collapse takes from 50 to 200 ns [30]. Current sheath velocity in the radial collapse phase ranges from 7 to 60 $\mathrm{cm}/\mu\mathrm{s}$ depending on many factors such as the electrode geometry, initial gas pressure, current sheath structure and the electrical characteristics of the device.

The plasma inductance rapidly changes during the radial phase and produces an induced electric field in the plasma column. For a constant charging current during this phase, the induced voltage can be expressed as:

$$V_i = I\frac{dL}{dt}, \qquad 2\text{-}1$$

where I is the discharging current and $\frac{dL}{dt}$ is the plasma inductance rate of change.

The importance of the radial phase is due to its extremely high energy density, transient character, intense radiation emissions, high-energy particles and copious nuclear fusion products (for deuterium or deuterium-tritium mixture working gas). The radial phase is subdivided into four sub-phases, namely, compression phase, quiescent phase, unstable phase and decay phase. This classification is based on the reported experimental data. In the following sections these phases will be explained in more detail.

2.3.3.1 *Compression phase*

The radial phase starts with a rapid collapse of azimuthally symmetric but non cylindrical funnel shape plasma sheath inward toward the axis under the influence of the $\vec{J} \times \vec{B}$ force and ends when the plasma column reaches a minimum radius (r_{min}) and maximum density ($\sim 10^{19}$ cm^{-3}). This instant, when $r = r_{min}$, is conventionally considered as a time reference (*t=0)*.

Two heating mechanisms have been observed during this phase. First is the shock heating which is responsible of heating the plasma before the current sheath fronts meet together at the Z-axis. The second mechanism is Joule heating, which becomes the main heating mechanism after the transformation of the plasma structure into a plasma column and the shock wave (reflected on itself at the axis) meets the magnetic piston [31]. The Joule heating mechanism works at the central part of the plasma column which is not being affected yet by the piston. The plasma column will be adiabatically compressed to form the final focus [32].

By the end of this phase a rapid penetration of the magnetic field to the plasma column happens associated with a sharp increase in the plasma anomalous resistivity which produces an increase in the total system resistance [33]. The observed large voltage spike and the dip in the current shown in Figure 2-3(b) are related to that increase in the plasma column impedance and enhanced due to the anomalous resistive effect [31].

Many diagnostic tools were used to determine the electron density maximum value in addition to the electron and ion temperatures. These tools include spectroscopy, interferometry and

laser scattering. The final electron temperature was estimated to range from 1 to 2 keV. The final temperature depends only on the current I and the linear density N based on the Bennett relation, $T \sim \frac{I^2}{N}$, [34], which means the lower the linear density the higher the temperature, while it is independent of the minimum radius of the pinched plasma column.

The pinch column is formed at the end of the compression phase with an approximate diameter on the order of 1 mm and a length of a few centimeters, while the plasma density at this phase is $\sim 10^{19}$ cm^{-3} [35].

Using the snowplow equation to model the pinch at this phase produces a zero radius column. Many attempts have been made to overcome this, for instance by devising a retarding kinetic pressure term or using a criterion for the minim radius such as the Larmour radius. S. Lee [36] indicated that these methods were not energy-consistent and hence he developed an energy balance model which provides the correct end point for implosion trajectory and estimated the correct quasi-equilibrium radius. Moreover, S. Lee [37] developed a complete energy-consistent trajectory when he combined the energy-balance criterion with the slug model. Computed pinch length and minimum radius agreed with the experimental measurements [35].

2.3.3.2 *The quiescent phase*

This phase starts with the expansion of the pinch plasma column. The expansion occurs in both radial and axial directions but the rate of radial expansion is resisted by the confining magnetic pressure. On the other hand, the axial rate of expansion forms an axial shock front due to the fountain-like geometry of the current sheath.

A sudden and sharp change in the plasma inductance starts in the compression phase, which induces an electric field in the plasma column. Under the influence of this electric field, ions and electrons are accelerated in two different directions. Micro-instabilities, such as electron-cyclotron and various forms of beam plasma instabilities, will start at the time when the relative drift velocity between ions and electrons reaches the increasing electron thermal velocities. The plasma temperature continues increasing by Ohmic heating. Moreover, the magnetically confined plasma column becomes hydro magnetically unstable under the sausage (m=0) and kink (m=1) instability modes, will be discussed later in this chapter. The lifetime of the pinch (t_p) can be defined as the time interval between the first compression and the instant of the m=0 instability [38].

2.3.3.3 *Unstable phase*

The induced electric field is enhanced by the growing of the *m*=0 instabilities. This accelerates the electrons to the inner electrode and the ions in the opposite direction. An axial ionization wave front was reported by J. W. Mather and P. J Bottoms [39] at which the measured peak velocity for deuterium is 120 $\mathrm{cm}/\mu\mathrm{s}$ as estimated by using time-resolved interferometry. This confirms that the ionization is formed by the fast deuterons [31, 39]. The hard X rays and neutron pulses start with the beginning of this ionizing front, which will be developed later into a bubble-like structure with several density gradients [40]. The first gradient is due to the separation of the ambient gas from the ionized structure which is caused by the ionization front.

A significant number of impurities are produced due to the bombardment of the fast electrons with the anode, especially the solid anode. Such impurities cause the plasma column to implode near the central electrode [41]. This implosion proceeds gradually through the plasma column which represents the second density gradient as observed by interferometric holograms [31]. This density gradients moves in opposite direction to the anode at a speed much slower than the ionization front until this disruption is broken completely. The estimated electron drift velocity calculated from both the current and the plasma density is on the order of 10^7 m/s, which is greater than the electron thermal velocity ($\sim 10^6$) m/s as estimated from the electron temperature. This is considered as a strong plasma heating mechanism. As indicated by the large amount of Bremsstrahlung radiation [38], the electron temperature then reaches about 4-5 keV.

2.3.3.4 *Decay phase*

The decay phase is the last phase of the radial collapse in addition to being the last stage in the plasma focus dynamics at which the plasma density drops below $2 \times 10^{17} \mathrm{cm}^{-3}$. After the complete breaking up of the plasma column, a large, thin and hot plasma cloud is formed emitting a large amount of Bremsstrahlung radiation. The soft X-ray emission starts suddenly during the pinch decay. Its first peak is reached after the break-up of the pinch and continues at a high and almost constant level for over 300 ns [42]. The neutron pulse, which started at the beginning of the unstable phase, reaches its peak during this phase as well. The implosion time is ~ 100 ns while the plasma column lifetime is ~ 20 ns for a Mather type device with a 1 cm anode radius [35]. During this phase strong emissions of X ray and neutrons also occur.

2.4 Plasma instabilities

Instabilities are one of the major obstacles for the plasma to be confined for controlled thermonuclear fusion. These instabilities create limitations on the amount of current and pressure that can be confined by the magnetic field. As described by the magneto-hydro-dynamic (MHD) equations, cylindrical plasma confined by a magnetic field produced by a current at the pinch plasma surface will produce a radial perturbation δr in the form of [43]:

$$\delta r = \xi_0 e^{i(m\theta + kz - \omega t)}, \qquad 2\text{-}2$$

where ξ_0 is the displacement amplitude and k is the wave number. The coefficient m is the poloidal mode number which determines the azimuthal periodicity of δr. For example when m=0 the perturbations independent of the azimuthal coordinates (sausage instability) while for m=1 helical perturbations exist (Kink instability), as will be explained in the following sub-sections.

2.4.1 *Rayleigh-Taylor instability*

Rayleigh-Taylor instability happens in the situation when there is a dense and incompressible fluid supported by another fluid of a lower density and both fluids exist in an accelerating field. In the case of dense plasma focus the heavy fluid is the plasma which is supported by the magnetic field, which acts as the light fluid.

During the radial compression, the interface between the plasma and the magnetic field, in a magnetically confined plasma, is found to be unstable [44] which causes the boundary of the plasma column to be fluted.

2.4.2 *Sausage (m=0) instability*

In early fusion experiments, the plasma column would spontaneously pinch itself off due to magneto-hydro-dynamic instabilities, especially the sausage instability (m=0). The growth of this instability is due to a poloidal symmetric radial perturbation, which constricts the plasma column slightly in some places. The constricted places are those at which the magnetic pressure is larger than the plasma kinetic pressure (∇p) [45] as shown Figure 2-4. At the constricted areas, the flowing current density (J_z) is producing a stronger magnetic field (B_θ) than the other areas. The stronger the magnetic field the greater the generated force which act inwards to these areas producing more constrictions. As a result a strong longitudinal electric field will be induced due to these rapidly changes in the magnetic fields. This induced electric field will accelerate the

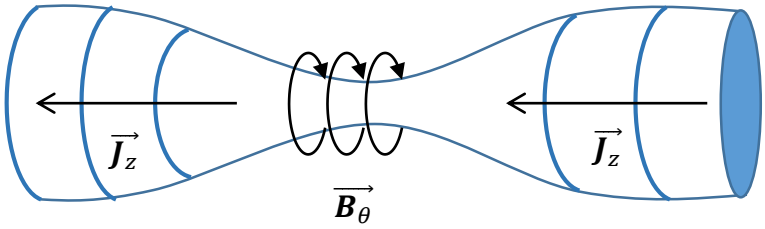

Figure 2-4. A Schematic of the sausage instability.

ions/deuterons within the plasma up to hundreds of keV energies leading to a burst of radiation emission. Sausage instabilities were reported in dense plasma focus by many researchers [45-47]. To stabilize the sausage instability, the plasma column is penetrated by a longitudinal magnetic field comparable in strength to the poloidal field around the column.

2.4.3 *Kink Instability (m=1)*

In the kink type of instability the plasma column twists into a helical shape like a corkscrew as shown in Figure 2-5. If any part of the plasma column is bent, the inner edge poloidal magnetic field will be stronger than the outer edge magnetic field which pushes the plasma for further bending. Kink (*m*=1) instability was observed by Rawat et al. [46] using X-ray pin hole imaging.

To stabilize the Kink instability a strong enough longitudinal magnetic fields is used in addition to a wide enough plasma column to prevent any part of the magnetic field between the plasma and the wall to be closed upon itself once along the length of the plasma column. This method is known as Kruskal-Shafranov criterion [44].

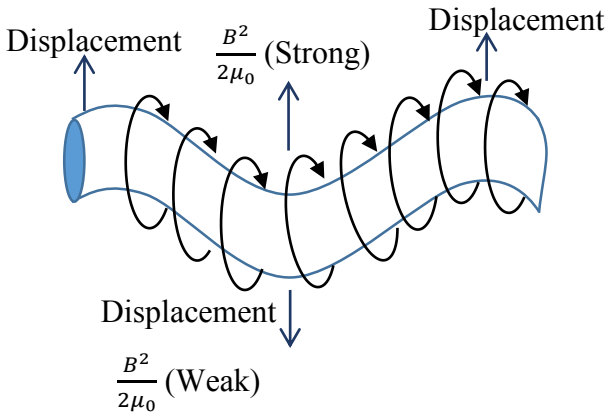

Figure 2-5. Schematic for the Kink (m=1) instability in plasma.

2.4.4 *Micro-instabilities and turbulence*

Bernard et al. [31, 47] studied the magnitude of density fluctuations as a function of direction by using of the light scattering diagnostic technique. They reported that the excitation of waves along the current direction is 1.5 times more intense than that is perpendicular to it which indicated the existence of micro-instabilities. It was also an indication about the correlation of these micro-instabilities with the drift velocity between electrons and ions due to the current flow along the electrode axis. More observations indicated the presence of micro-instabilities and turbulences in the dense plasma focus such as the observation of the anomalous resistivity of the pinched plasma [48], the non-thermal radiation in the microwave range [49] in addition to the high energy ions and electrons bursts.

The rapid change in the plasma inductance, during the radial phase, produces an induced electric field along the pinch. This electric field is enhanced by the growth of the m=0 instability at the end of the quiescent phase. The electron emission starts when the electric field reaches an amount greater than 300 kV/cm, the estimated values for the critical field strength [38].

By measuring the hard X-ray emission from dense plasma focus devices, electron energy was estimated to be in the range from 50 to 500 keV [50], which exceeds the plasma thermal velocity exerted from the electron temperature. Taking these facts into consideration, it was shown theoretically that number of instabilities occurs due to various types of beam-plasma interaction [51]. As indicated by infrared absorption experiments, these beam plasma instabilities will grow rapidly [52, 53].

2.5 Radiation emission from dense plasma focus

Dense plasma focus is a powerful source of radiations, as mentioned before, including energetic ions and electrons, intense X rays and fast neutrons. In this section, each type of radiation will be discussed in detail with the assumed mechanisms for each one.

2.5.1 *Electron emission*

A strong electron emission coming from the pinch was observed in the early experiments performed on dense plasma focus devices. It was proposed that the interaction of the electron beam with the metallic anode is the source of hard X-ray emission [54, 55]. Electron emission from DPF devices was studied in a wide range of devices with stored energy from 1 kJ to 1 MJ, a charging voltage from 10 to 200 kV and a maximum current from 100 kA to 3 MA. Accelerating the electron

beam up to energies more than 100 times higher than the applied voltage was explained by several proposals. One of the proposals relates the electron production in the DPF devices to the m=0 instabilities [45, 56]. As explained before, the growth of the sausage instability (m=0) during the unstable phase enhances the induced electric field which accelerates the electrons towards the anode. Another proposed reason for the high electric fields induced in the plasma is the rapid change of the magnetic flux which occurs at the moment of the plasma compression due to the Lorenz force [57]. One more important mechanism is a sudden increase in the plasma resistivity (anomalous resistivity) while the pinch current remains constant, which causes the pinch column voltage to increase and so the electric field.

Extracting the electron beam is not a simple issue, which makes its measurements difficult. The very low energy electrons are trapped by the strong magnetic field produced by the pinch, which makes them undetectable. The slightly higher energy electrons will also be undetected because they will interact with the filling gas. Only very high energy electrons will [58] be detectable as they will not strongly interact with the plasma, filling gas or electrode system although they might interact among themselves.

The direct coupling to the oscilloscope is difficult because of the high voltage involved in the pinch. Hence, indirect measurements for the electron beam were performed by measuring the X-ray emission from a target, such as the anode. Direct measurements were done also by using Faraday cups [58, 59]. Time resolved spectra were obtained by using a filter method in addition to a $\beta-$ray spectrometer. For time-integrated energy spectra, magnetic spectrometers with photographic recording media were used [58, 59]. Around one ns resolution is required to perform time-resolved measurements [60, 61].

The ion and electron peak energy is not related to the capacitor charging voltage nor to the energy stored in the capacitive pulser, as shown by the experimental measurements. High energy electrons, greater than 1 MeV, were reported from some small machines. As indicated in different investigations, the energy distribution seems to be extremely influenced by the electron detector [62]. As a result, it was very difficult to make a comparison among various experiments, which report one order of magnitude different results for the peak of energy distribution.

Electrons are emitted into low and high energy components. Each one has different characteristics [63]. The low energy component, less than 150 keV, starts when the shockwave reaches the electrode axis and reflects on itself. The time of this emission takes the whole dense plasma

lifetime, long after the pinch disruption [63]. The high energy component, more than 150 keV, takes a short period of time, 10-30 ns FWHM, during the first compression [60, 64] and after the disruption of the plasma pinch column [65, 66].

Direct measurements for the time-integrated electron energy were performed using the nuclear emulsion technique at which a power law was found to fit the experimental data:

$$I(E) = A\,E^{-\alpha}, \qquad 2\text{-}3$$

where the value of α, ranges from 2.5 to 5, depending on the measuring angle with the anode axis, and decreases with the increase of the operating voltage [59, 61, 67, 68].

The pressure of the operating gas is the most important factor that affects the electron emission in the DPF devices. The amount of hard X-rays emitted due to anode bombardment increases with decreasing gas pressure [69]. The energy of the emitted electrons increases with decreasing pressure. The increase in the amount of hard X-rays and the electrons' energies are only noticed with the pressure decrease up to a certain point beyond which the pinch will be weak and poorly formed, which decreases the emission intensity. Moreover, at low pressure the fraction of the current flowing through the main pinch column decreases with the gas pressure. T. Oppenlander et al. [70] indicated that this fraction falls from 80 to 60% with the pressure decrease from 2 to 0.2 torr. With increasing pressure, the beam-plasma interaction will be more effective. As a result, the electron emission from the pinch will decrease and so the bombardment with the anode causing the X-ray emission related to these phenomena will also be reduced [65, 71].

By observing the X-ray emitted [72], Harries et al. showed that the beam energy for electrons over 50 keV is of the order 1 J and current is of the order 200 A. Observing X-rays with energies more than 50 keV from the anode surface on axis implies that electrons are travelling in a beam towards the anode. Therefore, there is a strong electric field between the anode and the dense focus which accelerates the electrons over a distance on the order of 1 cm to energies of the order of 100 keV. Stygar et al. [59] measured a total electron beam current of 17 kA for a 12.5 kJ DPF device.

Emitted electrons from the DPF devices were used in material synthesis applications. Zhang et al. [73] used a DPF device for thin film deposition. They reported that using hydrogen produces the highest electron beam charge and high higher energy electrons (from 50 to 200 keV). Neon also is considered as the next best choice since it produces the next highest electron beam current and mid-energy electrons (from 30 to 70 keV).

2.5.2 *X-ray emission*

The dense plasma focus is a potential source for a wide range of electromagnetic radiations ranging from radio waves to hard X rays. It was developed in the beginning as a fusion device at various isotopes of hydrogen. X-ray emission was not a focus at the beginning but with time, its potential as an intense (soft) X-ray source [63, 74] led to further investigation. Higher-Z gases were used, such as neon (Z=10), krypton (Z=36) and xenon (Z=54), whether in pure form or mixed with light gases. Also, different electrode designs, materials and shapes were used to enhance the X-ray emission in certain energy ranges.

For a focused plasma column with $T_e = 1$ eV, the X-ray continuum is expected to peak in the soft X-ray region at $\lambda_o = 6.2$ A^o. In the case of the high-Z plasma focus, characteristic line emissions fall in the soft X-ray region as well. For instance, the K_α line radiation for nearly fully ionized argon plasma, at a suitably high temperature, is located at 4.2 A^o. For the K_α line for neon, it is at 12.132 A^o. This radiation emission is very useful not only as a probe for plasma diagnostics but also in many applications. Lithography ($\sim 0.9 - 1.5$ keV) [75-78], microscopy ($\sim 0.25 - 2.5$ keV) [79] and micromachining (~ 4 keV) [80] are some applications for the X-ray emission from dense plasma focus devises.

In the plasma focus the electromagnetic radiative processes are quasi-equilibrium thermal radiation from macroscopic plasma structures and radiation due to electrons interacting with non-plasma targets, like the electrodes and/or with periodic electron density structures [81]. The spectrum of emitted radiation in the X-ray region covers the range from 0.3 keV to over 500 keV in a time span from a few to a few hundred of nanoseconds. The emitted X rays can be classified based on energy to soft and hard X-rays. Three main processes for X-ray emission are discussed below.

i. ***Bremsstrahlung radiation (free-free transitions)***

Bremsstrahlung radiation happens when a charged particle is accelerated or retarded in the electric field of other charges. It mostly happens in the DPF because of the acceleration of electrons in the Coulomb field of the ions. Bremsstrahlung radiation is emitted over a continuous spectrum.

For a Maxwellian electron velocity distribution, the free-free emission depends on frequency as $\left(e^{-\frac{h\nu}{kT_e}}\right)$ and the emission intensity is proportional to $N_e N_i Z_i^2 T_e^{-1/2}$, where N_e is the electron density, N_i is the ion density, which has an effective charge Z_i, and T_e is the electron

temperature. Bremsstrahlung radiation can be a dominant radiation process in the case of highly ionized high-Z plasmas. Its spectral emission coefficient per unit wavelength peaks at:

$$\lambda_{max} = \frac{2500}{kT_e} \text{ Å}, \quad 2\text{-}4$$

where kT_e is in eV.

Which is known as the Wien displacement law.

ii. ***Recombination radiation (free-bound transitions)***

In the recombination radiation, a free electron is captured by a bound state of an ion to form a neutral atom or an ion in a lower ionization state. The excess energy of the electron is emitted as a free-bound radiation with energy of:

$$h\nu = {}^{1}/_{2}\ mv^2 + \chi_n, \quad 2\text{-}5$$

which produces a continuous spectrum of radiation for $h\nu > \chi_n$, where χ_n is the ionization potential of the n^{th} state of the atom or ion.

Another possibility may happen when two free electrons hit simultaneously an ion, which is called three-body recombination. One of the electrons will be captured by the ion while the other will carry the excess energy. In this case no radiation will be emitted. The probability of this process is high in the case of higher densities. This process should be minimized in the DPF devices when used as a continuum X-ray source which is difficult in practice because producing X-rays needs high electron density.

iii. ***Line radiation (bound-bound)***

Line radiation happens when an ion, atom or molecule in an excited state undergoes a transition to the ground state by spontaneous or stimulated emission. The emitted radiation will have energy equal to the difference between the energies of the initial and final states, E_i and E_f, respectively. This can be written as:

$$h\nu = E_i - E_f \quad 2\text{-}6$$

This emission appears as a discrete packet of energy because the atomic energy levels are quantized. It is known as characteristic radiation because it shows the characteristic properties of the emitting ions, atoms or molecules.

There are a certain series of line associated with the characteristic X-ray spectra, namely *K, L, M*, etc. series. The *K* series arises from the transition from higher energy levels (n=2, 3,…)

to the *K* shell and similarly the other series involve transitions to other shells. These lines associated with transitions from various higher energy levels are known as α, β, γ, etc.; for instance, the α line is associated with the transition when $\Delta n = 1$ and usually is the most intense and hence the intensity decreases with the lines β, γ, etc., which are associated with $\Delta n = 2,3$, ...

2.5.2.1 *Hard X-rays*

Hard X-ray emission ($E > 10$ keV) from dense plasma focus devices is mainly due to the non-thermal high-energy electron beam bombardment of the anode surface [81]. These electrons are accelerated by the intense electric field produced by the rapid change in the plasma inductance during the pinch compression. If any resistance effect is neglected and only the inductance is taken into account, the pinch voltage (V_p) can be written as [82]:

$$V_p = \frac{d(L_p\, I)}{dt}, \tag{2-7}$$

where L_p and I are the pinch inductance and current. The inductance is given by

$$L_p = \frac{\mu_o}{2\pi} h(t) \ln\left(\frac{r_e}{r(t)}\right), \tag{2-8}$$

where μ_o is the permeability of free space, *h(t)* and *r(t)* are the pinch height and radius and r_e is the anode radius.

If the pinch current, *I*, and height, *h(t)*, are considered constants through the pinching process, then the pinch voltage equation can be written as:

$$V_p \approx -\frac{I\,\mu_{oh}}{2\pi}\,\frac{1}{r}\frac{dr}{dt}. \tag{2-9}$$

By using deuterium as a working gas it was shown that there is a correlation between neutron yield and hard X-ray emission at which the total neutron yield is high when the hard X-ray emission is large [3].

2.5.2.2 *X-ray emission studies*

Time-integrated images showed that the soft X-ray (*E<10* keV) source has a roughly cylindrical shape and is located on the electrode axis at the electrode system open end. Its dimensions are related to the anode radius. The diameter ranges from less than 1 mm up to over 10 mm while the axial length ranges from a few mm to a few cm [35].

X-ray hot spots were reported by Choi et al. [83, 84] with typical dimensions of about 100 μm and occur within 5 ns from the first compression. They concluded that these hot spots are not a sign of the *m=0* instabilities that disrupt the pinch column.

Many techniques were used for soft X-ray emission diagnostics at DPF devices such as:

i. **Pinhole cameras**, with one or more pinholes with suitable filters to record the time integrated spatial/spectral of the X-ray emitting region.
ii. **Microchannel plates,** used for time-resolved spatial distribution of soft X-rays in conjunction with pinhole cameras.
iii. **Semiconductor detectors,** with suitable filters for space integrated temporal distribution of the soft X-ray emission.
iv. **Crystal X-ray spectrographs,** for space-resolved line spectrum analysis.
v. **X-ray streak photography,** for temporal distribution for the X-rays in one dimension (radial or axial).
vi. **X-ray films, X-ray resists and X-ray pulse calorimeters,** for absolute soft X-ray yield measurements.

K. Hirano et al. [62] reported an emission time of the soft X-rays, for low energy deuterium- filled plasma focus device, ranging from 60 to 70 ns and has three peaks. The first peak is located at the end of the compression phase, the second by the unstable plasma column and the third (corresponding to the disruption phase) is due to emission from the inner electrode face.

On a 28 kJ/60 kV device, Zoita et al. [85] studied the effects of radiation processes on the pinch column during the pinch and post-pinch phases. They found dramatic changes in the radiation characteristics of the discharge and in the pinch configuration as well. High aspect ratio pinches emit large amounts of soft X rays in conjunction with a modest number of neutrons and hard X rays in the absence of macroscopic instabilities, which confirmed results obtained from lower energy plasma focus experiments [86]. Moreover, they also reported that the line and the main continuum radiation in the spectral range from 3 to 4 keV are mainly emitted from an intense bright spot of dimension around 50 μm.

Many factors affect the characteristics of the X-ray emission. These include working gas composition and pressure, stored energy, discharge current, material of the electrode and its shape, polarity of the inner electrode and the insulator. Among these factors, gas composition and pressure have the strongest effect. For deuterium DPF the working pressures for the highest X-ray

yield don't coincide [61] with the optimum neutron yield. The insulator influence on the soft X-ray production was studied by Rawat et al. [46]. They discovered that the insulator sleeve length has a strong effect on the average soft X-ray yield. The yield increases with the increase of the insulator sleeve length up to certain optimum length. Increasing the insulator beyond this optimum length causes a decrease in the soft X-ray yield.

The X-ray output Y_X for an X-ray optimized plasma focus device is a function of both the peak discharge current I_{max} and the pinch radius r as in the following empirical formula [87], which is similar to the Z-pinches scaling law:

$$Y_X = \frac{I_{max}^4}{r^2}. \qquad 2\text{-}10$$

2.5.3 *Neutron emission*

Neutron production was noticed since the operation of the first DPF devices in both Mather and Filippov types when the filling gas is deuterium or deuterium-tritium mixture. The neutron production was noticed for all DPF sizes starting from the sub-kilo to the mega-joule energy devices. In high energy devices, two distinct phases were observed for neutron emission [88]. One of them happens during the compression phase and the other one after the pinch break-up. On the other hand, for small and medium scale devices the neutron emission starts by the end of the collapse phase and reaches a peak during the turbulent phase.

2.5.3.1 *Mechanisms of neutron production*

DPF is an intensive source of high energy neutrons with energies of 2.45 and 14.1 MeV when the filling gas is deuterium and deuterium-tritium mixture, respectively. D-D and D-T fusion happens according to the following equations:

$$D + D \rightarrow T\ (1.01\ \text{MeV}) + H\ (3.03\ \text{MeV}) \qquad (50\%), \qquad 2\text{-}11$$

$$D + D \rightarrow {}^3He\ (0.82\ \text{MeV}) + n\ (2.45\ \text{MeV}) \qquad (50\%), \qquad 2\text{-}12$$

$$D + T \rightarrow \alpha\ (3.5\ \text{MeV}) + n\ (14.1\ \text{MeV}), \qquad 2\text{-}13$$

unless there is a need for the 14.1 MeV neutrons, most of the DPF devices use D-D reactions as a source for neutrons. Therefore, the discussion here will be limited to using only the D-D fusion reaction.

Two main mechanisms were proposed for neutron productions in DPF devices; thermonuclear and non-thermonuclear. At the beginning, neutron production was assumed to be thermonuclear [3, 4] at which thermal collisions between deuterons in the plasma bulk produce the D-D fusion reactions and isotropic 2.45 MeV neutrons are expected. More research in this field indicated that there is anisotropy in the neutron production. More neutrons were found in the axial direction than the radial direction [56, 89]. Moreover, the average energy of the axial neutrons was found to be greater than the average energy of isotropic thermonuclear neutrons (2.45 MeV), which led to suggesting other neutron emission mechanisms.

A non-thermal neutron emission mechanism was proposed by Forrest and Peacock [90] when they were measuring the ion temperature in a DPF device using ruby laser light. They referred to a non-thermal mechanism in addition to the thermal one in which the production of neutrons is due to accelerated deuteron collisions with the thermal deuterons in the plasma bulk and the neutral gas atoms outside the pinch (beam target effect).

F. Castillo et al. [91]confirmed the existence of both mechanisms, thermonuclear and beam target. They found a correlation between the X-ray (soft/hard) emission and the neutron emission. They concluded that both mechanisms coexist but each one works separately. In some cases the beam target neutron mechanism is dominating when there is a high hard X ray and low soft X ray emission. In other cases the thermal mechanism is dominating when there is a high soft X-ray and low hard X-ray emission. A third situation arises when there is high emission for both hard and soft X rays which produces high neutron yield.

The neutron anisotropy in DPF devices is the expressed by the ratio of the axial ($\theta = 0^o$) to the radial ($\theta = 90^o$) neutron yields $\left(\frac{Y_{0^o}}{Y_{90^o}}\right)$. For a wide energy range of PDF devices in the kJ scale, anisotropy ratios range from 1.2 to 3.0 [91-93]. Ions are accelerated by the strong electric field produced by magneto-hydrodynamic effects that evolve after the pinch column breakdown, especially the sausage *(m=0)* instability [45, 94, 95] as explained before. As shown from the experimental work, the major contribution to the neutron production is due to the medium (50-100 MeV*)* and low energy deuterium (<50 keV) [96, 97].

Many models were developed to predict the deuteron velocity and neutron production, including the covering ion model [56], crossed field acceleration model [98], and the gyrating particle model [99]. Despite much experimental work and many modelling attempts, ion acceleration and neutron production mechanisms are still not fully understood.

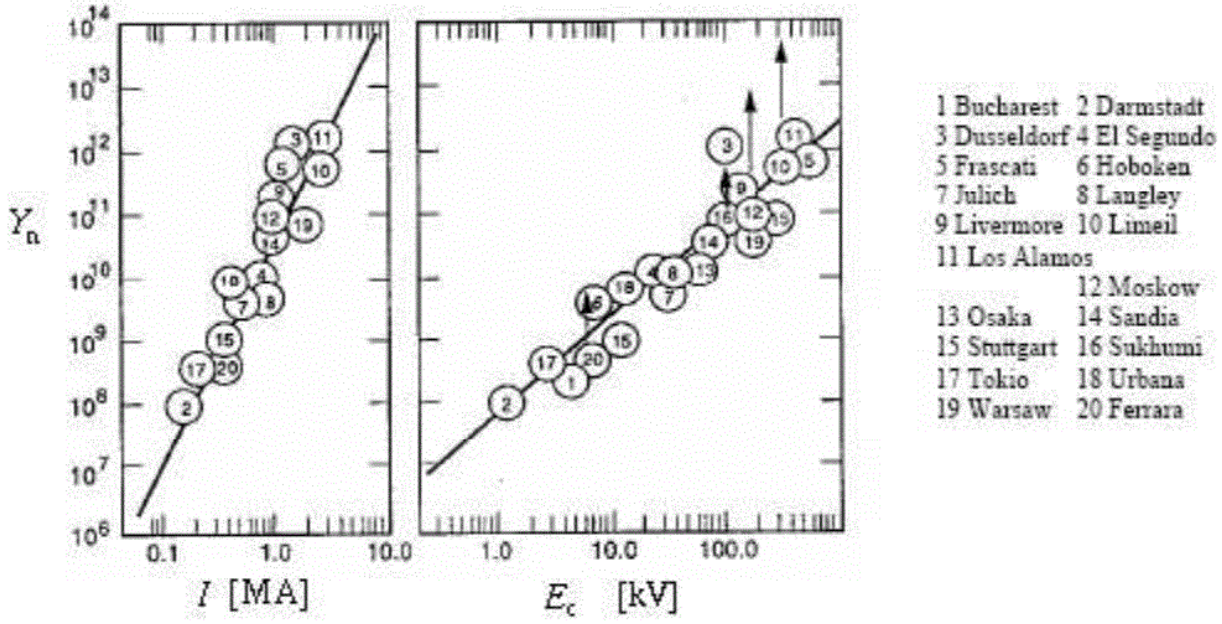

Figure 2-6. Empirical scaling law relates neutron yield to both capacitor bank energy and peak current [100].

2.5.3.2 *Scaling of neutron yield*

Neutron yield emitted from DPF devices is empirically related, separately, to the capacitor bank energy (E_C), peak discharge current (I_{max}), and the plasma current during the focus (I_p). These relations were developed after more than forty years of tests and work in a wide range of DPF devices. Experimental data for many worldwide DPF devices are shown in Figure 2-6.

The scaling law that relates the neutron yield (Y_n) to the capacitor bank energy is [100, 101]

$$Y_n = 10^6 \times E^{(1.5-2.5)}\, n/shot \qquad (E \text{ in kJ}) \qquad 2\text{-}14$$

This relation approximately works for the range of energy from 1 kJ to 1 MJ. The value of the exponent, from 1.5 to 2.5, is mainly based on the device operating parameters which should be optimized in terms of external inductances, charging voltage, gas pressure, gas purity and other factors.

Based on the pressure balance pinch relation [100] $\frac{B^2}{8\pi} = nkT$, where B is the magnetic field, n is the plasma density k is the Boltzmann constant and T is the plasma temperature, and the Bennett relation [102], which states that the plasma temperature depends on both current I and plasma density n, the maximum peak current appears to be the most important parameter that influences the total neutron yield according to the following equation [22, 100-103]:

$$Y_n = 10\, I_{max}^{n}\ \ n/shot, \qquad 2\text{-}15$$

where *n* is between 3 and 4. The uncertainty in the exponent of the current is due to the variability in the amount of current that goes to the pinch plasma even for similar DPF devices delivering similar amounts of peak of discharging current. S. Lee et al. [104] attributed this to the variation in the snowplow efficiency and electro-dynamical process of the machines. The current and energy scaling law is shown in Figure 2-6.

S. Lee et al. [105] stated that the neutron yield should be scaled to the pinch current (I_{pinch}) rather than the total current (I_{total}) or the maximum current, since the pinch current is the one which is involved directly in the pinch formation and responsible for the emission process. The reason that most researchers used the total current for neutron scaling is because it is easy to measure using a Rogowski coil. On the other hand, it is difficult to measure the pinch current even in the large scale devices at which there is enough space to place a magnetic probe. Measurements had high errors and the existence of the probe perturbs the plasma. S. Lee et al. [105] developed a more accurate and convenient way to estimate the pinch current (I_{pinch}) [29]. Based on the Lee Model, numerical experiments were performed using data from the universal plasma focus laboratory [106] which gave the following scaling laws for neutron yield (Y_n) using both peak and pinch currents [106]:

$$Y_n = 3.2 \times 10^{11}\, I_{pinch}^{4.5}\ \ n/shot, \qquad 2\text{-}16$$

$$Y_n = 1.8 \times 10^{10} I_{peak}^{3.8}\ \ n/shot, \qquad 2\text{-}17$$

for I_{pinch} = 0.2 to 2.4 and I_{peak} = 0.3 to 5.7 MeV.

Using the bank energy, the neutron yield will be:

$$Y_n \sim E_0^2\ n/shot \qquad (E \text{ tens of kJ}), \qquad 2\text{-}18$$

$$Y_n \sim E_0^{0.84}\ \ n/shot \quad (\text{at MJ level up to 25 MJ}) \qquad 2\text{-}19$$

Operating the DPF device with a mixture of deuterium and tritium (D-T), instead of only deuterium, will produce approximately two orders of magnitude higher neutron yield because of it has a higher cross section.

2.5.3.3 *Neutron yield enhancement*

An increase in the neutron emission from DPF devices was achieved experimentally in different ways. J. M. Koh et al. [92] recorded a six-fold increase, compared to same size devices,

in the average maximum total neutron yield from the NX2 DPF by using deuterium at relatively much higher pressure of 20 mbar with tapered anode geometry. The electrode material also has a significant effect on neutron emission [107]. The erosion resistance of the material was found to be one of the major factors that affects neutron yield. Using electrodes from different materials (Al, Ti and Cu, stainless steel and Cu-W alloy), the *Cu-W* produced higher neutron emission because it has high erosion resistance.

A five-fold increase was achieved in neutron emission by D. A. Freiwald et al. [108] by injecting a pulsed relativistic electron beam into the plasma focus at the time of the pinch. M. Zakaullah et al. [109] achieved a 25 % increase in the neutron emission of two low-energy (1.15 and 0.58 kJ) DPF devices when they used a mesh type β-source ($_{28}Ni^{63}$) to make a pre-ionization region around the insulator sleeve. S. L. Yap et al. [110] enhanced the neutron emission from a 3.3 kJ DPF device using a deuterium-argon mixture. The maximum neutron yield obtained in their work occurred when using optimum argon doping of 30 % by mass. They inferred that the presence of the small amount of high Z gas in the deuterium will induce the radiative collapse phenomena due to a stronger pinching action. In addition to adding a high Z gas to deuterium, A. R. Babazadeh et al. [111] studied the influence of the anode shape on neutron yield. They achieved an enhancement in the neutron yield by a factor of 3.5 for a flat anode and 1.5 for a conic insert anode by adding krypton with a pressure of 0.1 Torr to the deuterium.

2.5.4 *Ion emission*

Because the DPF device is a source of energetic ions, it has been used for many applications such as ion implantation [112], thin film deposition [113, 114], surface modification [115], short-lived isotope production [116] and semiconductor doping [117]. Understanding the ion emission process in DPF devices is important not only from the application point of view but also to understand the devices physics.

High energy deuteron beams emitted from the DPFs were studied in many laboratories. By using deuteron reactions with lithium and the time-of-flight method, H. Conrads et al. [118] reported more than 10^{15} cm^{-3} deuterons with an average energy of 1 MeV in a hybrid Filippov-Mather device. I.F. Belyaeva and N.V. Filippov [119] measured 10^{13} deuterons per shot in a Filippov type device using nuclear emulsions. In a small DPF device (1 kJ) and using magnetic spectrometer

and time-off-light calculations, H. Krompholz et al. [120] reported a neutron energy spectrum extended to above 400 keV which can be approximated by an exponential function. The estimated total ion flux was about 10^{14} $cm^{-2}s^{-1}$. The fluence of high energy deuterons was also measured by many nuclear activation techniques such as activation measurements with carbon targets [121] using the foil stack technique [122].

Ion emission was observed at pressures lower than the neutron emission pressure in many experiments [59, 95, 118, 123] and the maximum ion emission occurs at a lower pressure than the pressure at which the highest neutron yield is obtained. In addition to that, the angular distribution of the neutron beam usually peaks along the z-axis [14].

Sadowski et al. [124] reported that the DPF devices can emit high energy fast deuterons (>100 keV*)* in addition to impurity and admixture ions in a wide solid angle ($60^o - 80^o$ relative to the z-axis) with energy spectra ranging up to several MeV. The ion emission intensity depends on many factors such as electrode geometry, the supplied energy, working gas, and initial pressure.

Many models in the past were developed to explain the ion production and acceleration [56, 98, 125, 126] but none of them have shown a satisfactory agreement with the experimental measurements over the wide range of devices [127]. Maximum ion emission was observed along the Z-axis at an angle 0^o and decreases gradually with angle inside a conic geometry [128]. On the other hand, [129] reported a drop at angle 0^o of ion fluence for a 3.6 kJ device. The detected number of ions at 90^o was found to be 50% of the number at 0^o as reported by H. Kelly and A. Marquez in their work using a 5 kJ device [130].

Chapter 3- KSU-DPF Specifications

The KSU-DPF is a Mather type device. It was designed to be used as a multi-radiation source for a variety of applications in engineering and sciences at the Mechanical and Nuclear Engineering Department at Kansas State University [132]. This chapter has two parts, one to describe the device hardware and one to discuss the diagnostic tools used to measure the DPF electrical parameters and characterize its radiation emissions.

3.1 Hardware

The device is composed of the tube, an energy storage unit, a switch and triggering system, a charging unit, a vacuum system, and connectors. The diagnostic tools will be described separately in section 3.2.

3.1.1 *Plasma focus tube*

The plasma focus tube is composed of a coaxial electrode system, insulator and vacuum chamber. The anode has 7.5 mm radius and is 115 mm in total length from the cathode base. The active length of the anode above insulator is 100 mm. The top part of the anode in some cases used to be hollow, has a hole 20 mm deep, when it is new then it grows deeper with time due to the bombardment of the high energy electrons. Different anode geometries and materials were used in different experiments. Examples of the anodes used are shown in Figure 3-1.

Stainless steel cylindrical Flat-end	Stainless steel tapered Flat-end	Copper-tungsten alloy cylindrical Flat-end	Stainless steel composite Flat-end	Stainless steel cylindrical hemisphere-end	Copper cylindrical Flat-end

Figure 3-1. Different types and geometries of the anodes used.

The anode is surrounded by a squirrel cage cathode of 27.5 mm radius mounted on a brass disc. The cathode consists of six equally spaced brass bars each of a 120 mm length and 4 mm radius. The anode and cathode are electrically insulated by a Pyrex glass tube 68 mm high and having a wall thickness 1.6 mm. The active part of the insulator is 15 mm, as shown in Figure 3-2. A front and plan view of the device head is shown in Figure 3-3. The electrode system is enclosed in a vacuum steel cylindrical chamber of 290 mm length, 60 mm radius. The chamber has two glass rectangular windows, 55 × 120 mm, and different openings for diagnostic instruments and feeding the gas as shown in Figure 3-4.

3.1.2 *Vacuum system*

The vacuum chamber is connected though a stainless steel tube to a pumping station. The pumping station consists of two stages of vacuum pumps. The first stage is a rotary pump, called

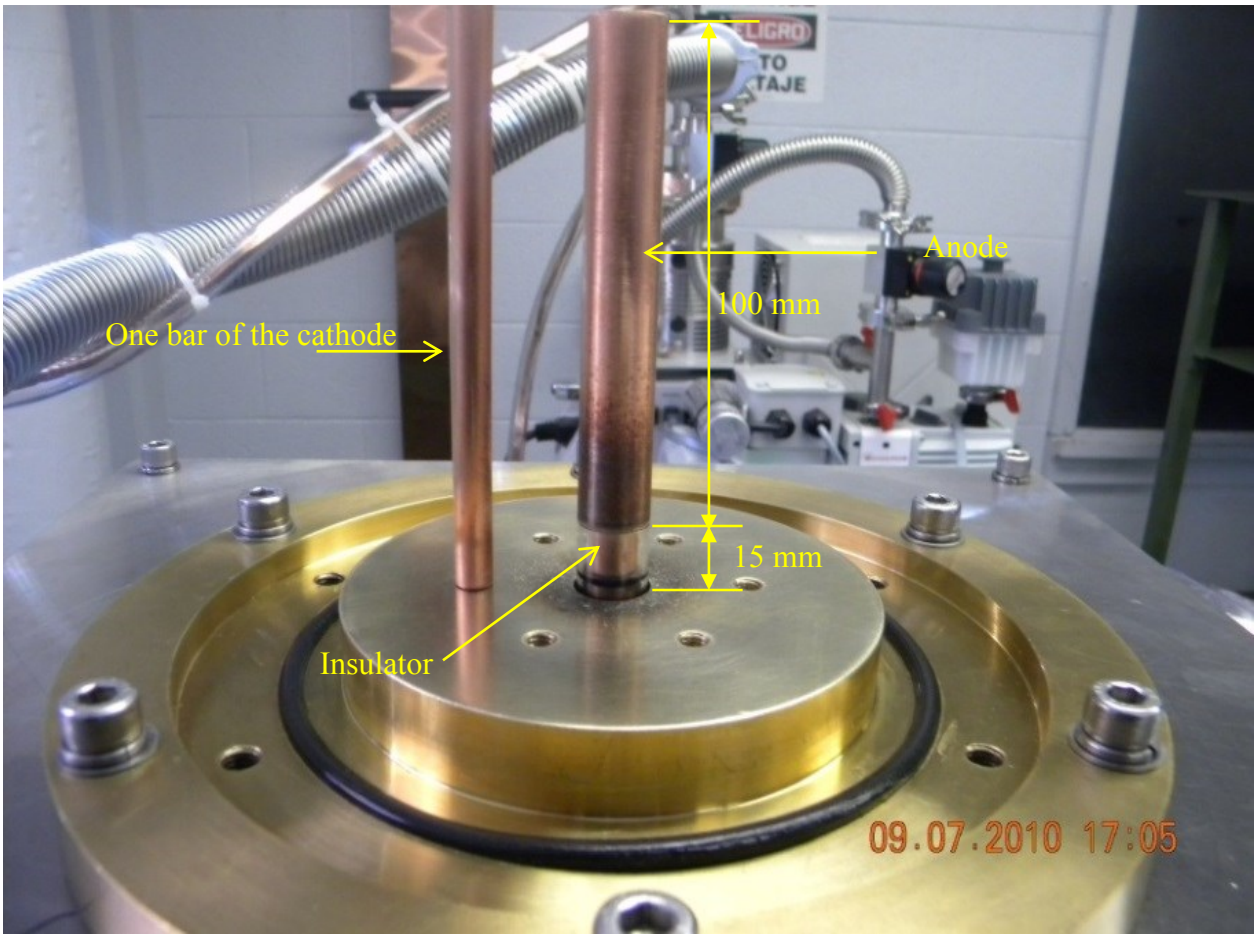

Figure 3-2. Electrodes assembly on the brass base.

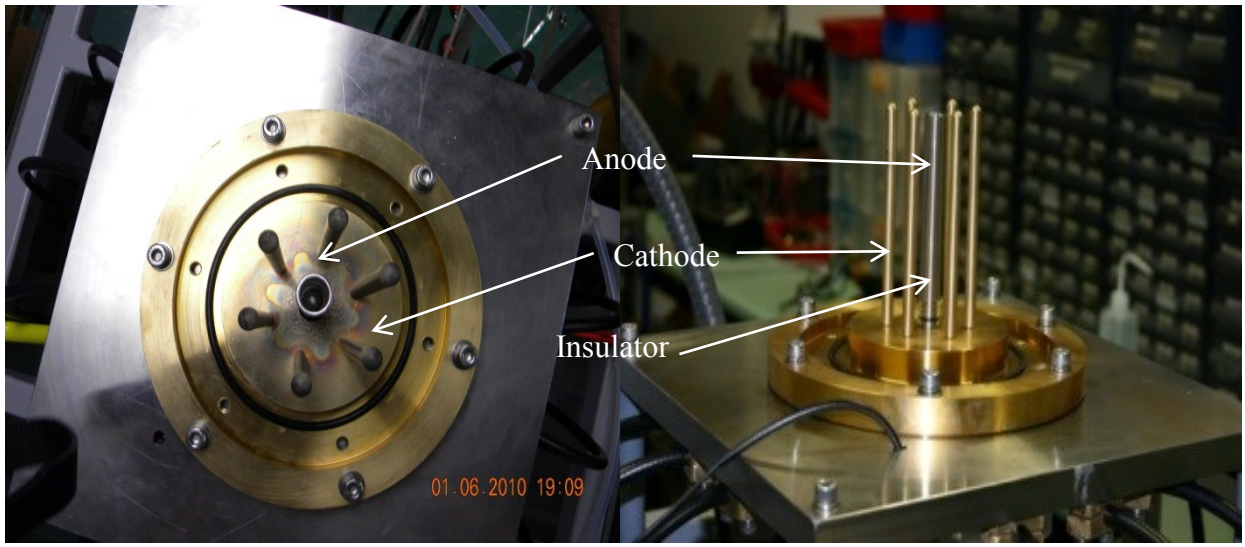

Figure 3-3. Device head- Plan view (left) and front view (right).

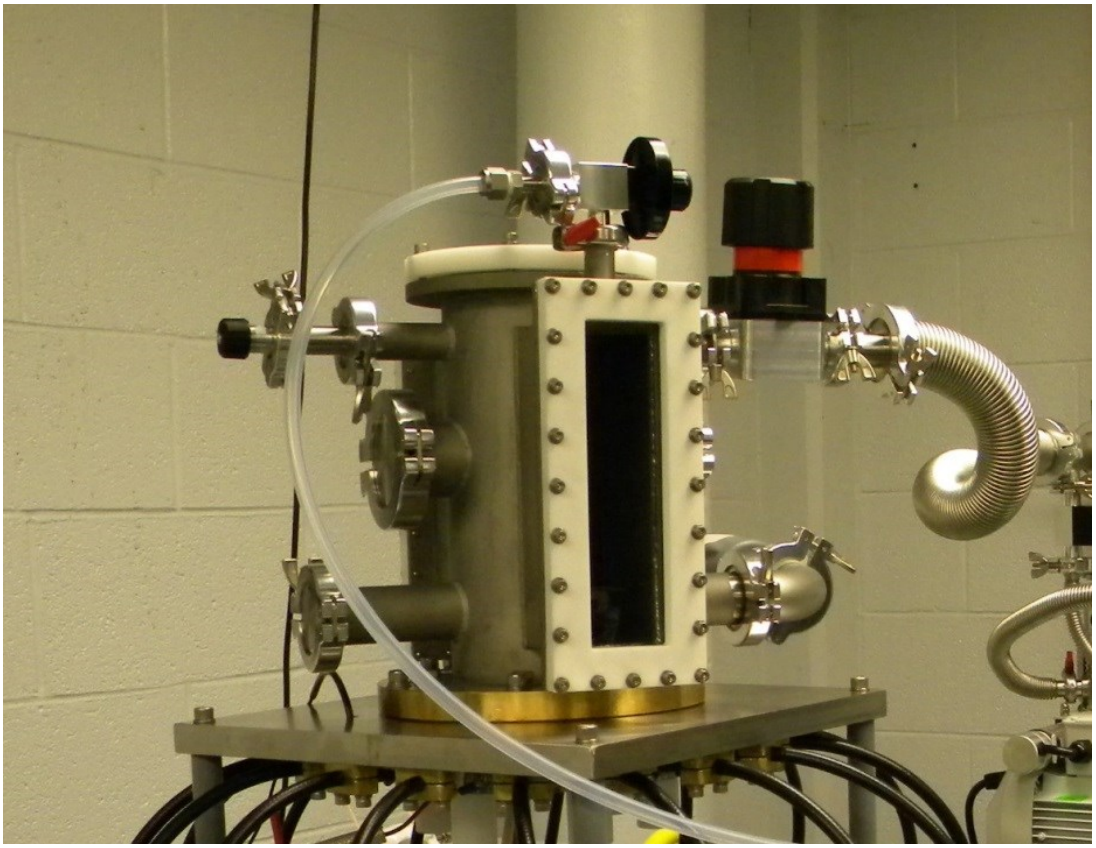

Figure 3-4. The vacuum chamber.

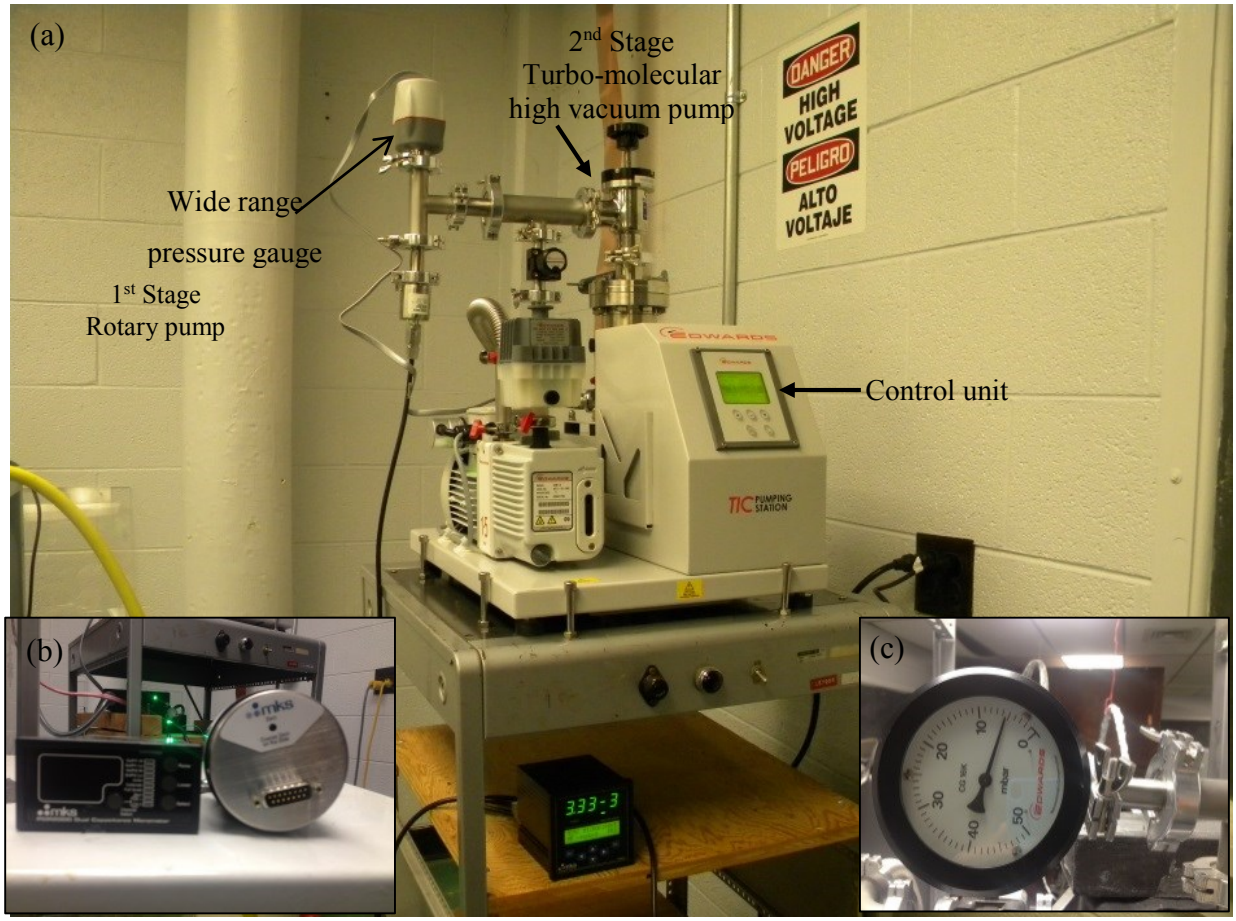

Figure 3-5. The Pumping station and the wide range pressure gauge (a), the MKS Baratron pressure gauge and its controller (b), mechanical gauge (c).

a backing/roughing pump, which works initially to evacuate the system up to the range of $\sim 10^{-2}$ Torr. The backing pump used in the KSU-DPF device is an EDWARDS E1M1.5 model which has a pumping speed displacement of 1.2 ft^3/min and an ultimate pressure of 1.1×10^{-3} Torr. After reaching values of $\sim 10^{-2}$ Torr inside the chamber, the next pump stage is placed into operation to reduce the pressure inside to a value in the order of $\sim 10^{-6}$ Torr. The second pump stage used in the device is an Edwards EXT75DX model turbo-molecular high vacuum pump which h has a pumping speed of 66 L/s. The ultimate pressure of this model can reach a value of the order of $\sim 10^{-10}$ Torr depending on the backing pump and the pumped gas. A picture of the pumping station is shown in Figure 3-5(a).

Three pressure gauges were used including a wide range gauge EDWARDS WRG-S-NW25, a MKS Baratron capacitance manometer and a mechanical pressure gauge. The wide range

pressure gauge, Figure 3-5(a), is a combined inverted magnetron and Pirani gauge in a single compact unit and works at the pressure range from 100 to 10^{-9} mbar. It is connected to a meter at the pumping station control unit. The MKS Baratron, type 627B, is an absolute pressure transducer designed to provide an accurate, reliable and repeatable pressure measurements in the range from 1 kTorr to as low as 0.02 Torr full scale. It is connected to a MKS controller, Model PDR200 Dual Capacitance Diaphragm Gauge, which supplies 615 V at up to 0.75 A to the MKS Baratron in addition to displaying the pressure. The MKS Baratron and its controller are shown in Figure 3-5(b). The mechanical gauge, an Edwards CG16K, shown in Figure 3-5(c), is capsule dial gauge barometrically compensated with a NW flange fitting. It covers a range from 0 to 50 mbar and is used to monitor the pressure during the device operation.

3.1.3 *Energy storage unit*

The energy storage unit in the experiment is the capacitor bank, shown in Figure 3-6(a). The capacitor bank consists of a single General Atomics capacitor of 12.5 μF ± 10% with a total inductance is ~40 nH. The capacitor can be charged up to 40 kV voltage storing an energy up to 10 kJ.

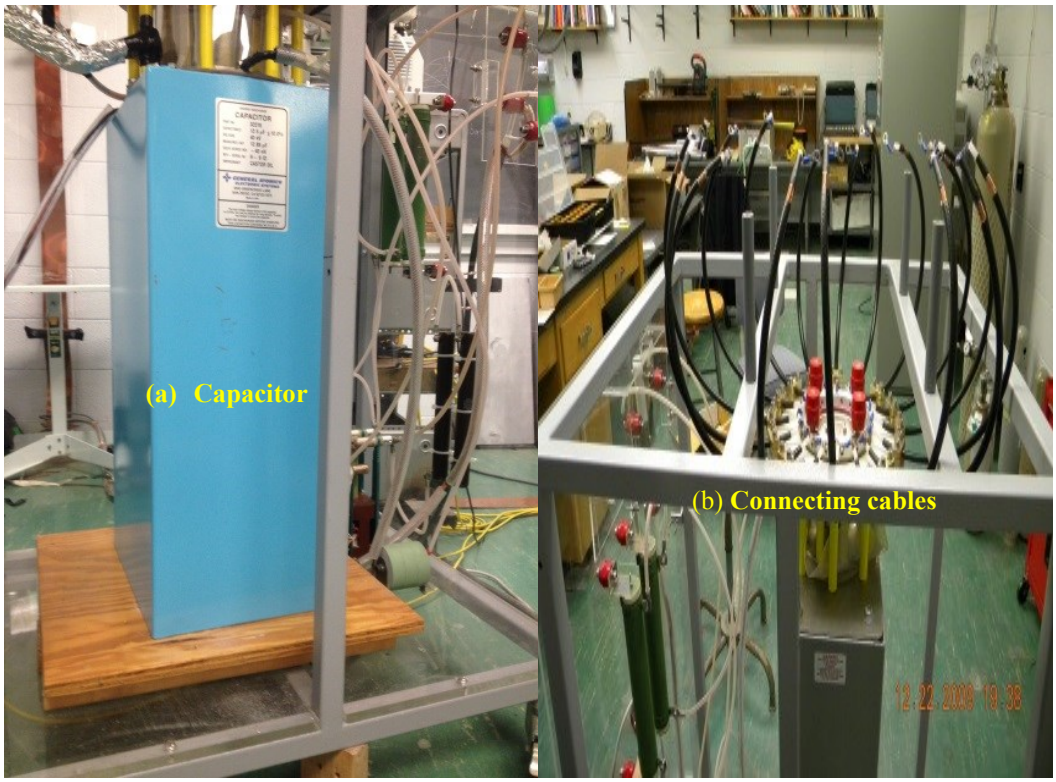

Figure 3-6. A picture of the capacitor unit (a) and connecting cables (b).

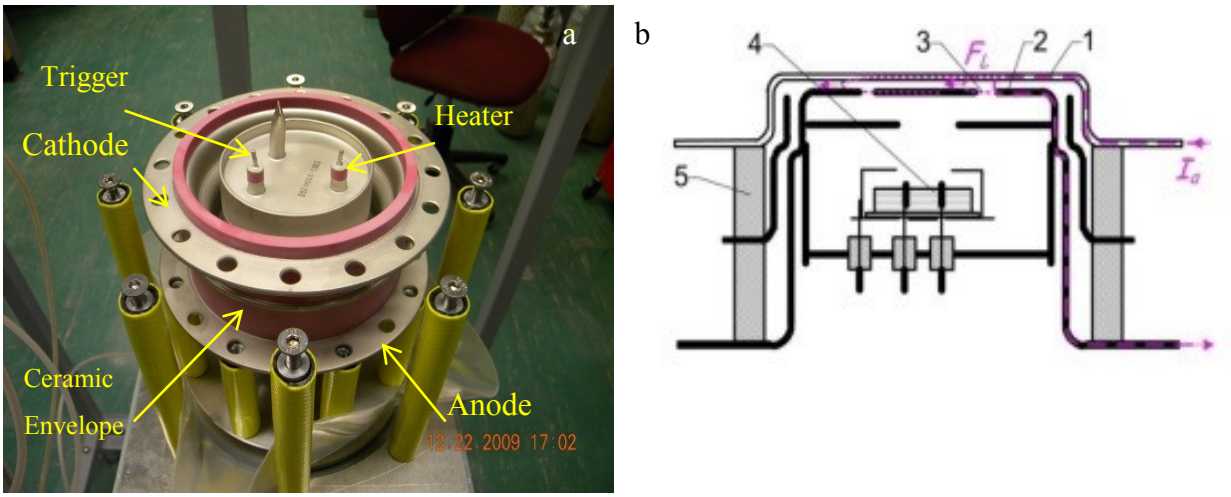

Figure 3-7. Thyratron (a) and its circuit diagram (b)

1- Anode, 2- cathode, 3- Injection hole, 4- trigger unit, 5- Insulator, I_a-thyratron current direction in case of one-side switching, F_L- Lorenz force direction [131].

3.1.4 *Switch and triggering system*

A fast way is needed to rapidly switch the energy stored in the capacitor bank to the electrode system. This process is implemented by using a low pressure switching device with a cold cathode, called a Pseudosparkgap (PSG) switch. The model is a hydrogen-filled thyratron TDI1-200 kA/25 kV with 10 ns time jitter. It is a gas-filled tube used as a high power electrical switch. The PGS switches have stacked ceramic metal construction using hydrogen as a filling gas in a pressure range from 0.2 to 0.6 mbar (in operational mode). The appearance and construction details for the TDI1-200 kA/25 kV are shown in Figure 3-7. The thyratron is connected to a heating and triggering circuit to be triggered remotely. It is connected to the electrode system by a set of 12 parallel coaxial cables RG58 C/U, 50 Ω impedance. Connecting cables are shown in Figure 3-6(b).

3.1.5 *Charging unit*

To be charged, the capacitor is connected to a power supply. The power supply that was used is a General Atomics Electronic Systems Inc. (GA-ESI) CCS power supply. The GA-ESI CCS series is a modular design, high efficiency capacitor charging power supply line. It is designed

Figure 3-8. The power supply (left-top), its remote control (right-bottom) and the cabinet (right).

for constant current capacitor charging. The power supply can be controlled locally using the front panel controls or remotely by a 25-pin remote control interface which was used in our device. The power supply is mounted in a cabinet with another unit to control its power input in addition to the power input to the dump switch. This dump switch is used to ground the capacitor after pulse or in the case of an emergency. The power supply, its remote control and the whole cabinet are shown in Figure 3-8.

3.2 Diagnostics

Diagnostics in the DPF devices can be divided into two main categories. The first is the electrical diagnostics which are used to investigate the performance of the pulsed power system that generates and drives the plasma. The second category is the radiation diagnostics, which are used to obtain information about the emitted radiation from the DPF device.

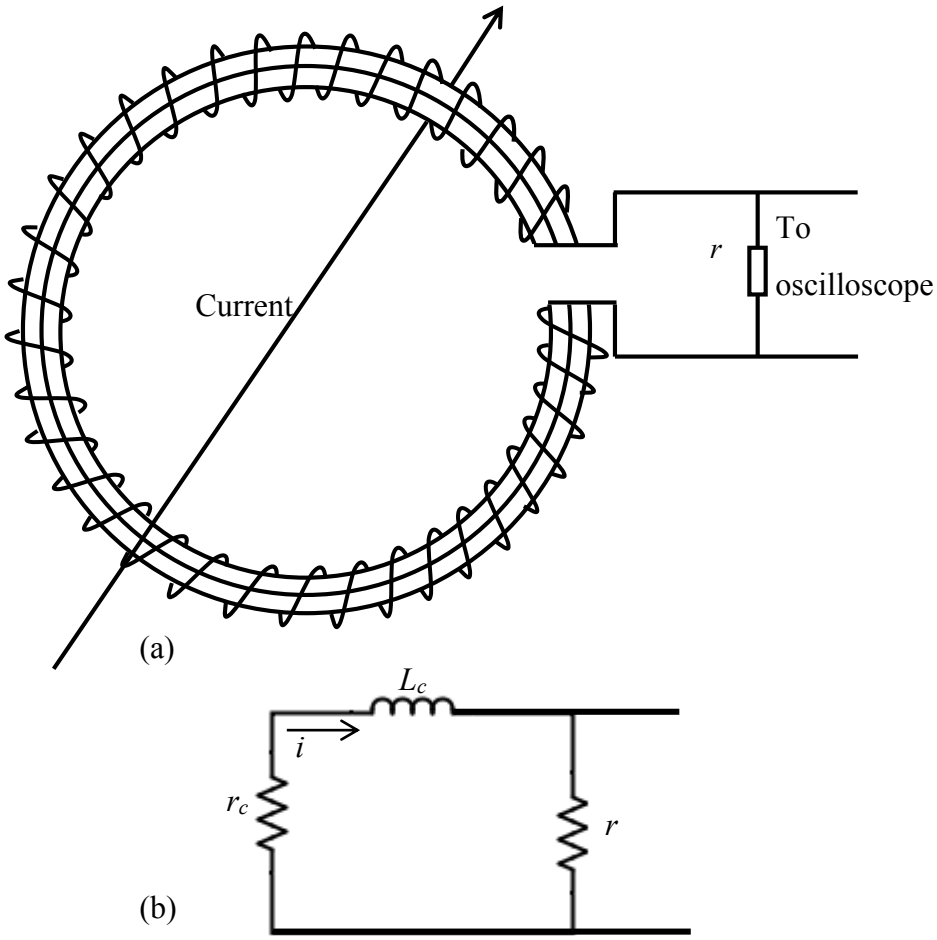

Figure 3-9. Schematic of the Rogowski coil (a) and its equivalent circuit (b).

3.2.1 *Electrical diagnostics*

Rogowski coils and voltage probes are among the most widely used electrical diagnostic tools for testing DPF devices.

3.2.1.1 *Rogowski coil*

Current signals are one of the main features used to characterize DPF devices. Many device characteristics can be investigated using the current signal, such as the axial and radial phase dynamics and the energy transferred to the plasma pinch. The most common way to record the current trace is to use a Rogowski coil. The Rogowski coil is a multi-turn solenoid bent to form a torus, see Figure 3-9 (a). It works as a secondary for a primary coil which is the current to be measured. The equivalent circuit of the Rogowski coil is shown in Figure 3-9(b) in which L_c and r_c represent

its inductance and resistance, respectively, *i* is the induced current in the coil and *r* is the terminating resistance. Changing the current (*I*) with time in the primary coil will produce an induced emf equal to $V = k_1 \frac{dI}{dt}$ in the coil. The equivalent circuit equation then is

$$L_c \frac{di}{dt} + (r + r_c)i = k_1 \frac{dI}{dt} \qquad 3\text{-}1$$

The coil can work in integrating or differentiating modes. In the integrating mode the inductance is much greater than the resistance ie. $L_c \frac{di}{dt} \gg (r + r_c)i$. Solving equation 3-1 based on this condition will produce the following equation for the voltage output on the coil terminals:

$$V_0 = ri = \left(r \frac{k_1}{L_c}\right) \times I = k_2 I \qquad 3\text{-}2$$

Equation 3-2 indicates that the voltage output of the coil is proportional to the transient discharge current going through it. On the other hand, in the differential mode the resistive part is much greater that the inductive one ie., $(r + r_c)i \gg L_c \frac{di}{dt}$. Solving equation 3-1 based on this condition will produce the following output voltage

$$V_0 = ri = \left(\frac{rk_1}{r_c + r}\right) \frac{dI}{dt} = k_3 \frac{dI}{dt} \qquad 3\text{-}3$$

Therefore, the output voltage is proportional to the derivative of the discharge current.

The Rogowski coil used at the KSU-DPF, shown in Figure 3-10(a), was designed to work in the differentiating mode, in order to observe the fast dynamic changes in the device impedance.

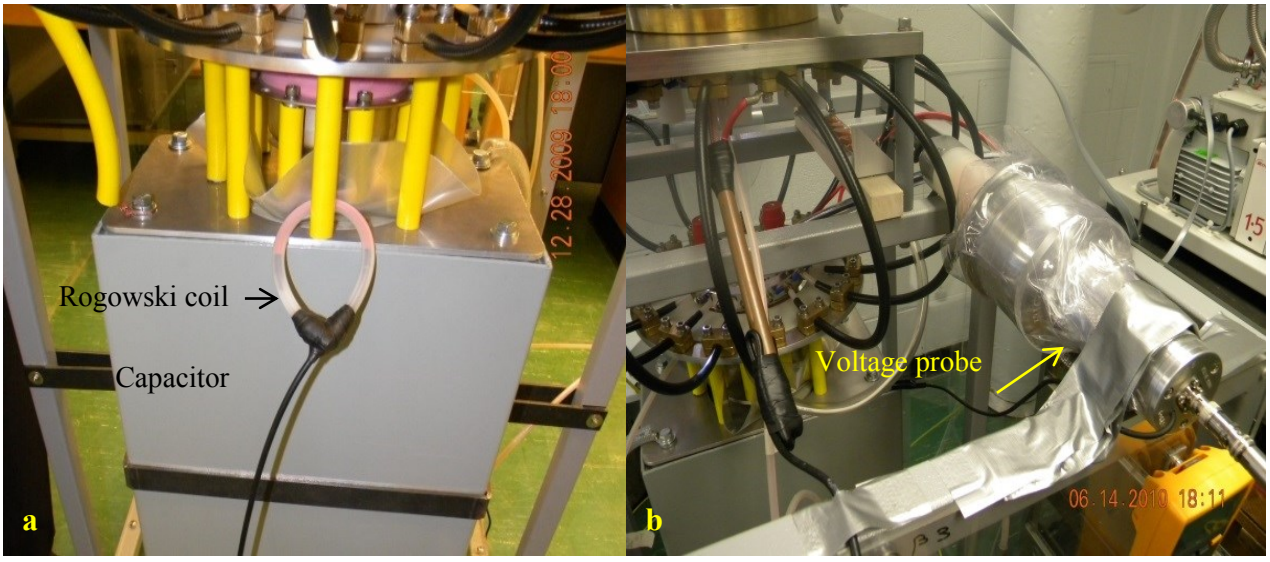

Figure 3-10. Pictures for the Rogowski coil (a) and the voltage probe (b).

The terminating resistor used was a 50 Ω current viewing resistor.

A calibration factor should be calculated for the Rogowski coil to be used to measure the absolute value of the peak discharge current. To obtain the calibration factor, the output signal of the coil, the current derivative (*dI/dt*), was numerically integrated to obtain the current signal (*I*). A sample of the numerically integrated signal at 17 kV discharging voltage is shown in Figure 3-11. The DPF is a low impedance device that can be represented by an RLC circuit. As a result, a discharge current trace will be in the form of a damped sinusoid [132], as shown in Figure 3-11. For an RLC circuit, the relation between the current and other circuit parameters will be [133]:

$$I_1(kA) = \frac{\pi C_0 V_0 (1+k)}{T}, \qquad 3\text{-}4$$

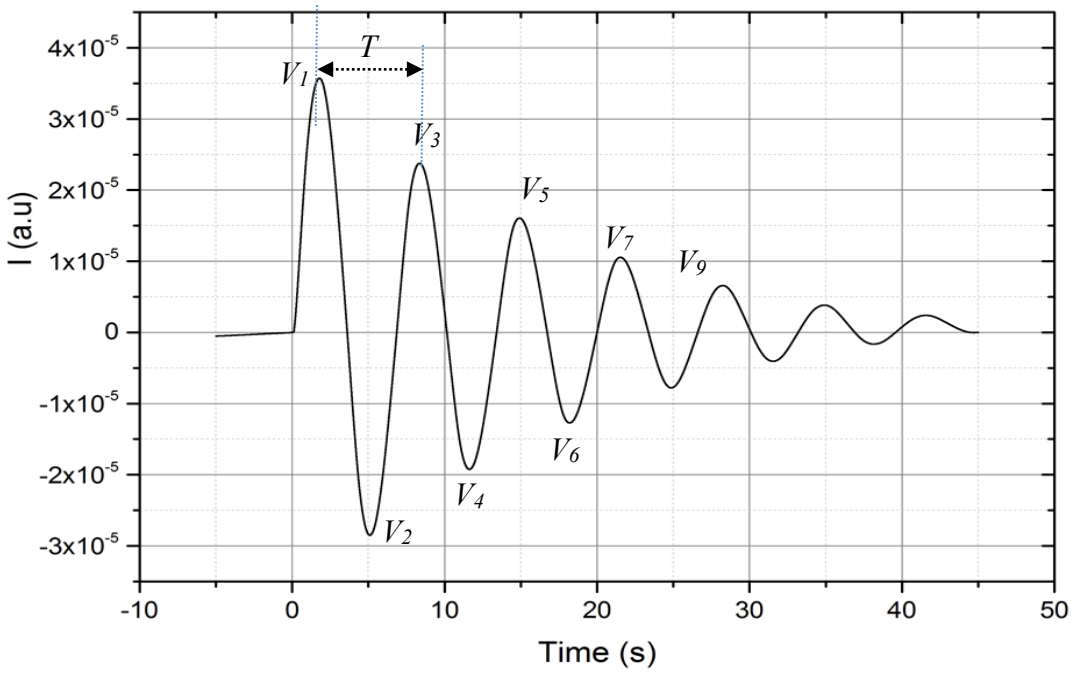

Figure 3-11. Numerically integrated signal for the Rogowski Coil output.

where I_1 is the peak discharge current, C_0 is the capacitance, T is the signal time period, 1.7 µs, and k is the reversal ratio identified below. The value of k can be calculated as follows:

$$k = \frac{1}{n-1}\left(\frac{V_2}{V_1} + \frac{V_3}{V_2} + \cdots + \frac{V_n}{V_{n-1}}\right), \qquad 3\text{-}5$$

where V_n (n = 1, 2, 3,….) are the amplitudes of the consecutive half cycles, as shown in Figure 3-11. By knowing the C_0, V_0 and calculating k and T using the current, the calibration factor of the coil (f) can be estimated by the equation:

$$f = \frac{I_1}{V_1} \quad \text{kA/V}, \qquad 3\text{-}6$$

where I_1 is the calculated value from equation 3-4 and V_1 is the first peak value obtained from the oscilloscope trace in volts. Using the previous equations, the calibration factor for the used Rogowski coil was estimated to be 5.1×10^6 kA/V.

3.2.1.2 *Voltage probe*

It is not possible to take the pinch voltage signal directly to the oscilloscope because of its high voltage, which in some shots goes beyond 100 kV for the KSU-DPF. A voltage probe is used for this purpose since it works as a voltage divider that allows the oscilloscope to be exposed to part of the voltage. The voltage probe used is a North Star Probe, Model PVM-5, which is designed for exceptional high frequency response [134]. Its maximum DC/Pulsed V (kV) is 60/100 and the maximum frequency is 80 MHz. A picture of the probe is shown in Figure 3-10(b).

3.2.2 *Radiation diagnostics*

Many diagnostic techniques were used to measure the radiation output, neutrons, hard/soft X rays and ions, of the KSU-DPF. These techniques and tools will be discussed in more details in the following subsections.

3.2.2.1 *Scintillation-photomultiplier detectors*

Two types of scintillation-photomultiplier detectors were used:

i. A Canberra, 3×3 in, sodium-iodide-thallium-activated NaI(Tl) scintillation detector, model 3M3/3-X to measure hard X-rays emission in the material detection experiments.
ii. A BC-418 plastic scintillator, 2×1 in, coupled with a HAMAMATSU PMT, model H7195, which is used for time resolved neutrons and hard X-ray diagnostics.

The characteristics of each type of scintillator is now explained.

3.2.2.1.1 *Sodium-iodide-thallium-activated scintillators (NaI(Tl))*

NaI(Tl) is a type of inorganic scintillators used for gamma ray detections. Inorganic scintillators are mainly crystals of alkali iodides, like sodium iodide, which contain a small percent of an impurity such as thallium (Tl). Depositing energy in the crystal will cause electrons to move from the valence gap to the conduction gap. In a pure crystal of NaI, the electron returns to the valence band producing photons with energy higher than visible light which are quickly reabsorbed in the crystal. A small amount of Tl, added to the crystal, creates extra energy level inside the crystal's forbidden gab. The transition of an electron to one of these additional energy levels will produce photons in the visible range of light as the electrons return to the valence band, as shown in Figure 3-12. Passage of an ionizing particle through the crystal will deposit energy, which is converted to visible light that is not reabsorbed. The visible light eventually hits a photocathode and is converted into electrons, which produce a small voltage pulse [135], see section 3.2.2.1.3 .

NaI(Tl) scintillators are widely used for γ rays detection because they have a relatively high density, 3.67 g/cm^3, they have high light-conversion (38,000 photons/MeV) and their emission spectra peaks at 415 nm as shown in Figure 3-13. They can be fabricated in large volumes which gives them superiority over other scintillation materials even those with better energy resolution. Some of their disadvantages include that NaI(Tl) is brittle and sensitive to temperature gradient and thermal shocks. They have a relatively long time decay of 230 ns. In addition, they must be kept encapsulated because it is so hygroscopic.

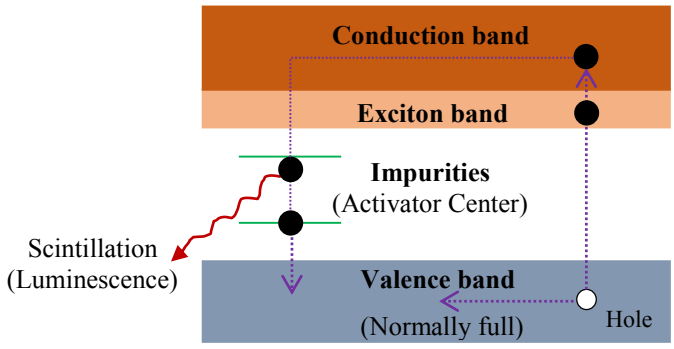

Figure 3-12. Energy band structure of an activated crystalline scintillator.

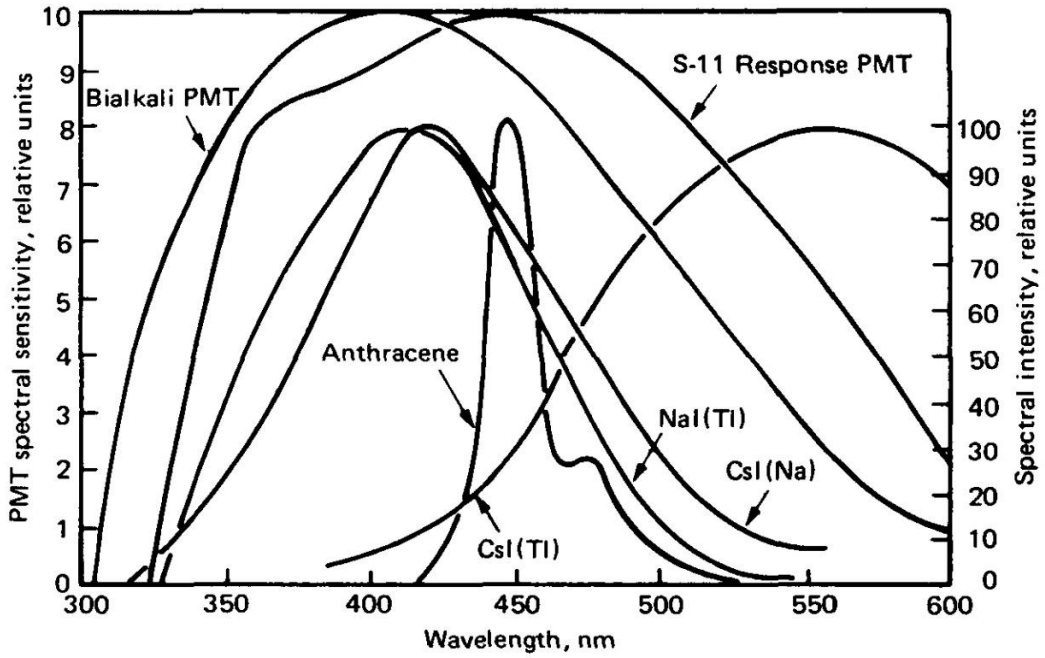

Figure 3-13. Emission spectra for some common inorganic scintillators [136].

(primarily from Harshaw Research Laboratory Report, Harshaw Chemical Company, 1978)

3.2.2.1.2 *Plastic scintillators*

Plastic scintillators are solid organic scintillators which belong in the aromatic compounds categories. They consist of planar molecules made up of benzenoid rings. They are composed of a mixture of a solvent with one or more solutes. They are classified as unitary, binary, ternary etc. based on the number of the components involved [135]. Light production in organic scintillators is mainly due to molecular transitions. Figure 3-14 shows that the change of the molecule potential energy with the interatomic distance. If an ionizing radiation passes through the crystal, it might take the molecule from the ground state at A_0 (a minimum energy point) to an excited state A_1. Since A_1 is not the minimum energy at that excited state, the molecule will lose part of that energy by lattice vibration to fall down to lowest energy at that level B_1. Another transition might happen after that from the point B_1, still an excited state, to the point B_0 which accompanied by a photon emission with an energy equal to $E_{B_1} - E_{B_0}$ which takes a time in the range of 10^{-8} s if happened. The difference between the emitted photon energy $(E_{B_1} - E_{B_0})$ and the excitation energy $(E_{A_1} - E_{A_0})$ make it possible to have a scintillation otherwise the emission spectrum will coincide with its absorption spectrum and no scintillation will be produced [135].

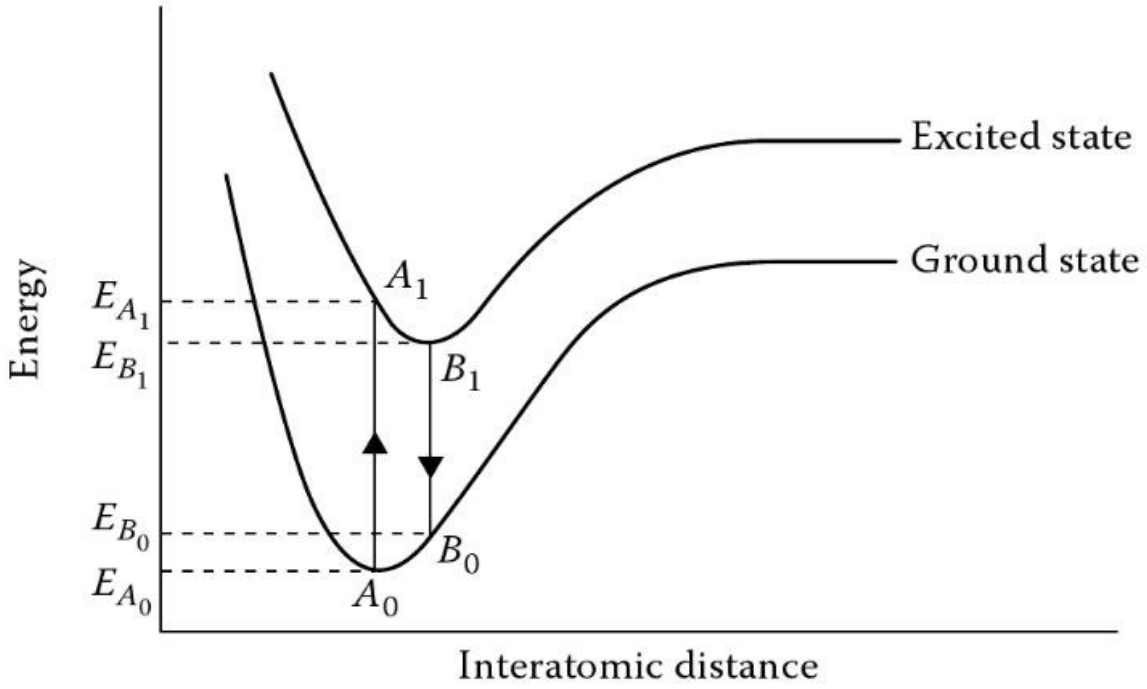

Figure 3-14. A Simplified energy diagram of a molecule [135].

Plastic scintillators have a fast response, less than 10 ns, compared to NaI(Tl) detectors which has a decay time of 230 ns. They are easy to fabricate into any shape and size. They can be used in contact with the radioactive samples because they are inert to water, air and many chemicals. On the other hand plastic scintillators have lower light yield than do inorganic scintillators. The emission spectrum of plastic scintillators peaks in the range from 350 to 450 nm.

Organic scintillators also work well as fast neutron detectors. They are characterized by their high efficiency and good energy resolution. Their efficiency is high because they are hydrogen-rich materials, having 1.1 hydrogen atoms for each carbon atom, and the hydrogen has a relatively high cross section, 2.5 b, for the 2.5 MeV neutrons. Moreover, they can be fabricated in large sizes. Fast neutrons interact with the hydrogen atoms (protons) in the organic scintillators by elastic and inelastic scattering. As a result, the neutron energy is (partially) transferred to the protons which will have the role to produce the scintillation light.

The plastic scintillators used in the experimental work reported here were BC-418 scintillators manufactured by SAINT-GOBAIN CRYSTALS Company. The decay time of this scintillator is 1.4 ns, which makes it suitable for ultra-fast timing applications. The wave length of maximum emission is 391 nm as shown in Figure 3-15.

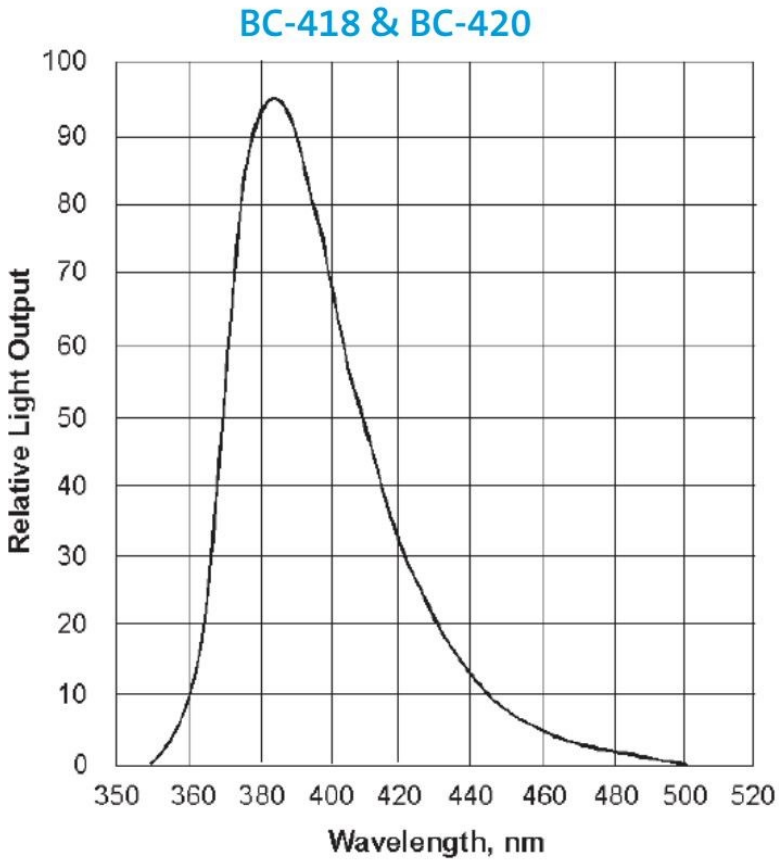

Figure 3-15. Emission spectra for BC-418 plastic scintillator [135].

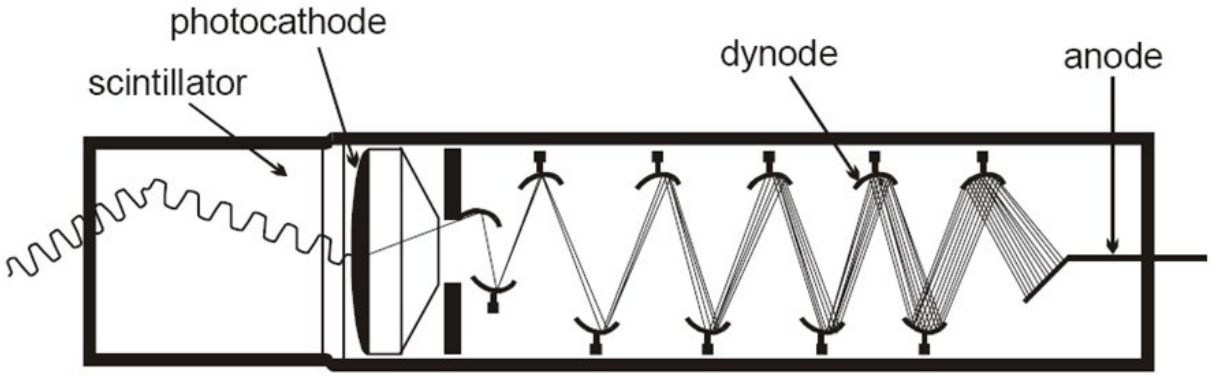

Figure 3-16. Schematic diagram for the photomultiplier tube [137].

3.2.2.1.3 *Photomultiplier tubes (PMTs)*

The light output of most scintillators is very weak. Typically a transducer, such as a photomultiplier (PMT) or avalanche photodiode (APD), is used to convert the light into a voltage pulse. In a PMT the light is converted into a small electrical signal through photoelectric interactions. PMTs then amplified the pulse though many stages to form current pulses that can be read by an oscilloscope. The PMT, as shown in Figure 3-16, is composed of three main parts: a photocathode, dynodes and an anode, see. The photocathode converts the incident light coming out from the scintillator into low energy electrons. After being accelerated by an electric field the electrons go directly to hit the first dynode at the beginning of electron multiplication process. The dynodes are made out of materials that produce secondary electrons when being impinged by electrons. The secondary electrons produced by the first dynode will be guided to hit the second one and so on until being collected at the end by the anode. An external voltage is applied to the PMT to provide the required electric field among dynodes.

The output voltage pulse for a typical scintillator-photomultiplier can be estimated from the equation, letting *e* be the charge of the electron,

$$V = \frac{dN}{dt} g\varepsilon GeR, \qquad 3\text{-}7$$

where N is the number of scintillation photons, g is the light collection efficiency, ε is the quantum efficiency of the photocathode, G is the photomultiplier tube gain and R is the terminating resistor.

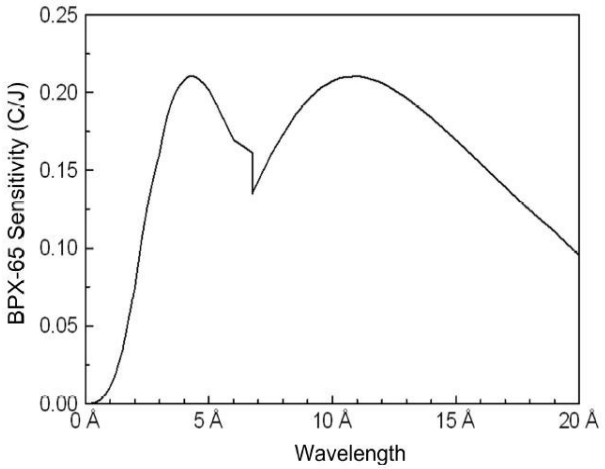

Specification of BPX-65 PIN diode	
Radiant sensitive area	: 1mm^2
Intrinsic Si wafer thickness	: 10μm
Dead layer thickness	: 0.5μm
Rise time (typical) (@ 900 nm)	: 0.5ns
Dark current	: < 5nA

Figure 3-17. BPX-65 PIN diode sensitivity curve below 20 A^o and its specifications [127].

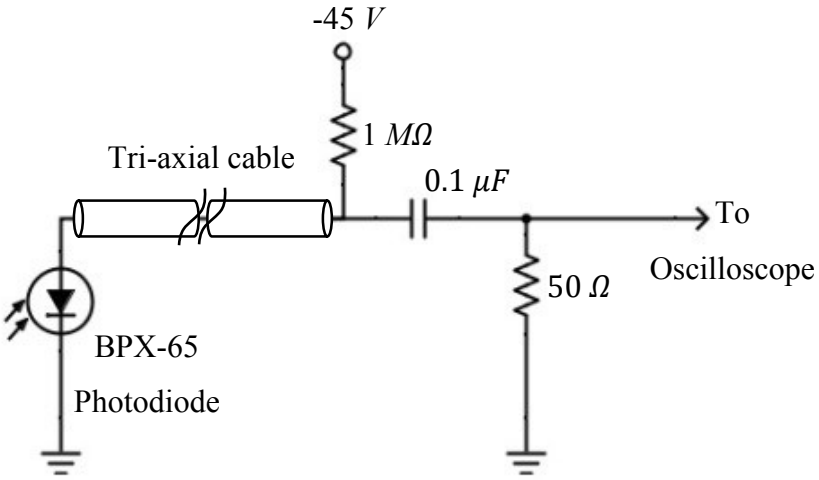

Figure 3-18. Electric circuit for connecting the photodiode and its coupling circuit.

3.2.2.2 *Photodiode*

A photodiode was used to measure the soft X rays. The model used was a BPX-65 PIN diode, which is normally used in the optical range. The glass window of the diode was removed for the X-ray measurements. Sensitivity curve and the specifications of the used BPX-65 PIN diode are shown in Figure 3-17. The electric circuit of the diode is shown in Figure 3-18. The diode was reverse biased with -45 V and connected to an RC circuit to be connected to the oscilloscope via a tri-axial cable.

The soft X-ray yield per shot can be estimated from the formula [138]:

$$E_{4\pi} = \frac{4\pi R^2 A}{R_0 A_D S}, \qquad 3\text{-}8$$

where R is the source-detector distance, A is the area under the X-ray signal, R_0 is the termination resistor (50 Ω), A_D is the sensitive area of the detector and S is the overall sensitivity at in the wavelength range taking into account any attenuation for the X-ray due to using any filters.

3.2.2.3 *^{3}He neutron detector*

^{3}He proportional counters are widely used in detecting thermal neutrons because of their high neutron detection efficiency and extremely low gamma ray sensitivity [139]. Detecting neutrons by using ^{3}He is based on the following reaction:

$$^3He + n \rightarrow {}^3H + {}^1H + 765\ \text{keV} \qquad 3\text{-}9$$

In this reaction the absorption of a neutron produces a tritium nucleus (^{3}H) and a proton in addition to an amount of energy equal to 765 keV that will be shared between the two components. The gas will be ionized by the charged particles, which will produce electrons that can be collected by the anode. Since the ionization potential for helium is 25 eV, it is expected for each neutron absorption to produce thousands of ions and electrons.

For thermal neutrons, the previous reaction's cross section is very high (5400 b at 0.025eV) and inversely proportional to v from 0.001 to 0.04 eV. Typically the ^{3}He efficiency is 77% for thermal neutrons (~0.025 eV), 2% at 100 eV, 0.2% at 10 keV and roughly 0.002% at 1 MeV [139]. Due to this strong energy dependency the ^{3}He gas filled detectors often are surrounded by a moderator which is usually made out of a hydrocarbon material to thermalize the neutrons before reaching the detector tube.

The ^{3}He detector used in the experiment is a Ludlum, model 42-30H, neutron detector [140]. It contains a 2 atm ^{3}He tube and is designed to measure thermal and fast neutrons (0.025 eV to approximately 12 MeV). The tube is surrounded by 10 in diameter polyethylene sphere to work as a moderator. The tube is connected a Ludlum scaler, model 2200 Scaler/Ratemeter. Figure 3-19 shows the detector used and the ^{3}He tube operation.

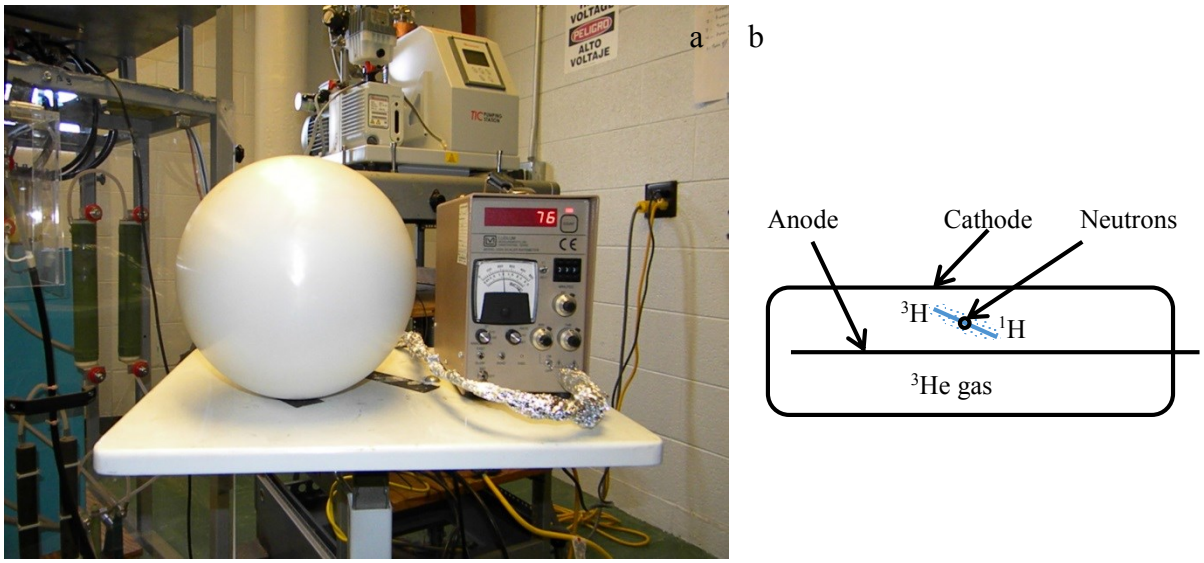

Figure 3-19. A picture of the ^{3}He detector used (a) and a schematic for the detection mechanism in the tube (b)

3.2.2.4 *Bubble detector*

Bubble detectors are sensitive and accurate neutron dosimeters that have been used for more than 15 years for applications in nuclear facilities, research institutes and medical communities. They provide instant visible measurements of the neutron dose. The theory of operation of the bubble detector is based on the existence of tiny droplets of superheated liquid distributed throughout a clear polymer. The droplet will immediately vaporize when it is hit by a neutron which forms a visible gas bubble in the gel, as shown in Figure 3-20. The number of droplets is a direct measurement for the tissue equivalent neutron dose. Bubble detectors have zero sensitivity for gamma rays. Their response is independent of the dose rate of energy. They are only used as neutron dosimeters. Two bubble detectors, model BD-PND manufactured by BT Bubble, were used for neutron measurements. Each had a conversion ratio of 6.7 b/mrem. They work in the energy range from less than 200 keV to more than 15 MeV.

Figure 3-20. A picture for the used neutron bubble detectors.

3.2.2.5 *^{6}LiI Neutron detector*

Another detector used for neutron detection is the Lithium Iodide scintillator (^{6}LiI). The ^{6}LiI scintillator is based on the reaction:

$$^{6}_{3}Li + ^{1}_{0}n \rightarrow ^{3}_{1}H + ^{4}_{2}He + 4.78\ MeV \qquad 3\text{-}10$$

The thermal neutron cross section for this reaction is 940 barns.

The detector used is a Ludlum, Model 42-5, which consists of 4 × 4 mm ^{6}LiI crystal coupled to a 3.8 cm a photomultiplier tube. It was designed for the crystal to be at the center of the moderator spheres. Moderator spheres made out of high density polyethylene with different diameters were supplied with the detector. A photograph of the detector is shown in Figure 3-21.

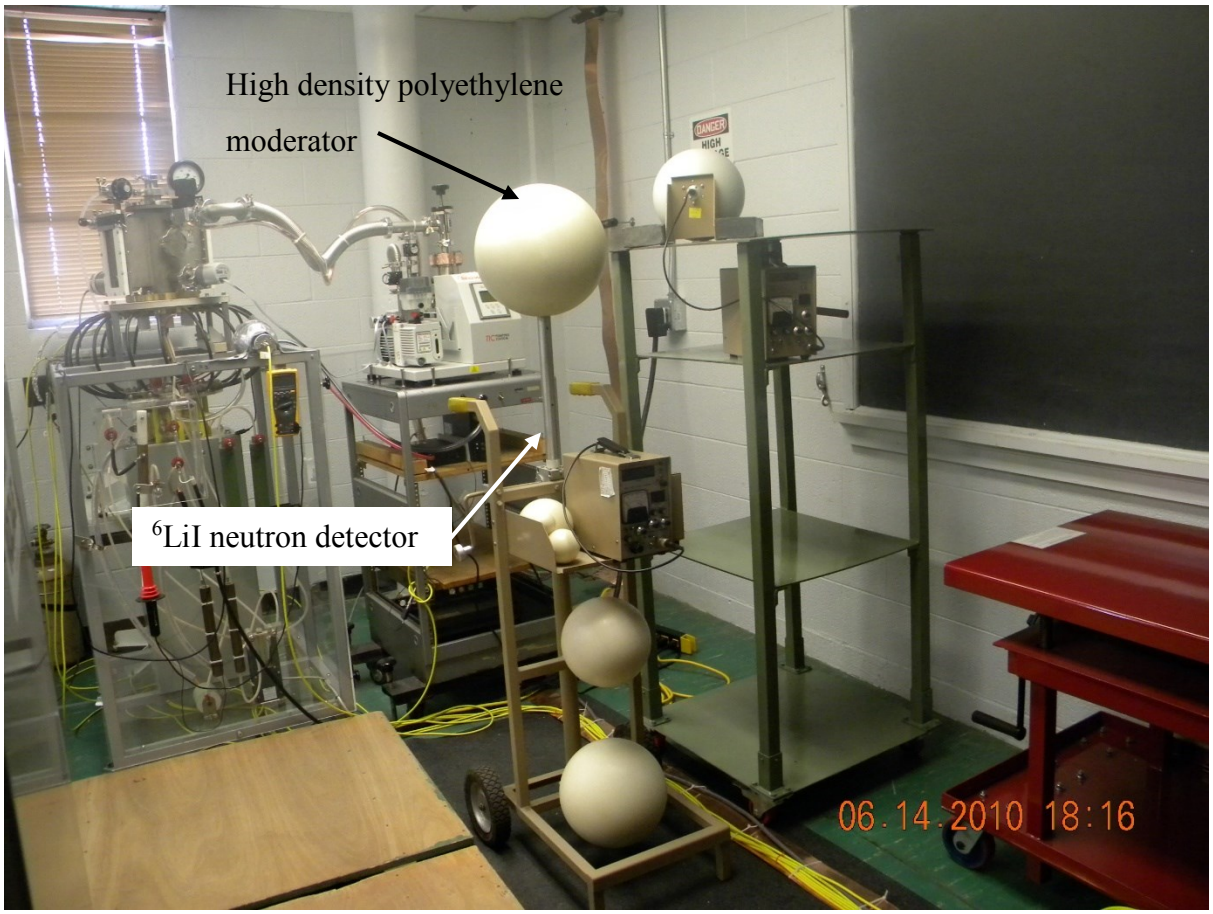

Figure 3-21. ^{6}LiI neutron detector.

3.2.2.6 *Faraday cup*

In deuterium operated plasma devices, Faraday cup used to be used to measure the velocity and energy distribution of deuterons. A schematic of Faraday cup is shown in Figure 3-22. It consists of a deep collecting cavity (cup), made out of copper, biased with negative potential ($-V$). The cup is located few millimeters away from an aperture around 0.5 mm diameter. Each Faraday cup has characteristic impedance which can be estimated form the equation [127]:

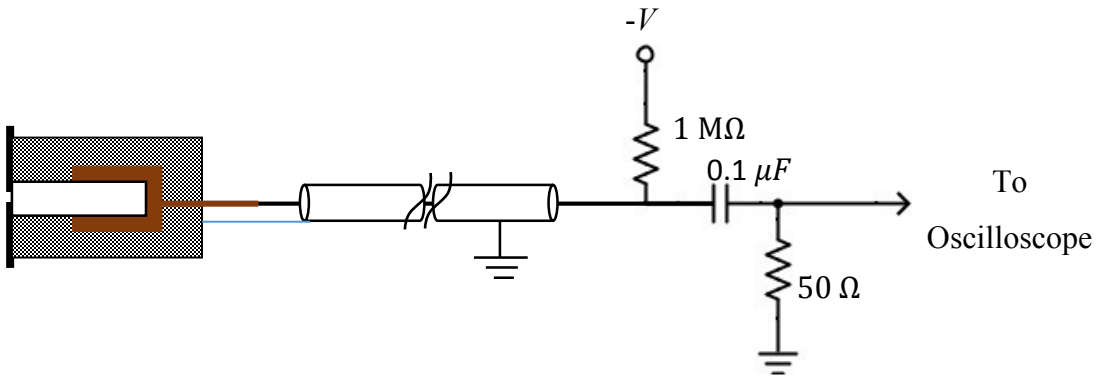

Figure 3-22. A schematic for Faraday cup and its connections.

$$Z = \frac{138.2}{\sqrt{\varepsilon_r}} log_{10}\left(\frac{D}{d}\right)\ \Omega, \tag{3-11}$$

where D is the inside diameter of the outer electrode, d is the outside diameter of inner electrode, and ε_r is the dielectric contestant of the spacer material. Parameters in equation3-11 were adjusted to produce a Faraday cup impedance that matches the coaxial cable impedance (50 Ω). Negative biasing voltage was used to prevent electrons from reaching the cup. This biasing voltage is applied such that [127] :

$$|V_{bias}| > V_c + V + V_e = \frac{1}{C}\int Idt + IR + V_e, \tag{3-12}$$

where V_c is the change in the capacitor voltage caused by the ion current source that is charging the capacitor and V_e the required potential to repel electrons. Applying this negative voltage to the collector causes deceleration and deflection for the stray electrons and hence reduces their effect on the ion current. The minimum negative voltage bias applied to a Faraday cup, for ion current measurements in dense plasma focus devices, working with different gases, can be estimated from the equation [127]

$$|V_{bias}| > \left(\frac{m_e}{m_i}\right) E_b + V, \tag{3-13}$$

where m_e, m_i are the electron and ion mass, E_b is the maximum expected beam energy and V is the voltage measured without biasing the collector.

The output signal from Faraday cup can be calculated form the equation:

$$V = IR, \tag{3-14}$$

where I is the ion current and V is the voltage measured across the resistance R.

By placing the Faraday cup at a known distance from the source (pinch), the ion velocity can be estimated from time of flight measurements. Assuming that the ions are created and accelerated in a very short time compared to the flight time, the ion speed (v_i) can be estimated by the equation:

$$v_i = \sqrt{\frac{2E_i}{m_i}} = \frac{d}{t}, \tag{3-15}$$

where E_i and m_i are the ion energy and mass, respectively, d is the distance of the Faraday cup from the pinch and t is the time.

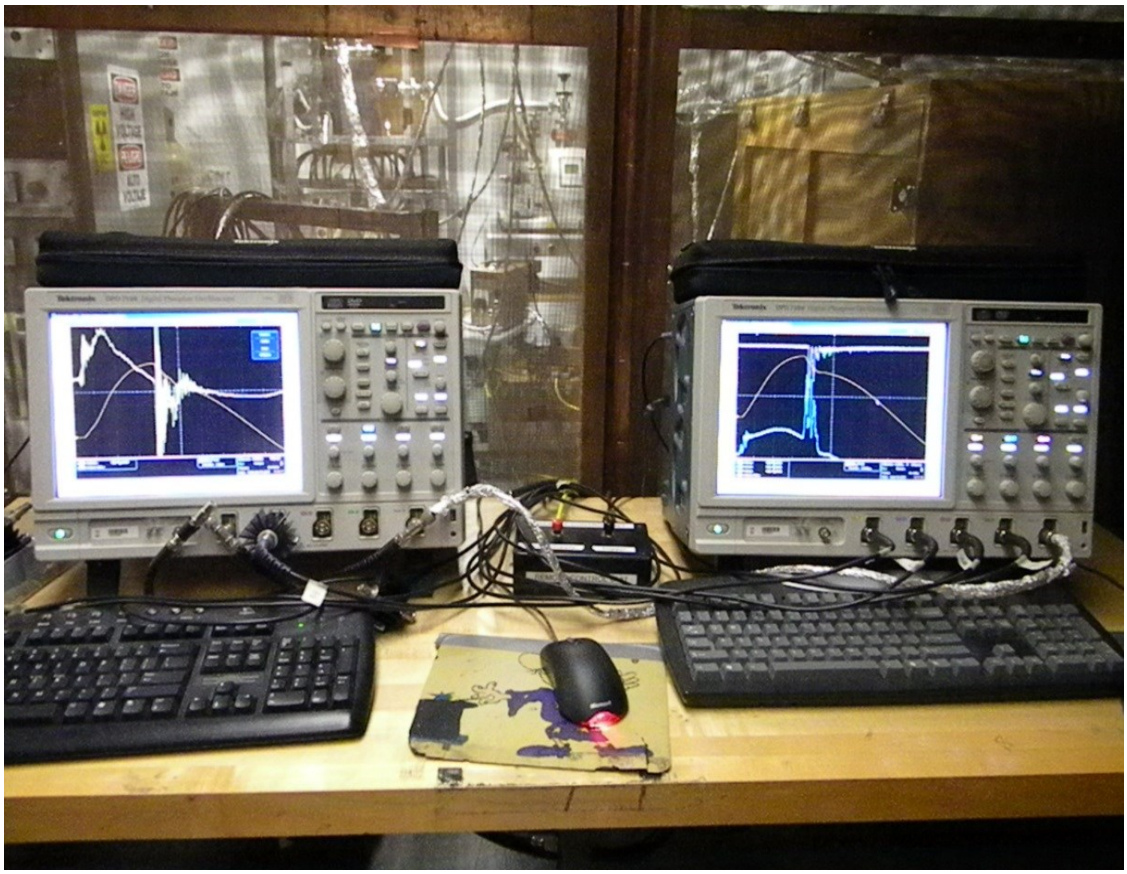

Figure 3-23. A picture of the used oscilloscopes.

Figure 3-24. The Faraday cage that contains the oscilloscopes.

Signals from different diagnostic tools were collected by two Tektronix Digital Phosphor Oscilloscopes, model DPO7104, 1 GHz bandwidth with a sampling rate up to 40 GS/s on one channel [141]. The DPO7000 series has an exceptional signal acquisition performance. To avoid signal noise, all signals were transferred from the diagnostic tools to the oscilloscopes by means of tri-axial cables. The cables used were manufactured by Belden, Model TRIAX 2479, with an impedance of 50 Ω. The fast high voltage signal, generated by the DPF device at the time of the pinch, produces a very strong electromagnetic field that affects the surrounding electrical devices including the oscilloscope. To avoid electromagnetic interference, the oscilloscopes were placed inside a Faraday cage with a switch to charge and discharge the capacitor. The used oscilloscopes and Faraday cage are shown in Figure 3-23 and Figure 3-24, respectively.

Chapter 4- Characterizing the Device

After discussing the diagnostics used in the KSU-DPF, some experiments will be discussed in the following section to characterize the performance of the device.

4.1 Measurements of the device static parameters (short circuit test)

First, it is important to know the static parameters of a DPF device. These include the static inductance (L_0), resistance (r_0) and capacitance (C_0); they represent the total inductance, resistance and capacitance of the device, excluding the plasma. The capacitance is already known from the capacitor bank. The static parameters are measured by performing a short circuit test for the device in which both anode and cathode are electrically connected together. In some cases this is difficult to do, especially when it is hard to access the device head or in the case of the high power devices in which the short circuit will produce a huge amount of current. Operating the device in a high pressure mode, > 20 Torr of neon, may be an alternative way to measure the static parameters. In the high pressure mode, the plasma sheath will not move that much distance in the axial phase which gives a quite good estimation about the static parameters.

In the short circuit test the device circuit is represented by a pure RLC circuit as shown in Figure 4-1 in which L_0 and r_0 represent the net inductance and resistance in the circuit including the capacitor bank, switches, transmission plates and connections. As explained in section 3.2.1 the resulting current will be in the form of an underdamped sinusoid with period T, i.e., $r_0 \ll 2\sqrt{L_0/C_0}$, for which the following approximate equations apply [132]:

$$L_0 = \frac{T^2}{4\pi^2 C_0}, \tag{4-1}$$

and

$$r_0 = \frac{2}{\pi}(lnk)\left(\frac{L_0}{C_0}\right), \tag{4-2}$$

where T is the time period and k is the average reversal ratio obtained from the successive peaks, V_1, V_2, V_3, V_4, *etc.*, using equation 3-5, as explained in section 03.2.1.1

To do the short circuit test in the KSU-DPF, both anode and cathode were completely removed and the circuit was shorted by a metal disc as shown in Figure 4-2. The test was performed

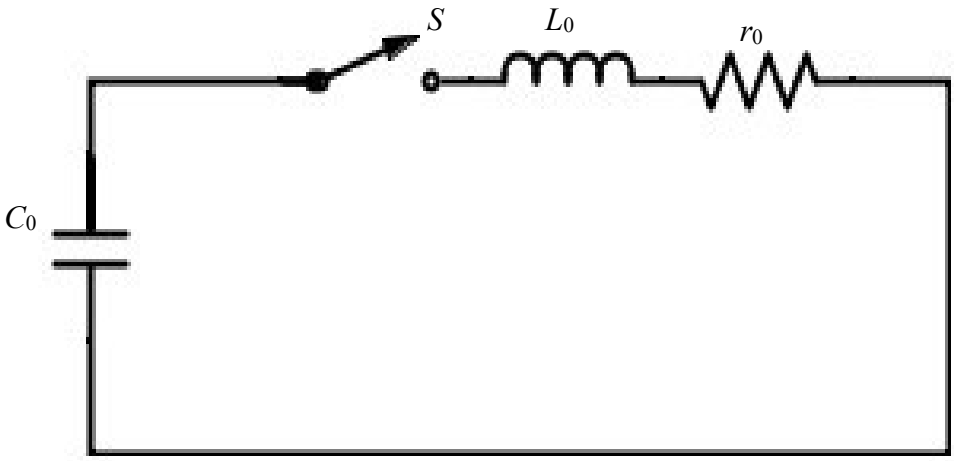

Figure 4-1. Device electric circuit for the short circuit test.

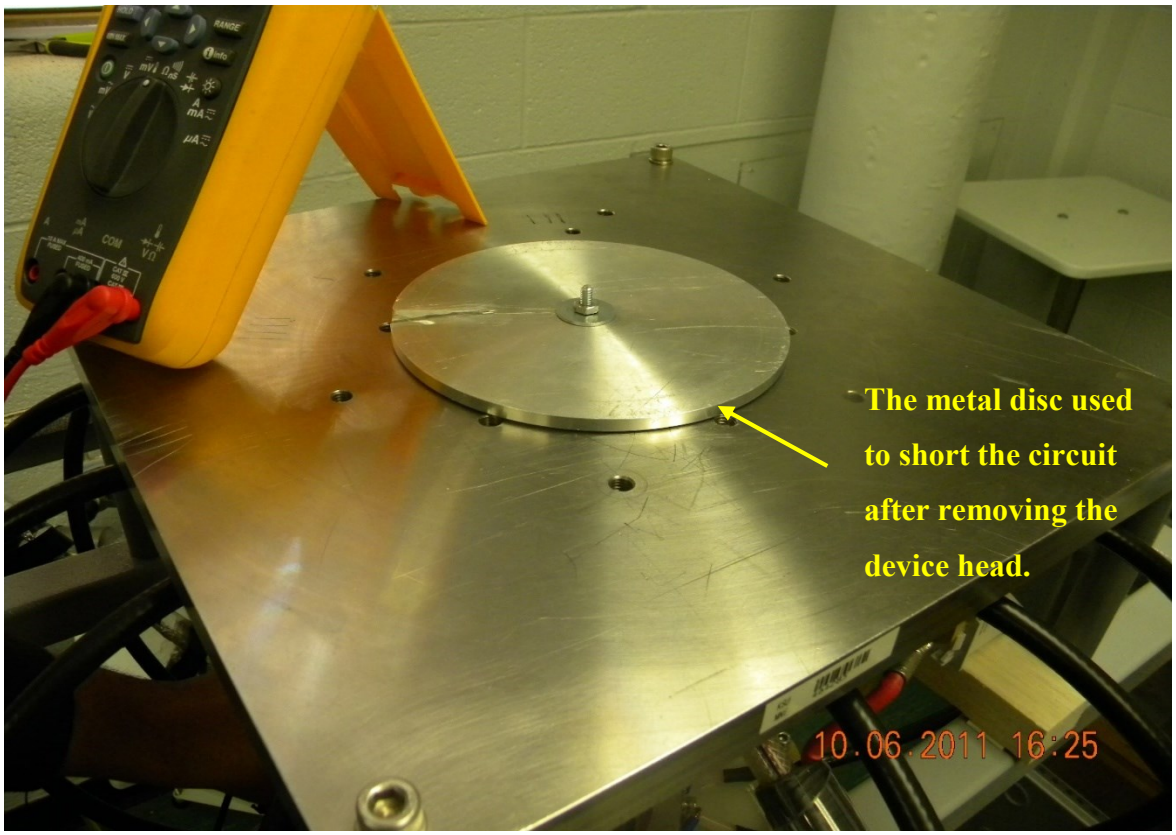

Figure 4-2. Short circuit test.

at different voltages; 5, 8, 10, 12, 14 and 17 kV to obtain the best estimation for the device static parameters. A sample of the damped current signals at these voltages are shown in Figure 4-3. As expected, the maximum peak current value is proportional to the charging voltage which varies from 57 kA at 5 kV charging voltage to 182 kA when the charging voltage is 17 kV. For each charging voltage, the first current peak I_1 was estimated using equation 3-4 by substituting the average reversal ratio (k) and the time period (T). The maximum peak current and stored energy changes with the charging voltage are shown in Figure 4-4. Using equations 4-1and 4-2 the values of L_0 and r_0 were also calculated for each charging voltage and the averages are then calculated. The calculated value for the average L_0 and r_0 over the 6 short circuit shots with different voltages were 91$\pm$2 nH and 13$\pm$3 mΩ. It is known that the device inductance is 12.5 μF which is mainly the capacitance of the capacitor.

One of the problems faced while doing the short circuit test was that the discharge current signal obtained using a Rogowski coil has a baseline shift as shown by the dotted line curve in Figure 4-5. This base-line shift is due to the electromagnetic pick up and the interference with the

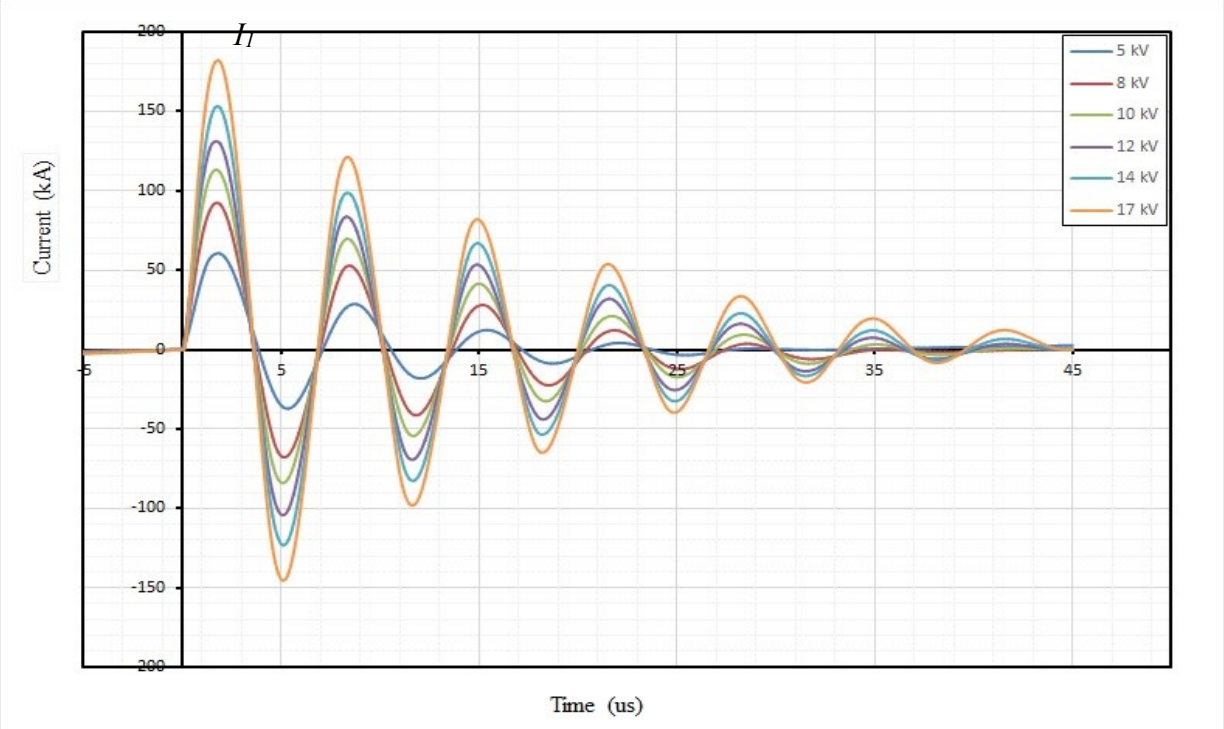

Figure 4-3. Samples of the short circuit current at different voltages.

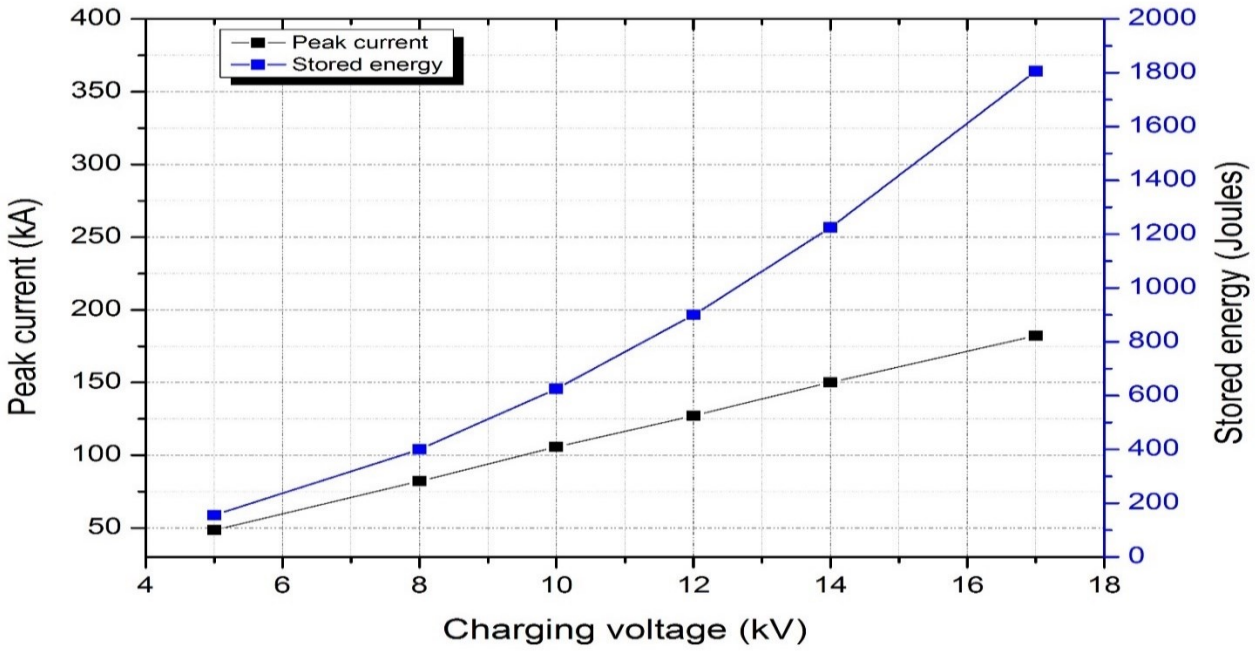

Figure 4-4. The maximum peak currents and stored energy at different charging voltages.

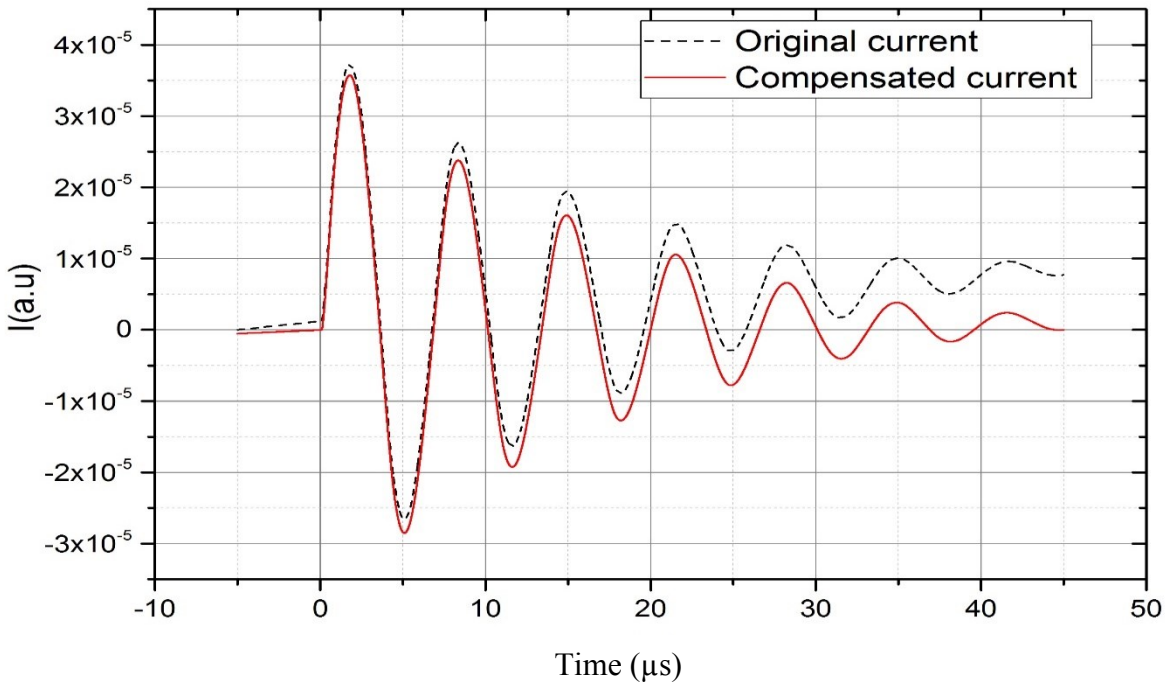

Figure 4-5. Rogowski coil before and after compensation.

regular power line [142]. Grounding problems or nonsymmetrical topology, which makes the coil not only monitor the current inside but also the current outside, cause the offset shown in the figure [143]. This problem has been solved by three different methods. The first method applies some digital filters on *di/dt* using suitable software. The second method is to find the average of the wave envelope. The positive peaks were connected together in curve and so for the negative peaks then an average of the two curves was calculated which is then subtracted from the original current signal. Finally, connecting a line between the first few nanoseconds from the curve and the last few nanoseconds and then subtracting this straight line from the original signals was used in this work as shown in Figure 3-11. The difference between the original current signal and the corrected one is shown in Figure 4-5.

4.2 Characteristic curve of the KSU-DPF

As seen from the short circuit test, the current signal is an under damped sinusoid without any deformation. In a typical plasma focus discharge, a dip in the current trace is observed as an indication of the pinch occurrence. It appears as a sharp spike in the voltage and current derivative signals. A large spike and dip are signs of an efficient focus. All low inductance devices have a large dip, called a regular dip (RD) and followed by a small extended dip (ED) in its current trace. It was thought that high inductance devices such as UNU/ICTP PFF [132] would act the same. S. Lee [29] succeeded to fit almost all devices to his 5-phase model, except the UNU/ICTP PFF mentioned before, which has relatively high inductance. The current dip for this device was usually loaded by large oscillation which has been treated always as noise. For the KSU-DPF device, which also has a relatively high inductance, a clean current wave form is obtained by using the high resolution DPO7104 oscilloscopes. The oscilloscopes allow one to make numerical integration for the d*i*/d*t* signal, picked up the Rogowski coil. By doing a frequency response analysis for the coil system, Lee et al. [144] showed that this integrated signal by the oscilloscope is free of any noise below 200 MHz. The d*I*/d*t* wave form is clean and showed a large extended dip beyond the regular one with a significant depth and duration. More than 95% of the KSU-DPF shots have more than one dip [144]. Typical signals for current, current derivative and voltage of the KSU-DPF are shown in Figure 4-6 in which multi dips are shown in the current (red) signal. Each dip is related to one of the spikes in the current derivative (black) signal, and the voltage (blue) signal. The KSU-DPF current signals didn't fit to the Lee model very well.

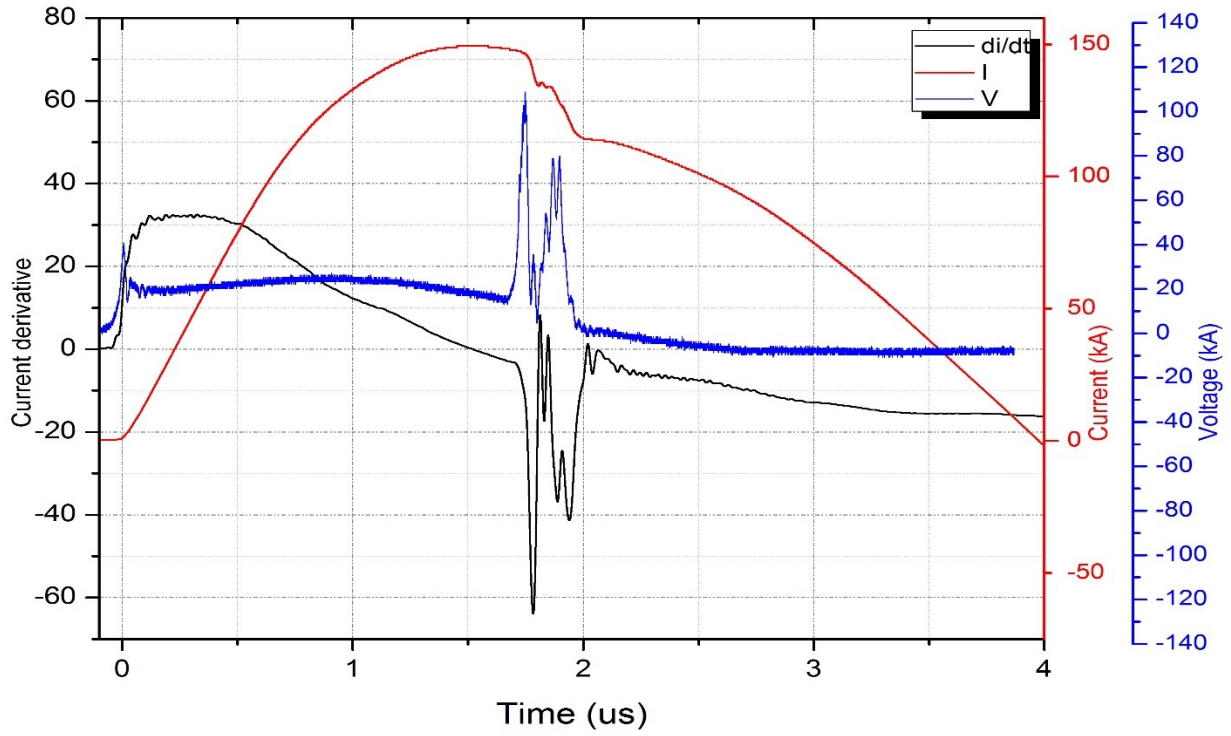

Figure 4-6. Typical signals for current, current derivative and voltage for 7 mbar of deuterium.

Based on the previous discussion, DPF devices were classified into two types, T1 and T2. The T1 category includes the devices with low static inductance L_0 which usually has one large RD, in the current trace followed by small ED. This type can easily modeled with the 5-phase Lee Model. On the other hand T2 type generally has high static inductance L_0, which usually has a large ED and some times more than one ED, such as KSU-DPF. A modification has been made to Lee model by adding an instability phase before the last phase using anomalous resistance terms, which make it possible to fit the current trace from the T2 type DPF like the KSU-DPF device. This model was developed after a workshop at Kansas State University, in 2010, with Professor Lee and the dense plasma focus group at which current traces of the device and its characteristics were studied and compared with other devices. Based on the work done at this workshop, Lee has modified his code to the 6-phase code which can fit both types.

4.3 Time of flight measurements

Time-of-flight (TOF) measurements have been performed to measure neutron energy. A scintillator-photomultiplier (PMT) detector located far enough from the source to distinguish the

hard X-ray and neutron signals was used. After a shot, the PMT registers the arrival times of the hard X-ray and neutron signals. It is assumed that the X-ray signal arrives at the PMT instantaneously, as it travels at the speed of light, while the neutron signal lags because the neutrons take more time to arrive depending on their energy. Based on this principle, the neutron energy can be estimated.

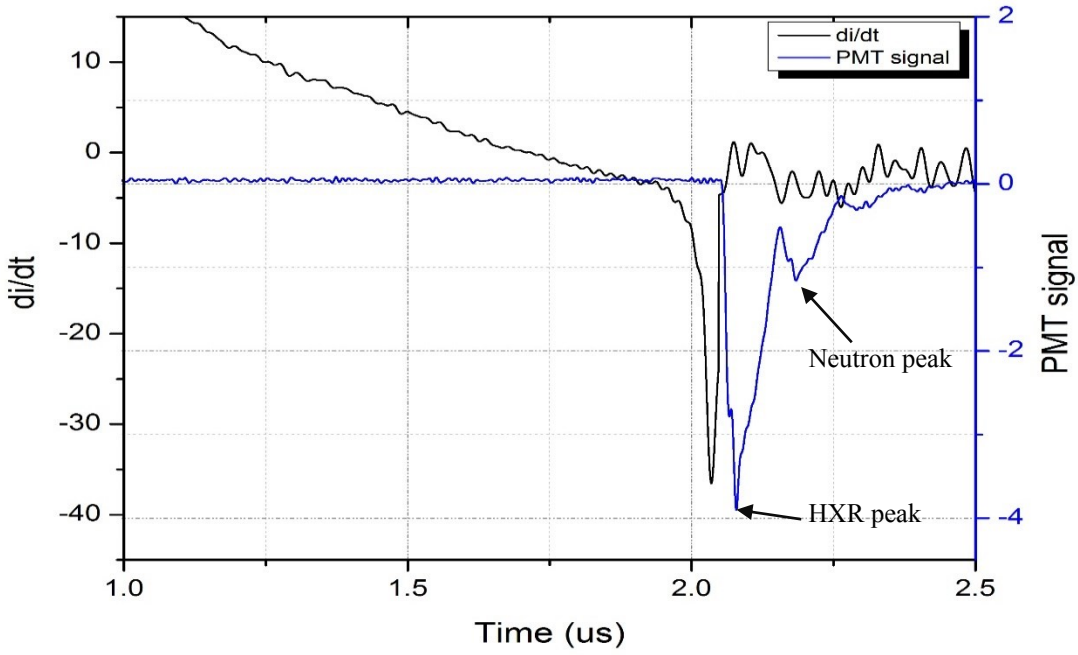

Figure 4-7. Current derivative trace with hard X-ray and neutron signals.

The TOF measurements were performed at KSU-DPF laboratory using a BC-418 scintillator coupled with Hamamatsu H7195 photomultiplier tube. The detector was located 2.3 m away from the device. The current derivative (*di/dt*) was register simultaneously with the detector signal using an oscilloscope for which both channels are triggered at the same time. The same type of cables with the same length were used. A typical signal for current derivative (*di/dt*) and photomultiplier is shown in Figure 4-7. In the PMT signal, the blue trace, the first peak is due to the hard X rays, which are produced by collisions of fast electrons with the anode, and is followed by the second peak, which is due to neutrons. The hard X-ray (HXR) peak should coincide with the current derivative spike, which is at the pinch moment, but due to an inherent delay the photomultiplier tube signal came around 40 ns later. The time difference between the HXR peak and the

neutron peak is ~104 ns. If the neutrons take 104 ns to travel 230 cm distance, the neutron velocity can be estimated to be $v = 22 \times 10^8$ cm/s. Calculating the neutron energy based on this velocity produces an energy of 2.5 MeV.

4.4 Neutron measurements

An efficient and consistent pinching was observed through a pressure range from 0.5 mbar up to 9 mbar for deuterium gas. An experiment was performed to estimate the neutron yield emitted from the device in this pressure range and to investigate the optimum pressure for neutron production. In this experiment the gas was pure deuterium. The anode was made of tapered stainless steel and the capacitor was charged to 17 kV. Two neutron detectors were used including a ^{3}He and a ^{6}LiI, each surrounded by a 10 in. polyethylene sphere as a moderator. The ^{3}He was fixed axially on the top of the device while the ^{6}LiI was mounted radially at the same distance from the anode tip, 94 cm. A schematic of the experiment is shown in Figure 4-8. Ten shots were taken at each pressure starting from 0.5 mbar up to 9 mbar of deuterium. The deuterium gas was purged every 10 shots to avoid the contaminations resulting from the bombardment of high velocity electrons with the anode. After each shot, the detector counts were registered and after ten shots at a given pressure the average calculated. The number of counts was transformed to number of neutrons using the calibration curve for each detector shown in Figure 3-9.

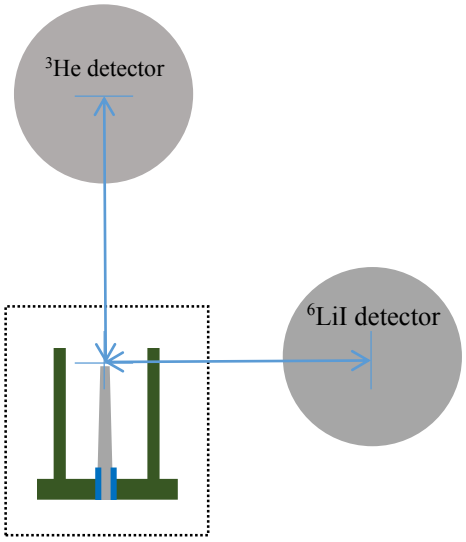

Figure 4-8. Schematic for the neutron measurement experiment.

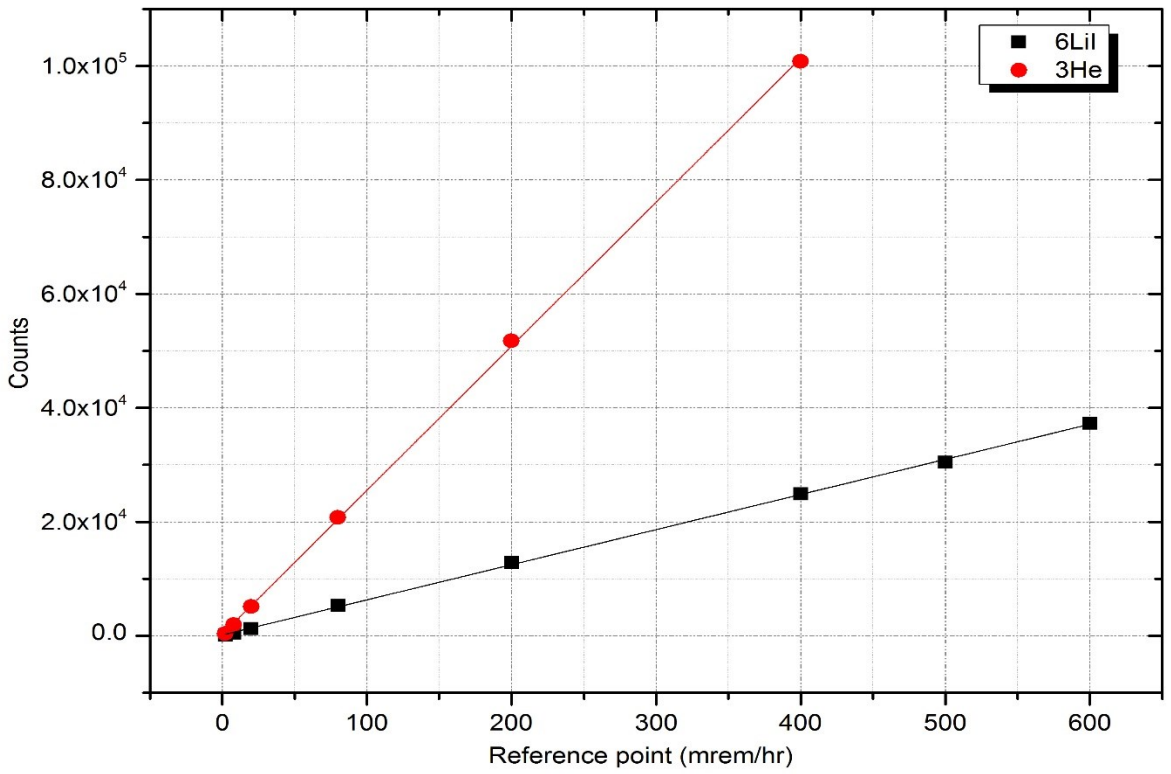

Figure 4-9. Calibration curves for the ^{3}He and ^{6}LiI neutron detectors.

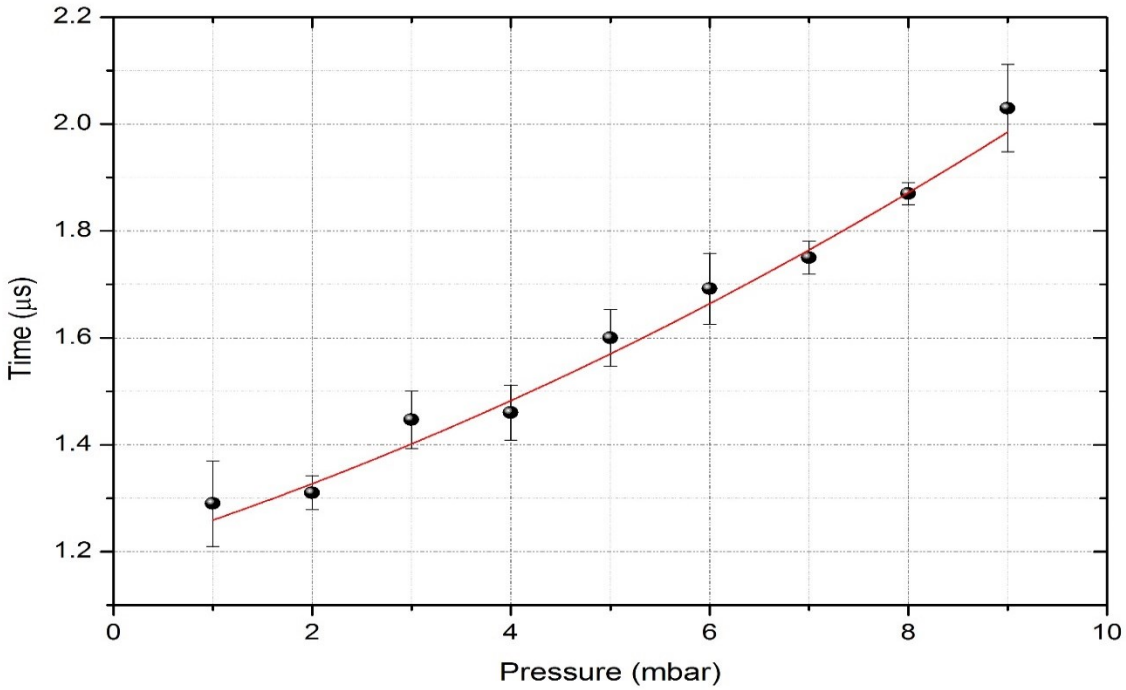

Figure 4-10. The variation of the time-to-pinch (t_p) with gas pressure.

The time-to-pinch (t_p) is the time period from the first breakdown to the pinch; this time includes both the axial and compression phases. This time (t_p) depends strongly on the gas pressure. Increasing the pressure slows down the current sheath in the axial phase and hence the time-to-pinch increases as the pressure increases. The dependency of t_p on the gas pressure for the neutron measurements experiment is shown in Figure 4-10.

The variation of the axial and radial neutron yield with the gas pressure is shown Figure 4-11 for the tapered stainless steel anode. Maximum neutron yields were obtained at 6 mbar of deuterium in both the axial and radial directions. In the axial direction, the maximum neutron yield was 1.9×10^7 n/shot, and in the radial direction the maximum neutron yield was 1.05×10^7 n/shot. It is clear from Figure 4-10 that the time to pinch at 6 mbar pressure is 1.7 µs, which is the time of the first peak of the current signal as shown from the short circuit test in section 4.1 Hence, the neutron yield is maximized at the highest amplitude of the discharging current. The neutron yield starts from a low value at 0.5 mbar increasing to a maximum at 6 mbar and then decreasing again up to 9 mbar. After 9 mbar it was difficult to have a pinch.

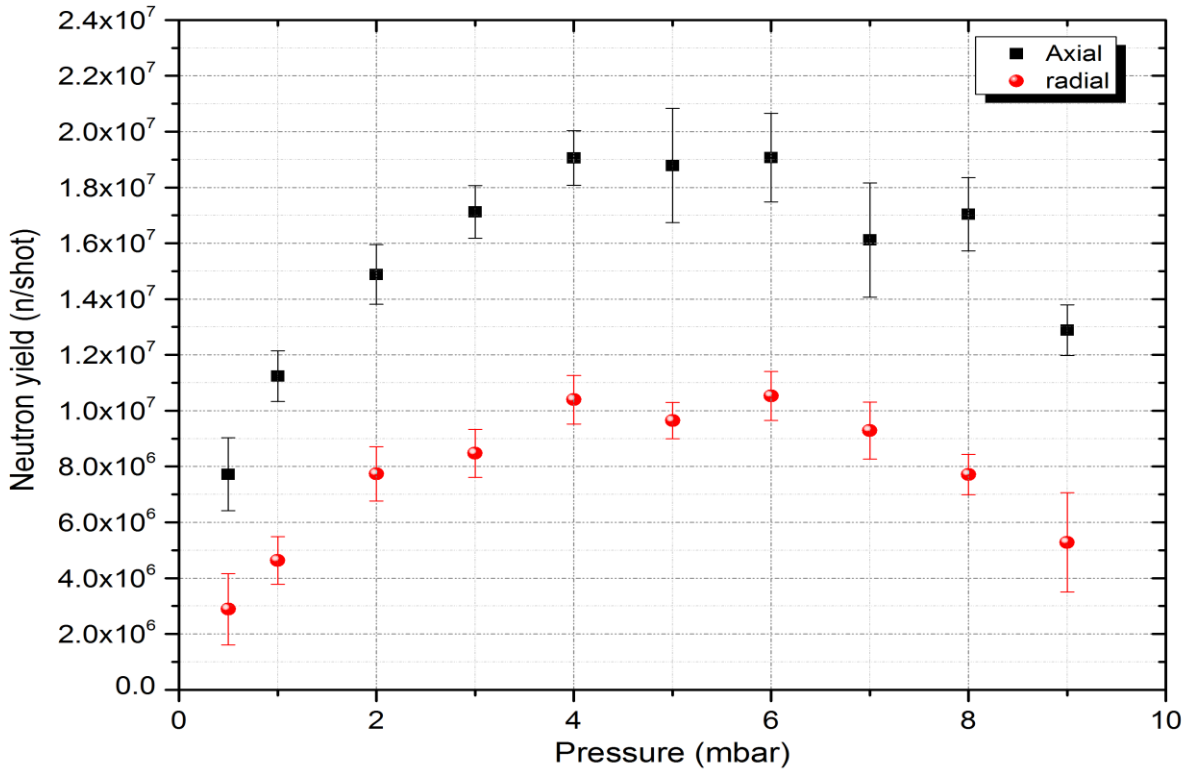

Figure 4-11. Variation of axial and radial neutron yield with pressure.

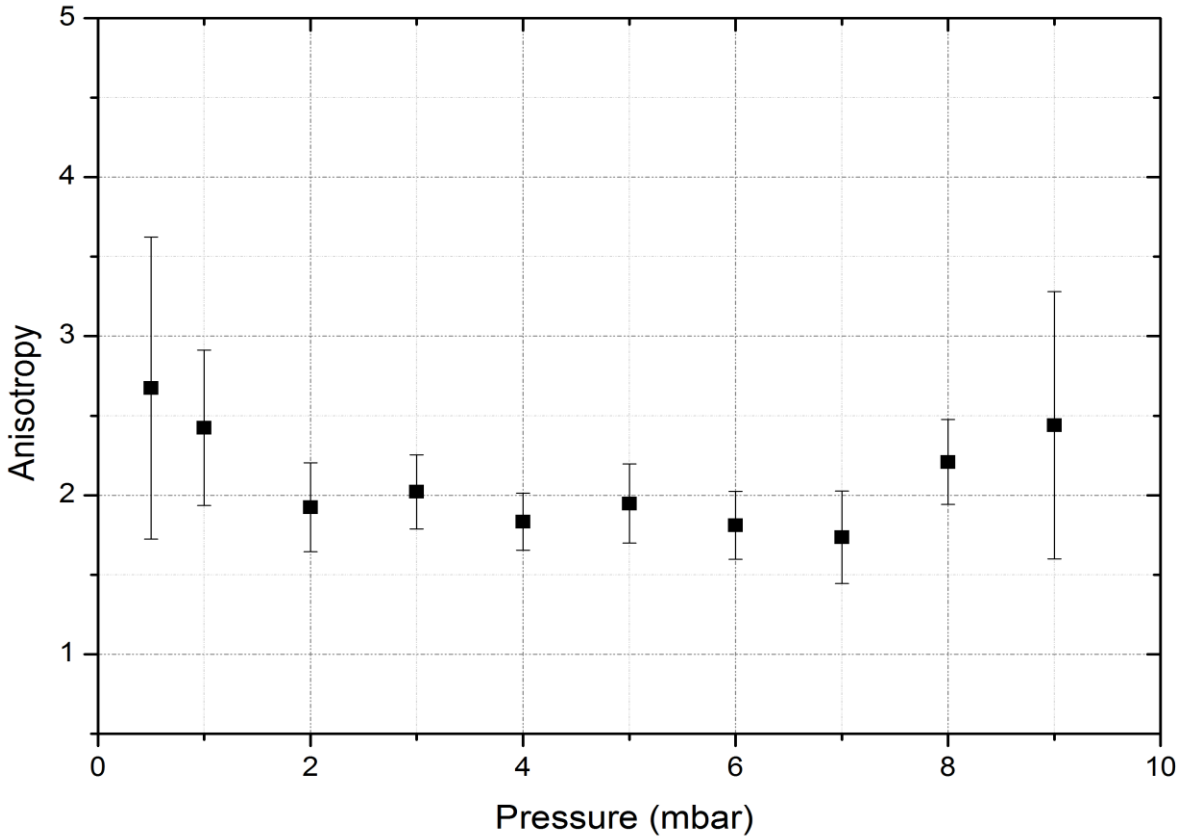

Figure 4-12. Variation of neutron anisotropy with gas pressure.

It was concluded that that optimum pressure at which the maximum number of neutrons are emitted from the device is 6 mbar. The effect of the gas pressure on the thermonuclear and beam target mechanisms for neutron production can be used to explain why the neutron production varies with the gas pressure. Moreno et al. [145] showed, for the thermonuclear mechanism, the optimum pressure for neutron production would be when the pinch happened at the first maximum of the discharging current. For constant charging voltage and anode length, increasing the gas pressure will increase the plasma density in the pinch, which will increase the reaction rate and hence the neutron yield up to a certain pressure. Beyond this pressure the time to pinch will increase and the pinch no longer happens at the peak current but at lower currents, which means lower heating for the pinch plasma and lower neutron yield. Yamamoto et al. [146] explained this from the beam target mechanism point of view. To produce a higher neutron yield, a strong formation of the Rayleigh Taylor (RT) instability is needed, which produces the accelerated deuterons

as explained in Chapter 1- The TR instability growing time is related to the current sheath acceleration g and perturbation wave length λ_p as $t_i = \sqrt{2\pi\lambda_p/g}$ [147]. At low pressures the current sheath acceleration g will be high, thus producing a very high growth rate of the TR instability, which doesn't form a well-defined pinch plasma column. As a result the neutron yield will be poor. Raising the pressure to a value near the optimum makes it likely that the current sheath acceleration is sufficient to produce an efficient RT instability, which leads to the formation of efficient deuterons. As result a good neutron yield will be produced. At pressures higher than the optimum, the value of g will be large, which will produce a slow TR instability resulting in a less efficient beam target. Therefore, the neutron yield again will be small. The anisotropy of the measured neutron yield as indicated by the ratio of the axial to the radial neutron yields, is shown in Figure 4-12 as a function of gas pressure.

4.5 Ion measurements

Due to a sudden change in the plasma inductance during the radial phase, an extensive electric field is produced that accelerates both electrons and ions in opposite directions. As mentioned before, one of the characteristics of high inductance DPF devices is their relatively long radial phase, which leads to more than one current dip in most of the shots producing multiple neutron emissions. Two experiments were performed to figure out the characteristics of the deuteron beam at KSU-DPF. The time-of-flight technique was used to estimate the ion energy. Three ion collectors were mounted axially in a tube on the top of the anode at distances of 28, 56 and 70 cm. The setup of the experiment is shown in Figure 4-13. The three collectors were made of 100 μm copper. The first two, from the bottom, were cylinders of diameters 15 and 10 mm and the third one was a disk of 10 mm diameter. Each collector is connected to an RC circuit, 50 Ω and 100 nF, and biased by -50 V through 1 MΩ resistor. To collimate the deuteron beam, a pinhole of 2 mm radius was mounted at the beginning of the drift tube. The electric configuration of the ion collector was shown before in Figure 3-22. One of the used ion collectors is shown in Figure 4-14. A photodiode, BPX-65, was used to measure the soft X-rays to correlate it with the ion production. The photodiode was mounted at the pinch level as shown in Figure 4-13. The photodiode circuit was shown before also in Figure 3-18.

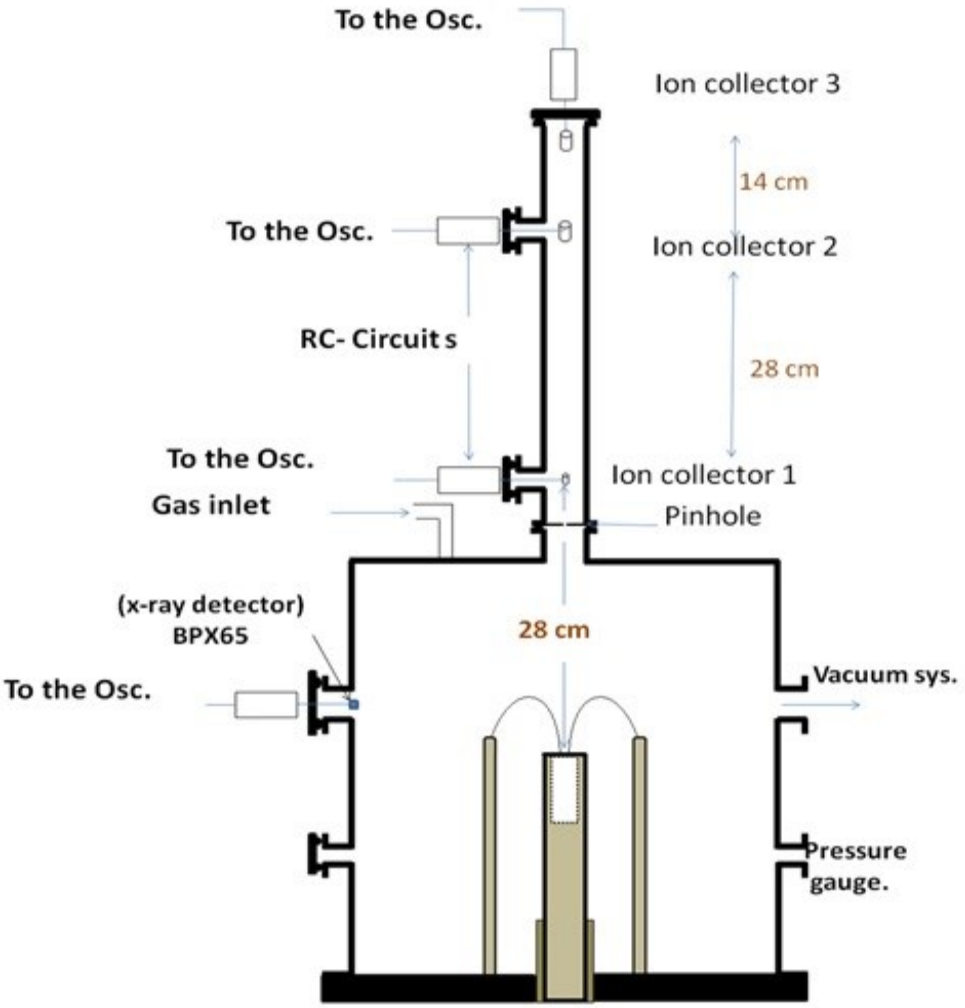

Figure 4-13. A schematic for ion time of flight measurements.

Figure 4-14. A view of the ion collector.

Figure 4-15 [148] shows typical signals for the ion collectors in addition to the SXR signal, for 5 mbar deuterium. Many peaks were reported for the ion collectors. Each peak is related to one of the peaks in the SXR detector. By using the TOF measurements the energies of the two observed bursts of ions was estimated to be 130 and 72 keV. Measurements for the main peak at different deuterium pressures showed that the deuteron energy increases from 80 keV at 0.5 mbar pressure to a maximum value $>$ 100 keV at 1.5 m bar and then decreases to a value of 30 keV at a pressure of 10 mbar.

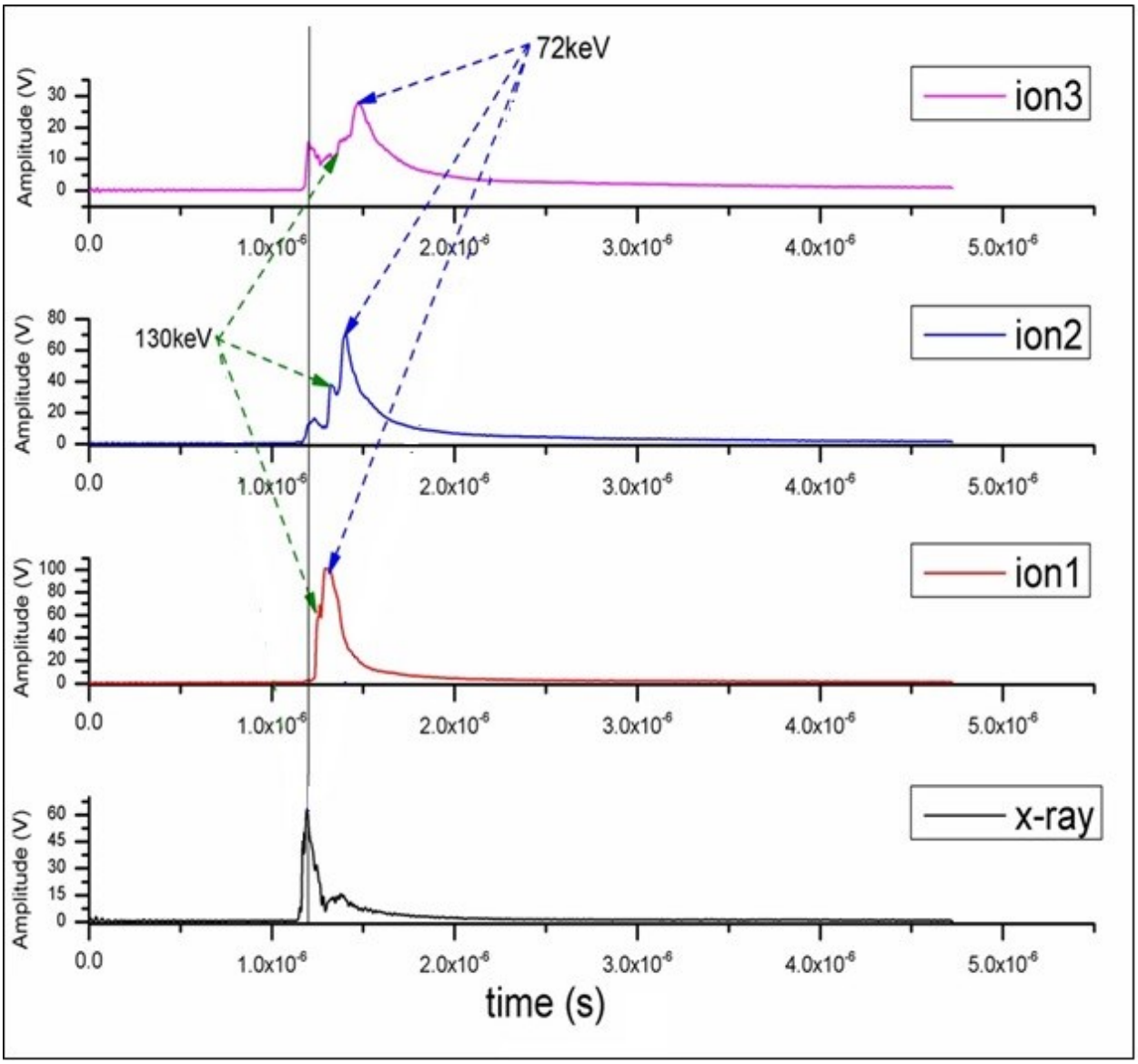

Figure 4-15. Ion detectors and SXR signals.

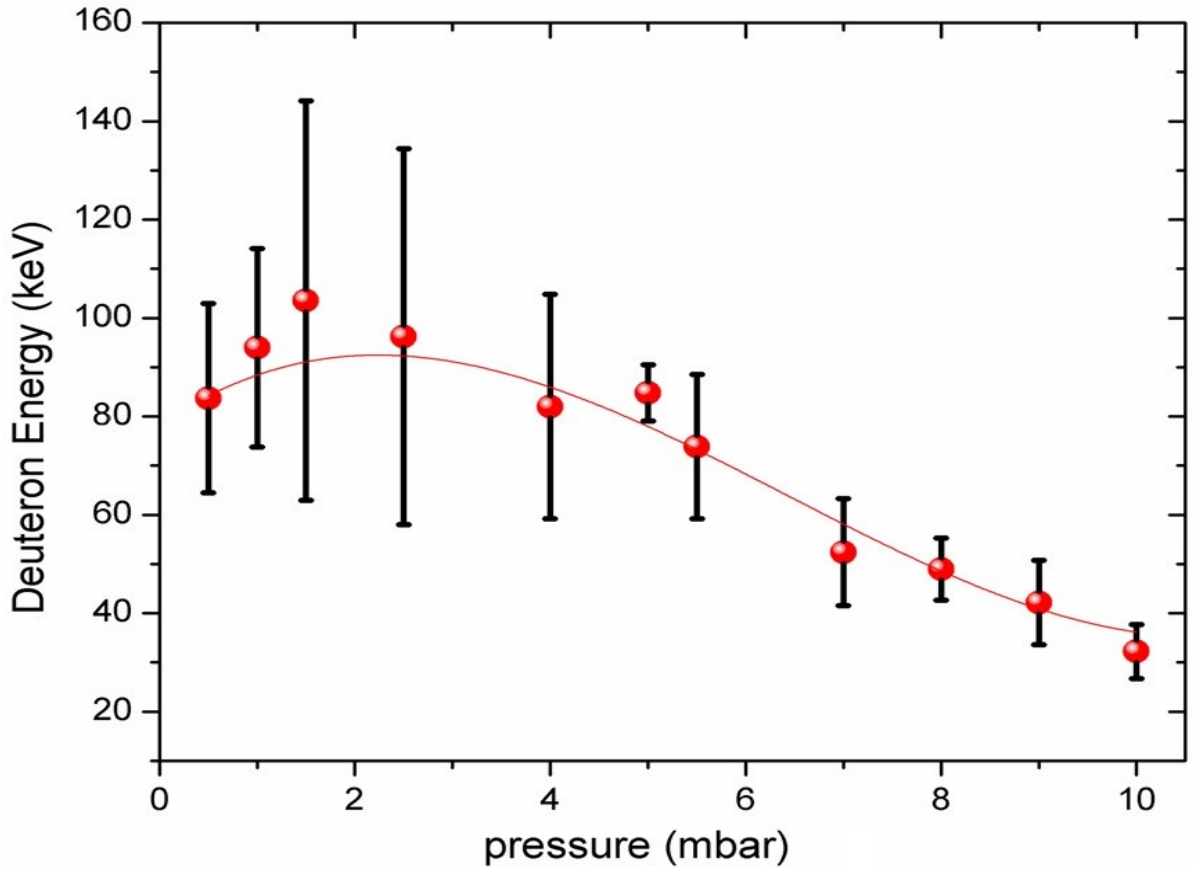

Figure 4-16. Deuteron energy variation with pressure.

The deuteron intensity spatial distribution was measured using a set of Faraday cups distributed at different angles of 0, 10, 20, 30^{o}, as shown in Figure 4-17(a). Faraday cups in this experiment were made out of SMA female connectors, each of which has a resistance of 50 Ω to match the cable. Each Faraday cup was connected to an RC circuit similar to the one used before in the ion collectors and biased by -50 V as well. This set up was mounted inside the chamber 14 cm away from the anode tip.

The deuteron intensity spatial distribution, Figure 4-17(b), shows a maximum value at the top of the anode, 0^{o}, and then the intensity deceases gradually with increasing angle up to 30^{o}. Taking errors into consideration, the deuteron intensity is almost constant in the pressure range from 0.5 to 5 mbar for all angles and then decreases when the pressure decreases beyond 5 to 8 mbar as shown in Figure 4-17.

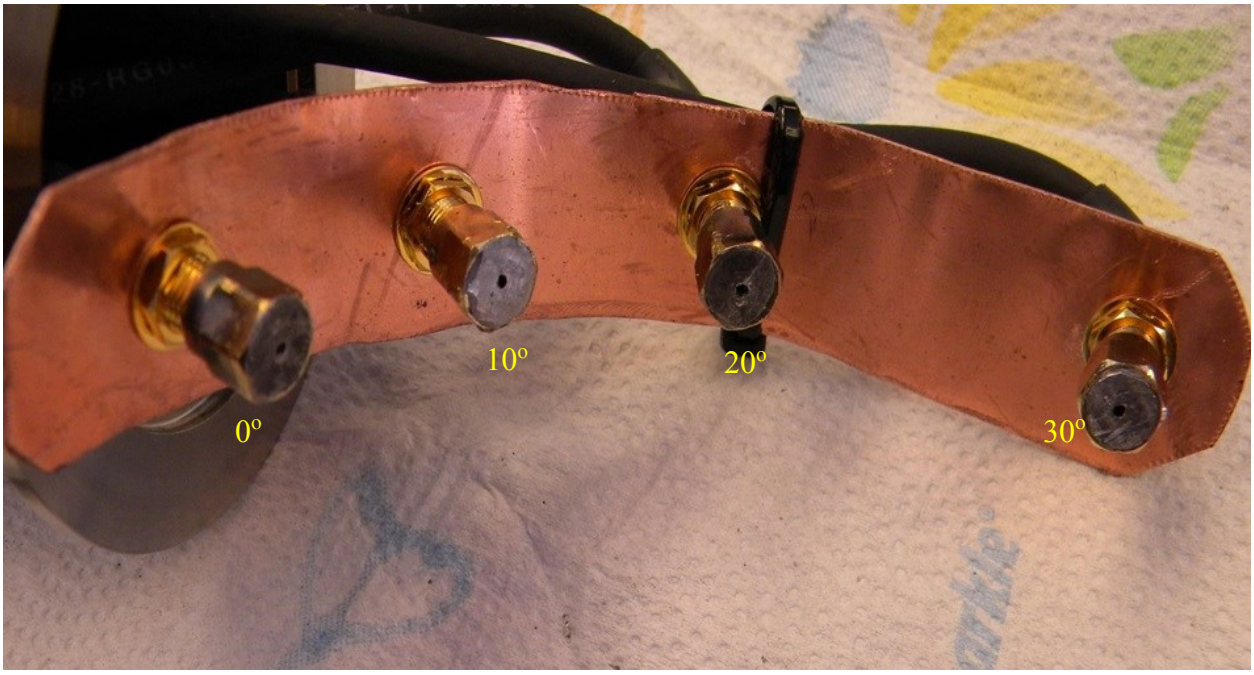

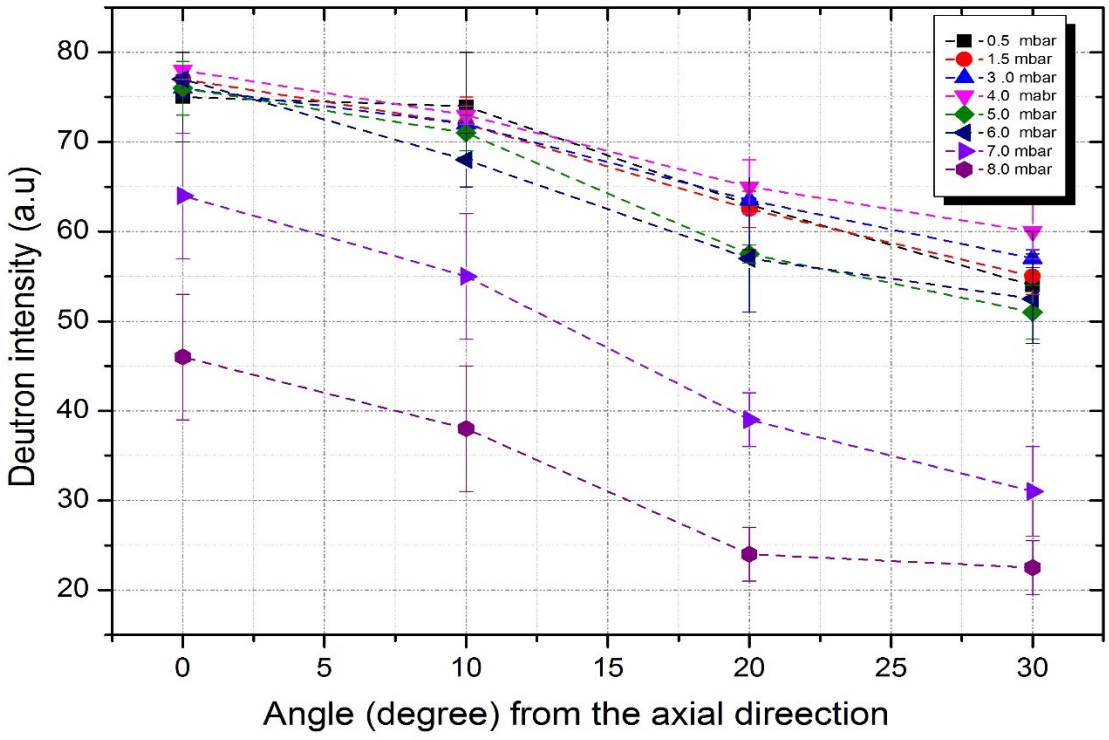

Figure 4-17. Faraday cups set used in deuteron intensity spatial distribution measurements (top), spatial distribution of deuteron intensity at different pressure (bottom).

4.6 Hard X-ray measurements

In order to to measure the hard X-ray (HXR) emission from the machine, the device was charged to 17 kV, which gives a peak current around 150 kA [149]. The gas was neon in the presence of a composite copper anode. A Rogowski coil and a voltage probe were used to measure the pinch current and voltage, respectivly. Two H7195 Hamamatsu photomultiplier tubes, coupled with a BC-418 plastic scintillator (2 × 1 in), were used as X-ray detectors.The PMT's were placed 90 cm away from the anode tip in both axial and radial directions. Figure 4-18 shows the configuratoin of the device and the measuring system. All signals are recorded by two Tektronix 7000 series DPO oscilloscopes through triaxial cables.

4.6.1 *Hard X-ray emission with pressure*

Different neon fill pressures were used in a range from 0.5 to 5 mbar. Ten shots were recorded at each pressure. The gas was purged after 10 shots to avoid contamination. An MKS Baratron pressure gauge, of 627B type, was used to measure the absolute pressure with an accuracy of ±12%. Typical signals for the current derivative along with the axial and radial PMT traces at 4 mbar gas pressure are shown in Figure 4-19. It has been shown that the high inductance dense plasma focus device, categorized as T2 like KSU-DPF, has more than one dip in more than 95% of its shots [144].

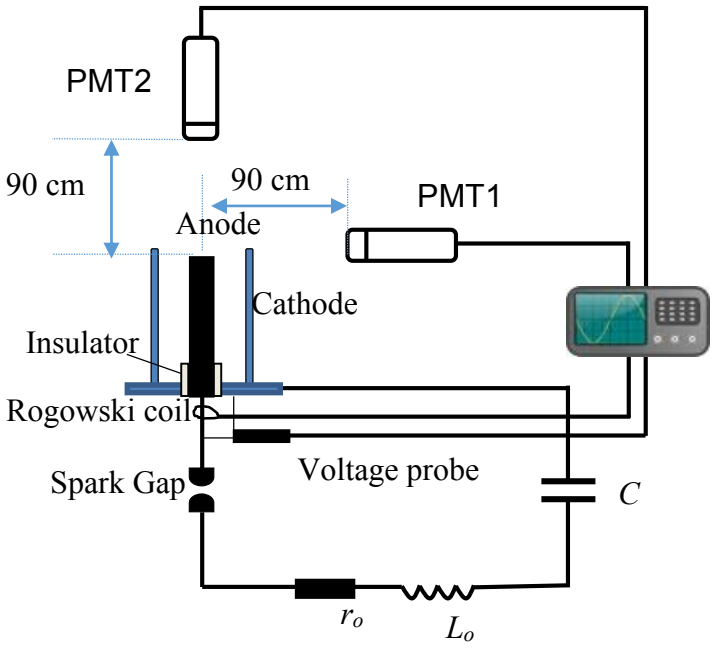

Figure 4-18. Schematic diagram of the device and the measuring system.

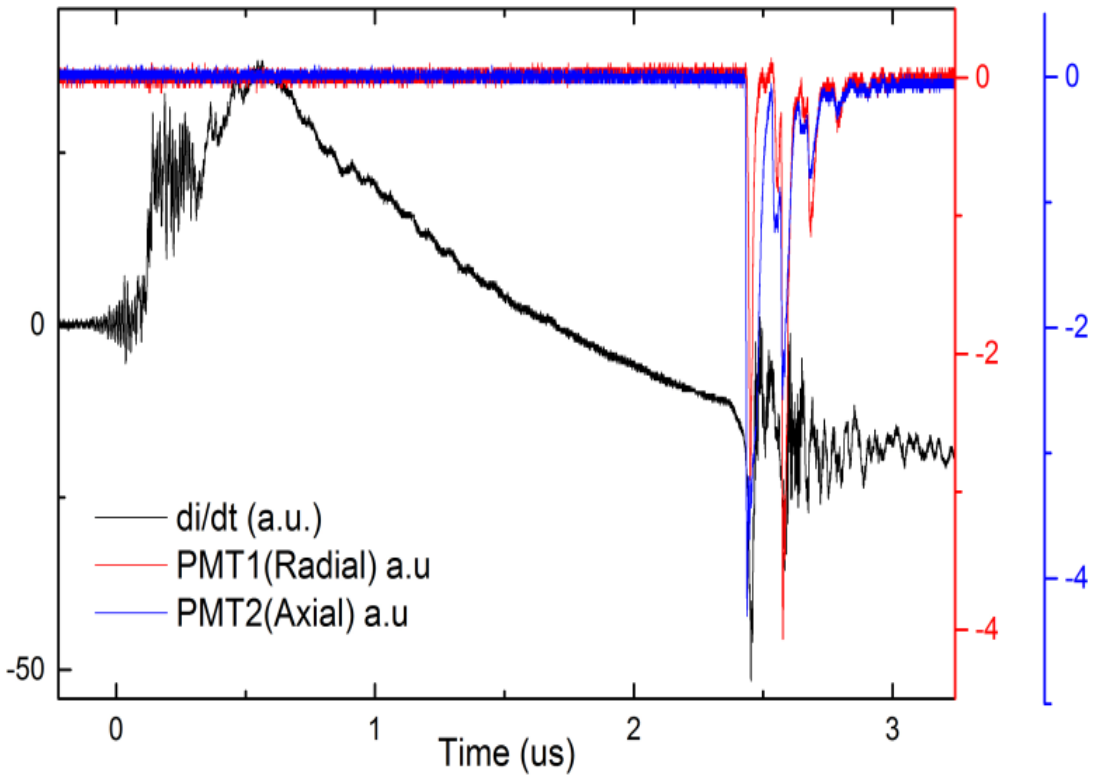

Figure 4-19. Typical signals for the current derivative and both axial and radial PMT's.

The relative HXR yield in both axial and radial directions was estimated by integrating the area under the peaks for both PMT's and calculating the average over the 10 shots for each pressure. Figure 4-20 shows the variation of HXR yield with gas pressure in both the axial and radial directions. It was found that a maximum yield of 727.7 and 570.2 Vns happened at 0.5 mbar for both axial and radial directions, respectively. Increasing the gas pressure produces a decrease in the HXR yield. It is known that the HXRs are produced due to the collision of the high energetic electron beam produced from the pinch with the anode material. Increasing the gas pressure causes the pinch formation to be weaker; furthermore, the electron energy will decrease producing less HXR yield [150]. HXR yield measurements in both radial and axial directions show higher axial yield producing anisotropy for all pressure values. The ratio of HXR yield in axial and radial direction (anisotropy) is shown in Figure 4-21. The HXR anisotropy is almost constant at 1.3 in the range from 0.5 to 3 mbar and then starts to increase up to 4 at 5 mbar. In the case of neon gas, the pinch starts to become unstable after 4 mbar, as evidenced by the errors at 4 and 5 mbar pressure.

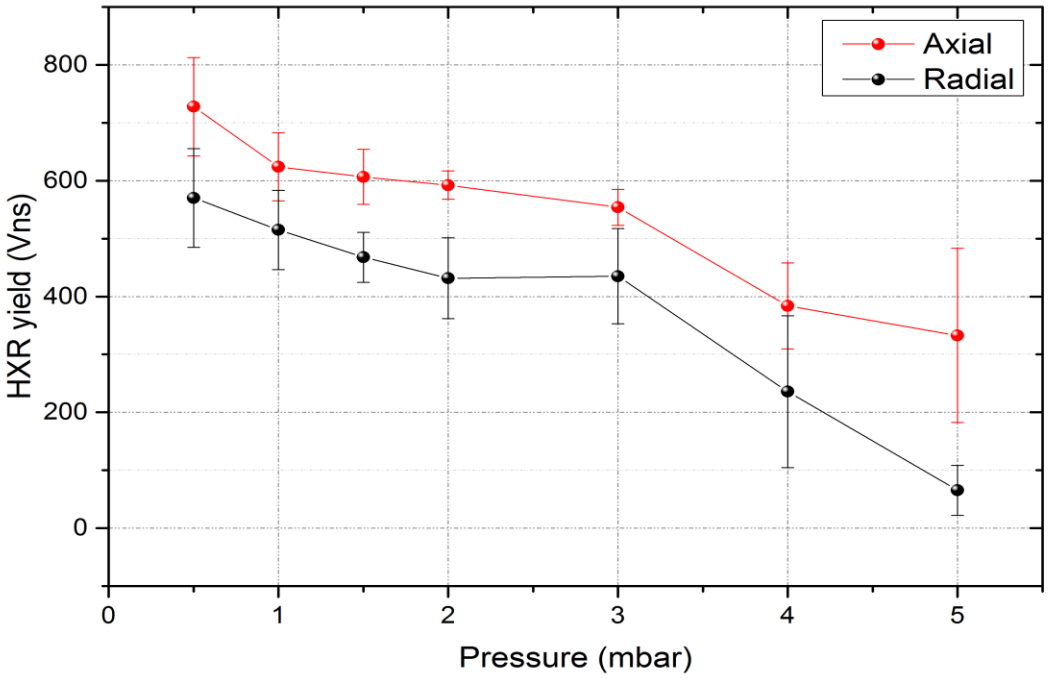

Figure 4-20. Comparison between the HXR in Radial and axial direction.

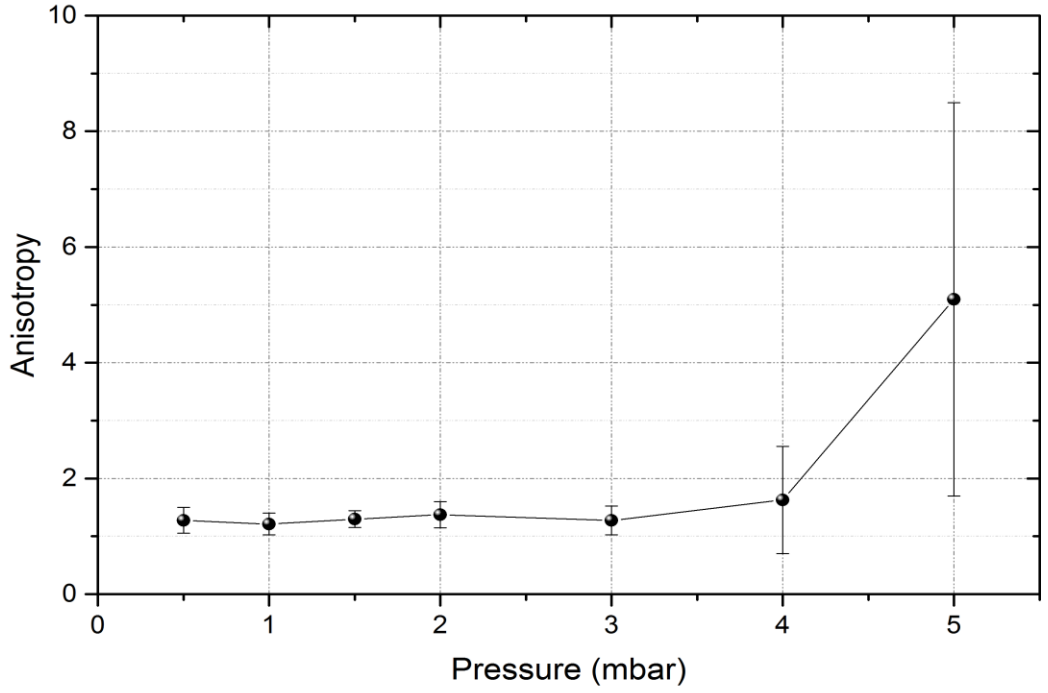

Figure 4-21. Anisotropy for HXR axial and radial measurements.

The anisotropy occurs mainly because of the anode configuration. Because the HXR is produced inside the hollow part of the cathode, the radial HXRs are attenuated through the thicker part of the cathode [5].

4.6.2 *Average effective energy*

Studying the hard X-rays radiated from the DPF device is important for the development of applications and for better understanding of the device physics. The hard X-ray spectrum radiated from the dense plasma focus machine is quite broad and fast, lasting only nanoseconds, which makes it is difficult to study using conventional spectrometry or single event spectroscopy [151]. Efforts were done before to estimate the hard X-ray spectrum emitted from dense plasma focus devices. H. Van Paassen et al. and N. Flippov et al. indirectly estimated hard X-ray spectra up to about 100 keV using K-5 nuclear emulsions [67] and differential absorption spectrometry with thermoluminescent dosimeters (TLDs) [152]. In both cases the spectrum was obtained after estimating the electron spectrum. Ross filters coupled with photo-detectors [67, 68, 153] were also used to estimate the spectrum but it worked only up the K-shell absorption edge of tantalum, 67.4 keV. Tartari et al. [154] estimated the spectrum for a 7 kJ plasma focus device using a multichannel differential absorption spectrometer based in TLDs). They used 40 shots to get a good signal-to-noise ratio. V. Raspa et al. [155-158] measured average effective energy and spectrum of HXR emission from a DPF using a method based on the differential absorption of radiation when passing through metallic plates with different thicknesses, called step filters. The same method was used to estimate both average effective energy and spectrum of the KSU-DPF hard X-ray emission.

When a beam of photons with a spectrum *S(E)* passes through a sample of thickness x, it will be attenuated according to the relation [159]:

$$\frac{I(x)}{I_0} = \frac{\int_0^\infty S(E) e^{-\boldsymbol{\mu(E)}x} dE}{\int_0^\infty S(E)\, dE}, \qquad 4\text{-}3$$

where $\mu(E)$ is the linear attenuation coefficient of the sample material at photon energy E, x is the penetration depth of the photon inside the material, I_0 and $I(x)$ are the photon intensities before entering the sample and at distance x inside the sample, respectively. The quantity $\frac{I(x)}{I_0}$ is called the transmission ratio. For average effective energy estimation equation 4-3 can be written as [155]

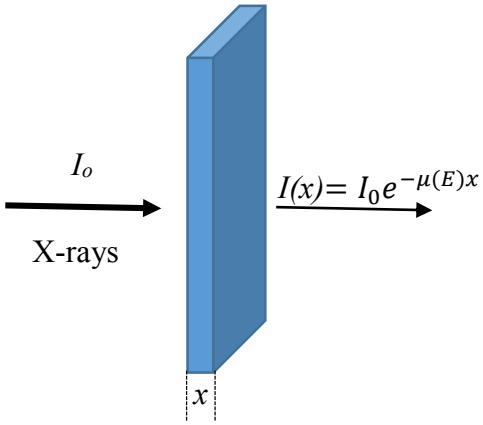

Figure 4-22. Schematic for photon attenuation through a material with thickness x.

$$\frac{I(x)}{I_0} = e^{-\mu^* x} \,, \qquad 4\text{-}4$$

where $\mu^* \equiv \mu(E^*)$ is the effective attenuation coefficient which is the linear attenuation coefficient at the average effective energy. The average effective energy can be defined as the energy of the monochromatic beam which produces the same effect. By calculating the value of $\frac{I(x)}{I_0}$ for the X rays through a material of thickness *x,* as shown in Figure 4-22 , μ^* can be estimated using equation 4-4. Once μ^* is known, E^* can be found from the tables [160].

An experiment was performed to estimate the effective energy and the spectrum of the hard X rays of the device. The filling gas in the experiment was neon at constant pressure of 1 mbar in the presence of a copper anode. The capacitor was charged up to 17 kV. X-ray films were used as X-ray detectors in addition to a Rogowski coil, voltage probe and photomultiplier tube coupled with BC-418, 2×1 in, plastic scintillator to monitor the device operation. Super HR-T green Fuji X-Ray Films, 8×10 in, were used. These were manually processed with the recommended developer and fixer from Fujifilm. The film was placed in a light tight aluminum X-ray cassette along with a terbium-doped gadolinium oxysulphide (Gd_2O_2S:Tb) intensifying screen. The intensifying screen works as a transducer from the hard X-rays to visible light, which can be detected by the X-ray film because the film itself is insensitive to any light with wavelengths more than 650 nm. Emission light from the intensifying screen has a dominant peak at 540 nm, green, in addition to two other peaks at 480 and 580 nm [161]. This light output matches the spectral sensitivity of the X-ray film which spans from 300 to 580 nm. The normalized conversion efficiency of the intensifying screen as a function of the photon energy, $\eta(E)$, is shown in Figure 4-23.

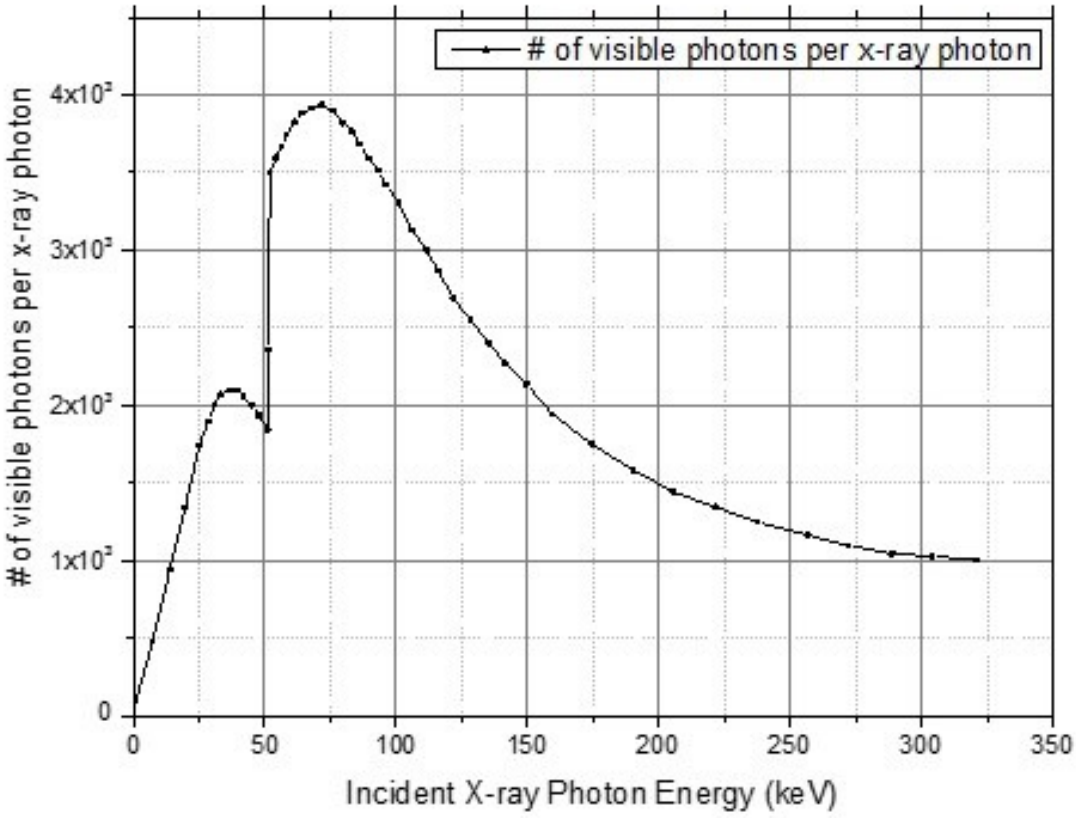

Figure 4-23. Normalized conversion efficiency of the intensified screen [157].

Filters from different materials and thicknesses were prepared as step filters. Information about material and thicknesses used are shown in

Table 4-1. A lead sample, *Pb ref.*, was used to determine the fog level reference. The step filters were mounted on the cassette surface that faced the X-ray source. As result, the X-rays coming from the device, after being attenuated by the filters, pass through the intensifying screen inside the cassette producing visible light, which is detected by the X-ray film. The detecting system, cassette and filters, were placed 40 cm from the source. A schematic of the experiment configuration is shown in Figure 4-24. Only one shot was taken at a neon pressure of 1 mbar. A photograph of the step filters used and the resulting radiograph is shown in Figure 4-25. Black and white film density was measured using an X-rite 301 densitometer, shown in Figure 4-26(a). Since the densitometer gives information about the optical density of the film rather than the transmission ratio ($I(x)/I_0$), a certified denstep was used. The denstep is a film strip with a calibrated grey scale,

provided by the film manufacturer, used to make a calibration between the densitometer reading, optical density (OD), and the transmission ratio ($I(x)/I_0$).

Material	Z	Thickness (cm)									
Cu1	29	0.013	0.026	0.039	0.052	0.065	0.078	0.091	0.104	0.117	0.13
		0.143	0.156	0.169	0.182	0.195	0.208	0.221	0.234	0.247	0.26
		0.273									
Cu2	29	0.033	0.066	0.099	0.132	0.165	0.198				
Pb	82	0.0074	0.0148	0.0222	0.0296	0.037	0.0444	0.0518	0.0592	0.0666	0.074
		0.0814	0.0888								
Al1	13	0.16	0.32	0.48	0.64	0.8	0.96	1.12			
Cd	48	0.06	0.12	0.18	0.24						

Table 4-1. Different materials used as step filters.

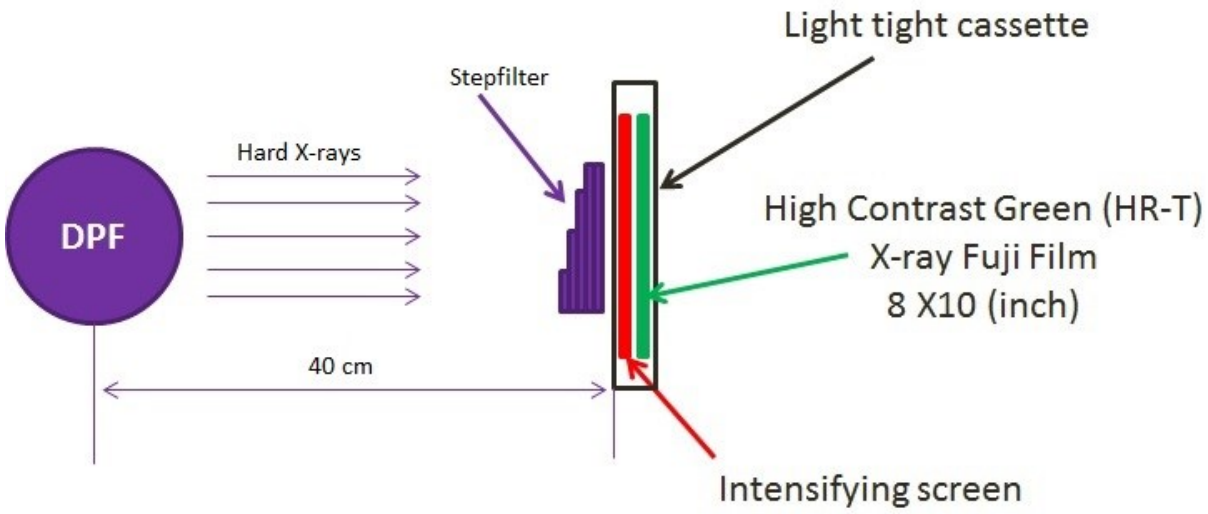

Figure 4-24. Schematic of HXR experiment.

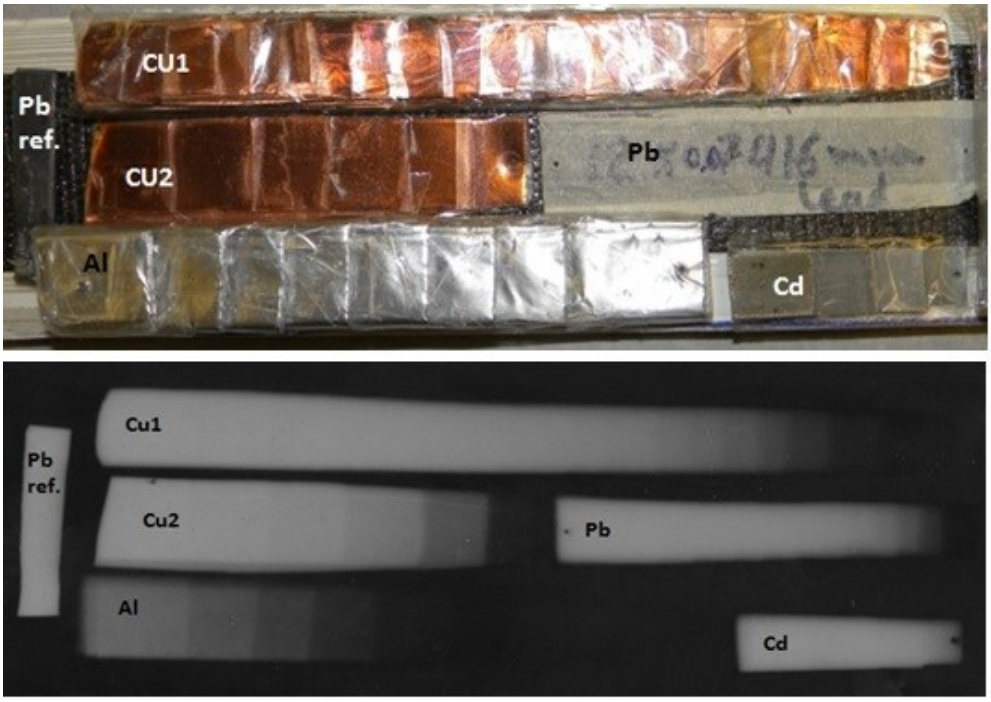

Figure 4-25. A photo for the step filters used (top) and their radiographs (bottom).

Figure 4-26. X-RITE 301 densitometer used to measure the optical density (a), calibrated transmission set (b).

The one used in this study was a certified density step wedge film that covers densities from 0.195 to 4.17 in 14 steps, as shown in Figure 4-26(b). The denstep was placed inside the cassette, between the intensifying screen and the film, to produce a radiograph of it at the same time as the step filters radiograph.

A calibration curve, Figure 4-27, was produced by doing densitometric analysis of the denstep radiograph and calibrated transmission values supplied by the denstep manufacturer. To avoid the inhomogeneity of the film, normalized optical density was used according to the following equation:

$$NOD(x) = \frac{OD(x) - OD_{min}}{OD_{max} - OD_{min}}, \quad 4\text{-}5$$

where $NOD(x)$ is the normalized optical density at any point on the film, $OD(x)$ is the optical density at that point measured by the densitometer, OD_{max} and OD_{min} are the maximum and minimum black level on the film, respectively. The normalized optical density for different samples as a function of sample thickness is shown in Figure 4-28. All curves displayed exponential decay, which indicated that the films were not saturated.

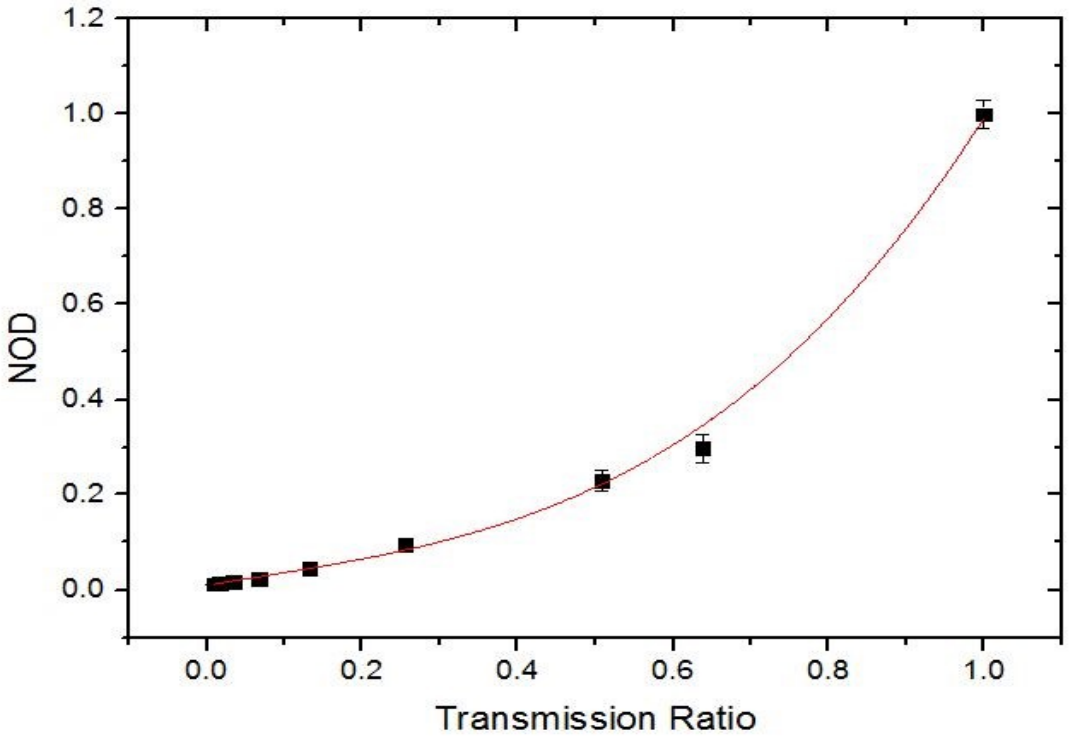

Figure 4-27. Calibration curve obtained from the densitometric analysis of denstep radiograph.

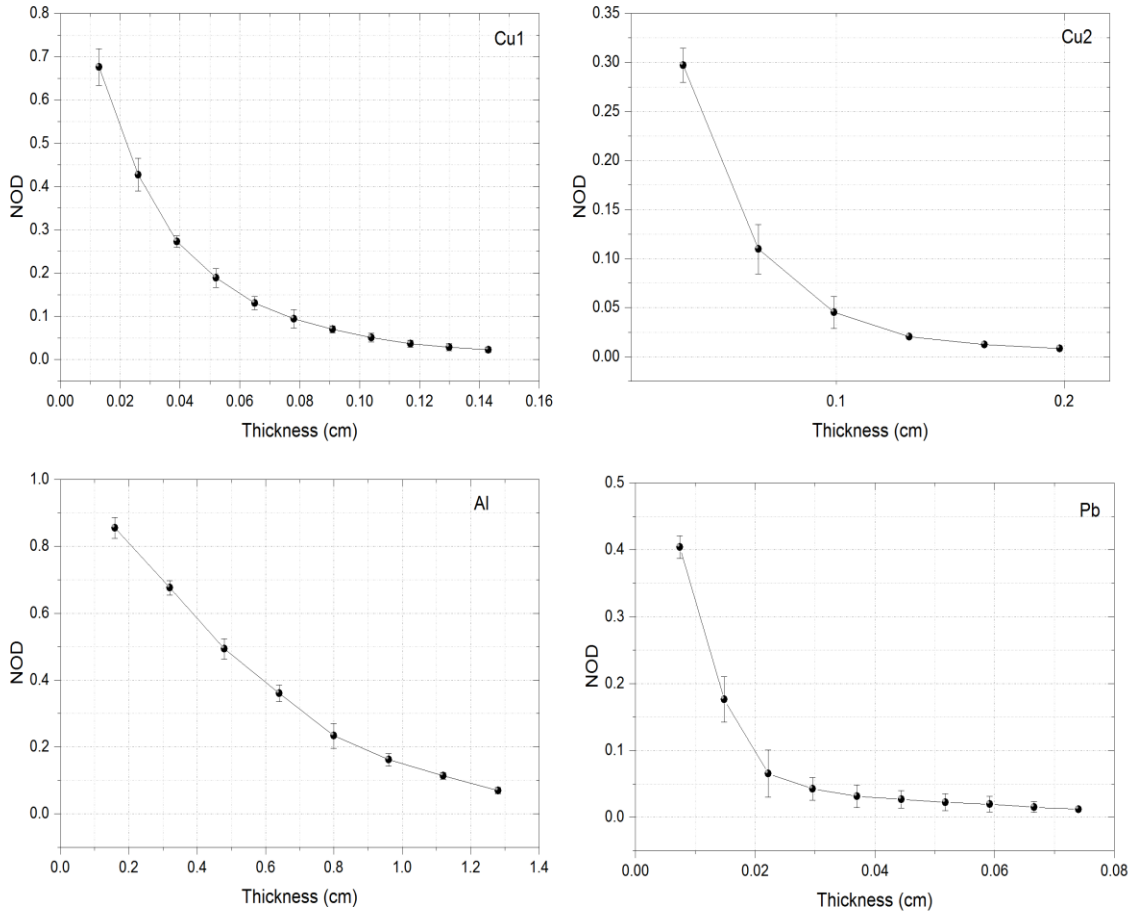

Figure 4-28. Normalized optical density for different filters used as a function of filter thickness

By interpolating the normalized optical densities, NOD, the calibrating curve, Figure 4-27 was used to estimate the transmission ratio $(I(x)/I_0)$. Once the transmission ratio was known, the effective attenuation coefficient, $\mu^* \equiv \mu(E^*)$ can be determined. This is then used to find the average effective energy, E^*, as explained before. The average linear attenuation coefficient (μ^*) and its corresponding average effective energy (E^*) for the different materials are shown in Table 4-2. All of the filters showed good agreement in calculating the average effective energy. The average effective energy obtained was 59 ± 3 keV.

To verify the calculated value for HXR average effective energy, the pinch voltage, V_p, was estimated theoretically using the Lee model [29]. The pinch voltage is the voltage drop that happened at the moment of the pinch due to the rapid change of plasma inductance. This voltage

Table 4-2. Measured Attenuation coefficient and its corresponding average effective energy

Material	Density	μ*	E*
Cu1	8.96	14.98±1.82	60±3
Cu2	8.96	17.87±2.34	56±3
Al	2.7	0.79±0.16	61±10
Pb	11.34	60.51±8.77	59±4
Average			59±3

is responsible for accelerating the ions and electrons. By neglecting any resistive contribution to the pinch, the pinch voltage can be estimated from [82]:

$$V_p = \frac{d(L_p I)}{dt}, \tag{4-6}$$

where L_p and I are the pinch inductance and current . The inductance is given by:

$$L_p = \frac{\mu_o}{2\pi} h(t) \ln\left(\frac{r_e}{r(t)}\right), \tag{4-7}$$

where μ_o is the permeability of free space, *h(t)* and *r(t)* are the pinch height and radius, respectively, and r_e is the anode radius.

Assume the pinch current, *I*, and height, *h(t)*, are constants through the pinching process. Then, the pinch voltage equation can be written as:

$$V_p \approx -\frac{I\,\mu_{oh}}{2\pi}\,\frac{1}{r}\frac{dr}{dt}, \tag{4-8}$$

where *dr/dt* is the convergent radial velocity.

For the KSU-DPF, the pinch current is I = 150 kA, the pinch height is $h \approx 6$ mm, the radius is $r \approx$ 0.6 mm and convergence radial velocity is 23 cm/μs as estimated from the Lee model and measured for similar devices. Thus, the pinch voltage is estimated to be 70 kV. Hence the electrons accelerated through this voltage will have energy of 70 keV. Therefore, it is reasonable to get 59±3 keV hard X-rays.

4.6.3 *Spectrum measurements*

To estimate the hard X-ray spectrum using an X-ray film the conversion efficiency $\eta(E)$ of the intensifying screen should be taken into account. Hence, equation 4-3 will be written as:

$$\frac{I(x)}{I_0} = \frac{\int_0^\infty \eta(E)S(E)e^{-\mu(E)x}dE}{\int_0^\infty \eta(E)S(E)\,dE}, \qquad 4\text{-}9$$

where $\eta(E)$is the conversion efficiency of the intensifying screen, shown in Figure 4-23. Because the transmission ratio $\left(\frac{I(x)}{I_0}\right)$ is experimentally measured and $\eta(E)$is known, the hard X-ray spectrum *S(E)* can be obtained by using equation 4-9. The MATLAB code used is shown in Appendix (i). The resulting spectrum is shown in Figure 4-29. Photons with energies less than 20 keV are attenuated by the 1 cm glass window. The spectral amplitude then rapidly increases to reach its maximum at 53 keV. It is then goes down again with increasing energy and becomes negligible beyond 120 keV. From the spectrum we can figure out that the value obtained experimentally for the average effective energy, $59 \pm 3\ keV$, is consistent.

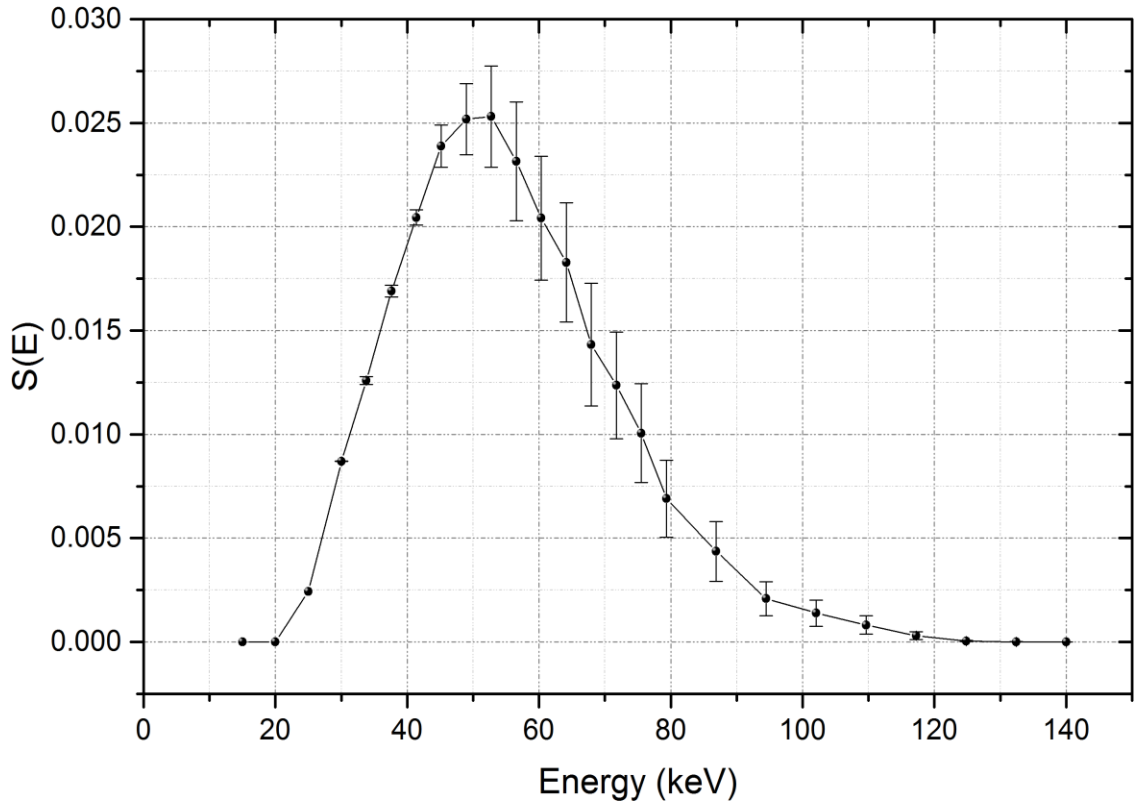

Figure 4-29. Measured X-ray continuum spectrum.

4.6.4 *Radiography using dense plasma focus*

Dense plasma focus devices have been used in radiographic imaging since 1976 [162]. Interesting results were achieved in this field using the soft region of the emitted X-ray spectra to produce radiographs for either small biological specimens or low absorption coefficient samples [79, 163]. The high energy part of the X-ray emissions was used in radiography since 2000 [164-[164-166]. C. Moreno et al. [164] used the DPF to produce non-conventional ultrafast introspective imaging for metallic objects. Such work demonstrates that DPF devices offer opportunities for many applications. V. Raspa et al. [155] used a 4.7 keV plasma focus device operated with a mixture of deuterium and argon to produce images for fast moving metallic objects. They produced images for a stainless steel ball bearing and aluminum turbine blade rotating at 2820 and 6120 rpm, respectively. The same device was used later by C. Moreno et al. [167] to produce fast radiography for metallic objects through metallic walls of several millimeters thickness. X-ray radiographic images were produced by the HXR emission of KSU-DPF using the same X-ray film used before. The cassette, containing the film and intensifying screen, was placed 60 cm away from the anode tip in the axial direction. Many metallic objects were mounted in front of the cassette to be imaged. Many trials were performed with different numbers of shots for various objects. It was found that the best resolution for radiographic images can be obtained within 3 to 5 shots. One shot can still give an image but not as clear as when 3 were used.

Figure 4-30 shows radiograph images for different metallic objects at 1 mbar neon pressure. As shown in the figure, the images have good resolution, showing most of the details even for closely spaced objects, such as in the case of the integrated circuit. Good spatial resolution and contrast by using multi-shots, 3 shots in this case, gives evidence that the radiation source almost happened each time at the same spot which means the KSU-DPF is a stable machine. An interesting application of HXR emission from DPF devices is to test metal objects for cracks that cannot be seen. Figure 4-31 shows a radiograph of aluminum phantom (1" cube), which has a crack and a hole in one side, imaged from two different sides. The cube was supplied by the Mechanical Testing and Evaluation Laboratory (MTEL) at Kansas State University. As seen from the image one can easily detect the crack from both sides which might be useful in the field of material testing.

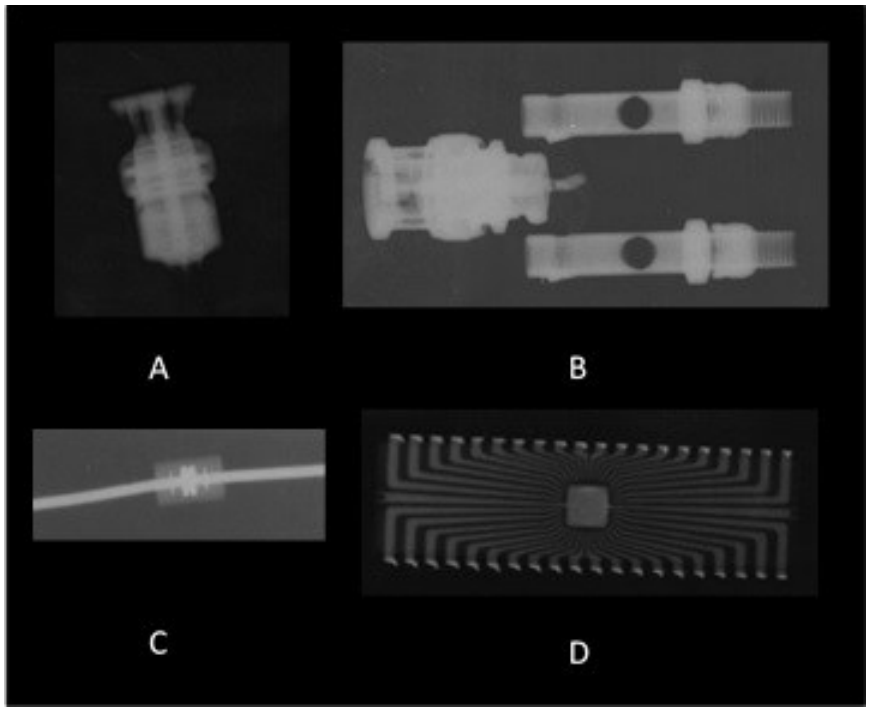

Figure 4-30. Radiograph for different objects at 17 kV, 1 mbar with 3 shots, A- BN connector, B- BNC male to dual binding post adapter, C- Resistor and D- Integrated circuit.

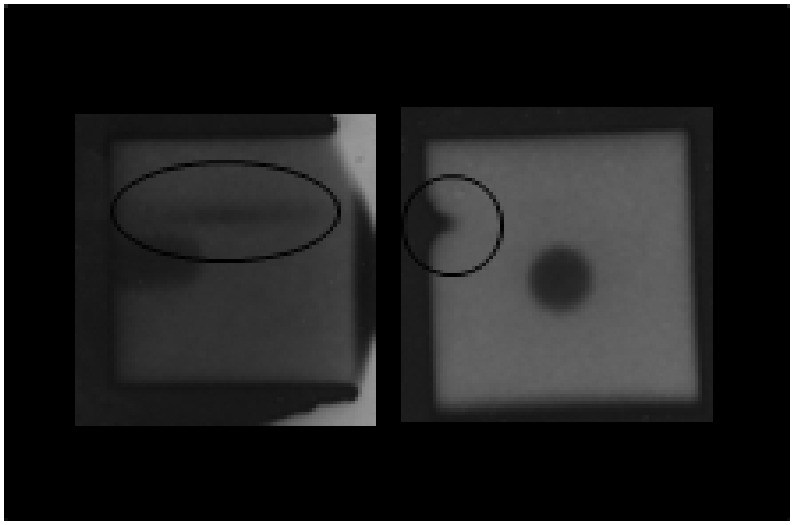

Figure 4-31. Radiograph of aluminum phantom (1" cube) has a crack and a hole in one side.

Chapter 5- Explosive Detection

5.1 Introduction

Explosives are compounds that contain potential energy, which can be released to create blasts. These blasts can be used constructively or destructively. Most chemical explosives have some common characteristics. Many traditional explosives contain metal components, such as casings and detonators. For these explosives, X-ray inspection by trained experts can be useful for explosive detection [168]. However, many new explosives don't have metal components or specific shapes to make them appear suspicious under the X-ray investigation. There is a class of nitrogen-rich explosives that have similar compositions and densities. The National Research Council has identified 26 nitrogen-rich explosives that contain only hydrogen (H), carbon (c), nitrogen (N) and oxygen(O), all of which have combined N and O weight fractions above 0.55 [169]. In addition, most of these explosives have higher densities than inert HCNO materials but lower densities than most metals. Thus, nitrogen-rich explosives can, in principle, be detected on the basis of their density and chemical composition. The nitrogen-rich characteristic of these explosives has been used by some investigators to detect explosives. However, some explosive materials, for example gasoline, black powder or peroxide-based liquid explosives, do not have any nitrogen. Plastic explosives, like C4 and its Czechoslovakian counterpart and semtex, are very dangerous because of their flexibility which makes them easy to hide and smuggle.

5.2 Explosive detection methods

There is no single way to detect all type of explosives because of their variability, so it is necessary to use different techniques to detect different explosives. Explosive detection methods can be divided into two many categories: those that detect chemical traces of the explosive residues and those that look for characteristics of the bulk explosive material.

5.2.1 *Trace-based explosive detections*

5.2.1.1 *Ion mobility spectrometer (IMS)*

IMS is widely used in the airports to check carryon bags by wiping surfaces by a cloth strip to collect any explosive material residues. These samples are then warmed up rapidly to

around 200 C^o to produce vapor. The vapor is injected inside the mobility spectrometer at which it will mix with a gas phase producing ions. The resulting ions are then accelerated through an electric field, around 200 V/cm, [170] gaining a characteristic drift velocity. The drift velocity can be estimated by measuring the time taken by the ions from the entrance to the exit of the spectrometer. The ions are then collected by a detector producing a current flow. The resulting signal is called a mobility spectrum and depends on the ion molecular mass and ion charges [171].

5.2.1.2 *Gas chromatography*

Gas chromatography can be used to separate molecules of different chemical compounds from each other by injecting them into a chromatographic column. A chromatographic column is a hollow tube equipped with beads covered with a substance which interacts at different rates with different compounds. Therefore this interaction produces different molecules at different times. This method is used to separate the negative ions in explosive materials which can be detected using other methods like electron capture, mass spectroscopy, flame ionization, chemiluminescence, or surface acoustic waves [168].

5.2.1.3 *Antibodies*

A vapor detection technique in which the vapor flow is allowed to pass through a vessel that contains immobilized antibodies and florescent labelled analogs of explosive molecules is also used. At the vessel the antibodies interact, with high precision, with only one specific explosive [172]. If that explosive exists in the air flow it will replace the labelled analog and is detected downstream. This method is fairly inexpensive, fast and fully automated but antibodies of all explosive materials are needed.

5.2.2 *Human and biological based methods*

5.2.2.1 *Animals*

Dogs are widely used for detection purposes [173]. They can be excellently sensitive and specific. Many federal agencies, such as the Transportation Security Administration, the United States Secret Service and Department of Defense as well as state and local agencies are using dogs in explosive detections. Using dogs has the advantages that it is relatively easy and inexpensive and dogs are mobile. The disadvantages of using dogs include the facts that this process depends

on the dog handler skills at interpreting dog responses, dogs can only detect scents that were included in their training and dogs require care and feeding. Recently, some investigations have been done to use other animals such as rats [174] and bees [175].

5.2.2.2 *Manual inspection*

Although it is time-consuming and has some risk, manual inspections by well-trained people are still being used. An example is by using metal detector and probing rods [168].

5.2.3 *Nonionizing radiation-based methods*

5.2.3.1 *Electromagnetic induction*

Electromagnetic induction is mainly used for detecting metal objects. The idea is based on sending electromagnetic pulses which will produce an induced oscillating electromagnetic field within any metallic object. The resulting electromagnetic field is then detected through the detector coil by producing an electric current passing in the coil [172]. Because most explosives don't have a significant amount of metal, it is recommended to use this with other bulk detection methods.

5.2.3.2 *Radar interrogation*

The use of radar is considered an efficient way for detecting buried explosives specially when used with another bulk detection method. Radar interrogations are based on sending high energy radio waves into the ground and filtering out the reflected wave. The reflected wave depends on the reflecting material density and the wave interaction with its boundary [176].

5.2.3.3 *Nuclear magnetic resonance (NMR)*

The nuclear magnetic resonance technique is based on the fact that protons inside nuclei will align themselves with an applied external magnetic field. Magnetic resonance is then measured by using a specific radio-frequency pulse to perturb the aligned nuclei and measuring the return rate to alignment. In this technique the resonance frequency depends on the external magnetic field strength and how much hydrogen is in the material [168].

5.2.3.4 *Nuclear quadrupole resonance (NQR)*

Unlike NMR, NQR doesn't need application of a magnetic field. It is based on the idea that electromagnetic radiation interaction with the nuclear charge density, in the interrogated material, splits the nuclear spin states. The NQR signal is determined by the coupling between existing

nuclear quadrupole moments and the gradient of the electric field which flips nuclear spin. Once the nucleus relaxes it emits a unique signal. This technique of detection works for crystalline solids and amorphous materials but doesn't work for liquids [170]. It has the ability to detect small amounts of some threat materials but it has some disadvantages. First, the lack of NQR signal on some explosive materials (those that are in a position where there is no electric field gradient). Second, the presence of a thick metallic container can shield the radiofrequency signals. Third, the AM radio-frequency signal can interfere with the original signals. Finally, thermally generated internal noise can increase the time required to get the signal.

5.2.3.5 *Terahertz imaging and spectroscopy*

Terahertz (THz) radiation is electromagnetic radiation in the range spectral region between high-energy microwaves and the far infrared. An ultra-short pulsed near-infrared laser, such as titanium-sapphire ($Ti:Al_2O_3$) is used to activate an ultrafast semiconductor, such as gallium arsenide (GaAs), to produce terahertz radiation, which is detected using a similar laser semiconductor combination [177]. A resonant absorption occurs when there is a match between the energy of the incident THz radiation and the rotational motions of dipoles in the interrogated material or the vibrations of atoms within the molecular lattice. This resonant absorption forms a unique fingerprint for each material [168]. One of the advantages of this technique is its high penetrability, since non-metallic and non-polar materials are transparent to this range of electromagnetic waves. Moreover, THz radiation is nonionizing, so exposure to it does not create electron-ion pairs, which can be harmful to people. However, the presence of metallic shielding can prevent this device from interrogating threat materials because THz radiation can't penetrate metals.

5.2.3.6 *Millimeter-wave interrogation*

Millimeter waves have frequencies between 30 and 300 GHz, with wavelengths from 1 to 10 mm. A wave with this length can penetrate many materials that are opaque to visible light. Millimeter waves can penetrate cloth and be reflected by the human body and metals [178]. Other materials such as plastic, ceramics and organic materials will partially reflect this type of wave. Millimeter-wave imaging provides an alternative to X-ray imaging at several airports. Recent investigations attempted to form three-dimensional images by use of two antennas to circle the target [179]. Although this method has excellent spatial resolution and doesn't produce ionizing radiation, it is not used on a large scale because of privacy concerns.

5.2.4 *Nuclear-based explosive detection methods*

5.2.4.1 *Neutron interrogation methods*

Neutrons are useful for material interrogation because of their penetration ability and because they interact with nuclei, providing information on composition. Both thermal and fast neutrons have been used. The collisions between neutrons and the nuclei in an interrogated object cause the nuclei to emit characteristic γ-rays or to change in the neutron energy in a way characteristic of the mass of the nucleus [180].

5.2.4.1.1 *Thermal neutron activation (TNA)*

Thermal neutron activation is based on the fact that different isotopes emit prompt-capture gamma rays of characteristic energies following (n, γ) or capture interactions. Capture cross sections are large at thermal energies and small above the thermal range. Hence, the source must provide thermal neutrons or the sample must be able to thermalize a fast neutron beam. The capture gamma rays mainly used in this technique are 2.223 MeV from ^{1}H, 3.684 and 4.945 MeV from ^{12}C and 10.83 MeV ^{14}N [180]. Generally, the capture gamma rays are analyzed to produce information about the density distribution of various elements in the target. Using TNA provides a nitrogen map which is considered an advantage for this technique because many explosives are nitrogen-rich materials. Thermal neutrons also can easily penetrate thin metal screens that can shield X rays. The main disadvantages of TNA are that it is expensive, most neutron sources are either radioactive or bulky and neutrons produce activation products in the interrogated object. However, DPF neutron sources are less bulky than most other machine sources and produce neutrons in short pulses. Thus, the KSU-DPF device is investigated in this research in order to investigate the feasibility of DPF-based TNA for rapid screening of packages for explosive materials. Coupling this technique with the conventional X-ray scanning technique provides additional information and can improve performance [170].

5.2.4.1.2 *Neutron backscatter*

Neutron backscatter has been used to search for buried explosives [181] and to measure moisture content of soils. Fast neutrons sent into the ground will slow as they scatter and the thermal neutron flux exiting the soil is a measure of hydrogen content, because hydrogen is the most efficient neutron moderator. In addition, the scattering properties of a material are dependent on

the composition of the material and so the backscatter spectra at various locations depends on sample material.

5.2.4.1.3 *Thermal neutron imaging*

Neutron radiography is based on passing a neutron beam through a target. Recent studies showed that structural defects and textures can be seen using energy-selective radiography performed around Bragg-cut-off wavelengths [182]. Thermal neutron imaging can be used to detect small amounts of materials that contain hydrogen or highly neutron absorbing materials.

5.2.4.1.4 *Fast neutron activation (FNA)*

FNA technique is based on using fast neutrons to probe the target material. The incident fast neutrons inelastically collide with the nuclei producing unique gamma rays for each element. FNA used to give more information that just nitrogen content as in the thermal neutron methods. Typical gamma rays detected with this technique from HCNO samples are shown in Table 5-1 [170]. Most FNA techniques use neutrons from the D-T reaction, which produces 14-MeV monoenergetic neutrons. The D-D reaction, which produces neutrons in the energy range from 2.45 and 7.71 MeV, depending on the deuteron energy, is also used as a neutron source.

At fast neutron energies, the common interaction between neutrons and target nuclei is elastic scattering. No photons are produced in this reaction. The scattering angles depend on the neutron energy and the mass of the struck nucleus. Thus, responses due to scattered neutrons contain information on the composition of the sample. In well controlled experiments, this method can provide a clear idea about the target's atomic mass [183].

Table 5-1. Relevant energies of inelastic scatter gamma rays.

Isotope	Characteristic gamma rays (MeV)
^{16}O	6.13
^{12}C	4.44
^{14}N	2.31, 5.11

5.2.4.1.5 *Pulsed fast neutron analysis (PFNA)*

The only difference between this technique and the FNA is that a pulsed beam of neutrons is used. A collimated beam is used to hit the target and the resulting gamma rays are analyzed [172]. One of the approaches is referred to as pulsed interrogation neutron and gamma (PING) [184] where neutrons, 14 MeV, are produced by an accelerator in pulses. Nitrogen, sulfur (5.42 MeV gammas from ^{32}S) and chlorine (6.111MeV gammas from ^{35}Cl) have been detected with PING. Chlorine is useful in detecting the non-nitrogen-based explosives and in the detection of some drugs, such as cocaine. Although there are difficulties in putting put neutron accelerators at air-ports, sealed tube neutron DT kHz-pulsed accelerators are used [185].

5.2.4.2 *X-ray based screening*

X-rays have been used for many years for material detections especially for luggage at airports. Using X-rays has many advantages such as:

i. It gives information about material density and effective atomic number Z_{eff}.
ii. X-ray technology has been developed over many years and its physics is well understood.
iii. X rays are easier to shield than are neutrons.
iv. It is cost effective.

When X-rays pass through a material they will be attenuated according to the relation

$$\frac{I}{I_0} = \exp[-\mu(E, Z, \rho)x], \qquad 5\text{-}1$$

where: I_0 is the incident intensity, I is the uncollided intensity at distance x into the material, μ is the linear attenuation coefficient of the material, which depends on the photon energy, E and the material atomic number, Z, and is directly proportional to the density ρ.

X-ray interactions with matter occur in four different modes as shown in Figure 5-1:

i. Coherent X-ray scatter (CXRS), in which an X ray photon interacts with the entire atom or crystal lattice, losing little energy in the process.
ii. Incoherent (Compton) scatter, which is a direct interaction between an X-ray photon and an electron that can be considered as a free electron. A simple formula has been developed by Compton [186] to relate the photon scatter angle. θ_s, incident energy, E, and energy after scatter, E' [159]:

$$\frac{1}{E'} - \frac{1}{E} = \frac{1}{m_e c^2}(1 - \cos\theta_s) \qquad 5\text{-}2$$

The microscopic cross section for Compton scattering depends on the number of electrons per atom and thus varies as:

$$\sigma \alpha z \qquad 5\text{-}3$$

iii. Photoelectric absorption is an interaction in which all of the photon energy is used to extract a bound electron from its orbit. The photoelectric cross section in the X-ray range in can be approximated by the equation [169]:

$$\tau \approx 10 \frac{Z^{4.5}}{E^3} \text{ (b/atom)}, \qquad 5\text{-}4$$

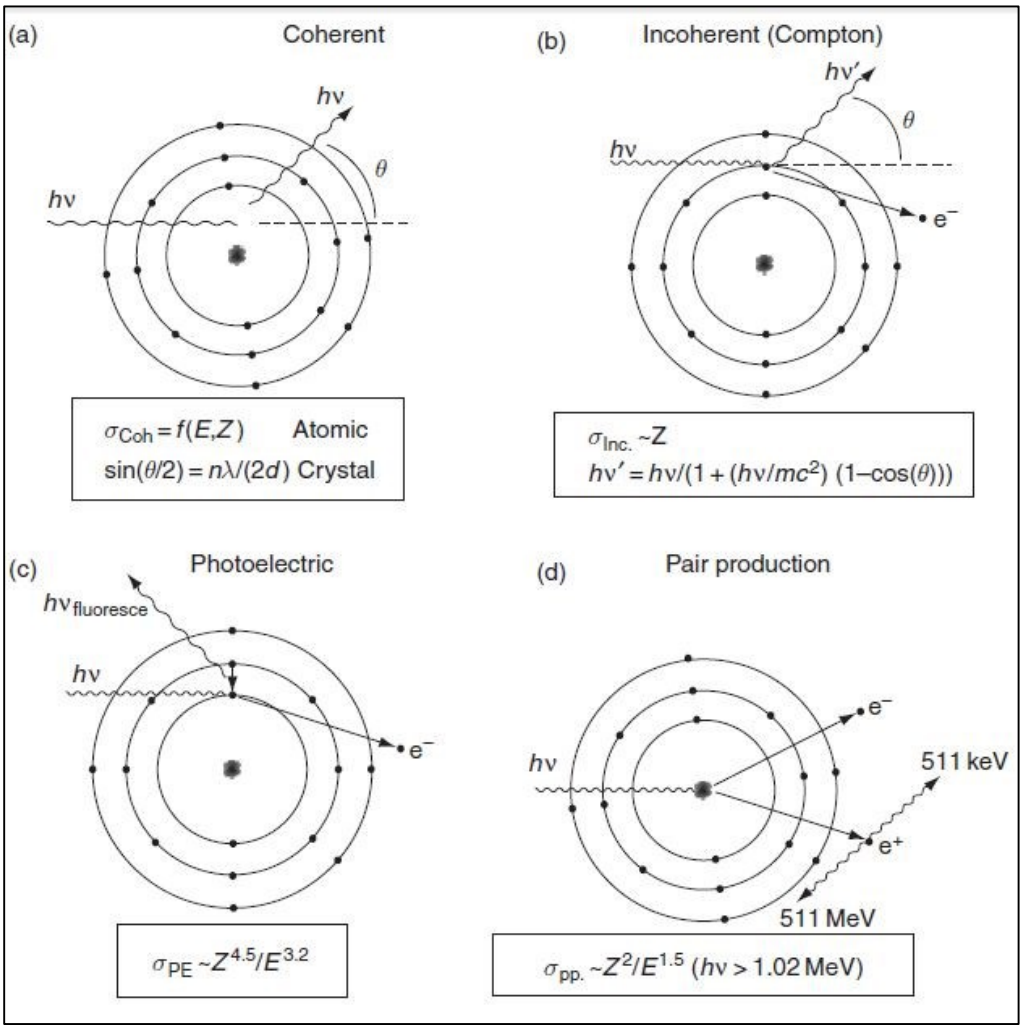

Figure 5-1. Schematic diagram for X-ray interaction modes [170].

where E is the photon energy (keV). Equation 5-4 shows that photoelectric absorption is significant for high Z elements but decreases rapidly with increasing photon energy for all elements.

iv. Pair production in which X-rays with energy 1022 keV or more reacts to produce an electron/positron pair making a local deposition of at least 511 keV at least.

Because the macroscopic Compton cross section depends on the density and the ratio of atomic number to mass number and most of elements have a mass number about twice its atomic number, Compton scatter cross section depends on the density of the scattering material. The macroscopic photoelectric cross section strongly depends on the atomic number.

5.2.4.2.1 *Conventional transmission X-ray radiography*

Conventional X-ray transmission techniques are widely used at screening check points. An operator inspects the X-ray images looking for threat or illicit materials. It is limited to checking luggage and inanimate objects because of high radiation doses. This technique cannot easily differentiate between a thin piece of a strong absorber and thick piece of a weak absorber. Examples of X ray transmission images are shown in Figure 5-2.

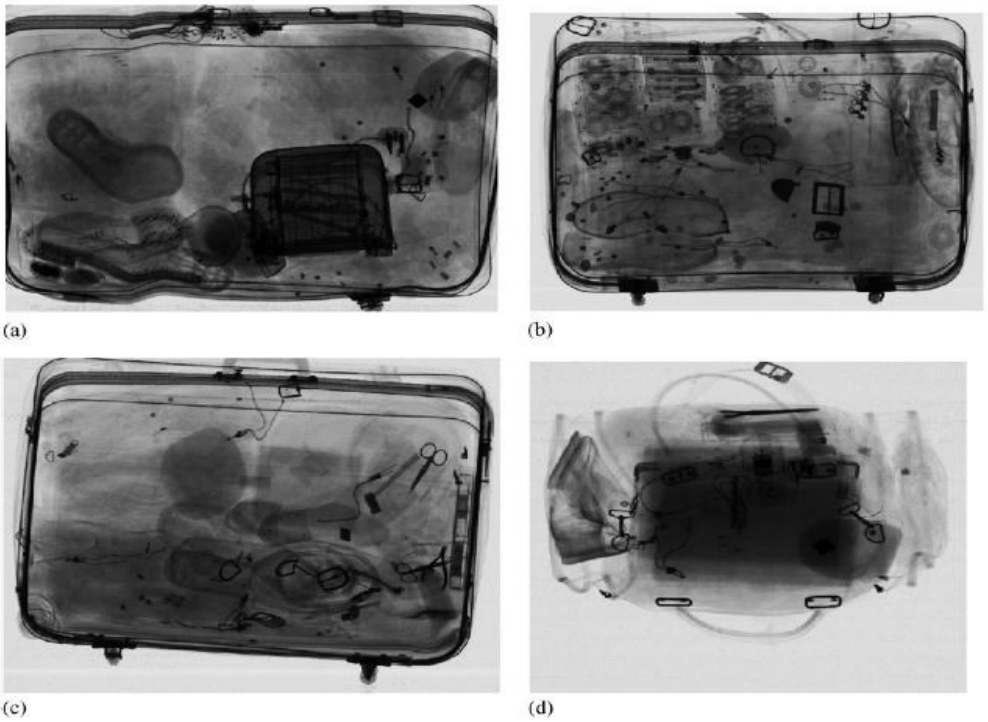

Figure 5-2. Examples of X-ray transmission images of luggage [172].

5.2.4.2.2 *Dual-energy X ray*

Taking the advantage of equations 5-3 and 5-4, dual energy X-ray techniques have been used. Two different X-ray energies or spectra are used, one high and one low. Two views of the inspected object are obtained in this technique, one for the high and the other for the low energy X rays. Heavy metal objects appear dark in both views while objects composed of only light elements will appear darker in the low-energy view than in the high-energy view [172]. Dual-energy X-ray techniques theoretically can provide information about material effective atomic number (z_{eff}). Many approaches have been investigated to improve the efficiency of this technique including using both transmission scattering modes and applying cotomography (CT) [187]. Because single-energy computed tomography gives information about localized electron density, it cannot distinguish inert materials that have similar electron densities to explosives [169]. In general dual-energy computed tomography, which includes weak information about composition, gives better results than single-energy computed tomography in explosive detection.

5.2.4.2.3 *Scatter imaging*

Back scatter imaging systems are based on the formation of images from the back scattered photons from targets. One of the problems of the back scatter method is the difficulty of differentiating between explosives and other low Z materials which have the same electron density [168]. Several X-ray scatter methods have been studied, such as X-ray diffraction [188], which provides information about the crystalline structure of the target, and the coded aperture method, which is useful in land-mine detection [189]. Many attempts have been made to improve the images resulting from scattered photons, including using coded aperture masks. The masks have transparent and opaque sets of pixels which focus the photons in the same manner as the pinhole camera [190].

5.2.4.2.4 *Gamma-ray resonance absorption*

The gamma-ray resonance absorption method is mainly used to detect the presence of nitrogen atoms in the target by using one of the unique nuclear reactions with nitrogen atoms. This method is frequently used with one of the other photon interrogation methods that depend on the electron density of target materials. One of the methods uses the nuclear resonance absorption of the 9.17 MeV gamma rays by the ^{14}N atoms. A high attenuation of the gamma rays of this energy implies a high density of ^{14}N atoms.

5.3 Signature-based radiation scanning (SBRS)

The signature-based radiation scanning (SBRS) method was developed by Dunn et al. [191]. It is a rapid method that uses active interrogation to detect explosives at standoff distances of meters. Standoff is very important in explosive detection to avoid or reduce injury to the operators. Loschke et al. [192] and Lowrey et al. [193] successfully used SBRS to detect explosive-like substances by using active photon and neutron interrogation, respectively. In the SBRS method, the scattered or generated radiation from the target is collected by different detectors. Each detector reading is called signature. One collects different signatures for each unknown target and compares them to templates. A template is a collection of the same number of signatures for a target containing a known explosive or explosive-like material. This template-matching procedure involves forming a figure of merit (FOM), whose value indicates whether the target contains an explosive material or not. The interrogating radiation may be photons, neutrons or both. Radiation detectors record different signatures, which may be due to back-scattered photons, back-scattered neutrons, prompt and inelastic-scattered gamma rays, and possibly even photon-induced positron annihilation radiation (PIPAR) [194].

Collected signatures from the unknown target are used to form a response vector R_j , where the j is the number of the signature. Similar signatures collected from a target containing an explosive in some configurations are used to form a template vector S_{jl}. The template- matching process uses a chi-square-like figure-of- merit [192] in the following form:

$$\zeta = \sum_{j=1}^{J} \alpha_j \frac{\left(\beta R_j - S_{jl}\right)^2}{\beta^2 \sigma^2\left(R_j\right) + \sigma^2\left(S_{jl}\right)}, \qquad 5\text{-}5$$

where $\sigma^2\left(R_j\right)$, $\sigma^2\left(S_{jl}\right)$ are the variances of the response R_j and the template signature S_{jl}, respectively, β is a scaling factor that accounts for differences in the conditions (such as count time and source intensity) under which the unknown target responses and the template responses were taken and α_j is a normalized positive weight factor calculated from the equation:

$$\alpha_j = \frac{\omega_j}{\sum_{j=1}^{j} \omega_j}, \qquad 5\text{-}6$$

where w_j is an assigned weight for signature j. The standard deviation of the figure-of-merit of equation 5-5 is estimated using the standard error propagation method [193]. For a function $f(a,b)$ the standard deviation will be:

$$\sigma(f)=\left(\left|\frac{\partial f(a,b)}{\partial a}\right|^2\sigma^2(a)+\left|\frac{\partial f(a,b)}{\partial b}\right|^2\sigma^2(b)+2\frac{\partial f(a,b)}{\partial a}\frac{\partial f(a,b)}{\partial a}\mathrm{cov}(ab)\right)^{1/2}, \quad 5\text{-}7$$

where $\sigma^2(a)$ and $\sigma^2(b)$ are the variances of parameters a and b and $\mathrm{cov}(ab)$ is the covariance between the two parameters. In case the variables a and b are independent of each other, $\mathrm{cov}(ab)$=0. Applying equation 5-7 to equation 5-5 leads to the following:

$$\sigma(\zeta)=\left[\sum_{j=1}^{J}\left(\frac{\partial\zeta}{\partial R_j}\right)^2\sigma^2(R_j)+\sum_{j=1}^{J}\left(\frac{\partial\zeta}{\partial S_j}\right)^2\sigma^2(S_j)+\sum_{j=1}^{J}\left(\frac{\partial\zeta}{\partial\sigma^2(R_j)}\right)^2\sigma^2\left(\sigma^2(R_j)\right)+\sum_{j=1}^{J}\left(\frac{\partial\zeta}{\partial\sigma^2(S_j)}\right)^2\sigma^2\left(\sigma^2(S_j)\right)\right]^{1/2} \quad 5\text{-}8$$

where the terms $\sigma^2\left(\sigma^2(R_j)\right)$ and $\sigma^2\left(\sigma^2(S_j)\right)$ are the variance of the variance (VOV) for response and target signatures, respectively. The partial derivative terms in equation 5-8 are:

$$\frac{\partial\zeta}{\partial R_j}=\frac{2\alpha_j\beta(\beta R_j-S_{jl})}{\beta^2\sigma^2(R_j)+\sigma^2(S_{jl})} \quad 5\text{-}9$$

$$\frac{\partial\zeta}{\partial S_{jl}}=\frac{-2\alpha_j(\beta R_j-S_{jl})}{\beta^2\sigma^2(R_j)+\sigma^2(S_{jl})} \quad 5\text{-}10$$

By neglecting the VOV terms in equation 5-8 and substituting with equations 5-9 and 5-10 in to it equation 5-8 will be:

$$\sigma(\zeta)=\left[\sum_{j=1}^{J}\left(\frac{2\alpha_j\beta(\beta R_j-S_{jl})}{\beta^2\sigma^2(R_j)+\sigma^2(S_{jl})}\right)^2\sigma^2(R_j)+\sum_{j=1}^{J}\left(\frac{-2\alpha_j(\beta R_j-S_{jl})}{\beta^2\sigma^2(R_j)+\sigma^2(S_{jl})}\right)^2\sigma^2(S_j)\right]^{1/2}, \quad 5\text{-}11$$

which after simplifying becomes

$$\sigma(\zeta) = 2\left[\sum_{j=1}^{J} \frac{\left(\alpha_j\left(\beta R_j - S_{jl}\right)\right)^2}{\left(\beta^2\sigma^2\left(R_j\right) + \sigma^2\left(S_{jl}\right)\right)}\right]^{1/2}, \quad 5\text{-}12$$

Equation 5-5 gives the value of a FOM that might vary from zero up to 10^6 or greater. To make it easier to find a suitable cutoff value the equation is normalized as follow:

$$\zeta = \frac{\sum_{j=1}^{J} \alpha_j \frac{\left(\beta R_j - S_{jl}\right)^2}{\beta^2\sigma^2\left(R_j\right) + \sigma^2\left(S_{jl}\right)}}{\sum_{j=1}^{J} \alpha_j \frac{\left(S_{jl}\right)^2}{\sigma^2\left(S_{jl}\right)}}, \quad 5\text{-}13$$

where the $\left[\sum_{j=1}^{J} \alpha_j \frac{\left(S_{jl}\right)^2}{\sigma^2\left(S_{jl}\right)}\right]$ term is the FOM value when the target gives zero response.

The standard deviation of the normalized FOM is given by:

$$\sigma(\zeta) = \frac{2\left[\sum_{j=1}^{J} \frac{\left(\alpha_j\left(R_j - S_{jl}\right)\right)^2}{\left(\sigma^2\left(R_j\right) + \sigma^2\left(S_{jl}\right)\right)}\right]^{1/2}}{\sum_{j=1}^{J} {\alpha^2}_j \frac{{S_{jl}}^2}{\sigma^2\left(S_{jl}\right)}}. \quad 5\text{-}14$$

The normalized FOM and its standard deviation are used to define another term which is called the filter function, $f_{\pm}(\lambda)$.

$$f_{\pm}(\lambda) = \zeta \pm \lambda\sigma(\zeta), \quad 5\text{-}15$$

where λ is a constant chosen according to the level of accuracy desired.

If $f_- > f_0$, where f_0 is a selected cut-off value, the target will be considered to be inert and will be labeled as a negative. If the sample is actually inert, this is identified as a true negative (TN). On the other hand, if $f_+ < f_0$ the target will be considered to be an explosive which will be labeled a positive. If the sample is actually explosive, this is labeled as a true positive (TP). The f_0 is a cut-off value chosen by the user to adjust for sensitivity and specificity. The sensitivity and specificity can be defined as follows:

$$Sensitivity = \frac{Number\ of\ true\ positives}{Number\ of\ true\ positives + number\ of\ false\ negatives}, \quad 5\text{-}16$$

$$Specificity = \frac{Number\ of\ true\ negatives}{Number\ of\ true\ negatives + number\ of\ false\ positives}, \quad 5\text{-}17$$

From the last two equations one can conclude that 100% sensitivity means there are no false negatives while 100% specificity means that there are no false positive. The ideal case is to have 100% for both sensitivity and specificity, which is rarely possible in real life. A high sensitivity is preferable over high specificity because missing one of the explosives through an investigating process might lead to significant negative consequences. On the other hand identifying an inert as an explosive will waste more time but still not be dangerous. Having high levels of both sensitivity and specificity is the ideal goal.

Chapter 6- Experimental Work for Explosive Detection

6.1 Equipment

All experiments were conducted at the Kansas State University Dense Plasma Focus (KSU-DPF) Laboratory, 142 Ward Hall, Mechanical and Nuclear Engineering Department. The system is described in the sub-sections that follow.

6.1.1 *X-ray Source*

The KSU-DPF was used as a hard X-ray pulsed source. The device was operated for all experiments with a cylindrical flat end copper anode, which was 10 cm long. The anode is surrounded by a squirrel cage, of 5.5 cm diameter, consisting of 6 brass rods as a cathode. Each rod has 12 cm length and 0.8 cm diameter. The anode and cathode are electrically insulated by a hollow Pyrex glass tube 6.8 cm long and 0.16 cm thickness. More details about the device construction were shown in Chapter 3- The filling gas for this experimental work was neon. The gas pressure was kept constant at 1 mbar. The capacitor was charged with a constant charging voltage of 17 kV. Characteristics of the X-ray pulses radiated from the device under the previous conditions were discussed in detail in Chapter 4-

6.1.2 *Shielding*

Lead bricks were used as shielding around the source except two square collimation windows, each 5×5 cm. The overall shield thickness was 5.08 cm. Further lead shielding was added around the detectors, except the front end, with overall thickness of 5 cm. Because X-ray emission from the DPF device is isotropic, the main purpose of this shielding is to direct photons to the target only. Therefore, very few photons will scatter from the walls or other equipment in the laboratory and be reflected back the detector.

6.1.3 *Target*

Three targets were used in the experiments:

- Experiment I: Five-gallon barrels, of 1 mm thick steel, were filled with different samples. Nine samples were used: Three explosive surrogates including 35% nitrogen fertilizer, denoted as FertC, 28% nitrogen fertilizer, denoted as FertD and 50/50 mixture of both fertilizers, denoted

as FertMix. The other used samples were inert materials, sand, water, chalk, rubber mulch, polyethylene and aluminum.

- Experiment II: One-gallon painting cans, 0.2 mm thickness steel. Twelve cans were used. Ammonium nitrate was used as an explosive surrogate in addition to the three types of fertilizers identified above. Graphite and sugar were added to the inert samples used in experiment I.
- Experiment III: Quart painting cans, 0.2 mm thickness steel. Same samples used in experiment II except graphite.

In all experiments, responses for the FertMix sample were chosen to be the template. As a result the main goal here was looking for nitrogen rich samples like the FertMix. All cans were placed 40 cm away from the source (the device anode).

6.1.4 *Detection instruments*

Two types of photon detectors were used to detect X-ray signals including:

- A Canberra, 3 × 3 in, sodium-iodide-thallium-activated scintillation detector, NaI(Tl), model 3M3/3-X.

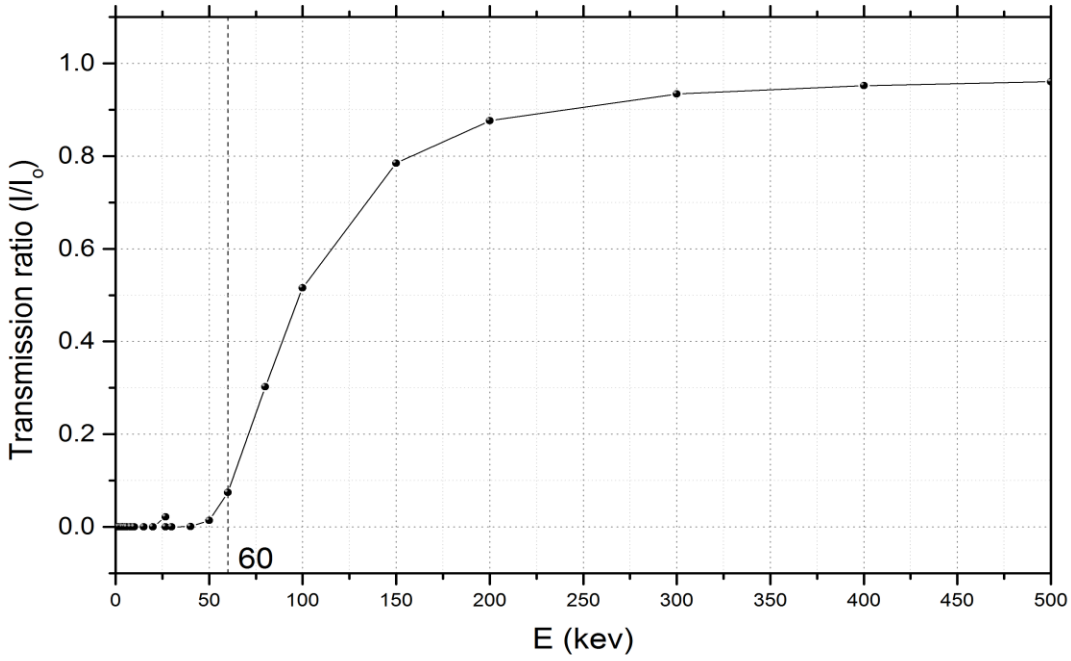

Figure 6-1. Transmission ratio for 0.5 Cd filter placed in front of D2.

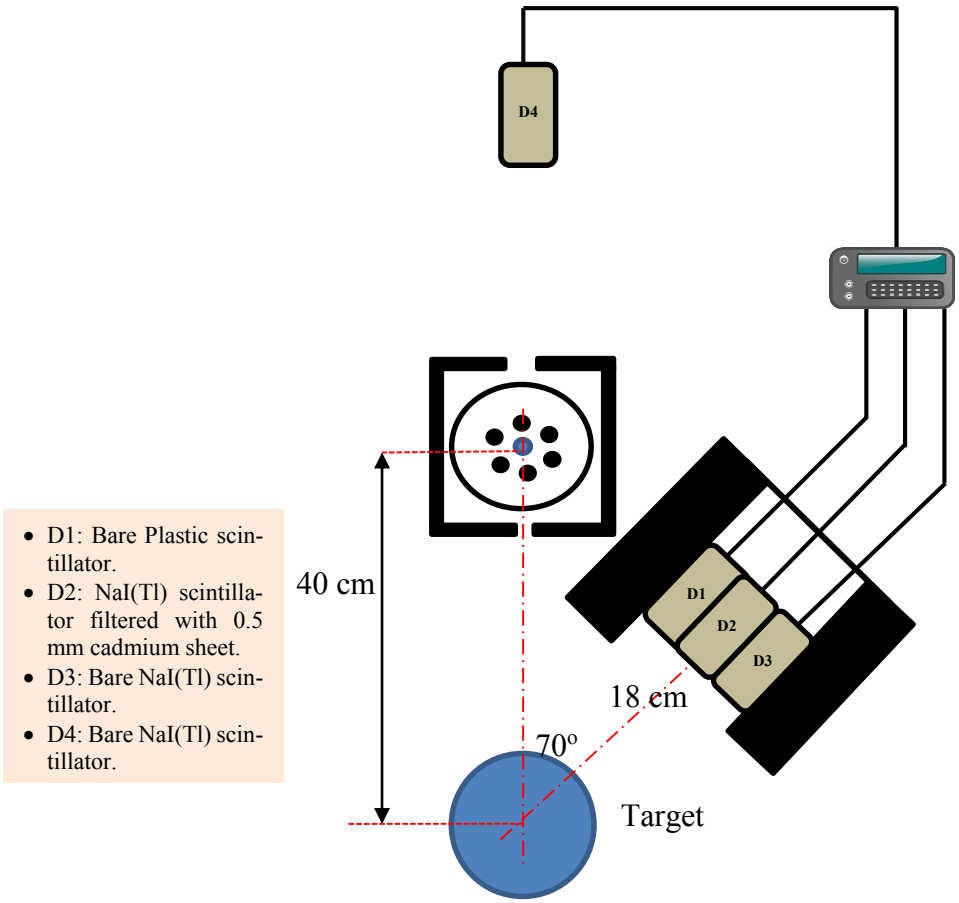

Figure 6-2 Schematic diagram of the experiment.

- BC-418 plastic scintillator, 2 × 1 in, coupled with a Hamamatsu PMT, model H7195.

More details about the two types of detectors were explained in Chapter 3- All detectors are connected to Tektronix 7000 series DPO oscilloscopes through a set of tri-axial cables to reduce the noise and signal interference.

Four specific detectors were used as follow:

- D1: Bare Plastic scintillator.
- D2: NaI(Tl) scintillator filtered with 0.5 mm cadmium sheet.
- D3: Bare NaI(Tl) scintillator.
- D4: Bare NaI(Tl) scintillator.

Detectors D1 and D3 were set to pick up the scattered X-rays of all energies. On the other hand D2 will pick up only the high energy X-ray photons, more than 60 keV, as indicated in Figure 6-1,

which shows the transmission ratio for a 0.5 mm cadmium filter. D1, D2 and D3 are called signature detectors. They were 18 cm away from the target at an angle of 70^o to pick up the scattered X-ray signals. Due to shot-to-shot variability of the dense plasma focus devices, a forth detector (D4) was used for normalization purposes. Detector D4, 100 cm away from the device, was allowed to looking directly at the source. A schematic diagram for the experiment configurations and a picture for the set up are shown in Figure 6-2 and Figure 6-3, respectively.

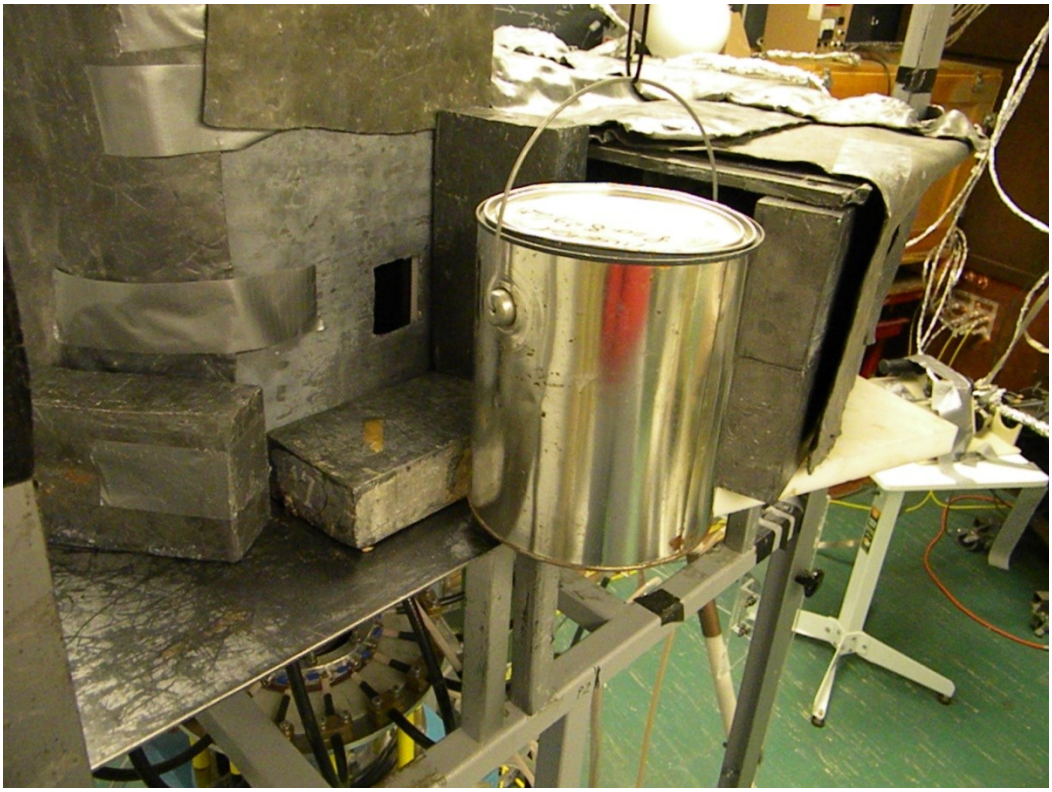

Figure 6-3. A picture for the 1 gallon detection experiment.

6.2 Nomenclatures

Here, we limit our consideration to materials that are like nitrogen-rich explosives, although the methodology applies to other threat materials. The following nomenclature will be used:

- A target is the container with its contents.
- A sample is the contents of a target.
- A sample is explosive if it is like a nitrogen-rich chemical explosive.
- A sample is inert if it is not explosive.

- A sample is suspect if it not clearly explosive or inert.
- True positive (TP): When an explosive is correctly identified as explosive.
- True negative (TN): When an inert is correctly identified as inert.
- False positive (FP): When an inert is identified as explosive.
- False negative (FN): When an explosive is identified as inert.

6.3 Experimental procedures

All experiments were performed with the configuration shown in Figure 6-2. Neon gas was used as a working gas. Neon pressure was kept constant at all experimental work at 1 mbar and the capacitor charging voltage at 17 kV as well. Targets were placed 40 cm away from the source in front of the 5×5 cm window to collimate the emitted X rays to the target only. Background measurements (measurement with no target present) were taken with the detectors placed at different angles to the beam. After many trials it was found that the least background was measured at an angle of 70^{o}. At this angle the reflected X-ray signals from walls and other devices in the room are minimal. After each shot the detector response, D1, D2 or D3, was normalized by the D4 detector. Ten shots were taken for each sample and gas used to be purged after that to reduce the effect of contaminations due to anode material sputtering. The average of the normalized ten shots represents the signature of each sample. Therefore, the response vector for each sample will have three signatures; one from each detector (D1, D2 and D3). All signals are registered by the two Tektronix oscilloscopes. A Rogowski coil and high voltage probe were used to measure pinch current and voltage signals, respectively. Using this type of advanced oscilloscope permits signal processing, such as integrating or differentiating the registered signals.

Chapter 7- Experimental Results

7.1 Introduction

As discussed in the previous chapter, ten shots were taken for each target to calculate the sample signature. Signals from a Rogowski coil and the voltage probe were registered by an oscilloscope to monitor the device operation. Figure 7-1 shows typical current and voltage signals for the pinch at a neon pressure of 1 mbar and charging voltage 17 kV. The figure shows that the current and the voltage signals reach a peak of more than 150 kA and 90 kV, respectively, at the pinch time. Each current dip is coincident with a voltage spike. More than one current dip appeared in more than 95% of the shots, which is the characteristic of high inductance dense plasma focus devices, known as T2 type [144].

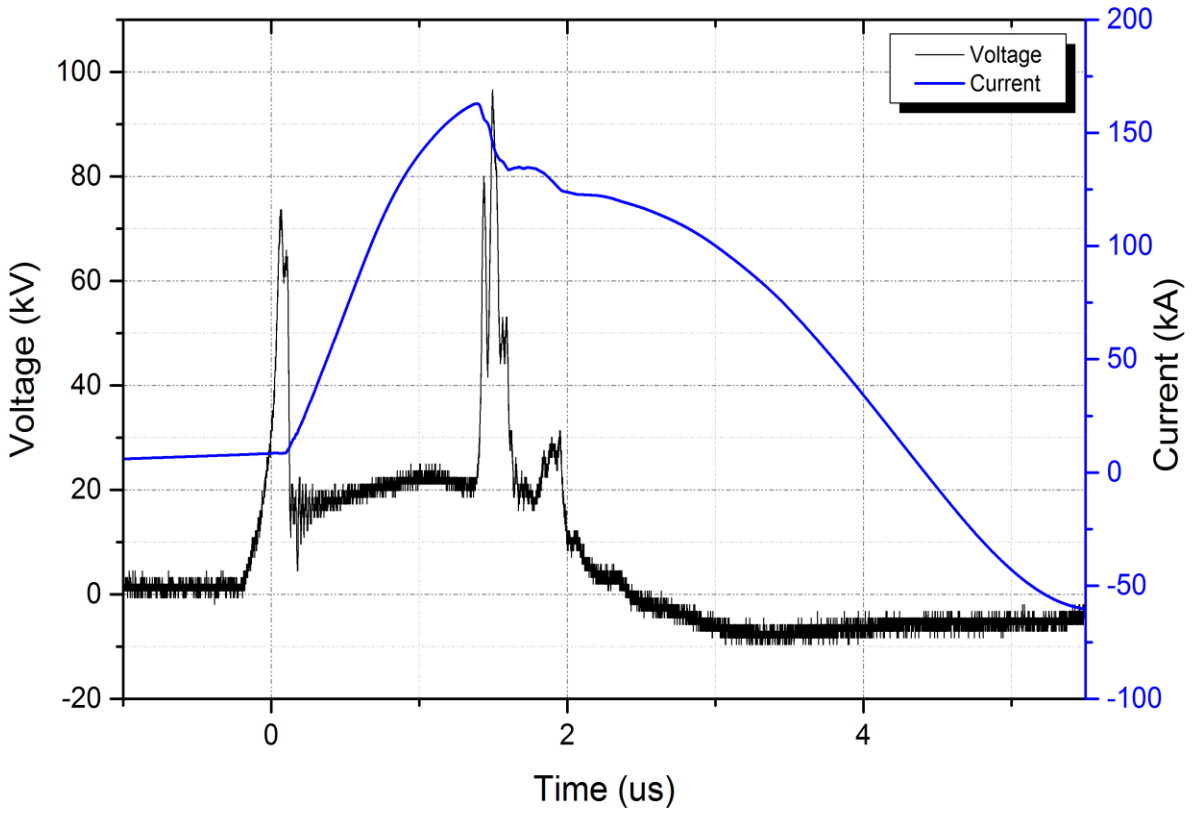

Figure 7-1. Typical signals for pinch current and voltage.

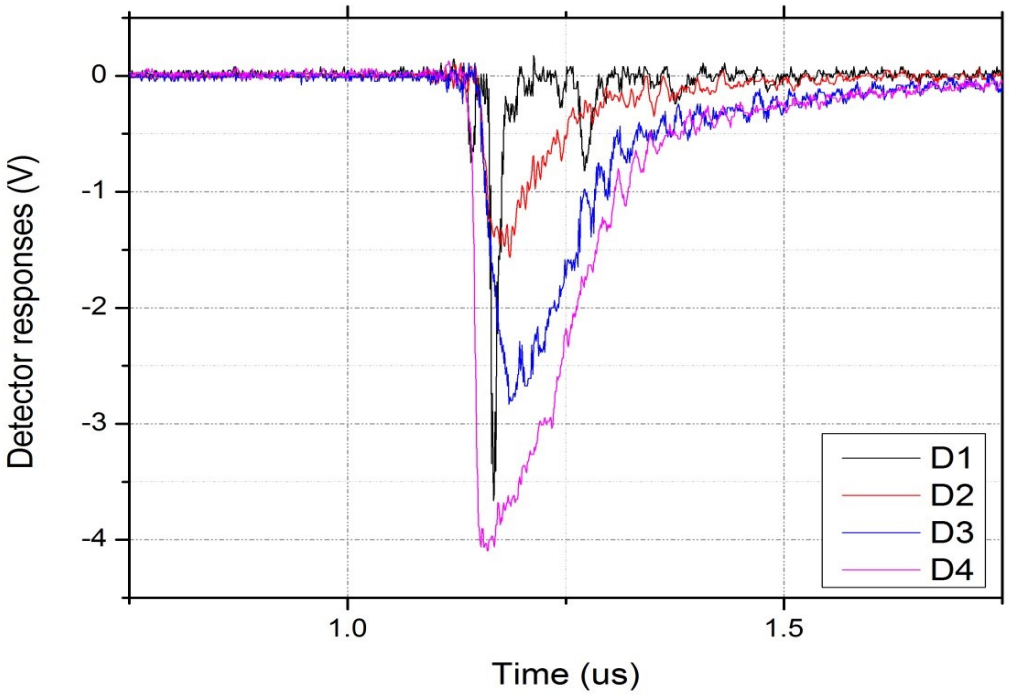

Figure 7-2. X-ray signals for signature and direct detectors.

Figure 7-2 shows typical signals for the X-ray detectors as registered by the oscilliscope for a quart size aluminum sample. The black, red and blue represenst the responses of signature detectors. Signature detectors, D1, D2 and D3, were placed at 70^{o} from the the source-target line. They were directed to the target to detect the scattered X rays as explained in Chapter 6- The pink signal represents the direct detector which was looking dirctly at the source for normalizing purpose.

7.2 Calculating R_j and S_j vectors

Response vector, R_j, for each material is composed of 3 componenets, R_1, R_2 and R_3. Each component is related to one of the signature detectors D1, D2 and D3, respectivly. For each shot, the integration of the signature detector curve, as shown in Figure 7-2, was normalized to that of the direct detector, D4, curve. An average of 10 shots was taken for each sample to calculate its detectors' responses, R_1, R_2 and R_3. Therefore, the response is a ratio of the scattered X-ray from the target to the direct X-ray signal from the device averaged over 10 shots.

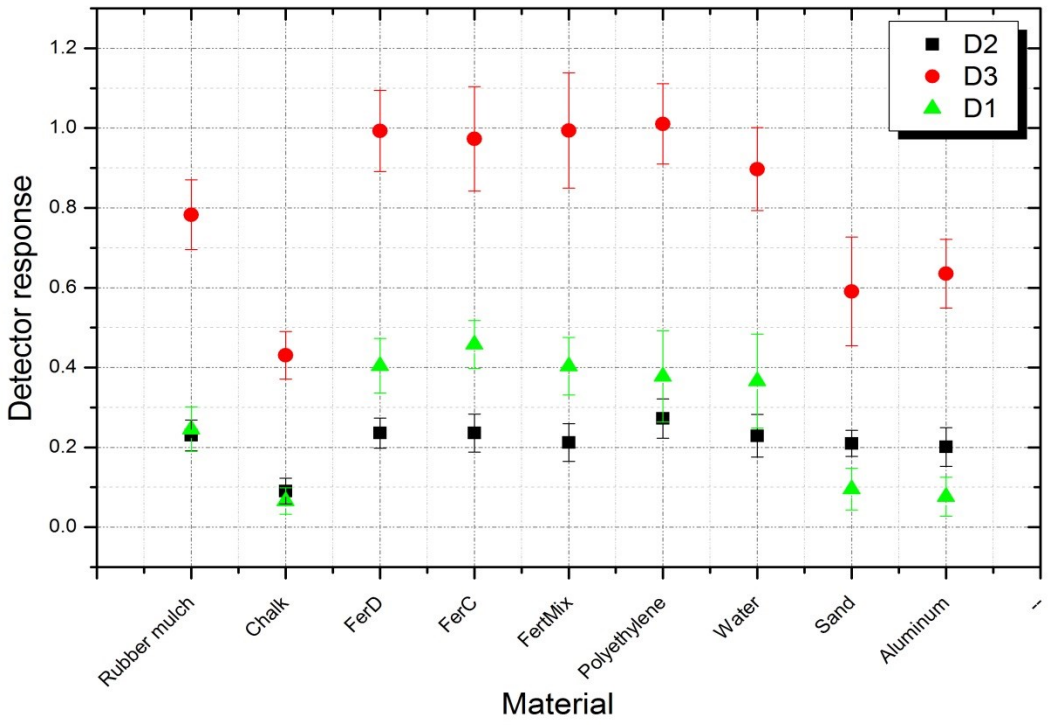

Figure 7-3. Detectors' response for 5-gallon cans.

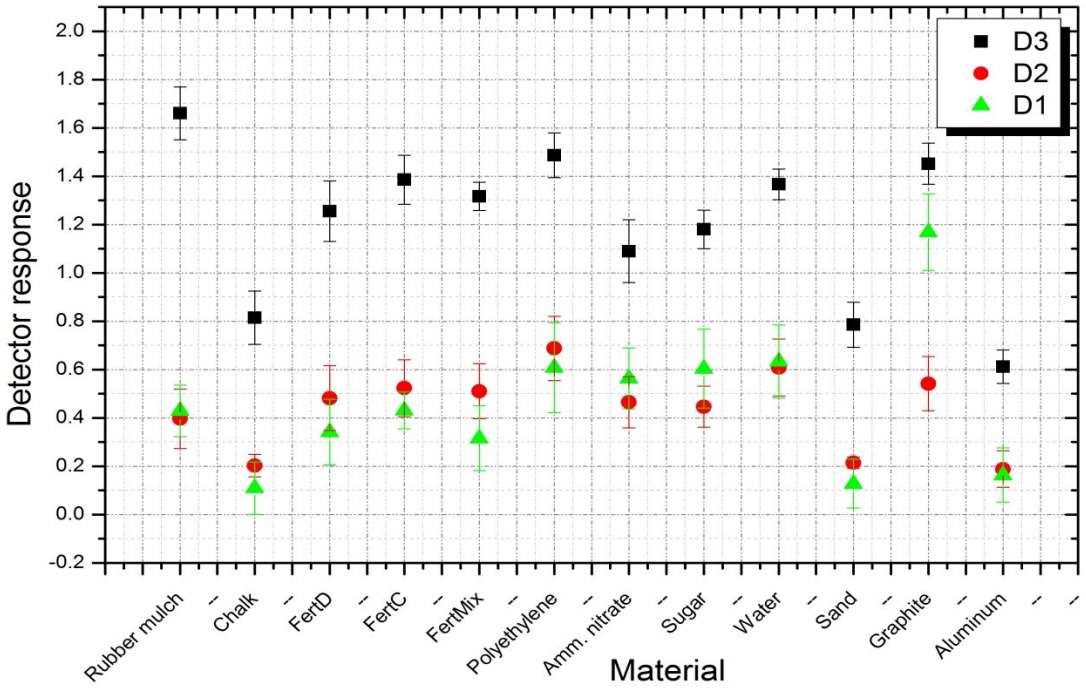

Figure 7-4. Detectors' response for 1-gallon cans.

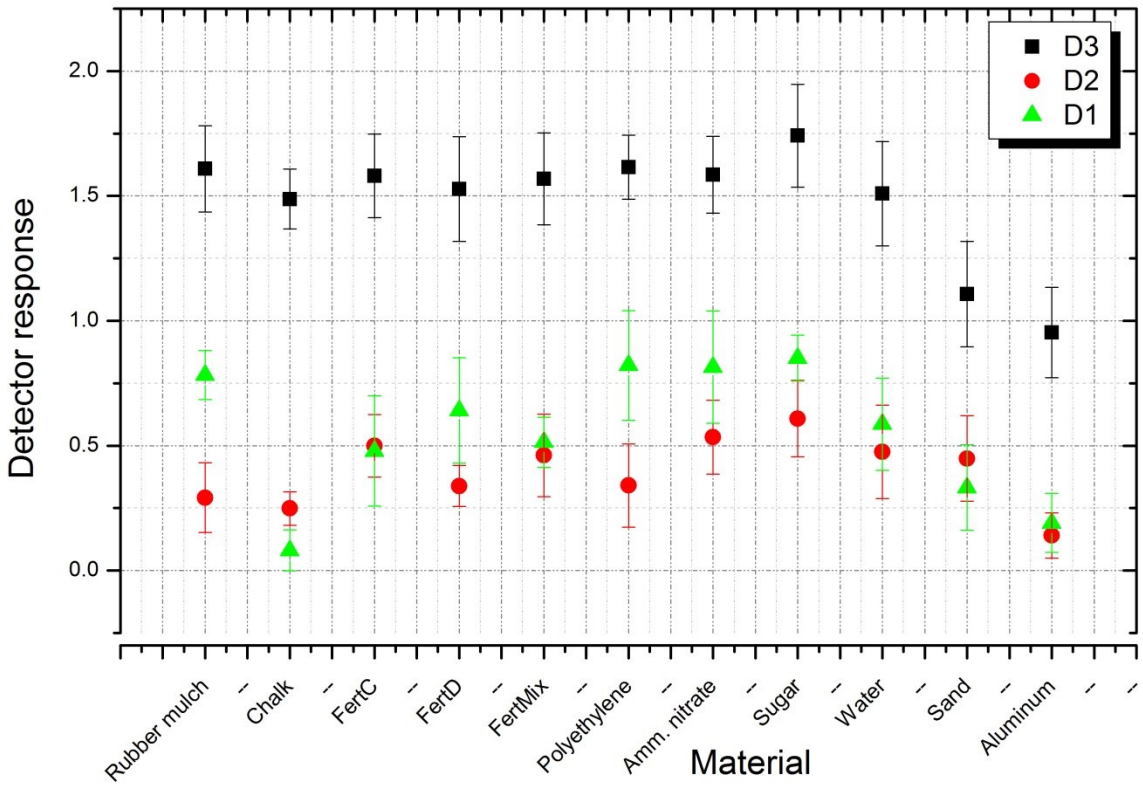

Figure 7-5. Detectors' response for quart cans.

Normalizaiton is improtant to avoid shot-to-shot variablity for dense plasma focus devices. In the same way the tempelate vector, S_j, was calculated by using the FertMix sample as a target and following same procedures as before. Detector responses for all samples in the three experiments are shown in Figure 7-3, Figure 7-4 and Figure 7-5.

By using template response, S_j, and target response, R_j, vectors and their standard deviations the figure-of-merit, FOM, for each sample and its standard deviation can be calculated using equations 5-13 and 5-14 . By choosing a suitable cut-off valuef_0, the user can decide if the sample is explosive, inert or suspect based on the following rule:

For $(f-\sigma) > f_0$, the sample will be identified as inert (true negative) while for $(f+\sigma) < f_0$, the sample will be identified as explosive (true positive). If both conditions don't

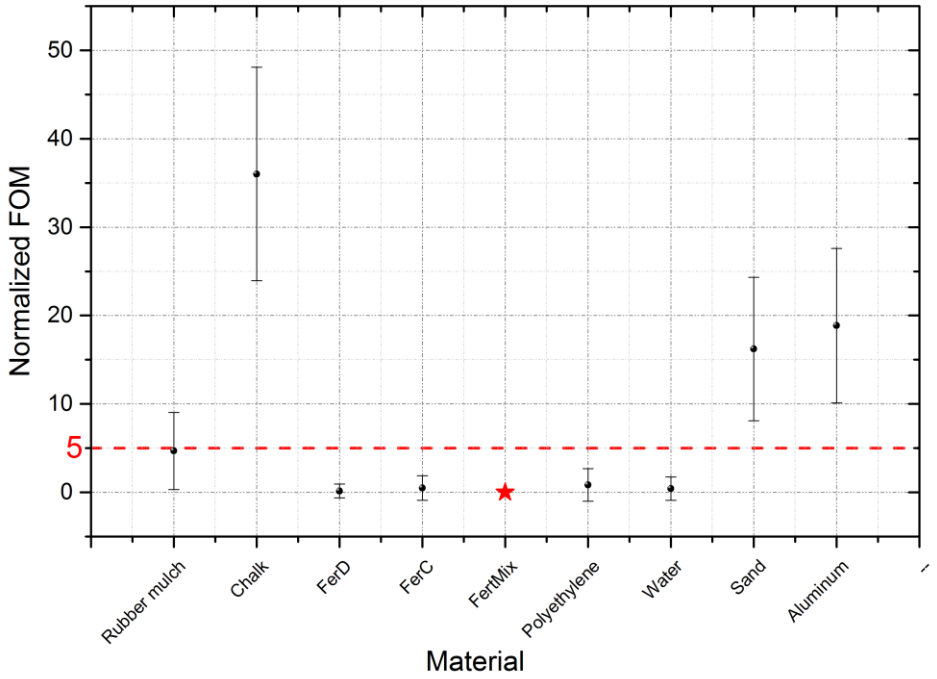

Figure 7-6. Normalized figure of merit (FOM) for the 5-gallon samples.

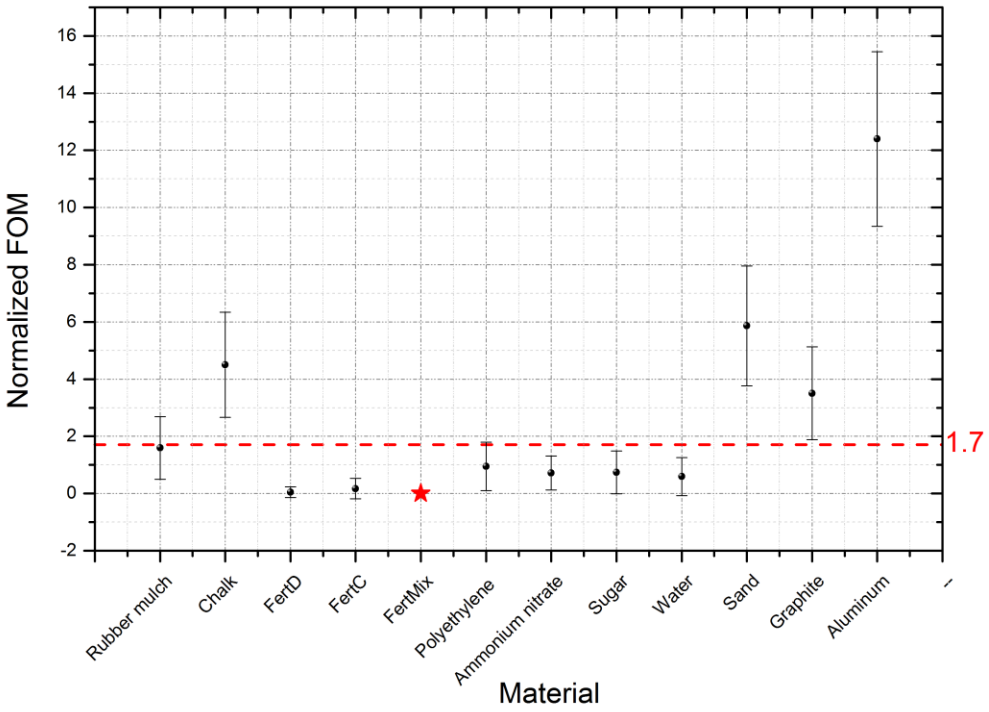

Figure 7-7. Normalized figure of merit (FOM) for the 1-gallon samples.

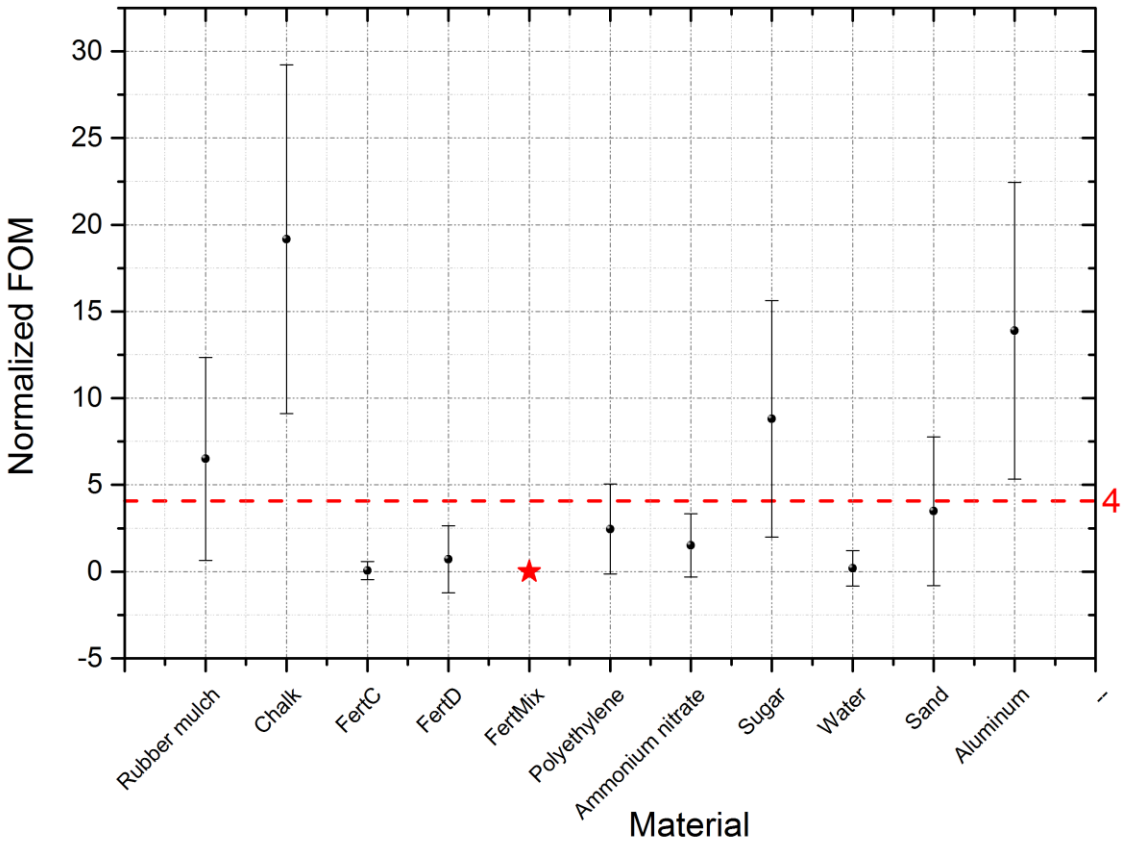

Figure 7-8. Normalized figure of merit (FOM) for the quart samples.

Apply, the sample will be identified as suspect. The suspect sample needs more investigation with another method. For the three experiments conducted, the following results were obtained:

Five- gallon samples: The normalized FOMs for the 5-gallon samples are shown in Figure 7-6. By choosing a cut-off value (f_0) equal to 5, all explosive-like samples, FertC, FertD, were successfully identified as true positives, producing 100% sensitivity. Three inert samples, Chalk, sand and aluminum, were successfully identified as true negatives, producing 50% specificity. Two false positives were obtained, for polyethylene and water, because they were identified as explosives. Finally, because the rule mentioned before didn't apply for the rubber mulch sample, it was considered as subsect.

One-gallon samples: As shown in Figure 7-7, by choosing a cut-off value (f_0) equal to 1.7, the explosive-like samples, FertC, FertD and ammonium nitrate, were successfully identified

as true positives, producing 100% sensitivity. Four inert samples, chalk, sand, graphite and aluminum, were successfully identified as true negatives, producing 50 % specificity. Two false positives were obtained for water and sugar (not used in the 5-gallons). Finally, both rubber mulch, as in the 5-gallon sample experiment, and polyethylene were identified as suspect samples.

Quart samples: By choosing a cut-off value (f_0) to be 4.0, all explosive-like samples, FertC, FertD and ammonium nitrate, were successfully identified, producing 100% sensitivity, as in the first two experiments. Two inert samples, aluminum and chalk, were successfully identified producing 28.6 % specificity. Only one false positive was obtained here for the water sample. Rubber mulch is still classified as a suspect sample in addition to polyethylene, sugar and sand. A summary for all tested samples is shown in Table 7-1.

Since it was hard to do the experiment on real explosives, it was decided to simulate the problem using MCNP-5. Initial results, shown in Figure 7-9, for detector responses for 1-gallon have good agreement with the experiments which encouraged making more simulations using real explosives and more samples. In the next chapter the MCNP-5 simulation will be discussed in detail.

Table 7-1. Summary of all tested materials.

	5-gallons	1-gallon	Quart
Total # samples	8	11	10
Inert	6	8	7
Explosive-like	2	3	3
True (+ve)	2	3	3
True (-ve)	3	4	2
False (+ve)	2	2	1
False (-ve)	0	0	0
Suspect	1	2	4
Sensitivity%	100	100	100
Specificity%	50	50	28.6

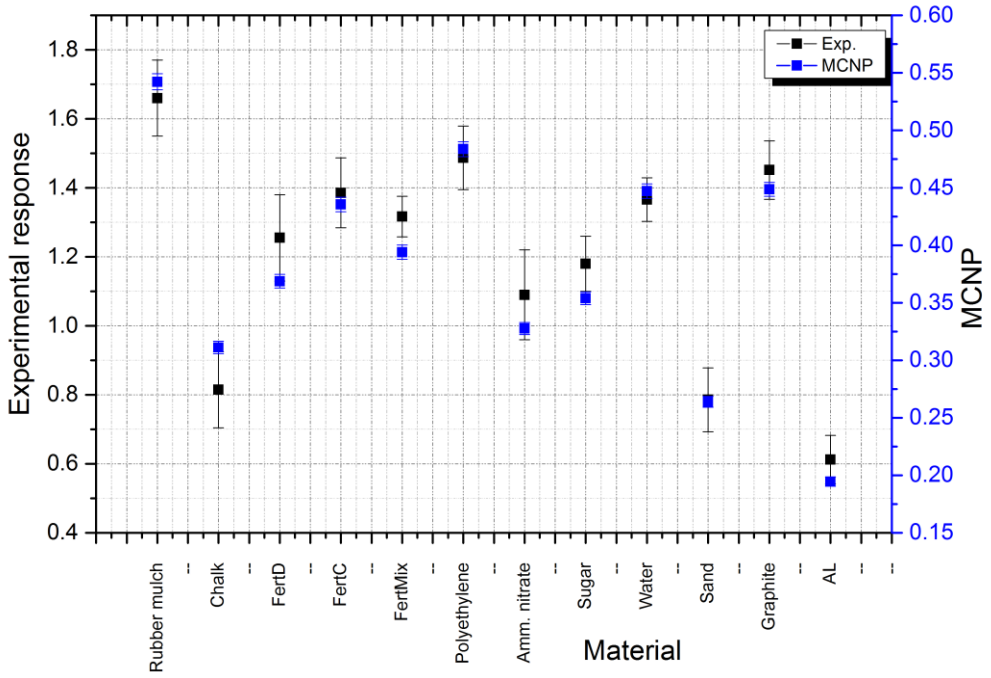

Figure 7-9. Comparison between experimental and simulation response for 1-gallon samples.

Chapter 8- Simulation

8.1 Introduction

Computer simulation has the advantage that cases that are difficult or expensive to consider experimentally can be studied. For instance, responses from real explosives can be estimated. However, such simulation results should be benchmarked or verified in some way so that confidence can be placed in them. In this chapter the simulation computer code will be discussed along with the procedures used and the results obtained.

8.2 MCNP simulation code

The simulation computer code used in this study was Monte Carlo Neutral Particle (MCNP-5) [195]. MCNP is a general purpose code used for neutrons, photons, and electrons individually or in combination. It was developed by Los Alamos National Laboratory. MCNP can be used in many areas such as radiation protection and dosimetry, radiation shielding, radiography, medical physics, nuclear criticality safety and detector design and analysis [196]. It works on a neutron energy range from 10^{-11} to 20 MeV for all isotopes and up to 150 MeV from some of them. The photon range from 1 keV to 100 GeV and the electron energy range from 1 keV to 1 GeV [197] can be simulated.

MCNP uses the Monte Carlo methodology for particle simulation by using sample means to estimate population means. Monte Carlo is a form of quadrature, or numerical integration, which is characterized by high flexibility and which works for a wide range of direct or inverse problems. The Monte Carlo method differs from deterministic transport methods. Deterministic transport methods solve the transport equation, or the diffusion equation, for the expected particle behavior using analytic or numeric methods that are not probabilistic. Monte Carlo, on the other hand, simulates individual particle behavior using probabilistic models to estimate tallies of the average behavior of an ensemble of particles. Then the average behavior of particles in the physical system is inferred from the average behavior of simulated particles [197].

To simulate a problem using MCNP an input file should be prepared which includes all information needed to run the experiment. The input file consists of three main parts including cell cards (Block 1), surface cards (Block 2) and data specification cards (Block 3). More details about each part will be discussed in the following sections.

8.2.1 *Cell cards (Block 1)*

Cell cards, or block1, are used to provide information about all cells used in the experiment geometry. Each cell is identified by intersections, unions and complements of different surfaces which are defined in block 2. Each cell is characterized by a number (which identifies the cell), a material number (which later identifies the material composition), and a material density. Material number and density are replaced by a single zero in the case of a void cell. Each material number refers to a specific material, which is described in the data specification card (block3). Moreover, the importance of both neutrons (n) and photons (p) is specified in the cell card. An example of cell card or record is the following:

3 1 -7.86 17 -16 IMP: P, N=1 $ Cask iron shell,

This record identifies the cell as number 3, describes the cell as filled with material number 1 (defined later in Block 3), which has a density 7.86 g cm^{-3}. This cell is the space inside surface number 16 and outside surface number 17. The IMP: P, N=1 part means both neutrons and photons will be transported in this cell.

8.2.2 *Surface cards (Block 2)*

Surface cards (Block 2) describe all surfaces used to build the geometry of the experiment. MCNP has first and second-degree surfaces in addition to forth degree elliptical tori of analytical geometry. The surfaces are defined by mnemonics such as C/Z for a cylinder parallel to the z-axis. A cylinder at an arbitrary orientation is defined by the general quadratic (GQ) mnemonic. In MCNP there are two ways to specify any surface parameters including using appropriate coefficients for the surface equation and using known geometrical points on a symmetric surface about a coordinate axis. An alternative way to describe surfaces is by using of macrobodies which can be mixed with the standard cells and surfaces. For example the command:

10 RCC 0 0 0 0 0 30 10 $ Right circular cylinder,

describes a right cylinder with a base center at the origin, its height is 30 cm, its radius is 10 cm and its axis is parallel to the z-axis. The number 10 at the beginning is the card number.

8.2.3 *Data specification cards (Block 3)*

Data specification cards (Block 3) contain all problem specifications other than geometry such as material specification, source type and description, output type (tallies) and any variance

reduction techniques to be used. In addition, the cross section library to be used, how many histories will be used, and the physics models involved in the experiment are identified. Material description in this card includes a unique number for each material, the elemental, or isotopic, composition and the cross section compilation that will be used. Source and type of radiation particles are specified by the SDEF command which has many variables to describe a variety of sources. Only one SDEF card is used to describe all sources. Different types of tallies can be used in MCNP according to the desired output. The most frequently used tallies are: F1 for surface current, F2 for average flux at a surface, F5 for the flux at a point or ring, F4 flux averaged over a cell, in addition to energy deposition tallies such as F6 and F7. Some optional commands can be used with the tally like tally energy card which arrange the tally result in energy groups or the dose energy and function cards which are used to calculate the dose. Each input file should have a mode card which determines the type of source particles to be tracked in addition to a time or a history card to determine how long or how many histories MCNP should simulate. Moreover, PHYS command is used to specify energy cutoffs and other physics treatments for different radiation particles.

8.3 MCNP Simulation for our problem

As an example, consider an MCNP-5 input file that was designed to simulate the 1-gallon experiment. The geometrical configuration of the simulation is shown in Figure 8-1. The dense plasma focus device was simulated as an X-ray isotropic point source at the origin (A). The energy of the source has the same X-ray spectrum estimated experimentally by the step filters method described in Chapter 4. Ten centimeters thick lead shielding (F) was used to prevent X-rays to reach detectors directly since the main purpose is to detect the scattered X-rays from the target. The target (B) was a 1-gallon steel can with 0.2 mm can thickness filled with the required sample and placed 40 cm away from the source.

Three detectors were simulated as follows:

i. Detector C: A bare sodium iodide (NaI) scintillator, 3×3 in.
ii. Detector D: A sodium iodide (NaI) with the same dimensions, 3×3 in, surrounded by 0.5 mm cadmium filter to measure relatively higher X-ray energies.
iii. Detector E: A bare plastic scintillator, $2x1$ in.

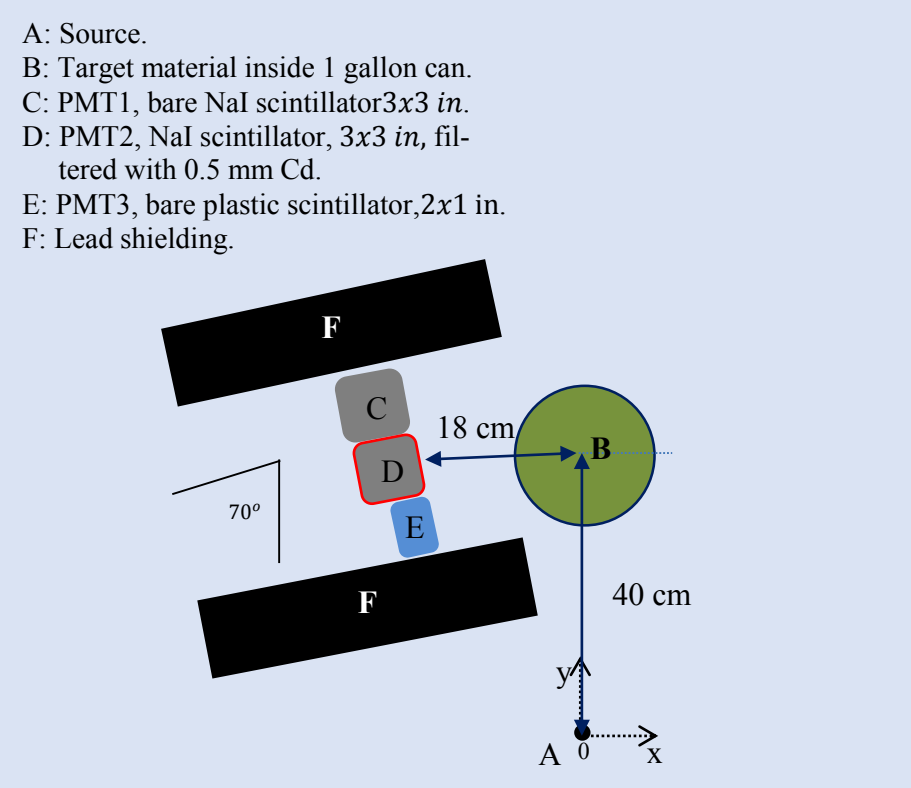

Figure 8-1. Schematic diagram of the MCNP simulated experiment.

Table 8-1. List of materials used in the simulation.

1	Rubber mulch	8	Chalk	15	Sand	22	Glass
2	Ash	9	Natural rubber	16	Soil	23	Ceramic
3	Gasoline	10	Wax	17	TNT	24	Aluminum
4	Ammonia	11	Polyethylene	18	Ammonium Nitrate	25	Granite
5	FertC	12	Water	19	RDX	26	Iron
6	FertD	13	Sugar	20	Graphite	27	copper
7	FertMix	14	Nitroglycerin	21	HMX		

The three detectors were placed at an angle of 70^o with the line connecting the source to the target center and 18 cm away from the center of the target. A schematic of the geometry is shown in Figure 8-1. The F6 tally was used because the main objective was to estimate the energy deposited in each detector cell. The tally reading is multiplied by the number of histories to have total deposited energy which will represent the signature for each detector. Each experiment was

conducted with 10^8 histories. Twenty seven different samples were used; five of them are the following real explosives:

i. Nitroglycerin (NG), C3H5N3O9
ii. trinitrotoluene (TNT), C7H5N3O6
iii. Royal Demolition Explosive (RDX), C3H6N6O6
iv. High Melting Explosive (HMX), C4H8N8O8
v. Ammonium nitrate, NH_4NO_3.

All used samples are shown in Table 8-1. Figure 8-2 shows the signatures of each detector calculated from the simulation for the 27 samples used. These signatures were used to form the response, R, and target, S, vectors in equations 5-13 and 5-14 to calculate the normalized figure of merit (ζ) and its standard deviation (σ). In the same manner as explained in ,one can decide if the sample is explosive, inert or suspect. To achieve the best results, four different samples were used as templates, separately including RDX, HMX, TNT and Nitroglycerin. Three signatures were used in FOM calculations in addition to other trials to use different combinations of two signatures to find the best results.

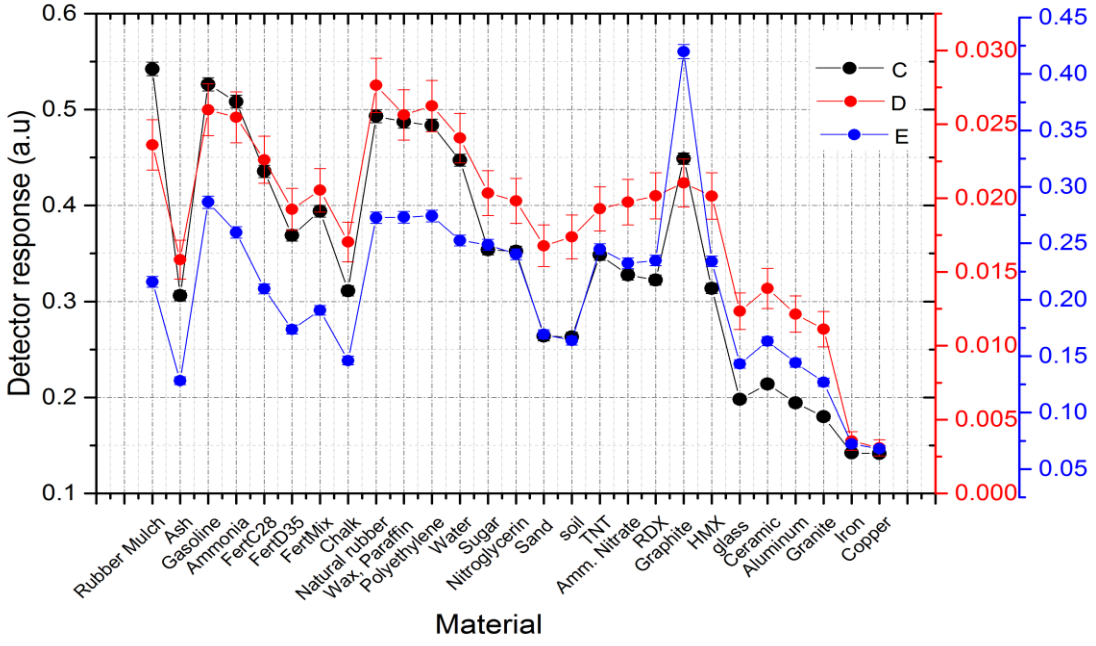

Figure 8-2. Simulated signatures for the three detectors.

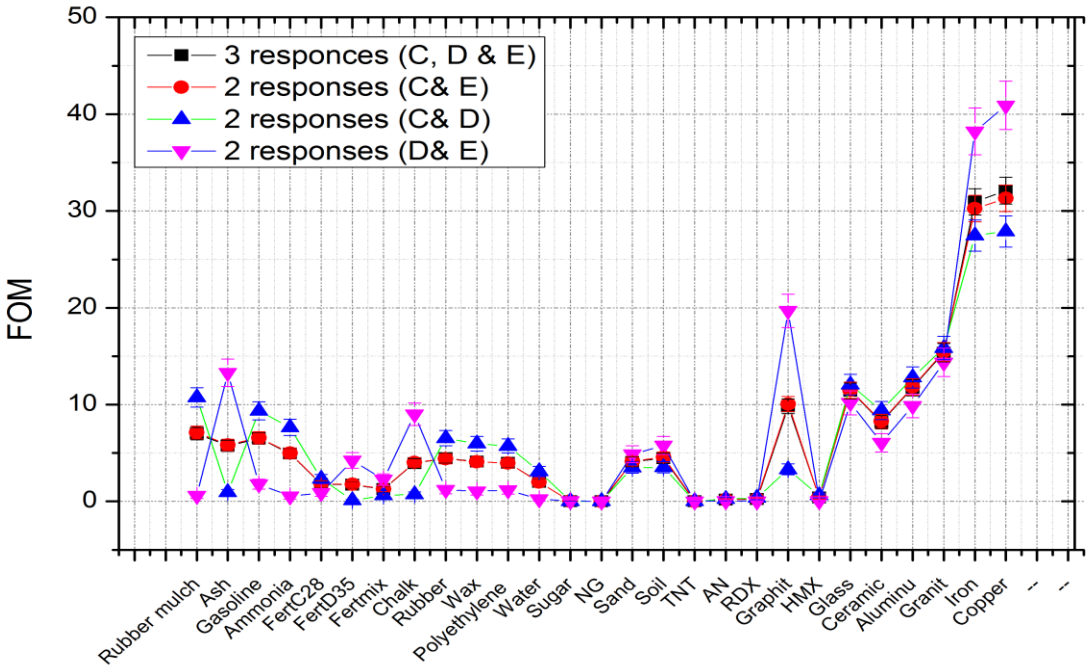

Figure 8-3. Figure of merit of 3 responses versus different combinations of 2 responses using NG template.

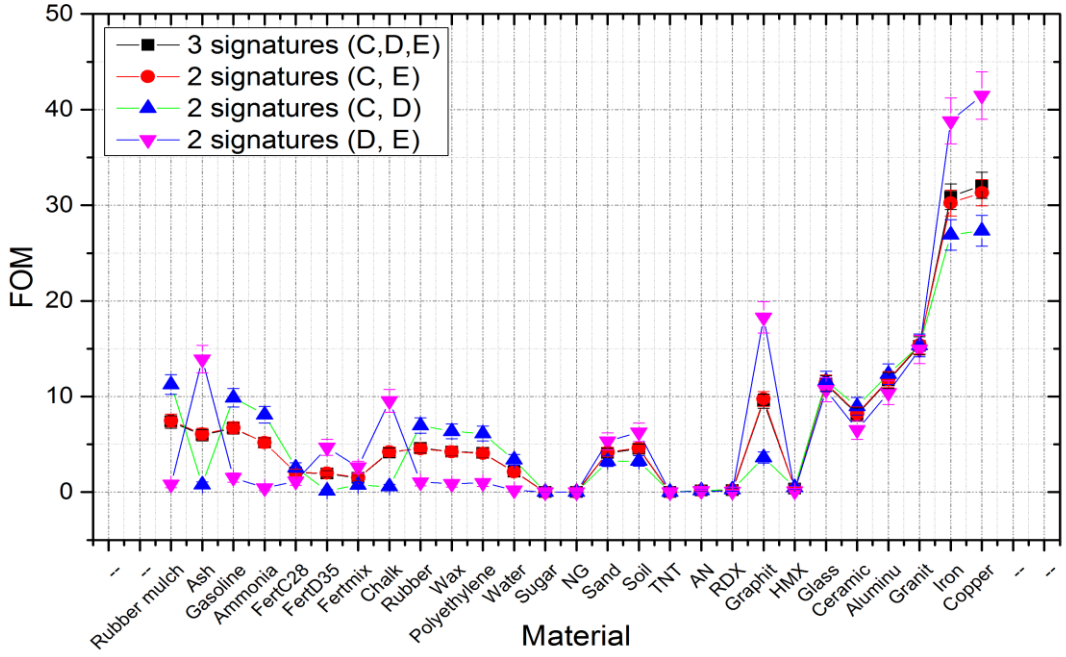

Figure 8-4. Figure of merit of 3 responses versus different combinations of 2 responses using TNT template.

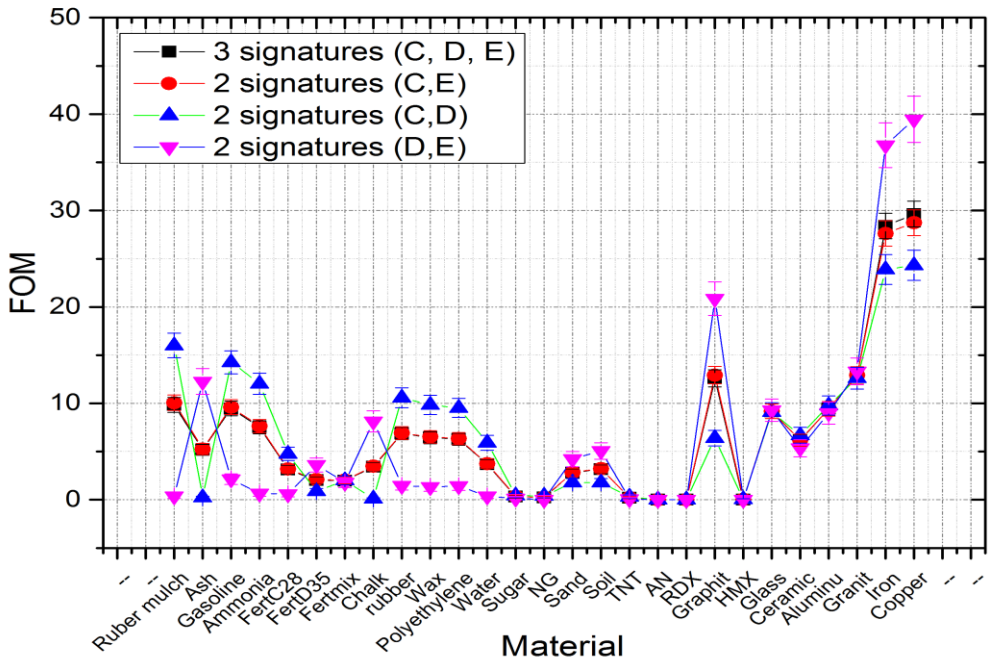

Figure 8-5. Figure of merit of 3 responses versus different combinations of 2 responses using RDX template.

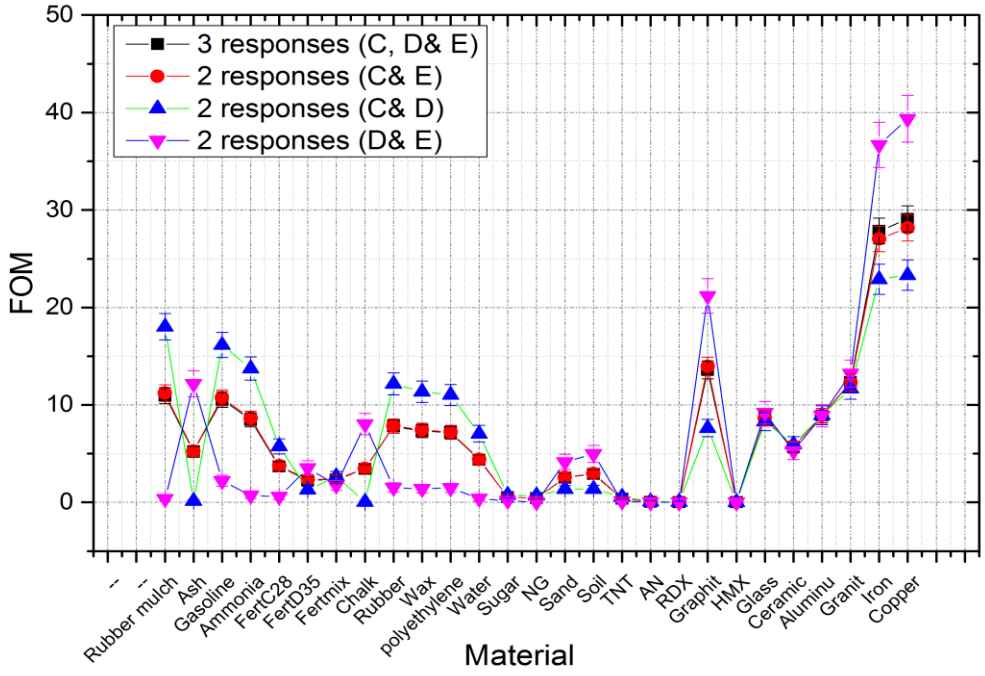

Figure 8-6. Figure of merit of 3 responses versus different combinations of 2 responses using HMX template.

Figure 8-3 to Figure 8-6 show a comparison of the FOM calculation using three responses versus using different combinations of only two responses for different templates. The maximum number of false positives was obtained by using the two responses from detector D, the filtered NaI, and detector E, the bare plastic scintillator. Using two responses from detectors C and D produces better results but still produces false positives for ash, chalk, FertD35 and sugar. Results of using the three responses are close to the results of using the two responses from detectors C and E.

From the previous results one can conclude that the contribution of detector D in the figure of merit calculations is less significant than the contributions from the other two detectors. However, in the remainder of this work the three responses will be used to calculate the figure of merit as it gives the best results to detect both explosive and inert samples.

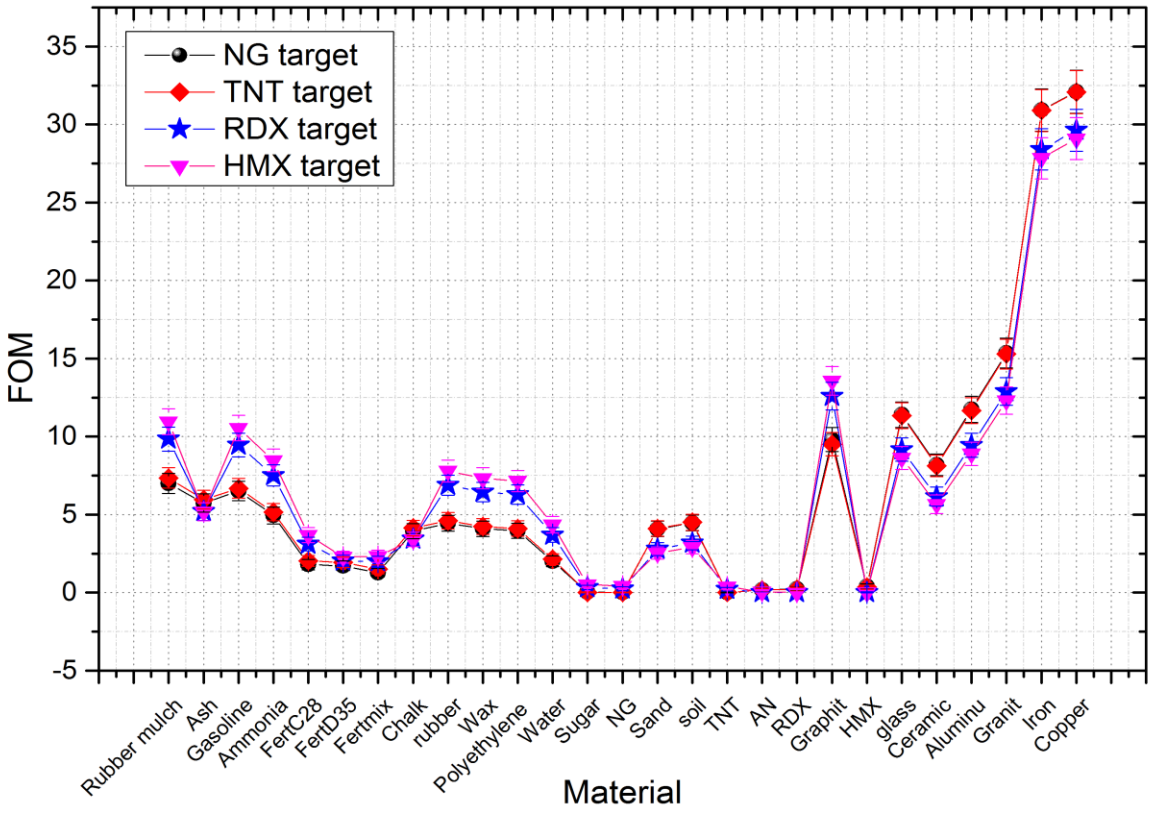

Figure 8-7. Comparison between the FOM for 3 responses using different templates.

Five real explosives were simulated in the experiment in addition to 22 inert materials. Four real explosive materials were used as templates including nitroglycerine, TNT, RDX and HMX. The FOM, for all samples, was calculated by using the signatures from one of the explosive samples as a template. A comparison among the FOMs calculated for the four different templates is shown in Figure 8-7. Quite similar results were obtained, with a slight superiority of using RDX and HMX in the low density samples and of using NG and TNT for the high density samples. Because the FOM values for high density samples are high enough for all templates to be distinguished, it was better to use either HMX or RDX template. Furthermore, better results were obtained for HMX than for RDX as template for low density samples. As a result HMX was chosen as the template because it produced better results for low density samples and its results for high density samples are still reasonable.

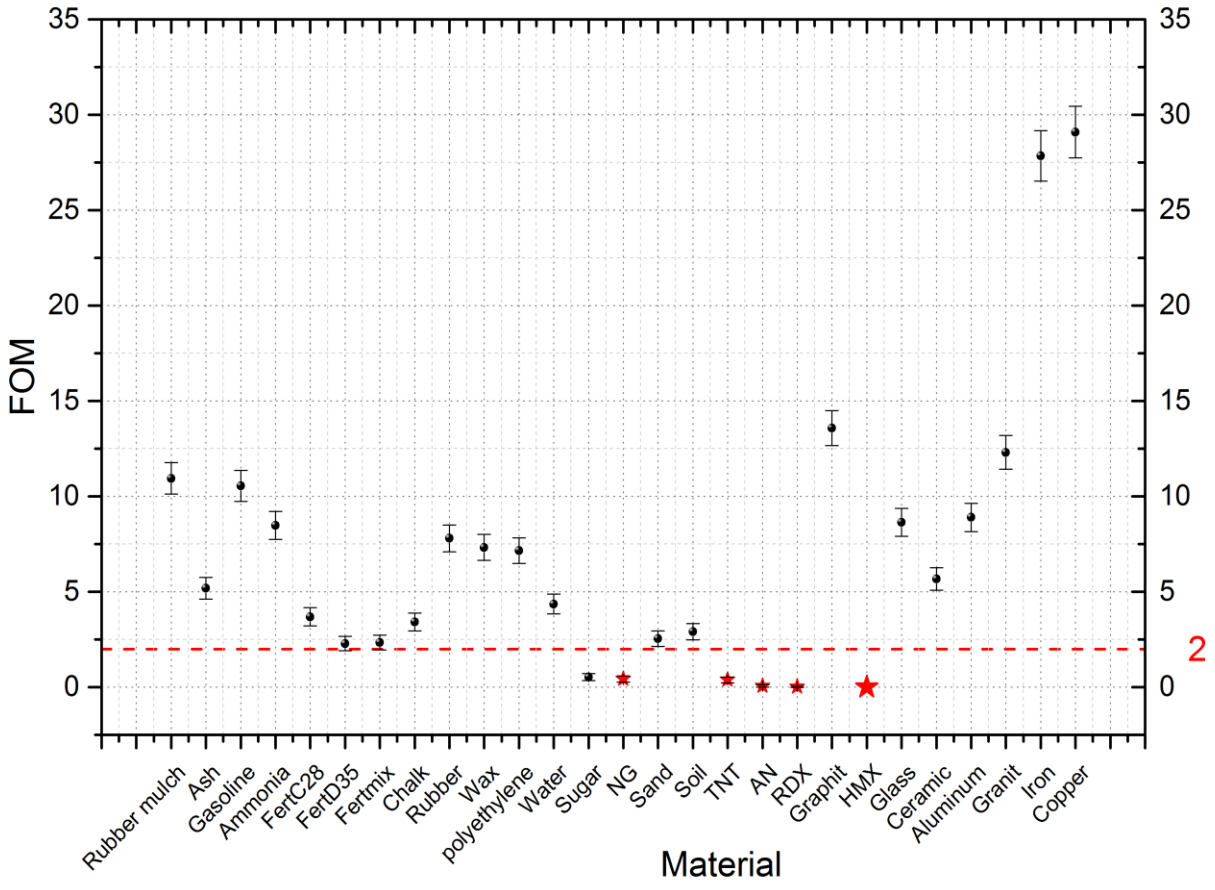

Figure 8-8. Figure of merit for HMX template using 1σ

Figure 8-8 shows the calculated figure of merit values (with standard deviations) from the simulated detector responses by using HMX as the template. To achieve good sensitivity, a cut off value (f_0) was chosen to be 2. As shown in the figure, all explosive samples, red stars, are correctly identified (true positives) because their figures of merit plus one standard deviation are all under the cut off line. Eighteen inert samples, out of 22, are correctly identified also (true negatives) because their figures of merit minus one standard deviation are located above the cut off line. The figure of merit for the sugar sample is located below the cut off line and thus sugar is the only false positive. The cut off line passes within one standard deviation of three inert samples (FertD35, FertMix and sand), so they will be considered as suspect. These results produce 100% sensitivity and 81.8 % specificity.

To increase the confidence level, the errors were extended to be ±2σwith the same cut off line. As shown in Figure 8-9, one more sample, soil, is counted as suspect which reduces the correctly identified inert samples to 17 producing a specificity of 77.3% (the sensitivity is still 100%).

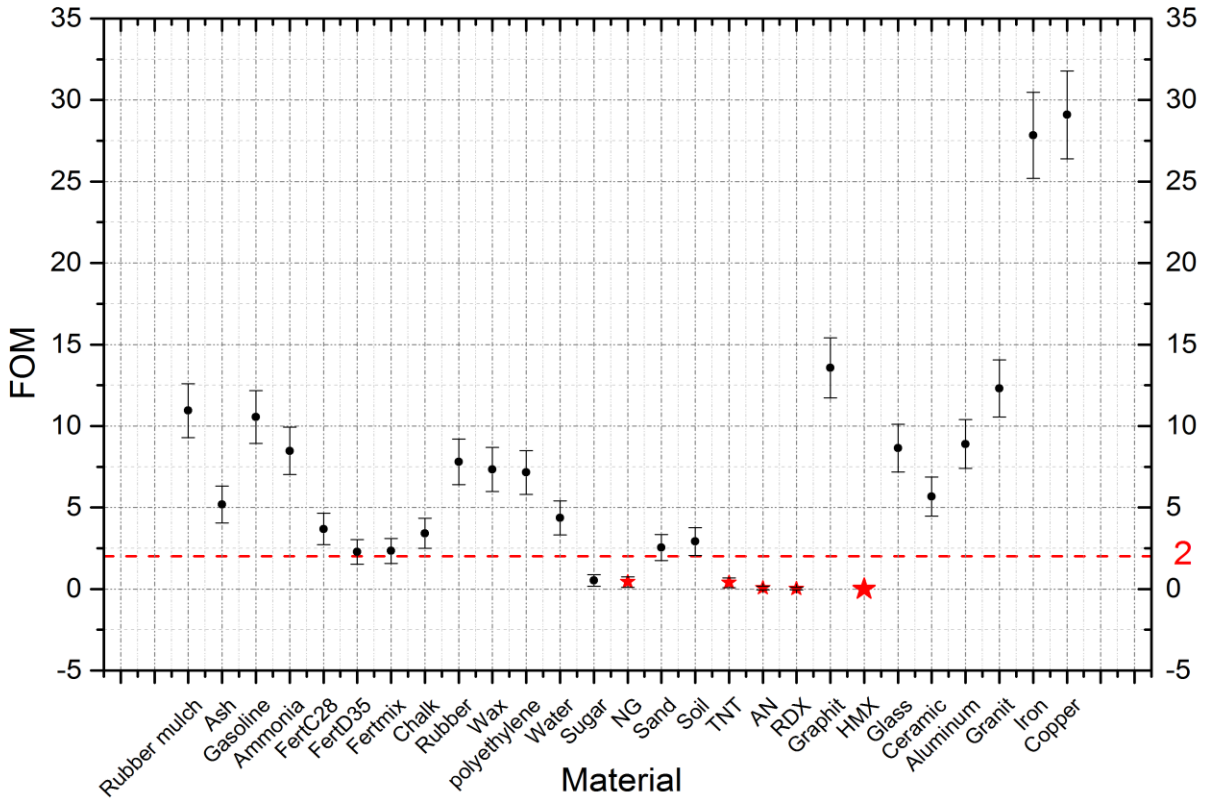

Figure 8-9. Figure of merit for HMX template using 2σ

Table 8-2. Summary of obtained results for using 1, 2 and 3 σ

	1 $\boldsymbol{\sigma}$ (68% confidence)	2$\boldsymbol{\sigma}$ (95% confidence)	3 $\boldsymbol{\sigma}$ (99% confidence)
Inert samples	22	22	22
Explosives	5	5	5
True positives	5	5	5
True negatives	18	17	15
False positives	1	1	1
False negatives	0	0	0
Suspect	3	4	6
Sensitivity %	100	100	100
Specificity %	81.8	77.3	68.2

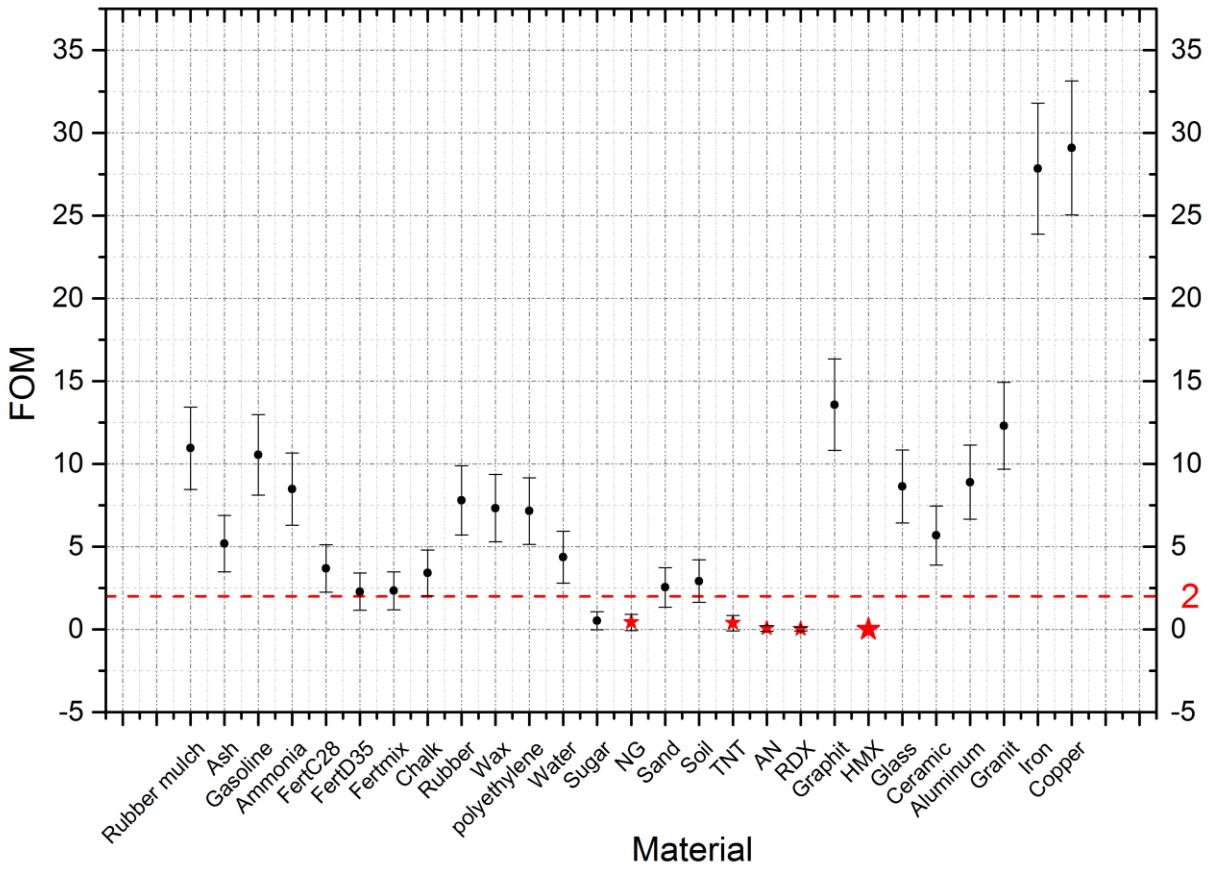

Figure 8-10. Figure of merit for HMX template using 3σ

In the same manner, 3σ error was used to increase the confidence level to 99%. As shown in Figure 8-10 the number of suspect samples increased to six, including chalk and FertC28 in addition to sand, soil, FertMix and FertD35, which lowers the specificity to 68.2% while the sensitivity is still at 100%. A summary for all results of using three different errors are shown in Table 8-2.

8.4 Simulation with another source

To confirm the feasibility of using the dense plasma focus device in explosive detection, the emitted spectrum from another dense plasma focus device was used as a source. The used device is called GN1 and is located in Argentina. The device is 4.7 kJ when charged at 30 kV. The hard X-ray spectrum of the device when operated at pressure of 3.5 mbar of deuterium-argon mixture is shown in Figure 8-11[158].

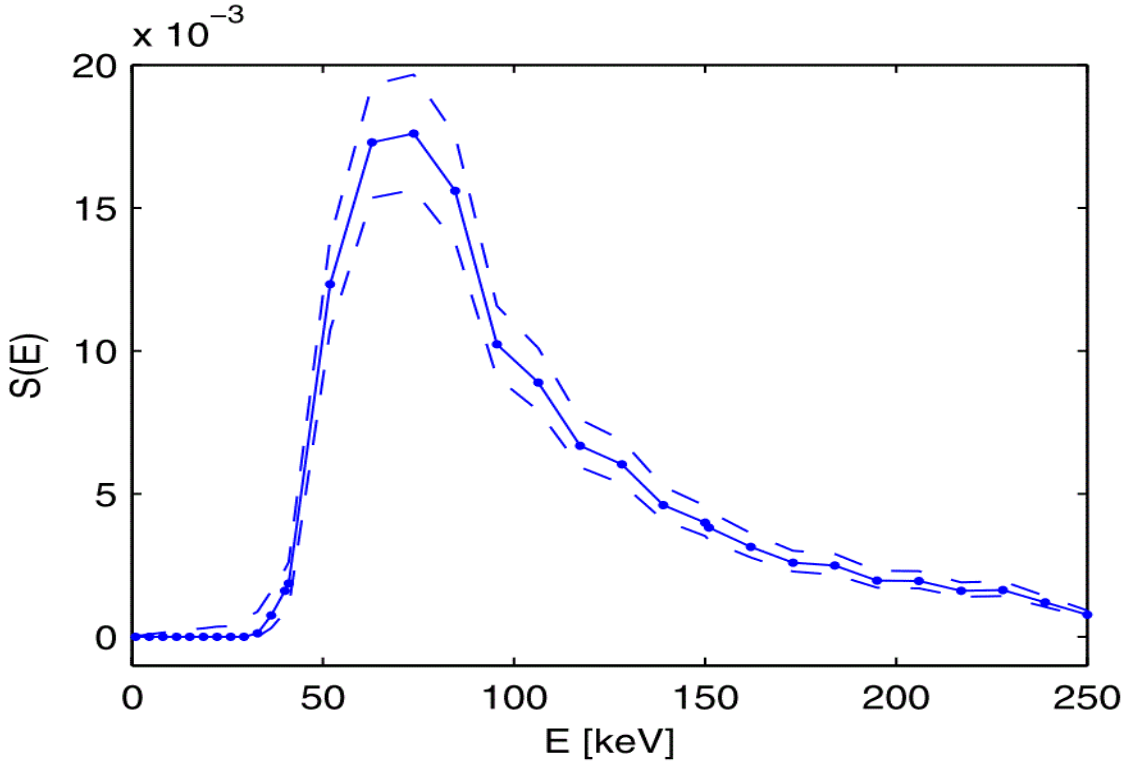

Figure 8-11. GN1 dense plasma focus device hard X-ray spectrum.

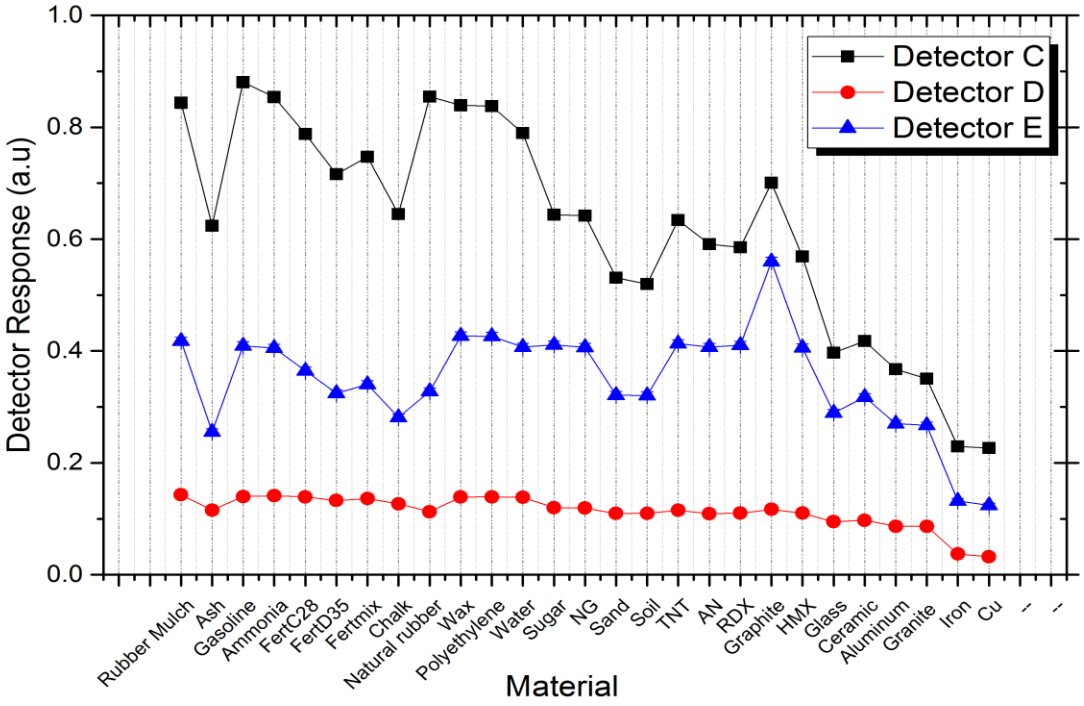

Figure 8-12. Different detector responses for using GN1 hard X-ray spectrum.

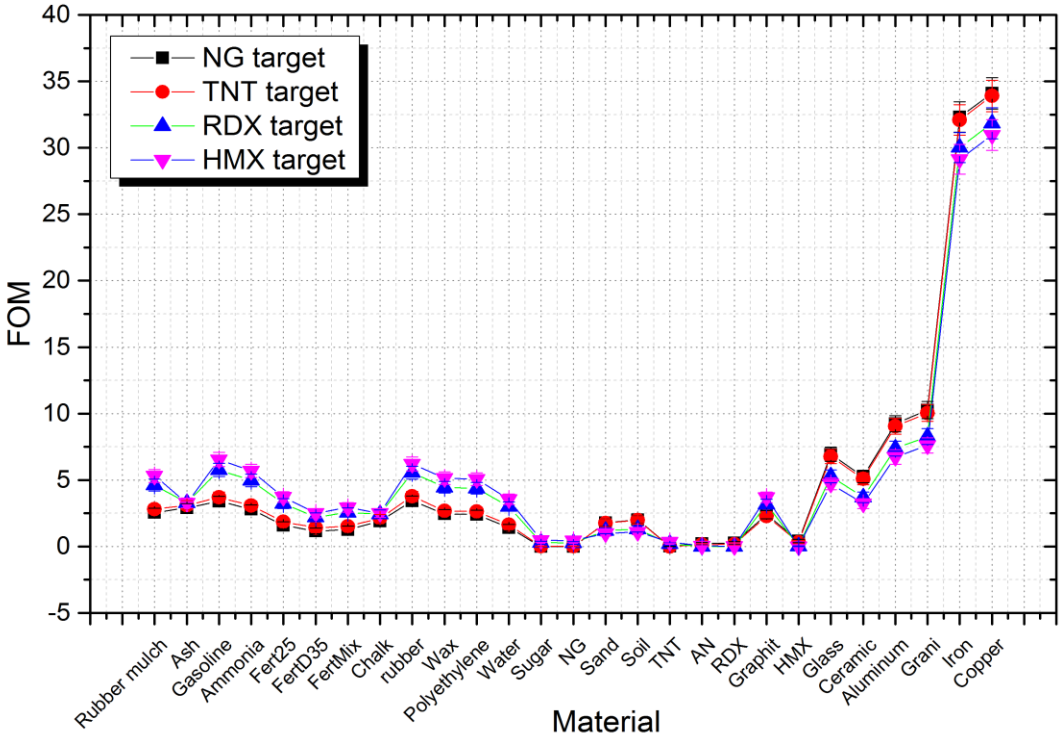

Figure 8-13. FOM for GN1 device by using 4 different templates.

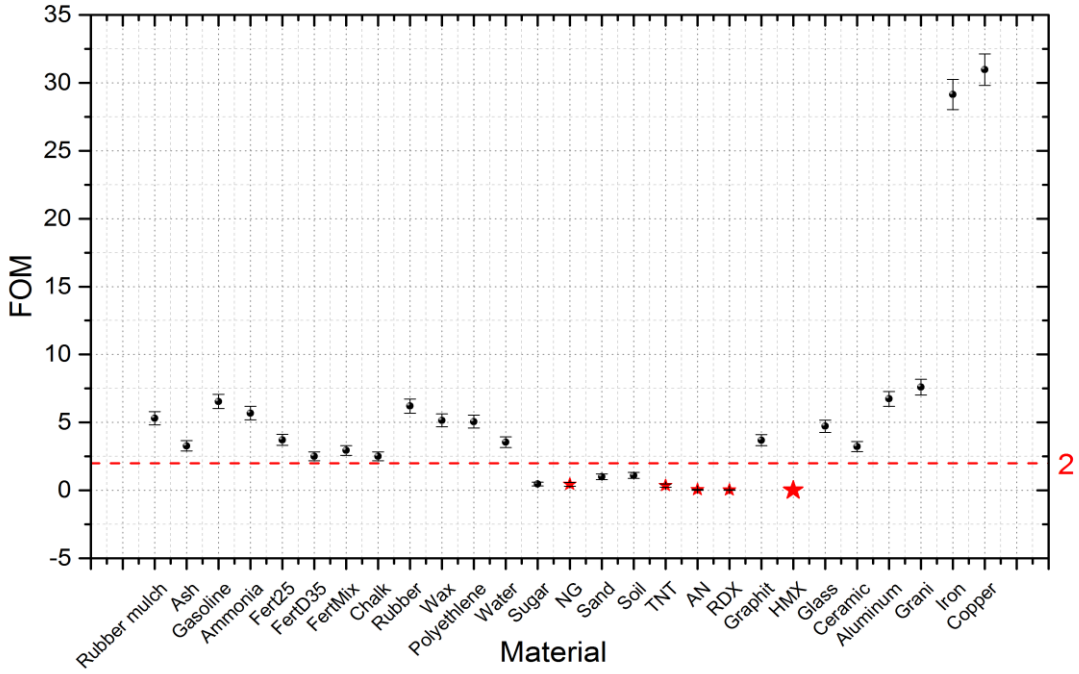

Figure 8-14. FOM for GN1 device by using HMX as a template for 1σ .

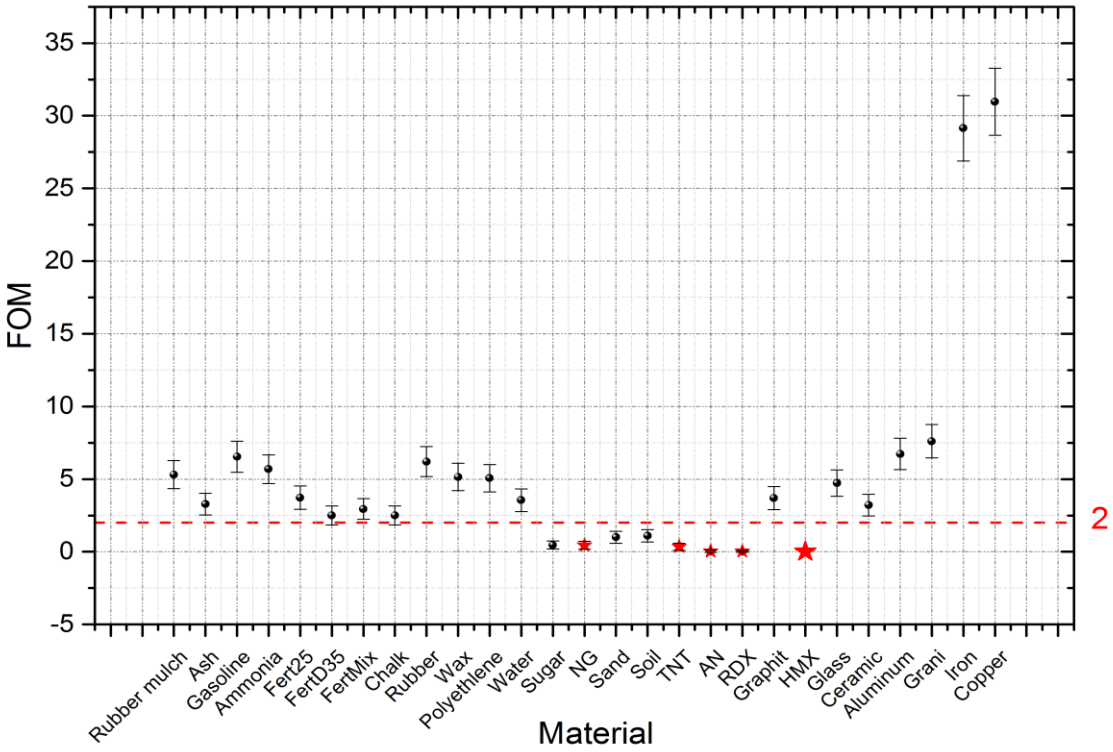

Figure 8-15. FOM for GN1 device by using HMX as a template for 2σ.

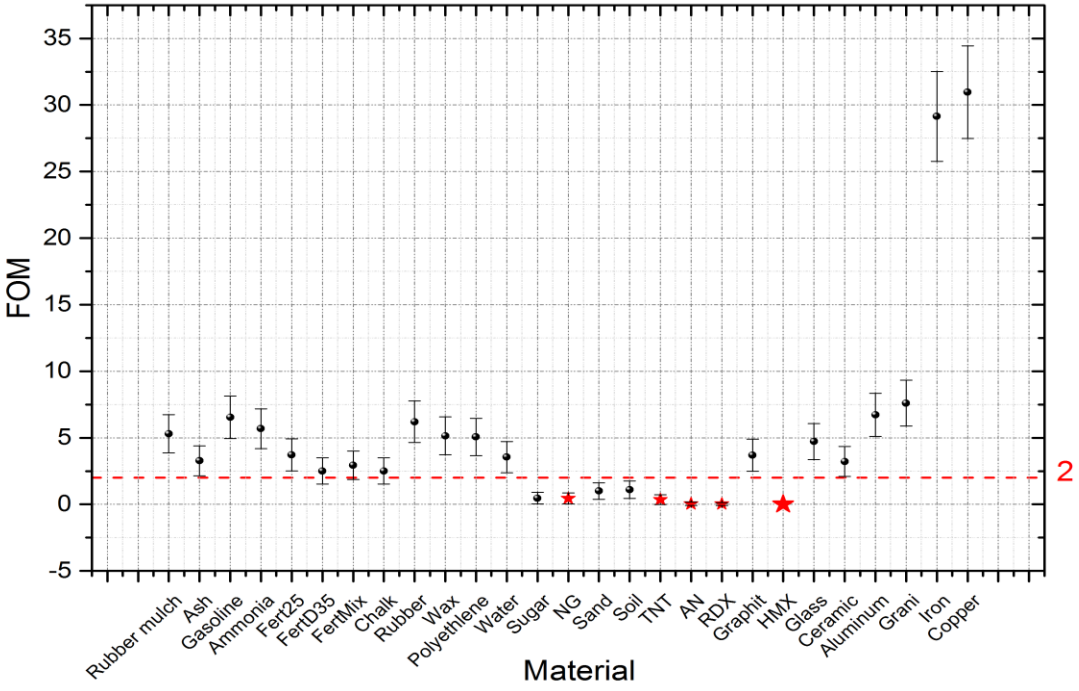

Figure 8-16. FOM for GN1 device by using HMX as a template for 3σ.

Table 8-3. Summary of obtained results of GN1 device for using 1, 2 and 3 σ

	1 $\boldsymbol{\sigma}$ (68% confidence)	2$\boldsymbol{\sigma}$ (95% confidence)	3 $\boldsymbol{\sigma}$ (99% confidence)
Inert samples	22	22	22
Explosives	5	5	5
True positives	5	5	5
True negatives	17	16	14
False positives	3	3	3
False negatives	0	0	0
Suspect	2	3	5
Sensitivity %	100	100	100
Specificity %	77.3	72.7	63.6

The GN1 spectrum, shown in Figure 8-11, was used in the simulation instead of the KSU-DPF spectrum with everything else in the simulation kept constant. The program was run for 10^8

histories as well using same samples used before for the KSU-DPF device. Responses for the three detectors are shown in Figure 8-12. By using these responses, FOMs for each sample were estimated. Figure 8-13 show the FOM of using the four different explosives for the template. As shown in the figure the best results were obtained using HMX as the template, which is exactly the same situation when using KSU-DPF spectrum. Figure 8-14,Figure 8-15 and Figure 8-16 show the FOM results by using 1, 2 and 3σ with the HMX as the template. The sensitivity was 100% for all confidence levels; in addition, the specificity was 77.3, 72.7 and 63.6% for the three cases considered. The results for the GN1 device are shown in Table 8-3. A comparison between the GN1 and KSU-DPF devices is shown in Figure 8-17. The figure shows quite similar behavior for the FOM estimation with better results for using KSU-DPF in most of the samples.

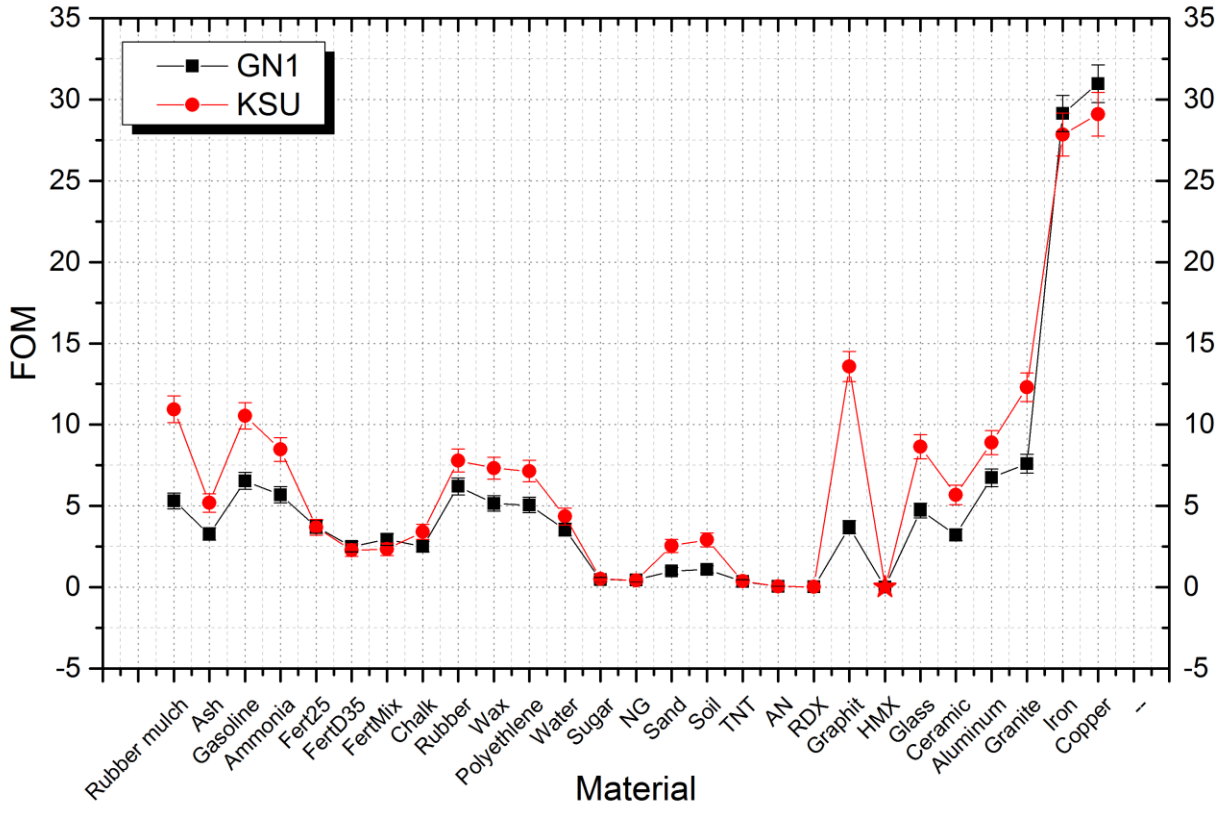

Figure 8-17. Comparison between FOM for using KSU-DPF and GN1 DPF hard X-ray spectrum by using HMX as a template.

Chapter 9- Conclusion and Future Work

In this work the Kansas State University dense plasma focus (KSU-DPF) device has been described, characterized, and considered as an X-ray source for rapid material interrogation. Experimental and simulation work using the MCNP-5 code have given promising results for explosive detection.

The static papameters of the KSU-DPF device have been estimated using a short circuit test. The calcuated static inductance L_0 and resistance r_0 were found to be 91 ± 2 nH and 13 ± 3 mΩ, respectivley, while the capacitance was known from the connected capacitor to be 12.5 μF. The device stores energy up to 10 kJ but it was opertaed during the experimental work at 1.8 kJ by charging the capacitor to 17 kV. Current traces have shown that around 95% of the current signals of the KSU-DPF have an extra dip beyond the single dip that chracterizes most DPF devices. Now, DPF devices are divided into two categories; low inductance and high inductance devices. The high inductance devices, such as the KSU-DPF, have relatively long emission times which might be usefull in certain applications.

Neutron measurements for the KSU device at different pressures showed that the optimum pressure for neutron production is 6 mbar of deuterium. The optimum pressure is the pressure at which the device produces the maximum neutron emission. The neutron yield produced at the optimum pressure was around 1.9×10^7 and 1.05×10^7 n/shot in both axial and radial directions, respectively. The anisotropy in the neutron emission is a measure of how the axial and radial components differ. In the DPF devices the neutron anisotropy is due to the beam target mechanism for neutron production which produces more neutron in the axial phase than the in the radial. As noticed from the time-to-pinch relation with the pressure, at 6 mbar the time to pinch is 1.7 μs, which is the time of the first peak in the current signal. Hence, the maximum compression occurs in the plasma pinch at this moment. The energy of neutrons emitted from the D-D reaction is known to be 2.45 MeV. The emitted neutron energy from the KSU-DPF was confirmed by the time of flight technique to be 2.45 MeV. Ions with energies up to 130 keV were measured with a Faraday cup using the time of flight technique. The average ion energy increases with increasing the pressure up to a value greater than 100 MeV at 1.5 mbar and then decreases gradually with increasing pressure up to 10 mbar. The spatial distribution of the ions was measured by using a set

of Faraday cups distributed at angles of 0^o, 10^o, 20^o and 30^o measured from the anode axis. Measurements showed that the deuteron intensity is a maximum at the top of the anode (0°), where they are generated and accelerated due to the intensive electric field produced during the evolution of the sausage instabilities ($m = 0$). The ion intensity decreases as the angle from the anode tip increases. The ion intensity was almost constant at 0^o angle over the pressure range from 0.5 to 6 mbar and started decreasing with increasing pressure beyond that. On the other hand, increasing the angle decreases the intensity rapidly with increasing pressure.

The effect of changing gas pressure in the hard X ray emission from the KSU-DPF was studied with a heavy gas (neon). Measurements showed that the maximum hard X ray (HXR) yield was obtained at a neon pressure of 0.5 mbar in both the axial and radial directions. The yield gradually decreases with increasing pressure up to 3 mbar. Between 3 and 5 mbar of neon pressure, the HXR yield decreases rapidly. This because the electron intensity decreases with increasing pressure. Because the electrons are responsible for HXR production, it is logical that the HXR yield should decrease with increasing pressure. Anisotropy was reported with a value of 1.3 in the pressure range from 0.5 to 3 mbar; it then increased to a value of 4 at 5 mbar. The probable reason for the anisotropy is the anode geometry. The anode was a hollow cylinder with wall thickness about 3 mm. As a result, the radial emission will be attenuated by the anode wall thickness. The increase in the anisotropy at high pressure may be explained by the ion energy at these pressures. As shown from the ion energy relation with pressure, at high pressure the ion energy was low which means the electron energy will be low as well. As a result the produced HXR will be less energetic and hence will be more highly attenuated.

Using radiographies of step filters from different materials, the average effective energy of the HXR emission was estimated by 59 ± 3 keV, which was a reasonable value for a theoretically estimated pinch voltage of 72 kV. The calculated HXR spectrum for the device as estimated using the same radiographies of the step filters and ranged from 20 to 120 keV. The spectrum increases from 20 keV until it reaches a maximum value at 53 keV and then decreases to zero at 120 keV. The HXR emission was tested by taking radiographs of different objects. The resulting radiographies were precise, clear and have good spatial resolution. The good resolution with 3 shots indicates that the HXR emission is relatively stable shot to shot.

In this work, the KSU-DPF was used as an X ray source for explosive detection. In the experimental work, three different responses were obtained experimentally. The target samples

differed in density and effective atomic number. Three nitrogen rich fertilizers in addition to ammonium nitrate were used as explosive surrogates in experiments using one gallon and quart samples. The template used was that for a 31% N fertilizer in the sample. All explosive surrogates were correctly identified for all sizes of samples producing 100% sensitivity within the tested samples. In the five and one-gallon experiments, half of the inert samples were correctly identified producing 50% specificity while only 28.6% specificity was achieved for the one quart samples.

Water samples of all sizes were always identified as false positives. Rubber mulch also was always considered as a suspect. The sand sample can be correctly identified in volumes of one gallon or more. The sugar sample gave a false positive at the one-gallon size and improved a little to be suspect in the quart size. Finally, polyethylene gave a false positive in the 5-gallon sample but became a suspect in both one-gallon and one-quart samples. All previous measurements were done at the 68% (one sigma) confidence level.

The MCNP-5 simulations gave detector responses in good agreement with the experimental ones, which encouraged to simulate other problems. Computer simulations allowed us to study more samples including real explosive samples. Twenty seven one-gallon samples, which were filled with five explosives and 22 inert materials were simulated. Responses from four out of the five explosives were used as templates, separately, and results were compared. Moreover, different combinations of two responses were used in and compared to using three responses and results were compared. The best results were obtained by using responses from the three detectors and using the HMX sample responses as a template. The first simulations were done using the HXR spectrum of the KSU-DPF. The simulation results were tested at 68, 95 and 99% confidence by extending the errors at the one, two and three sigma levels. Based on the simulation results, we can conclude the following:

i. All explosive samples are correctly identified for all confidence levels.
ii. All inert samples with density higher than explosives were correctly identified as true negatives. These included graphite, glass, ceramic, aluminum, granite and copper.
iii. Most inert samples with density lower than explosives were also correctly identified, except for those that have one or more elements that exist in explosives, such as fertilizers.
iv. Samples that have a density close to the density of an explosives were usually identified as suspects, or very close to be suspects. These samples include soil and sand. Sugar was always wrongly identified as explosive (false positive). This presumably is because sugar, in addition to

having a similar density to the explosive used for the template, is also a compound rich in carbon and oxygen, which are among the four main elements of the explosives (oxygen, carbon, hydrogen and nitrogen).

With 68% confidence, the simulation result produced 100% sensitivity and around 82% specificity. Increasing the confidence level to 95% produced 100% sensitivity and 77% specificity while using 99% confidence level produced 100% sensitivity and 68% specificity. These percentages were based on doing the simulation on 27 samples only. It cannot be generalized for all types of samples and materials but at least the results are encouraging for the samples considered.

Another simulation was performed using the HXR spectrum from another DPF device, called GN1. The same procedures were followed as in the first simulation with the spectrum from the KSU-DPF. The results obtained the same level of sensitivity, 100% for all confidence levels, with little decrease in the specificity levels to around 77, 73 and 64% for the one, two and three sigma levels, which is still good.

Experimental and simulation results showed the possibility of using the DPF device as an X-ray source for explosive detection with sample volumes ranging from a quarter up to 5-gallons. The advantages of using this method can be summarized as follows.

i. Using the SBRS technique for explosive detection provides an automatic decision. There is no need for any operator experiences to judge the results.
ii. The DPF devices provides fast HXR signals, within 200 nanoseconds, which will save a lot of time especially in areas when a large number of samples need to be investigated.
iii. The DPF devices might be an alternative to radioactive sources. The radiation is emitted at the push of a button rather than continuously.
iv. A Table-top DPF device can be designed and can be used as a portable system to be used anywhere.

Based on the experience on the KSU-DPF device the disadvantages can be concluded in the following points:

i. One shot was not enough to judge the samples. To get a good estimation at least 10 shots are needed, which can be resolved by operating the device in a repetitive mode.
ii. Higher energy HXR was need for better penetration, especially for big samples.
iii. The smaller the sample, the bigger the error.

iv. The DPF devices can be used at standoff but within certain limits. Currently standoff distance is limited to 1 m because at larger distances solid angle considerations reduce the number of photons received from the sample.

v. Good shielding should be designed for the experiment to ensure that most of the signals picked up by the detectors are scattered from the target.

vi. Shot-to-shot variability in radiation production. This was accounted for in this work by normalizing the scattered signal to the signal emitted directly from the device for multiple shots, but this is a tedious process to implement in the field.

In conclusion, we claim that the DPF devices with simple, room-temperature detectors may provide a portable way to perform rapid screening for threat materials.

For future work, more simulation needs to be done by using more samples to get better statistics. Samples with mixed materials inside also need to be investigated. The KSU-DPF device was not originally designed as a collimated radiation source to be used for material interrogation. Thus, suitable shielding had to be designed to block radiation escaping from many openings and tubes connected to the vacuum chamber. Also, the KSU-DPF was designed for an operating rate in excess of 1 Hz. Another device can be designed specifically for the purpose of material interrogation. This device could operate with a smaller vacuum chamber and fewer openings. The new device should work also in a repetitive mode by adding an external electronic circuit.

References

[1] J. Marshall, "Performance of a hydromagnetic plasma gun," *Physics of Fluids (1958-1988),* vol. 3, pp. 134-135, 1960.

[2] J. Osher E., "Trapping and Prolonged Confinement of an Energetic Deuterium Plasma in a Static Cusped Magnetic Field," *Phys. Rev. Lett.,* vol. 8, pp. 305, 1962.

[3] J. W. Mather, "Formation of a High-Density Deuterium Plasma Focus," *Physics of Fluids (1958-1988),* vol. 8, pp. 366-377, 1965.

[4] N. Filippov V., T. Filippova I. and V. Vinogradov P., "Dense high-temperature plasma in a non-cylindrical z-pinch compression," *Nucl.Fusion, Suppl.,* 1962.

[5] R. Verma, R. Rawat S., P. Lee, M. Krishnan, S. Springham V. and T. Tan L., "Miniature Plasma Focus Device as a Compact Hard X-Ray Source for Fast Radiography Application," *IEEE Transactions on Plasma Science,* vol. 38, 2010.

[6] M. Scholz, R. Miklaszewski, V. A. Gribkov and F. Mezzetti, "PF-1000 device," 2000.

[7] P. Chatterton A., Ed., *Electrical Breakdown in Gases, edited by Meek and Craggs*. New York: Wiley, 1978.

[8] A. Donges, G. Herziger, H. Krompholz, F. Rühl and K. Schönbach, "The breakdown phase in a coaxial plasma gun," *Physics Letters A,* vol. 76, pp. 391-392, 1980.

[9] H. Krompholz, W. Neff, F. Rühl, K. Schönbach and G. Herziger, "Formation of the plasma layer in a plasma focus device," *Physics Letters A,* vol. 77, pp. 246-248, 1980.

[10] M. Borowiecki and S. Kaliski, "Influence of inulator on plasma-focus discharge," *Institute of Plasma Physics and Laser Microfusion,* pp. 86-89, 1985.

[11] J. Nowikowski and Z. Jankowicz, *Proc. 9th Europ. Conf. on Controlled Fusion and Plasma Phys.,Vol. 2,* 1979, pp. 542.

[12] G. Decker, W. Kies and G. Pross, "Experiments solving the polarity riddle of the plasma focus," *Physics Letters A,* vol. 89, pp. 393-396, 1982.

[13] A. Donges, G. Herziger, H. Krompholz, F. Rühl and K. Schönbach, "The breakdown phase in a coaxial plasma gun," *Physics Letters A,* vol. 76, pp. 391-392, 1980.

[14] A. e. a. Bernard, "Scientific Status of plasma focus research," *J. Moscow Phys. Soc.,* vol. 8, pp. 93-170, 1998.

[15] D. Potter E, "Numerical studies of the plasma focus," *Physics of Fluids (1958-1988),* vol. 14, pp. 1911-1924, 1971.
[16] S. Bazdenkov V. and V. Vikhrev V., "Three-fluid MHD model for the current shell in a Z pinch," *Soviet Journal of Plasma Physics,* vol. 1, pp. 250-253, 1975.
[17] M. Scholz and I. Ivanova-Stanik M., "Initial phase in plasma focus device—model and computer simulation," *Vacuum,* vol. 58, pp. 287-293, 2000.
[18] V. Yordanov, D. Genov, I. Ivanova-Stanik and A. Blagoev, "Ionization growth in the break-down of plasma focus discharge," *Vacuum,* vol. 76, pp. 365-368, 2004.
[19] S. Chow Pew, S. Lee and B. C. Tan, "Current sheath studies in a co-axial plasma focus gun," *Journal of Plasma Physics,* vol. 8, pp. 21-31, 1972.
[20] K. Kwek H., T. Tou Y and S. Lee, "Current sheath structure of the plasma focus in the run-down phase," *Plasma Science, IEEE Transactions On,* vol. 18, pp. 826-830, 1990.
[21] S. Al-Hawat, "Axial velocity measurement of current sheath in a plasma focus device using a magnetic probe," *Plasma Science, IEEE Transactions On,* vol. 32, pp. 764-769, 2004.
[22] H. Krompholz, F. Rühl, W. Schneider, K. Schönbach and G. Herziger, "A scaling law for plasma focus devices," *Physics Letters A,* vol. 82, pp. 82-84, 1981.
[23] M. Mathuthu, T. Zengeni G. and A. Gholap V., "Measurement of magnetic field and velocity profiles in 3.6 kJ United Nations University/International Center For Theoretical Physics plasma focus fusion device," *Physics of Plasmas (1994-Present),* vol. 3, pp. 4572-4576, 1996.
[24] T. Tou Y., "Multislit streak camera investigation of plasma focus in the steady-state run-down phase," *Plasma Science, IEEE Transactions On,* vol. 23, pp. 870-873, 1995.
[25] G. Basque, A. Jolas and J. Watteau P., "Comparison of a Two-Dimensional Snowplough Model with Experiment," *Physics of Fluids (1958-1988),* vol. 11, pp. 1384-1386, 1968.
[26] J. Keck C, "Current distribution in a magnetic annular shock tube," *Physics of Fluids (1958-1988),* vol. 5, pp. 630-632, 1962.
[27] P. Hart J., "Modified snowplow model for coaxial plasma accelerators," *J. Appl. Phys.,* vol. 35, pp. 3425-3431, 1964.
[28] C. Moreno, F. Casanova, G. Correa and A. Clausse, "Experimental study and two-dimensional modelling of the plasma dynamics of magnetically driven shock waves in a coaxial tube," *Plasma Phys. Controlled Fusion,* vol. 45, pp. 1989, 2003.

[29] *Radiative Dense Plasma Focus Computation Package:RADPF20011*. Available: http://www.intimal.edu.my/school/fas/UFLF.

[30] A. Patran Constantin, "Electron and medium energy X-ray emission from dense plasma focus," *National Institute of Education, Nanyang Technological University,* vol. PhD, 2002.

[31] A. Bernard, A. Coudeville, A. Jolas, J. Launspach and J. De Mascureau, "Experimental studies of the plasma focus and evidence for nonthermal processes," *Physics of Fluids (1958-1988),* vol. 18, pp. 180-194, 1975.

[32] A. Toepfer J., "Finite-Temperature Relativistic Electron Beam," *Physical Review A,* vol. 3, pp. 1444, 1971.

[33] Y. Chen H. and S. Lee, "Coaxial plasma gun in mode 1 operation," *International Journal of Electronics,* vol. 35, pp. 341-352, 1973.

[34] W. Bennett H., "Magnetically self-focussing streams," *Physical Review,* vol. 45, pp. 890, 1934.

[35] S. Lee and A. Serban, "Dimensions and lifetime of the plasma focus pinch," *Plasma Science, IEEE Transactions On,* vol. 24, pp. 1101-1105, 1996.

[36] S. Lee, "An energy-consistent snow-plough model for pinch design," *J. Phys. D,* vol. 16, pp. 2463, 1983.

[37] S. Lee, "Energy balance and the radius of electromagnetically pinched plasma columns," *Plasma Physics,* vol. 25, pp. 571, 1983.

[38] A. Serban, "Anode geometry and focus characteristics," *PhD Dissertation, Nanyang Technological University,* 1995.

[39] J. Mather W. and P. Bottoms J., "Characteristics of the dense plasma focus discharge," *Physics of Fluids (1958-1988),* vol. 11, pp. 611-618, 1968.

[40] T. Butler D., I. Henins, F. Jahoda C., J. Marshall and R. Morse L., "Coaxial snowplow discharge," *Physics of Fluids (1958-1988),* vol. 12, pp. 1904-1916, 1969.

[41] J. Shearer W., "Contraction of Z pinches actuated by radiation losses," *Physics of Fluids (1958-1988),* vol. 19, pp. 1426-1428, 1976.

[42] G. Neil R. and R. Post S., "Infrared emission from the plasma focus," *Plasma Physics,* vol. 23, pp. 515, 1981.

[43] M. Kruskal and M. Schwarzschild, "Some instabilities of a completely ionized plasma," *Proceedings of the Royal Society of London.Series A.Mathematical and Physical Sciences,* vol. 223, pp. 348-360, 1954.
[44] A. Jeffrey and T. Taniuti, *Magnetohydrodynamic Stability and Thermonuclear Containment: A Collection of Reprints.* Academic Press, 1966.
[45] V. Vikhrev V., V. Ivanov V. and G. Rozanova A., "Development of sausage-type instability in a Z-pinch plasma column," *Nucl Fusion,* vol. 33, pp. 311, 1993.
[46] R. Rawat S., T. Zhang, Phua, C.,B.,L., Then, J.,X.,Y., K. Chandra A., X. Lin, A. Patran and P. Lee, "Effect of insulator sleeve length on soft x-ray emission from a neon-filled plasma focus device," *Plasma Sources Sci. Technol.,* vol. 13, pp. 569, 2004.
[47] A. Bernard, P. Cloth, H. Conrads, A. Coudeville, G. Gourlan, A. Jolas, C. Maisonnier and J. Rager P., "The dense plasma focus—A high intensity neutron source," *Nucl. Instrum. Methods,* vol. 145, pp. 191-218, 1977.
[48] A. Bernard, J. Garconnet P., A. Jolas, J. Le Breton P. and J. De Mascureau, "Turbulence caused by the interaction between plasma and electric current in the focus experiment," in *Plasma Physics and Controlled Nuclear Fusion Research 1978, Volume 2,* 1979, pp. 159-172.
[49] W. Bostick H., V. Nardi and W. Prior, "Sixth European Conf. on Contr," *Fus.and Plasma Phys., Moscow,* vol. 2, pp. 395, 1973.
[50] E. Beckner H, E. Clothiaux J. and D. Smith R., "Dominant source of soft X radiation from coaxial discharge tubes," *Physics of Fluids (1958-1988),* vol. 12, pp. 253-254, 1969.
[51] R. Lee and M. Lampe, "Electromagnetic instabilities, filamentation, and focusing of relativistic electron beams," *Phys. Rev. Lett.,* vol. 31, pp. 1390, 1973.
[52] K. Kuriki, M. Forrest J., P. Morgan D. and N. Peacock J., "Experiments on turbulence in plasma focus," in *Pulsed High Beta Plasmas,* 1976, pp. 395-399.
[53] G. Decker, G. Pross, B. Ruckle and H. Schmidt, "Recent experimental results of plasma focus research at stuttgart," in *Pulsed High Beta Plasmas: Proceedings of the Third Topical Conference Held at Ukaea Culham Laboratory, Abingdon, Oxfordshire, UK, 9-12 September 1975,* 2013, pp. 401.
[54] J. Mather W., "Dense Plasma Focus," *Methods in Experimental Physics,* vol. 9, pp. 187-249, 1971.

[55] M. Bernstein J., "Acceleration Mechanism for Neutron Production in Plasma Focus and z-Pinch Discharges," *Physics of Fluids (1958-1988),* vol. 13, pp. 2858-2866, 1970.
[56] J. Lee H., L. Shomo P., M. Williams D. and H. Hermansdorfer, "Neutron production mechanism in a plasma focus," *Physics of Fluids (1958-1988),* vol. 14, pp. 2217-2223, 1971.
[57] N. Peacock J., M. Hobby G. and M. Galanti, "Satellite spectra for helium-like ions in laser-produced plasmas," *Journal of Physics B: Atomic and Molecular Physics,* vol. 6, pp. L298, 1973.
[58] J. Smith R., C. Luo M., M. Rhee J. and R. Schneider F., "Operation of a plasma focus device as a compact electron accelerator," *Physics of Fluids (1958-1988),* vol. 28, pp. 2305-2307, 1985.
[59] W. Stygar, G. Gerdin, F. Venneri and J. Mandrekas, "Particle beams generated by a 6–12.5 kJ dense plasma focus," *Nucl Fusion,* vol. 22, pp. 1161, 1982.
[60] P. Choi, C. Deeney, H. Herold and C. Wong S., "Characterization of self-generated intense electron beams in a plasma focus," *Laser and Particle Beams,* vol. 8, pp. 469-476, 1990.
[61] R. Gullickson L. and R. Barlett H., "X-ray analysis for electron beam enhancement in the plasma focus device," in *Presented at 23d Ann. Conf. on Appl. of X-Ray Analysis, Denver, 7 Aug. 1974,* 1974, .
[62] K. Hirano, I. Kaneko, K. Shimoda and T. Yamamoto, "A method for measuring electron energy distribution in a plasma focus," *Japanese Journal of Applied Physics,* vol. 29, pp. 1182, 1990.
[63] A. Bernard, H. Bruzzone, P. Choi, H. Chuaqui, V. Gribkov, J. Herrera, K. Hirano, A. Krejci, S. Lee and C. Luo, "Proposal document for international centre for dense magnetized plasmas," *Prepared on the Request of UNESCO,* 1994.
[64] L. Jakubowski, M. Sadowski and J. Zebrowski, "Measurements of charged particle beams from plasma focus discharges," *Nucl Fusion,* vol. 41, pp. 755, 2001.
[65] V. Gribkov A., "Application of the relativistic electron beams originating in the discharges of plasma focus type for the combined laser-REB plasma heating," in *Energy Storage, Compression, and Switching*Anonymous Springer, 1976, pp. 271-276.
[66] W. Neff, R. Noll, F. Rühl, R. Lebert, C. Haas R., B. Weikl and G. Herziger, "Monochromatic x-ray emission of a fully ionized hydrogen plasma," *Nuclear Instruments and Methods in Physics Research Section A: Accelerators, Spectrometers, Detectors and Associated Equipment,* vol. 285, pp. 253-257, 1989.

[67] Van Paassen, H, L, L, R. Vandre H and R. White Stephen, "X-Ray Spectra from Dense Plasma Focus Devices," *Physics of Fluids (1958-1988),* vol. 13, pp. 2606-2612, 1970.
[68] D. Johnson J., "Study of the x-ray production mechanism of a dense plasma focus," *J. Appl. Phys.,* vol. 45, pp. 1147-1153, 1974.
[69] V. Krauz I., R. Salukvadze G. and E. Khautiev, "Energy spectra of ion beams formed in plasma focus," 1985.
[70] T. Oppenlander, G. Pross, G. Decker and M. Trunk, "The plasma focus current in the compression phase," *Plasma Physics,* vol. 19, pp. 1075, 1977.
[71] V. Gribkov A., S. Isakov I. and A. Romanov B., "On harmonics of epithermal infrared radiation of a plasma focus," 1984.
[72] W. Harries L., J. Lee H. and D. McFarland R., "Trajectories of high energy electrons in a plasma focus," *Plasma Physics,* vol. 20, pp. 95, 1978.
[73] T. Zhang, J. Lin, A. Patran, D. Wong, S. Hassan M., S. Mahmood, T. White, T. Tan L., S. Springham V. and S. Lee, "Optimization of a plasma focus device as an electron beam source for thin film deposition," *Plasma Sources Sci. Technol.,* vol. 16, pp. 250, 2007.
[74] W. Neff, J. Eberle, R. Holz, R. Lebert and F. Richter, "The plasma focus as soft X-ray source for microscopy and lithography," in *1989 Intl Congress on Optical Science and Engineering,* 1989, pp. 13-20.
[75] P. Lee, X. Feng, G. Zhang X., M. Liu H. and S. Lee, "Electron lithography using a compact plasma focus," *Plasma Sources Sci. Technol.,* vol. 6, pp. 343, 1997.
[76] R. Petr, A. Bykanov, J. Freshman, D. Reilly, J. Mangano, M. Roche, J. Dickenson, M. Burte and J. Heaton, "Performance summary on a high power dense plasma focus x-ray lithography point source producing 70 nm line features in AlGaAs microcircuits," *Rev. Sci. Instrum.,* vol. 75, pp. 2551-2559, 2004.
[77] Y. Kato, I. Ochiai, Y. Watanabe and S. Murayama, "Plasma focus x-ray source for lithography," *Journal of Vacuum Science & Technology B,* vol. 6, pp. 195-198, 1988.
[78] S. Lee, P. Lee, G. Zhang, X. Feng, V. A. Gribkov, M. Liu, A. Serban and T. K. Wong, "High rep rate high performance plasma focus as a powerful radiation source," *Plasma Science, IEEE Transactions On,* vol. 26, pp. 1119-1126, 1998.
[79] F. Castillo, M. Milanese, R. Moroso, J. Pouzo and A. Santiago, "Small plasma focus studied as a source of hard X-ray," *Plasma Science, IEEE Transactions On,* vol. 29, pp. 921-926, 2001.

[80] V. A. Gribkov, A. Srivastava, P. L. C. Keat, V. Kudryashov and P. Lee, "Operation of NX2 dense plasma focus device with argon filling as a possible radiation source for micro-machining," *Plasma Science, IEEE Transactions On,* vol. 30, pp. 1331-1338, 2002.
[81] V. Gribkov A., " Plasma instabilities in a dense plasma focus ," *Chin. Phys. Lett.,* vol. 10 (Suppl.), pp. 1-22, 1993.
[82] F. Di Lorenzo J., A. Lazarte I., R. Vieytes E., P. Cobelli J., P. Knoblauch T., A. Clausse and C. Moreno H., "Compact Repetitive plasma focus as a powerful source for hardX-ray and Neutron Scanning," *Pulsed Power Conference,* 2005.
[83] P. Choi, C. Wong S and H. Herold, "Studies of the spatial and temporal evolution of a dense plasma focus in the X-ray region," *Laser and Particle Beams,* vol. 7, pp. 763-772, 1989.
[84] P. Choi, R. Aliaga-Rossel, C. Dumitrescu-Zoita and C. Deeney, "Dynamics of hot spots formation in a dense plasma focus optical and x-ray observations," in *Dense Z-Pinches: 3rd International Conference,* 1994, pp. 288-298.
[85] V. Zoita, R. Presura, F. Gherendi and C. Dumitrescu-Zoita, "Plasma configuration and radiation properties in the pinch and post-pinch phases of plasma focus discharges produced in deuterium-noble gas mixtures," in *Plasma Science, 1993. IEEE Conference Record-Abstracts., 1993 IEEE International Conference On,* 1993, pp. 186.
[86] V. Zambreanu and V. Zoita, "The relative role of the macroscopic and microscopic phenomena in the plasma focus performance," 1992.
[87] D. Gates C., *Proc. Int. Conf. on Energy Storage and Switching,* vol. 2, pp. 329, 1978.
[88] H. Herold, L. Bertalot, K. Hirano, U. Jager, H. Kaeppeler J., M. Sadowski J., H. Schmidt, R. Schmidt, M. Shakhatre, A. Shyam, G. Bockle, K. Matl, N. Wenzel, R. Wolf, R. Batzner, H. Hinsh and K. Hubner, *Plasma Physics and Controlled Nuclear Fusion Research (IAEA, Vienna, 1985),* vol. 2, pp. 579, 1985.
[89] M. Bernstein J., D. Meskan A. and Van Paassen, H.,L.,L., "Space, time, and energy distributions of neutrons and x rays from a focused plasma discharge," *Physics of Fluids (1958-1988),* vol. 12, pp. 2193-2202, 1969.
[90] M. Forrest J and M. Forrest J., "Measurement of the ion temperature in the dense plasma focus by laser beam scattering," *Plasma Physics,* vol. 16, pp. 489, 1974.

[91] F. Castillo, M. Milanese, R. Moroso and J. Pouzo, "Evidence of thermal and non-thermal mechanisms coexisting in dense plasma focus DD nuclear reactions," *J. Phys. D,* vol. 33, pp. 141, 2000.
[92] J. Koh M., R. Rawat S., A. Patran, T. Zhang, D. Wong, S. Springham V., T. Tan L., S. Lee and P. Lee, "Optimization of the high pressure operation regime for enhanced neutron yield in a plasma focus device," *Plasma Sources Sci. Technol.,* vol. 14, pp. 12, 2005.
[93] M. Zakaullah, I. Akhtar, A. Waheed, K. Alamgir, A. Shah Z. and G. Murtaza, "Comparative study of ion, x-ray and neutron emission in a low energy plasma focus," *Plasma Sources Sci. Technol.,* vol. 7, pp. 206, 1998.
[94] M. Haines G., "Ion beam formation in an< i> m= 0 unstable< i> Z pinch," *Nuclear Instruments and Methods in Physics Research,* vol. 207, pp. 179-185, 1983.
[95] T. Yamamoto, K. Shimoda and K. Hirano, "Neutrons, X-rays and charged particle beams emission in a 65 kV plasma focus," *Japanese Journal of Applied Physics,* vol. 24, pp. 324, 1985.
[96] J. Rager P., "The plasma focus," in *Unconventional Approaches to Fusion*Anonymous Springer, 1982, pp. 157-192.
[97] I. Tiseanu, N. Mandache and V. Zambreanu, "Energetic and angular characteristics of the reacting deuterons in a plasma focus," *Plasma Phys. Controlled Fusion,* vol. 36, pp. 417, 1994.
[98] M. Bernstein J. and G. Comisar G., "Neutron Energy and Flux Distributions from a Crossed-Field Acceleration Model of Plasma Focus and Z-Pinch Discharges," *Physics of Fluids (1958-1988),* vol. 15, pp. 700-707, 1972.
[99] U. Jäger and H. Herold, "Fast ion kinetics and fusion reaction mechanism in the plasma focus," *Nucl Fusion,* vol. 27, pp. 407, 1987.
[100] M. Frignani, "Simulation of gas breakdown and plasma dynamics in plasma focus devices," *PhD Thesis, Alma MAter Studiorum Universita Degli Studi Di Bologna,* 2007.
[101] G. Decker, L. Flemming, H. Kaeppeler J., T. Oppenlander, G. Pross, P. Schilling, H. Schmidt, M. Shakhatre and M. Trunk, "Current and neutron yield scaling of fast high voltage plasma focus," *Plasma Physics,* vol. 22, pp. 245, 1980.
[102] W. Bennett H., "Magnetically self-focussing streams," *Physical Review,* vol. 45, pp. 890, 1934.
[103] S. Lee and S. Saw H., "Neutron scaling laws from numerical experiments," *J. Fusion Energy,* vol. 27, pp. 292-295, 2008.

[104] S. Lee, P. Lee, S. Saw H. and R. Rawat S., "Numerical experiments on plasma focus pinch current limitation," *Plasma Phys. Controlled Fusion,* vol. 50, pp. 065012, 2008.
[105] S. Lee, S. Saw H., Lee, P.,C.,K., R. Rawat S. and H. Schmidt, "Computing plasma focus pinch current from total current measurement," *Appl. Phys. Lett.,* vol. 92, pp. 111501-111501-3, 2008.
[106] S. Saw H. and S. Lee, "Scaling laws for plasma focus machines from numerical experiments," *Energy and Power Engineering,* vol. 2, pp. 65, 2010.
[107] A. Shyam and R. Rout K., "Enhancement of neutron emission from a plasma focus nuclear fusion device by the use of anode with low spark erosion," *Phys. Scripta,* vol. 57, pp. 290, 1998.
[108] D. Freiwald A., K. Prestwich R., G. Kuswa W. and E. Beckner H., "Neutron enhancement from relativistic electron beam-dense plasma focus interactions," *Physics Letters A,* vol. 36, pp. 297-298, 1971.
[109] M. Zakaullah, A. Waheed, S. Ahmad, S. Zeb and S. Hussain, "Study of neutron emission in a low-energy plasma focus with β-source-assisted breakdown," *Plasma Sources Sci. Technol.,* vol. 12, pp. 443, 2003.
[110] S. Yap L., C. Wong S., P. Choi, C. Dumitrescu and S. Moo P., "Observation of two phases of neutron emission in a low energy plasma focus," *Japanese Journal of Applied Physics,* vol. 44, pp. 8125, 2005.
[111] A. Babazadeh R., M. Roshan V., H. Habibi, A. Nasiry, M. Memarzadeh, A. Banoushi, M. Lamehi and S. Sadat Kiai M., "X-ray and neutron emission studies in a new Filippov type plasma focus," *Brazilian Journal of Physics,* vol. 32, pp. 89-94, 2002.
[112] W. Jiang, W. J. Weber and S. Thevuthasan, "Ion implantation and thermal annealing in silicon carbide and gallium nitride," *Nuclear Instruments and Methods in Physics Research Section B: Beam Interactions with Materials and Atoms,* vol. 178, pp. 204-208, 2001.
[113] C. Kant R., M. Srivastava P. and R. Rawat S., "Thin carbon film deposition using energetic ions of a dense plasma focus," *Physics Letters A,* vol. 226, pp. 212-216, 1997.
[114] C. Kant R., M. Srivastava P. and R. Rawat S., "Dense plasma focus energetic ions based fullerene films on a Si (111) substrate," *Physics Letters A,* vol. 239, pp. 109-114, 1998.
[115] R. Rawat S., M. Srivastava P., S. Tandon and A. Mansingh, "Crystallization of an amorphous lead zirconate titanate thin film with a dense-plasma-focus device," *Physical Review B,* vol. 47, pp. 4858, 1993.

[116] M. Roshan V., R. Rawat S., A. Talebitaher, R. Verma, P. Lee and S. V. Springham, "High energy deuteron emission in NX2 plasma focus," 2009.
[117] M. Srivastava P., S. Mohanty R., S. Annapoorni and R. Rawat S., "Diode like behaviour of an ion irradiated polyaniline film," *Physics Letters A,* vol. 215, pp. 63-68, 1996.
[118] H. Conrads, P. Cloth, M. Demmeler and R. Hecker, "Velocity distribution of the ions producing neutrons in a Plasma Focus," *Physics of Fluids (1958-1988),* vol. 15, pp. 209-211, 1972.
[119] I. Belyaeva F. and N. Filippov V., "Location of fast Deuterons in a Plasma Focus," *Nucl Fusion,* vol. 13, pp. 881, 1973.
[120] H. Krompholz, L. Michel, K. Schoenbach H. and H. Fischer, "Neutron-, ion-, and electron-energy spectra in a 1 kJ plasma focus," *Applied Physics,* vol. 13, pp. 29-35, 1977.
[121] R. Gullickson L. and H. Sahlin L., "Measurements of high-energy deuterons in the plasma-focus device," *J. Appl. Phys.,* vol. 49, pp. 1099-1105, 1978.
[122] C. Maisonnier and J. Rager P., "Generation of ion beams in the frascati plasma focus devices," in *High-Power Electron and Ion Beam Research & Technology, 1979 3rd International Topical Conference On,* 1979, pp. 233-249.
[123] A. Bernard, J. Garconnet P., A. Jolas, J. Le Breton P., J. De Mascureau and P. Romary, "Plasma focus research at the Center d'Etudes de limeil
," *In Proc. IEEE Int. Conf. on Plasma Sci. (Monterial),* 1979.
[124] M. Sadowski, E. Sadowska Skladnik, J. Baranowski, J. Zebrowski, H. Kelly, A. Lepone, A. Marquez, M. Milanese, R. Moroso and J. Pouzo, "Comparison of characteristics of pulsed ion beams emitted from different small PF devices," *NUKLEONIKA,* vol. 45, pp. 179-184, 2000.
[125] W. Bostick H., H. Kilic, V. Nardi and C. Powell W., "Time resolved energy spectrum of the axial ion beam generated in plasma focus discharges," *Nucl Fusion,* vol. 33, pp. 413, 1993.
[126] U. Jäger and H. Herold, "Fast ion kinetics and fusion reaction mechanism in the plasma focus," *Nucl Fusion,* vol. 27, pp. 407, 1987.
[127] R. Verma, "Construction and Obtimization of Low Energy (<240) Miniature Repetitive Plasma Focus Neutron Source," *A Thesis Submitted to the National Institute of Education, Nanyang Technological University,* 2010.
[128] R. Gullickson L., J. Luce S. and H. Sahlin L., "Operation of a plasma-focus device with D2 and He3," *J. Appl. Phys.,* vol. 48, pp. 3718-3722, 1977.

[129] M. Sadowski, J. Zebrowski, E. Rydygier and J. Kucinski, "Ion emission from plasma-focus facilities," *Plasma Phys. Controlled Fusion,* vol. 30, pp. 763, 1988.
[130] H. Kelly and A. Marquez, "Ion-beam and neutron production in a low-energy plasma focus," *Plasma Phys. Controlled Fusion,* vol. 38, pp. 1931, 1996.
[131] J. Slough, C. Pihl, V. Bochkov D., D. Bochkov V., P. Panov V. and I. Gnedin N., "Prospective pulsed power applications of pseudospark switches," in *Pulsed Power Conference, 2009. PPC'09. IEEE,* 2009, pp. 255-259.
[132] S. Saw H., S. Lee, F. Roy, P. Chong L., V. Vengadeswaran, Sidik, A., S., M., Y. Leong W. and A. Singh, "In situ determination of the static inductance and resistance of a plasma focus capacitor bank," *Rev. Sci. Instrum.,* vol. 81, pp. 053505, 2010.
[133] S. Lee, "Transverse Ionizing Shock Waves in a Planar Electromagnetic Shock Tube." *PhD Thesis, ANU, Australia,* 1970.
[134] (). *North Star High Voltage*. Available: http://www.highvoltageprobes.com/high-voltage-probes.
[135] (). *Saint-Gobain Crystals*. Available: http://www.crystals.saint-gobain.com/uploadedFiles/SG-Crystals/Documents/SGC%20BC418-420-422%20Data%20Sheet.pdf.
[136] F. Knoll Glenn, *Radiation Detection and Measurement.* USA: John Wiley & Sons, Inc., 2010.
[137] *http://nsspi.tamu.edu/nsep/courses/basic-radiation-detection/gamma-ray-spectroscopy/scintillation-detectors/scintillation-detectors*.
[138] M. Zakaullah, K. Alamgir, G. Murtaza and A. Waheed, "Efficiency of plasma focus for argon K-series line radiation emission," *Plasma Sources Sci. Technol.,* vol. 9, pp. 592, 2000.
[139] *http://fas.org/sgp/othergov/doe/lanl/lib-www/la-pubs/00326408.pdf*.
[140] *http://www.ludlums.com/images/stories/product_manuals/M42-30H.pdf*.
[141] *http://www.tek.com/sites/tek.com/files/media/media/resources/DPO7000C-Oscilloscope-Datasheet-13.pdf*.
[142] D. Ward A. and Exon, J., La, T., "Using Rogowski coils for transient current measurements," *Engineering Science & Education Journal,* vol. 2, pp. 105-113, 1993.
[143] S. Lee, S. Saw, R. Rawat, P. Lee, R. Verma, A. Talebitaher, S. Hassan, A. Abdou, M. Ismail and A. Mohamed, "Measurement and processing of fast pulsed discharge current in plasma focus machines," *J. Fusion Energy,* vol. 31, pp. 198-204, 2012.

[144] S. Lee, S. Saw H., A. Abdou E. and H. Torreblanca, "Characterizing Plasma Focus Devices—Role of the Static Inductance—Instability Phase Fitted by Anomalous Resistances," *J Fusion Energ,* vol. 30, pp. 277, 2010.
[145] C. Moreno, H. Bruzzone, J. Martínez and A. Clausse, "Conceptual engineering of plasma-focus thermonuclear pulsors," *Plasma Science, IEEE Transactions On,* vol. 28, pp. 1735-1741, 2000.
[146] T. Yamamoto, K. Shimoda, K. Kobayashi and K. Hirano, "Correlation between Plasma Dynamics and Emmision of Deuteron Beam, X-Rays and Neutrons in a Plasma Focus Discharge," *Japanese Journal of Applied Physics,* vol. 23, pp. 242, 1984.
[147] M. Zakaullah, I. Akhtar, G. Murtaza and A. Waheed, "Imaging of fusion reaction zone in plasma focus," *Physics of Plasmas (1994-Present),* vol. 6, pp. 3188-3193, 1999.
[148] A. Mohamed E., "A dense plasma focus device as a pulsed nuetron source for material identification," *PhD Dissertation, Kansas State University,* 2015.
[149] A. Abdou E., M. Ismail I., A. Mohamed I., S. Lee, S. Saw H. and R. Verma, "Priliminary results of Kansas State University Dense Plasma Focus," *IEEE Transactions on Plasma Science,* vol. 40, pp. 2741, 2012.
[150] N. Neog K. and S. Mohanty R., "Study on electron beam emission from a low energy plasma focus device," *Physics Letters A,* vol. 361, pp. 377-381, 2007.
[151] P. Knoblauch, F. Lorenzo Di, V. Raspa, A. Clausse and C. Moreno, "Design, hard X-ray source chracterization and applications of a plasma focus tailored for flash hard X-ray imaging," *Phys. Scr.,* vol. T131, 2008.
[152] N. Filippov V., T. Filippova I., M. Karakin A., V. Krauz I., V. Tykshaev P., V. Vinogradov P., Y. Bakulin P., V. Timofeev V., V. Zinchenko F. and J. Brzosko R., "Filippov type plasma focus as intense source of hard X-rays (E x ≃ 50 keV)," *Plasma Science, IEEE Transactions On,* vol. 24, pp. 1215-1223, 1996.
[153] M. Shafiq, S. Hussain, A. Waheed and M. Zakaullah, "X-ray emission from a plasma focus with high-Z inserts at the anode tip," *Plasma Sources Sci. Technol.,* vol. 12, pp. 199, 2003.
[154] A. Tartari, R. Da A., C. Bonifazzi and M. Marziani, "Energy spectra measurements of X-ray emission from electron interaction in a dense plasma focus device," *Nuclear Instruments and Methods in Physics Research Section B: Beam Interactions with Materials and Atoms,* vol. 213, pp. 206-209, 2004.

[155] V. Raspa, L. Sigaut, R. Llovera, P. Cobelli, P. Knoblauch, R. Vieytes, A. Clausse and C. Moreno, " Plasma focus as a powerful hard X-ray source for ultrafast imaging of moving metallic objects ," *Brazilian Journal of Physics,* vol. 34, pp. 1696--1699, 2004.
[156] V. Raspa, C. Pavez, L. Sigaut, C. Moreno, R. Vieytes, A. Clausse, P. Silva, M. Zambra and L. Soto, "Determination of the effective energy of pulsed powerful hard X-ray sources based on pinch plsama focus disharges," *American Institute of Physics,* vol. 6th International conference on dense Z-pinches, 2006.
[157] V. Raspa, C. Moreno, L. Sigaut and A. Clausse, "Effective hard x-ray spectrum of a tabletop Mather-type plasma focus optimized for flash radiography of metalic objects," *Journal of Applied Physics,* vol. 102, 2007.
[158] V. Raspa and C. Moreno, "Radiographic method for measuring the continuum hard X-ray output spectrum of a Plasma Focus device," *Physics Letters A,* vol. 373, pp. 3659-3662, 2009.
[159] J. Shultis Kenneth and R. Faw E., *Fundamentals of Nuclear Science and Engineering.* NW: Taylor & Francis Group, 2007.
[160] *Tables od X-ray Attenuation Coefficinet*.
[161] S. Duclos J., "Scintillator Phosphors for Medical Imaging, enabling life-saving diagnostics," *Electrochem. Soc. Interface,* vol. 7, pp. 34-38, 1998.
[162] G. Decker and R. Wienecke, "Plasma focus devices," *Physica B + C,* vol. 82, pp. 155-164, 1976.
[163] F. Castillo, J. Herrera, J. Rangel, A. Alfaro, M. Maza, V. Sakaguchi, G. Espinosa and J. Golzarri, "Neutron anisotropy and X-ray production of the FN-II dense plasma focus device," *Brazilian Journal of Physics,* vol. 32, pp. 3-12, 2002.
[164] C. Moreno, J. Martínez, M. Vénere, A. Clausse, R. Barbuzza and M. Del Fresno, "Non-conventional radiographic and tomographic applications of a compact plasma focus," in *Proceedings of the Regional Conference on Plasma Research in 21st Century: 7–12 may 2000; Bangkok, Thailand,* 2000, pp. 61-63.
[165] J. F. Martínez, R. Llovera and A. Tartaglione, "Ultrafast x-ray introspective imaging of metallic objects using a plasma focus," *Nukleonika,* vol. 46, pp. S33-S34, 2001.
[166] M. Venere, C. Moreno, A. Clausse, R. Barbuzza and M. Del Frenso, "Tomographic system based on plasma focus X-ray," *Nukleonika,* vol. 46 (supplement 1), pp. S93, 2001.

[167] C. Moreno, V. Raspa, L. Sigaut, R. Vieytes and A. Clausse, "Plasma-focus-based tabletop hard x-ray source for 50 ns resolution introspective imaging of metallic objects through metallic walls," *Appl. Phys. Lett.,* vol. 89, pp. 091502-091502-3, 2006.
[168] A. Lehnert L. and K. Kearfott J., "The Detection of Explosive Materials: Review of Consideration and Methods," *Nuclear Technology,* vol. 172, pp. 325-334, 2010.
[169] Hussein,Esam, M., A., "Detection of Explosive Material Using Nuclear Rdaiation: A critical review," *Detector Physics and Apllication,* vol. 1736, 1993.
[170] M. Marshal and J. C. Oxley, Eds., *Aspects of Explosives Detection.* Great Britain: Elsevier B. V., 2009.
[171] R. Ewing G., D. Atkinson A., G. Eiceman A. and G. Ewing J., "A critical review of ion mobility spectrometry for the detection of explosives and explosive related compunds," *Talanta,* vol. 54, pp. 515-529, 2001.
[172] S. Singh and M. Singh, "Explosives detection systems (EDS) for aviation security," *Signal Process,* vol. 83, pp. 31-55, 1, 2003.
[173] K. Furton G. and L. Myers J., "The scientific foundation and efficacy of the use of canines as chemical detectors for explosives," *Talanta,* vol. 54, pp. 487-500, 2001.
[174] R. Verhagen, C. Cox, M. Mauchangu, B. Weetjens and M. Billet, *Mine Detection Dogs: Training, Operations and Odour Detection.* Geneva, Switzerland: Geneva International Center for Humanitarian Demining, 2003.
[175] J. Shaw A., N. Seldomridge L., D. Dunkle L., P. Nugent W., L. Spangler H., J. Bromenshenk J., C. Henderson B., J. Churnside H. and J. J. Wilson, "Polarization lidar measurements of honeybees in flight for locating landmines," *Optics Express,* vol. 13, pp. 5853-5863, 2005.
[176] C. Bruschini, B. Gros, F. Guerne, P. Pièce and O. Carmona, "Ground penetrating radar and imaging metal detector for antipersonnel mine detection," *J. Appl. Geophys.,* vol. 40, pp. 59-71, 10, 1998.
[177] J. Federici F., B. Schulkin, F. Huang, D. Gary, R. Barat, F. Oliveira and D. Zimdars, "THz imaging and sensing for security applications- explosive, weapons and drugs," *Semiconductor Science and Technology,* vol. 20, 2005.

[178] D. Sheen M., D. McMakin L., H. Collins D., T. Hall E. and R. Severtsen H., "Concealed explosive detection on presonnel using a wideband holographic millimeter-wave imaging system," *Signal Processing, Sensor Fusion, and Target Recognition V,* vol. 2755, pp. 503-513, 1996.

[179] D. Sheen M., D. McMakin L. and T. Hall E., "Three-dimensional millimeter-wave imaging for concealed weapon detection," *IEEE Trans. Microwave Theory and Techniques,* vol. 49, pp. 1581-1592, 2001.

[180] A. Buffler, "Contraband detection with fast neutrons ," *Radiation Physics and Chemistry,* vol. 71, pp. 853-861, 2004.

[181] B. Király, L. Oláh and J. Csikai, "Neutron-based techniques for detection of explosives and drugs," *Radiat. Phys. Chem.,* vol. 61, pp. 781-784, 6, 2001.

[182] N. Kardjilov, A. Hilger, I. Manke, M. Strobl, M. Dawson and J. Banhart, "New trends in neutron imaging," *Nuclear Instruments and Methods in Physics Research Section A: Accelerators, Spectrometers, Detectors and Associated Equipment,* vol. 605, pp. 13-15, 6/21, 2009.

[183] A. Buffler, K. Bharuth-Ram, F. Brooks D., M. Allie S., M. Herbert, M. Nchodu R. and B. Simpson R., "Elemental analysis by fast neutrons," *Proc. SPIE,* vol. 2867, 1997.

[184] F. Schultz J., D. Hensley C., D. Coffey E., D. Chapman J., B. Caylor A. and R. Bailey D., "The Pulsed Interrogation Neutron and Gamma (PING) System," *CONF-9110168,* 1992.

[185] P. Bach, M. Jatteau, J. Ma L. and C. Lambermont, "Industrial analysis possibilities using long-life sealed-tube neutron generators," *Journal of Radioanalytical and Nuclear Chemistry,* vol. 168, 1993.

[186] A. Compton H., "A quatum theory of the scattering of x-rays by light elements," *Phys. Rev.,* vol. 21, pp. 483-502, 1923.

[187] L. Grodzins, "Photons In - Photons Out: Non-Destructive Inspection of Containers Using X-Ray and Gamma Ray Techniques," *Proceeding of the First International Symposium on Explosive Detection Technology,* pp. 201-211, 1991.

[188] M. C. Green and L. D. Partain, "High-throughput baggage scanning employing x-ray diffraction for accurate explosives detection," in *NDE for Health Monitoring and Diagnostics,* 2003, pp. 63-72.

[189] S. Tang and E. M. A. Hussein, "Use of isotopic gamma sources for identifying anti-personnel landmines," *Applied Radiation and Isotopes,* vol. 61, pp. 3-10, 7, 2004.

[190] A. A. Faust, R. E. Rothschild, P. Leblanc and J. E. McFee, "Development of a coded aperture x-ray backscatter imager for explosive device detection," *Nuclear Science, IEEE Transactions On,* vol. 56, pp. 299-307, 2009.
[191] W. Dunn L., K. Banerjee, A. Allen and v. Meter J., "Feasibility of a method to identify targets that are likely to contain a conventional explosives," *Nuclear Instruments and Methods in Physics Research,* vol. B 263, pp. 179-182, 2007.
[192] K. Loschke W. and W. Dunn L., "Detection of Chemical Explosives using Multiple Photon Signature," *Applied Radiation and Isotopes,* vol. 68, pp. 884-887, 2010.
[193] J. Lowrey D. and W. Dunn L., "Signature- Based Radiation Scanning using Radiation Interrogation to Detect Explosives," *Applied Radiation and Isotopes,* vol. 68, pp. 893-895, 2010.
[194] G. Harding, W. Gilboy and B. Ulmer, "Photon-induced Positron Annihilation Radiation (PIPAR) – a Novel Gamma ray Imaging Technique for Radiographically Dense Materials," *Nuclear Instruments and Methods in Physics Research,* vol. 398, pp. 409-422, 1997.
[195] *https://rsicc.ornl.gov/codes/ccc/ccc7/ccc-740.html*.
[196] *A general Monte Carlo N-Particle (MCNP) transport code*.
[197] Anonymous "MCNP — A general Monte Carlo N-particle transport code, version 5,
Volume 1; overview and theory," Los Alamos National Laboratory, X-5 Monte Carlo Team, 2003.

Appendix (i) MATLAB code used to calculate the Hard X-ray Spectrum

```
clear;
load alltables;
% N=number of energy points, no of Energy bins are N-1
N=100; E_min=30; E_max=140;
Energy=zeros(N,1);
Initial_Spectrum=zeros(N,2);
%----------Initial spectrum-------------------------
Energy(1)=E_min;
for i=2:N
    Energy(i)=Energy(i-1)+(E_max-E_min)/(N-1);
end
Energy_bin=Energy(2)-Energy(1); %The energy in keV.
phi=sin(pi*(Energy-E_min)./(E_max-E_min)).*exp(-0.030*(Energy-
E_min));
Initial_Spectrum(:,2)=phi;
Initial_Spectrum(:,1)=Energy;
% normalizing the spectrum distribution
Initial_Spectrum(:,2)=Initial_Spectrum(:,2)/(trapz(Initial_Spec-
trum(:,1),Initial_Spectrum(:,2)));
Initial_Spectrum(:,:)=abs(Initial_Spectrum(:,:));
plot(Initial_Spectrum(:,1),Initial_Spectrum(:,2));
figure;
% --------------lambda is the initial factor--------------
lambda=ones(N,2);
lambda(:,1)=Initial_Spectrum(:,1);
% -----------------screen response match-----------------
screen_response_matched=zeros(N,2);
screen_response_matched(:,1)=Energy;
for i=1:100
    screen_response_matched(i,2)=interpolation_screen(En-
ergy(i));

end
%--------------------attenuation response match (/mm not cm)
%--this one is for cupper, if you want one elese you should go
to the
%attenuation function and choose the material table.
Attenuation_tables_matched=zeros(N,2);
Attenuation_tables_matched(:,1)=Energy;
for i=1:100
    Attenuation_tables_matched(i,2)=interpolation_attenua-
tion(Energy(i));
end
%------------------------we need equations equal to thicknesses
we have
```

```
%-------- in our case we have 100 thickness after interpolating
data.--
system1=zeros(N,N);
system2=zeros(N,N);
for j=1:100
    for k=1:100
        system1(j,k)=(lambda(k,2))*(Initial_Spec-
trum(k,2))*(screen_response_matched(k,2))*exp(-(Attenuation_ta-
bles_matched(k,2))*(strip_attenuation(j,3)));
        system2(j,k)=(lambda(k,2))*(Initial_Spec-
trum(k,2))*(screen_response_matched(k,2));

    end
end

summation1=zeros(N,1);
summation2=zeros(N,1);
for j=1:100
    for k=1:100
        summation1(j)=summation1(j)+ system1(j,k) ;
        summation2(j)=summation2(j)+ system2(j,k) ;
    end
end
summation= summation1./summation2;
hold on;
%figure;
plot(strip_attenuation(:,3),strip_attenuation(:,4),strip_attenu-
ation(:,3),summation(:,1));
%--- starting from here we will change lambda values to match
the responses
%to eachother.
% ************************************************************
system1=zeros(N,N);
system2=zeros(N,N);
trials=20;
lambda1=ones(1,trials);
lambda2=ones(1,N);
B=zeros(N,trials);
for i=1:N              % number of trials to see which is best!
    for m=1:trials
        lambda1(1,m)=(m/10)*lambda1(1,trials/2);
    end
    for l=1:trials
    lambda2(1,i)=lambda1(1,l);

        for j=1:100
            for k=1:100
```

```
                system1(j,k)=(lambda2(1,k))*(Initial_Spec-
trum(k,2))*(screen_response_matched(k,2))*exp(-(Attenuation_ta-
bles_matched(k,2))*(strip_attenuation(j,3)));
                system2(j,k)=(lambda2(1,k))*(Initial_Spec-
trum(k,2))*(screen_response_matched(k,2));
            end
        end
summation1=zeros(N,1);
summation2=zeros(N,1);
for j=1:100
    for k=1:100
        summation1(j)=summation1(j)+ system1(j,k) ;
        summation2(j)=summation2(j)+ system2(j,k) ;
    end
end
summation= summation1./summation2;
%error=strip_attenuation(:,4)-summation(:,1);
A=cov(summation(:,1),strip_attenuation(:,4));
B(i,l)=A(1,2);

%hold on;
%plot(strip_attenuation(:,3),error);
%plot(strip_attenuation(:,3),summation(:,1));
    end
    lambda2=ones(1,N);

end
**************************************************************************

function [ g ] = interpolation_screen(xi)
load alltables;
A=find(screen_response(:,1)>=xi);
b=A(1);
x1=screen_response(b-1,1);
x2=screen_response(b,1);
y1=screen_response(b-1,3);
y2=screen_response(b,3);
g=y1+(((xi-x1)*(y2-y1))/(x2-x1));

end

..........................................................................
function [g] =interpolation_attenuation(xi)
load alltables;
if xi>=300
    xi=300;
end
A=0;b=0;x1=0;x2=0;y1=0;y2=0;
```

```
A=find(Attenuation_tables(:,3)>=xi);
b=A(1);
x1=Attenuation_tables(b-1,3);
x2=Attenuation_tables(b,3);
y1=Attenuation_tables(b-1,4);
y2=Attenuation_tables(b,4);
g=y1+(((xi-x1)*(y2-y1))/(x2-x1));
end
```

Appendix (ii) An example of the input file of the MCNP-5 code

```
c Material Detection with X ray scatter on Al Target
c ********** Block 1: Cell Cards ******************
  1 0 -11                          IMP:P=1 IMP:N=1      $ INSIDE THE CHAMBER
  2 2 -0.0012  11 -10              IMP:P=1 IMP:N=1      $ THE CHAMBER THICKNESS air
  3 2 -0.0012 10 30 -12 17 18 19
        37  40                     IMP:P=1 IMP:N=1      $ THE ROOM
  4 3  -0.96  12 -13               IMP:P=1 IMP:N=1      $ WALL THICKNESS CONCRETE wall
  5 0  13                          IMP:P=0 IMP:N=0      $ THE GRAVE YA4RD OUTSIDE
  8 49 -3.667 -16                  IMP:P=1 IMP:N=1      $ Sodium Idiode PMT2
  9 13 -2.6989 -41                 IMP:P=1 IMP:N=1      $ target Material
  118 49 -3.667 -18                IMP:P=1 IMP:N=1      $ Sodium Idiode PMT1
  119 6 -1.032 -19                 IMP:P=1 IMP:N=1      $ plastic cyntillator PMT3
  130 37   -8.65 -30 16            IMP:P=1 IMP:N=1      $ Cd filter on PMT2
  137 7 -11.35  -37                IMP:P=1 IMP:N=1      $ lead shield
  140 7 -11.35  -40                IMP:P=1 IMP:N=1      $ lead shield
  141 1 -7.8212 -17 41             IMP:P=1 IMP:N=1      $ target thickness

c ********** Block 2: Macrobodies ******************
   10  RCC 0 0 -14.5 0 0 29 6.4                    $ THE Outer CYLINDER of the chamber
   11  RCC 0 0 -14.5 0 0 29 6.0                    $ THE Inner CYLINDER of the chamber
   12  RPP -663 102 -196 597 -152 208              $ THE Inner BOX of room
   13  RPP -693 132 -226 627 -182 238              $ THE Outer BOX of room
   16  RCC -17.3 45.3 0 -7.142 2.599 0 3.8         $ PMT2 NaI
   17  RCC  0 40 -15 0 0 30 14.52                  $ target outer surface
   41  RCC  0 40 -15 0 0 30 14.5                   $ target inner surface
   18  RCC -14.5 53 0 -7.142 2.599 0 3.8           $ PMT2 NaI
   30  RCC -17.193 45.27 0 -7.3296 2.6678 0 3.9    $ 0.5 mm Cd filter at PMT2
   19  RCC -19.8 38.8 0 -2.39 0.87 0 2.54          $ PMT3 Plastic
   37  box -14.8 22.7 -15 1.7365 9.8481 0 -44.3163 7.8142 0 0 0 30   $ Shield Lead
   40  box  2.8 55 -15 3.4748 9.5472 0 -42.3 15.36 0 0 0 30          $ Shield lead

c ********** Block 3: Data Cards ******************
```

```
c ----- Xray source at the origin----------------------------------------------------
SDEF  POS 0 0 0 PAR=2   ERG=d1                    $ particle type (photons), position, Energy
si1 A  0 0.02 0.025742 0.030199 0.031391 0.034172 0.036954
       0.04053 0.043444 0.04649 0.049139 0.051788 0.05404
       0.055497 0.058675 0.061457 0.063974 0.066887 0.069801
       0.071921 0.074967 0.077881 0.08053
       0.083444 0.086755 0.089139 0.091921 0.095232 0.098808
      0.103576 0.108079 0.111788 0.115629
       0.119338 0.123974 0.129007 0.133907 0.137881
      0.142 0.142384
sp1   0 0 0.00 0.000295 0.002295 0.006131 0.009475 0.012492
      0.014492 0.016098 0.017016 0.017508 0.017869 0.017900
      0.017967 0.017639 0.017246 0.016689 0.015967 0.01531
      0.014426 0.013541
      0.012656 0.011672 0.010623 0.00977 0.008852 0.007869 0.00682
      0.005541 0.004459 0.003639
      0.002885 0.002262 0.001574 0.000918
      0.000459 0.000164
      0.000033 0.0
F16:p  118                              $ FLUENCE AVERAGE OVER CELL 8,   PMT2
F26:p  8                                $ FLUENCE AVERAGE OVER CELL 118, PMT1
F36:p  119                              $ FLUENCE AVERAGE OVER CELL 119, PMT3
MODE p
NPS 100000000
c PRINT 110
c ---------------------------------------------------------------
c  Energy groups
c ---------------------------------------------------------------
  E16   0.005  0.01  0.015  0.02  0.025  0.03  0.035  0.04  0.045  0.05
        0.055  0.06  0.065  0.07  0.075  0.08  0.085  0.09  0.095  0.100
        0.105  0.110 0.115  0.120 0.125  0.130 0.135  0.14  0.145  0.150
        0.155  0.16  0.165  0.17  0.175  0.18  0.185  0.19  0.195  0.200
  E26   0.005  0.01  0.015  0.02  0.025  0.03  0.035  0.04  0.045  0.05
        0.055  0.06  0.065  0.07  0.075  0.08  0.085  0.09  0.095  0.100
```

```
      0.105  0.110 0.115  0.120 0.125  0.130 0.135  0.14  0.145  0.150
      0.155  0.16  0.165  0.17  0.175  0.18  0.185  0.19  0.195  0.200
 E36  0.005  0.01  0.015  0.02  0.025  0.03  0.035  0.04  0.045  0.05
      0.055  0.06  0.065  0.07  0.075  0.08  0.085  0.09  0.095  0.100
      0.105  0.110 0.115  0.120 0.125  0.130 0.135  0.14  0.145  0.150
      0.155  0.16  0.165  0.17  0.175  0.18  0.185  0.19  0.195  0.200
c ************** MATERIALS **********************
c ----------steel-------------------------------------------------------
c          Carbon Steel TN-68 (Table 5.3-1)
c         Density = 7.8212 g/cm^3;  Composition by atom fraction
c ---------------------------------------------------------------------
m1   26000.50c  0.95510
     6000.60c   0.04490
c ---------Air------------
m2    7014.50c  -0.7558
      8016.50c  -0.2314
      18000.35c -0.0128
c --------Concrete--------
m3    1001.50c   -.0056
      8016.60c   -.4983
      11023      -.0171
      12000      -.0024
      13027.50c  -.0456
      14000.50c  -.3158
      16000      -.0012
      19000.50c  -.0192
      20000.50c  -.0826
      26000.50c  -.0122
c -------Helium----------
m4    2003.60c 1
c ---------------------------------------------------------------------
c       material: borated polyethylene d=1.00 g/cm^3  CH2 + 8 wt% B4C
c               B-11 5.029; B-10 1.234; C 80.595; H 13.143
c ---------------------------------------------------------------------
```

```
 m5   1001.50c -0.13143
      5010.50c -0.01234
      5011.50c -0.05029
      6000.50c -0.80594
c ---------------------------------------------------------------
c plastic cyntillator material with density 1.032 g/cm3
c ---------------------------------------------------------------
m6   1001 -0.085000
     6012 -0.915000
c  ---------------------------------------------------
c  Natural LEAD (nominal density 11.35 g/cm^3
C    [1.4% 204Pb;  24.1% 206Pb; 22.1% 207Pb; 52.4% 208Pb]
c  ---------------------------------------------------
m7   82000.50c -1.00000
c    ***********************************************************
c     Polypropylene Disk TN-68 (Table 5.3-1)
c        Density = 0.90 g/cm^3;   Composition by atom fraction
c    ***********************************************************
m8     6012.50c .33480
       1001.50c .66520
c ********************************************************************
c Cadmium, rho = 8.65 g/cc
C ********************************************************************
m9 48000 -1.000000
c ********************************************************************
c Material inside the target
C Water Rho= 1g/cm3
c ********************************************************************
m10     1001 -0.111894
        8016 -0.888106
c -------------the stinless steel  rho = 7.92
m11         24000.50c -0.190 $ Cr
           25055.50c -0.020 $ Mn
           26000.50c -0.695 $ Fe
```

```
         28000.50c -0.095 $ Ni
c ************************************************************
c ------------ Hydrogen
m12     1001.60c   -1.00000
c ************************************************************
c ------Aluminum composition   rho=2.6989
m13     13027.50c   -1.00000
c ************************************************************
c ------Tungsten  rho = 19.3
m14     074000.50c   -1.00000
c ************************************************************
c ----- copper-----  rho=8.960
m15     29000.50c     -1.00000
c ************************************************************
c ----- plate glass     rho=2.4
m16       8016.50c -0.459800
          11023.50c -0.096441
          14000.50c -0.336553
          20000.50c -0.107205
c ************************************************************
c     SOIL: [Jacob, Radn. Prot. Dos. 14, 299, 1986]**** 1.625 g/cm^3
m17     1001.60c  -0.021
        6000.50c  -0.016
        19000.50c  -0.013
        26000.50c  -0.011
        20000.50c  -0.041
        13027.50c  -0.050
        14000.50c -0.271
        8016.50c  -0.577
c ************************************************************
c Carbon, Graphite, rho = 1.70 g/cc
m18  6000.60c 1.00
c ************************************************************
c Explosive Compounds
```

```
c ***********************************************************
c TNT, rho = 1.654
m19 1001.60c  -0.022189
        6000.50c -0.370160
        7014.50c  -0.185004
        8016.50c  -0.422648
c ***********************************************************
C RDX rxplosive C 3  H 6  N 6  O 6 --- rho=1.806
m20 1001.60c  -0.027227
        6000.50c -0.162222
        7014.50c -0.378361
        8016.50c -0.432190
c ***********************************************************
c HMX Density ( g / cm3 )= 1.902
m21 1001.60c  -0.027227
        6000.50c -0.162222
        7014.50c -0.378361
        8016.50c -0.432190
c ***********************************************************
c NG ( Nitroglycerin) Density ( g / cm3 )= 1.13
m22 1001.60c  -0.022193
        6000.50c -0.158671
        7014.50c  -0.185040
        8016.50c  -0.634096
c ***********************************************************
c PETN Density ( g / cm3 )= 1.773
m23 1001.60c  -0.025506
        6000.50c -0.189961
        7014.50c  -0.177223
        8016.50c  -0.607310
c ***********************************************************
c EGDN (Ethylene Glycol Dinitrate) Density ( g / cm3 )= 1.490
m24 1001.60c  -0.026514
        6000.50c -0.157970
```

```
        7014.50c -0.184222
        8016.50c -0.631294
c ************************************************************
c AN (Ammonium Nitrate) Density ( g / cm3 )= 1.730
m25 1001.60c   -0.050370
        7014.50c  -0.349978
        8016.50c  -0.599652
c ************************************************************
c NC (Nitrocellulose) Density ( g / cm3 )= 1.660
m26 1001.60c -0.028320
        6000.50c -0.289258
        7014.50c -0.168664
        8016.50c -0.513758
c ************************************************************
c Fertilizer Density (Fert B) ( g / cm3 )= 0.990
m27 1001.60c  -0.0000504
        8016.50c  -0.0007176
       11023.50c -0.0087350
       12000.50c -0.0002058
       16000.50c -0.0001590
       17000 -0.4778000
       19000.50c -0.5117000
       20000.50c -0.0002758
       35000.50c -0.0003303
c ************************************************************
c Gasoline, rho = 0.6837
m28 1001.60c   -0.160000
        6000.50c  -0.840000
c ************************************************************
c Oil
c Crude Oil Density ( g / cm3 )= 0.973
m29 1001.60c   -0.120000
        6000.50c  -0.850000
        7014.50c  -0.010500
```

```
        8016.50c  -0.007750
       16000.50c -0.030250
c ************************************************************
c Hydraulic Oil Density ( g / cm3 )= 1.28
m30 1001.60c    -0.040509
        6000.50c   -0.585083
        8016.50c   -0.078042
        15000.50c -0.037771
        17000 -0.258941
c ************************************************************
c Lard Oil  Density ( g / cm3 )= 0.915
m31  1001.60c   -0.117673
         6000.50c  -0.779024
         8016.50c  -0.103657
c ************************************************************
c Paraffin Wax Density ( g / cm3 )= 0.930
m32         1001.60c -0.148605
         6000.60c -0.851395
c ************************************************************
c Polyethylene Density ( g / cm3 )              = 0.94
m33 1001.50c -0.143716
        6000.50c -0.856284
c ************************************************************
c Polyethylene Terephthalate    Density      = 1.380
m34 1001.50c -0.041960
        6000.50c -0.625016
        8016.50c -0.333024
c ************************************************************
c UREA: Density (g/cm3)                      = 1.323
m35         1001.50c    -0.067131
          6000.50c    -0.199999
          7014.50c    -0.466459
          8016.50c     -0.266411
c ************************************************************
```

```
c PARAFFIN WAX: Density (g/cm3)   0.93
m36  1001.50c    -0.148605
         6000.50c   -0.851395
c ************************************************************
c Cadmium   Density ( g / cm3 )= 8.65
m37  48000.50c -1.000000
c ************************************************************
c                Lead (density 11.35 g/cc)
c -------------------------
M38   82000.50c  -1.0   $elemental Pb and atomic abundance
c ****************************************************
c             Ceramic (2.403)
c ---------------------------------------------------
M39   8016.50c    0.6364  $Oxygen
     13027.50c   0.1818  $Al
     14000.50c   0.1818  $Si
c ****************************************************
c    Granite (2.73 g/cc)
c ---------------------------------------------------
M40   1001.50c   0.027122  $Hydrogen
     6000.50c   0.000502  $Carbon
     8016.50c   0.607735  $Oxygen
    11023.50c   0.025866  $Sodium
    12000.50c   0.018081  $Magnesium
    13027.50c   0.062783  $Alumminum
    14000.50c   0.205927  $Silicon
    19000.50c   0.013939  $Potassium
    20000.50c   0.018960  $Calcium
    26000.50c   0.019086  $Iron
c ****************************************************
c    Limestone (2.35 g/cc)
c ---------------------------------------------------
M41   6000.50c   0.2       $Carbon
     8016.50c   0.6       $Oxygen
```

```
    20000.50c   0.2       $Calcium
c ***************************************************
c      Ash (0.641 g/cc) General Wood wrong components
c ---------------------------------------------------------
M42    6000.50c   0.1300  $Carbon
       8016.50c   0.4200  $Oxygen
      12000.50c   0.0100  $Magnesium
      13027.50c   0.0200  $Aluminum
      19000.50c   0.0800  $Potassium
      20000.50c   0.3400  $Calcium
c ---------------------------------------------------
c Acetone  C3H6O  Density (g/cm3) = 0.789900
m43  1001.50c  -0.104122
         6000.50c  -0.620405
         8016.50c  -0.275473
c ---------------------------------------------------------
c Ammonia  NH3 Density (g/cm3) = 0.771
m44  1001.50c  -0.177547
         7014.50c -0.822453
c ---------------------------------------
c Asphalt  (the black glue only) Density (g/cm3) = 1.3
m45  1001.50c    -0.103725
     6000.50c    -0.848050
       7014.50c    -0.006050
      8016.50c    -0.004050
      16000.50c    -0.037700
      23000.50c   -0.000393
       28000.50c   -0.000034
c ---------------------------------------
c  Asphalt Pavement, blacktop. rho=2.5784
m46  1001.50c           -0.007781
        6000.50c           -0.076175
         7014.50c           -0.000363
        8016.50c           -0.459103
```

```
          11023.50c         -0.011659
        12000.50c         -0.021757
         13027.50c         -0.051009
          14000.50c         -0.231474
           16000.50c         -0.002804
          19000.50c         -0.017058
           20000.50c         -0.084471
          22000.50c         -0.003403
           23000.50c         -0.000024
           25055.50c         -0.000362
          26000.50c         -0.031375
          28000.50c         -0.000002
         82000.50c         -0.001179
c -------------------------------------------------
c ---------------- sand 1.7 g/c3 -----
m47  1001.50c   -0.007833
         6000.50c   -0.003360
         8016.50c   -0.536153
        11023.50c  -0.017063
        13027.50c  -0.034401
        14000.50c  -0.365067
       19000.50c   -0.011622
       20000.50c   -0.011212
      26000.50c    -0.013289
c -------------------------------------------------
c            Sugar (1.54 g/cc
c -------------------------------------------------
M48  1001.50c    -0.067134702
         6000.50c    -0.400017318
         8016.50c    -0.532847979
c -----------------------------------------------------------
c Sodium Idiode  Density (g/cm3) = 3.667000
M49  11000 -0.153373
    53000 -0.846627
```